Muad, Anuar Mikdad (2011) Super-resolution mapping. PhD thesis, University of Nottingham.

SUPER-RESOLUTION MAPPING

by

ANUAR MIKDAD MUAD, M.Sc.

Thesis submitted to the University of Nottingham for the degree of Doctor of Philosophy

DECEMBER 2011

Abstract

Super-resolution mapping is becoming an increasing important technique in remote sensing for land cover mapping at a sub-pixel scale from coarse spatial resolution imagery. The potential of this technique could increase the value of the low cost coarse spatial resolution imagery. Among many types of land cover patches that can be represented by the super-resolution mapping, the prediction of patches smaller than an image pixel is one of the most difficult. This is because of the lack of information on the existence and spatial extend of the small land cover patches. Another difficult problem is to represent the location of small patches accurately. This thesis focuses on the potential of super-resolution mapping for accurate land cover mapping, with particular emphasis on the mapping of small patches. Popular super-resolution mapping techniques such as pixel swapping and the Hopfield neural network are used as well as a new method proposed. Using a Hopfield neural network (HNN) for super-resolution mapping, the best parameters and configuration to represent land cover patches of different sizes, shapes and mosaics are investigated. In addition, it also shown how a fusion of time series coarse spatial resolution imagery, such as daily MODIS 250 m images, can aid the determination of small land cover patch locations, thus reducing the spatial variability of the representation of such patches. Results of the improved HNN using a time series images are evaluated in a series of assessments, and demonstrated to be superior in terms of mapping accuracy than that of the standard techniques. A novel super-resolution mapping technique based on halftoning concept is presented as an alternative solution for the super-resolution mapping. This new technique is able to represent more land cover patches than the standard techniques.

List of publications

1. **Muad, A.M. and Foody, G.M. (2011)**, Super-resolution mapping of lakes from imagery with a coarse spatial and fine temporal resolution, International Journal of Applied Earth Observation and Geoinformation. In Press.

2. **Muad, A. and Foody, G.M. (2010).** Super-resolution mapping using multiple observations and Hopfield neural network. In Proceedings of the SPIE Remote Sensing, Toulouse, France, 20-23 September 2010.

3. **Muad, A.M. and Foody, G.M. (2010)**. Super-resolution analysis for accurate mapping of land cover and land cover pattern. In Proceedings of the IEEE International Geoscience and Remote Sensing Symposium (IGARSS), Honolulu, Hawaii, USA, 25-30 July 2010.

4. **Muad, A.M. and Foody, G.M. (2010).** Super-resolution mapping of landscape objects from coarse spatial resolution imagery. In Proceedings of the GEOgraphic Object-Based Image Analysis (GEOBIA), Ghent, Belgium, 29 June - 2 July 2010.

Acknowledgements

First of all, I would like to express my sincere gratitude and thanks to my supervisor, Professor Giles M. Foody. I am grateful to Professor Foody for accepting me as his student and providing guidance, helps and continuous support throughout the period of this study. Without all his help and suggestions, this work would not have been possible. Thanks also to Dr. Doreen Boyd as my co-supervisor. Also, I would like to extend my gratitude and thanks to the Ministry of Higher Education of Malaysia and Universiti Kebangsaan Malaysia for sponsoring my research for a PhD degree at the University of Nottingham and getting my study leave sanctioned. I would like to convey my thanks to all the staff members at the School of Geography, University of Nottingham for their co-operation and support, especially to Jenny Ashmore, Andrea Payne, Carol Gilbourne, Ian Conway, Jonathan Walton, Louise McIntyre, and John Milner. Thanks also to post-doctorate and postgraduate students, especially Wan Hazli Wan Kadir, Dr. Mahesh Pal, Dr. Yuan-Fong Su, Dr. Nurul Islam, Sani Yahaya, Pantelis Arvanitis, and Oluwakemi Akintan for their invaluable assistance and advice as well as their friendship during this work. I wish to extend my thanks to Prof. Aini Hussain, Prof. Azah Mohamed, Prof. Marzuki Mustafa, Dr. Hafizah Husain and Mrs. Normah Adam from Universiti Kebangsaan Malaysia and Dr. Nooritawati Md. Tahir from Universiti Teknologi Mara for their kind help throughout my study. Special recognition is due to my parents, Muad Kulop Mat Alip and Jamaeyah Kamaruddin, family and relatives in Malaysia for their continuous encouragement and support. Special thanks is due to my wife, Rizamul Aili Tajuddin for her endless patience and understanding during all long hours of work that kept me busy in my research.

Table of contents

List of figures

List of tables

List of abbreviations and acronyms

ART	Adaptive Resonance Theory
ARTMAP	Adaptive Resonance Theory MAP
AVHRR	Advanced Very High Resolution Radiometer
DN	Digital Number
ETM+	Enhanced Thematic Mapper Plus
GLCM	Gray-Level Co-occurrence Matrix
HNN	Hopfield Neural Network
HRG	High Resolution Geometry
IBP	Iterative Back-Projection
IDM	Inverse Difference Moment
LIDAR	Light Detection and Ranging
MAP	Maximum A Posteriori
MERIS	Medium Resolution Imaging Spectrometer
ML	Maximum Likelihood
MLP	Multi-Layer Perceptron
MODIS	Moderate Resolution Imaging Spectroradiometer
MRF	Markov Random Field
MS	Multispectral
PAN	Panchromatic
POCS	Projection Onto Convex Sets
RMSE	Root Mean Squared Error
RSR	Relative Spectral Response
RVM	Relevance Vector Machine
SPOT	Système Probatoire d'Observation de la Terre
SVM	Support Vector Machine
UTM	Universal Transverse Mercator

1. Introduction

1.1. Overview

The mosaic of land cover types that occur on the Earth's surface is a key variable in a range of environmental systems (Falcucci et al., 2007; Lucas et al., 2007). For example, the landscape mosaic impacts on a large and diverse array of issues that include the aesthetic appeal of a region, its biodiversity and its climate. Land cover and land cover change are, for example, critical variables affecting ecological systems (Ruelland et al., 2010; Brink and Eva, 2009; Serra et al., 2008). Information on land cover is, therefore, required in a range of studies, with some, especially those associated with landscape ecology, requiring information on the nature of landscape patches (e.g. their size, shape etc). Remote sensing has considerable potential as a source of information on land cover at a range of spatial and temporal scales (Boyd and Foody, 2011; Addink et al., 2010; Buermann et al., 2008).

Although remote sensing is widely used as a source of land cover information for ecological studies (Newton et al., 2009) there are many factors that limit the accuracy of derived land cover information (Foody, 2002). These include the classification algorithm and pre-processing methods used as well as the temporal and

spatial resolution of the data. The latter is the key focus of attention in this thesis, with the accuracy may be characterised known to be a function of the spatial resolution of the imagery and minimum mapping unit used (Saura, 2002).

The land cover mosaic of a region typically comprises a set of patches of relatively homogenous cover that can be considered as objects within a remotely sensed image. To characterise objects accurately it is important that the image spatial resolution or pixel size is smaller than the typical size of the objects (Woodcock and Strahler, 1987). This may require use of imagery with a fine spatial resolution.

Spatial resolution can be treated as a variable in sensor selection for a project and needs to be determined in relation to the project's specific goals and sensing systems properties (Warner et al., 2009). Imagery with a fine spatial resolution have been acquired from space for many years, notably through military systems such as the US Keyhole (KH) or CORONA series of satellites from the late 1950s to early 1970s (McDonald, 1995; Toutin, 2009). A large number of fine and very fine spatial resolution systems have also been developed in recent years. There are ~36 satellite systems in orbit or scheduled for launch that are able to provide imagery with a spatial resolution of < 3 m (Toutin, 2009). These systems have revolutionised aspects of remote sensing with, for example, the new fine spatial resolution sensing systems now allow mapping at scales ~1:5,000 from ~0.6 m resolution QuickBird imagery (Topan et al., 2009). The main drawback to the use of these systems is the cost of the imagery (Toutin, 2009). For example, Toutin (2009) suggests that even relatively basic image products from fine spatial resolution sensors costs ~US$20 km^{-2} and more highly processed products may be several times more expensive still. Imagery from slightly coarser spatial resolution

systems such as Système Probatoire d'Observation de la Terre High Resolution Geometry (SPOT HRG) (spatial resolution ~4-10 m) costs only ~US$3-5 km^{-2}. Moreover, the extent of the imagery from SPOT HRG is much larger than from IKONOS; some 36 IKONOS images would be required to cover the same area as a single SPOT HRG image (Toutin, 2009). There have also been many major developments in medium-coarse spatial resolution systems (Goward et al., 2009; Justice and Tucker 2009) and, critically, these can provide inexpensive imagery of relatively large areas. Projects may often be constrained to use such relatively coarse spatial resolution imagery for pragmatic reasons.

Often the spatial resolution of a remote sensor is too coarse for the intended application and inappropriate for optimal mapping. Land cover data derived in such circumstances should be used with care. The errors and uncertainties in land cover derived from remote sensing may sometimes go unrecognised and can greatly impact on the characterisation of landscapes (Shao and Wu, 2008). One major problem arising from the use of coarse spatial resolution imagery is mixed pixels (Fisher, 1997). A mixed pixel contains more than one land cover class and cannot be appropriately represented by the standard 'hard' allocation process used in conventional image classification algorithms (one pixel − one class). Unfortunately mixed pixels may be common and the proportion of mixed pixels tends to increase with an increase in pixel size, with mixed pixels typically vastly dominating imagery acquired at a coarse spatial resolution.

There are four common land cover mosaic scenarios that could cause mixed pixel (Fisher, 1997) (Figure 1.1). They are: (1) sub-pixel sized patches: the size of a land

cover class captured within a pixel is smaller than the size of the pixel, thus allowing a space within the pixel for another land cover class; (2) boundary pixel: the size of two or more land cover classes on the ground may be bigger than the size of the pixel, but parts of their boundaries lie in a single pixel; (3) inter-grade: a pixel allocates a space for a transition from a cluster of one class to a cluster of another class; and (4) linear sub-pixel: the length of a land cover class may be longer than a pixel but its width is thinner, and the land cover class runs through a pixel.

A popular adaptation of the standard approach to land cover mapping that allows for mixed pixels is the use of a fuzzy or soft classification (Foody, 1996). The latter allows a pixel to have multiple and partial class membership and outputs typically a set of fraction images, each showing the proportion of the pixel's area that is covered by a specific land cover class. Although attractive in reducing the mixed pixel problems a concern is that the soft classification does not show the spatial distribution of the sub-pixel class fractions limiting its value as a source of information on landscape objects (Atkinson, 1997).

An alternative way to address the mixed pixel problem is to adopt some form of spatial resolution enhancement technique to increase the spatial resolution of imagery (i.e. to reduce the effective pixel size). For example, methods based on image sharpening, especially if the sensor operates at more than one spatial resolution (Mather, 2004) or super-resolution analyses (Tatem et al., 2001a; Lu and Inamura, 2003; Ling et al., 2010). The aim of the latter is to effectively decrease the pixel size, allowing
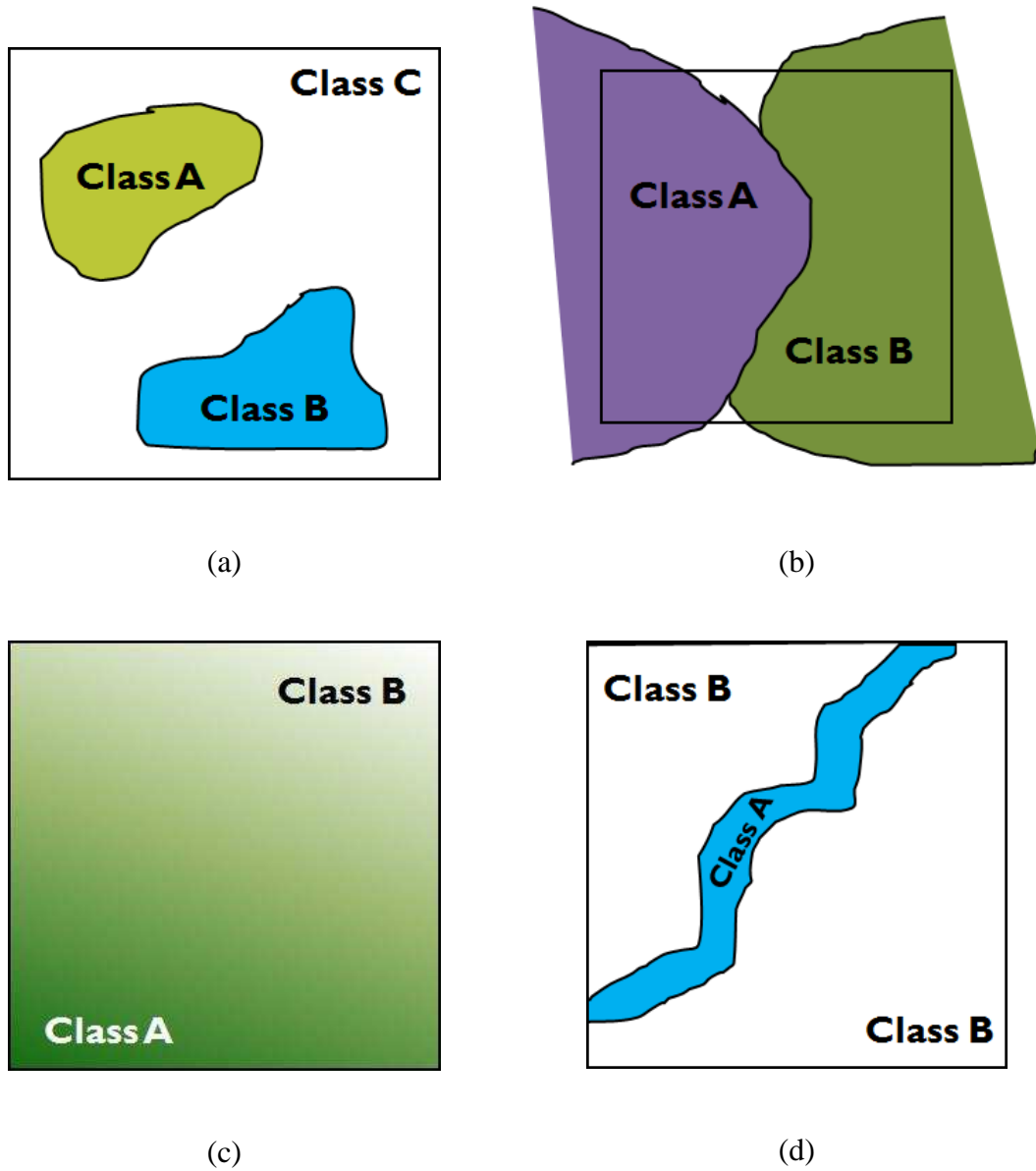
Figure 1-1 Four causes of mixed pixel: (a) sub-pixel sized patches, (b) boundary pixel, (c) inter-grade, and (d) linear sub-pixel (adapted from Fisher, 1997).

interpretation of sub-pixel scale features. Approaches adopted are typically based on either super-resolution restitution or super-resolution mapping (Ling et al., 2010) and their use can add value to relatively inexpensive image data sets.

A variety of super-resolution mapping techniques have been used in remote sensing and related research (Tatem et al., 2001a; Verhoeye and De Wulf, 2002; Mertens et al., 2003, 2004; Foody et al., 2005; Farsiu et al., 2006). Typically these techniques have been applied with a single coarse spatial resolution image as their input. Although the technique may be used to derive a land cover map at a finer spatial scale than the input imagery, there are many concerns with their use. One is that small isolated patches of a land cover class are often not represented or only inaccurately (Kasetkasem et al., 2005). Additionally the use of a single input image may limit the accuracy of land cover representation and the use of multiple coarse resolution images may offer an ability to enhanced accuracy. Given that coarse spatial resolution systems often have a relatively fine temporal resolution it may be possible to derive multiple images of the same site over a short period of time as input to a super-resolution analysis. The images in the time series may differ in subtle ways, with the location of pixels varying slightly due to, for example, minor orbital translations of remote sensing satellites. The slight differences between images can be exploited by combining a time-series coarse spatial resolution images into an integrated image which may contain more information than a single coarse spatial resolution image (Packalen et al., 2006). Exploiting the fine temporal resolution that is characteristic of many coarse spatial resolution remote sensing systems (Ling et al., 2010) may, therefore, facilitate super-resolution analyses.

1.2. Objectives

The work reported in this thesis focuses on the representation of small land cover patches. As illustrated graphically in Figure 1.1 that there are four cases that cause the mixed pixel problem. Many of the current super-resolution mapping techniques are able to solve the 'boundary pixel', 'inter-grade' (e.g. Tatem et al., 2001a), and 'linear sub-pixel' (Thornton et al., 2007) cases. However, there is lack of comprehensive research study on the 'sub-pixel' sized patches case (Zhan et al., 2002). The attention of this thesis is on the 'sub-pixel' case, which the size of the land cover patches is smaller than a pixel.

The key thrust of this thesis is on the derivation of accurate land cover map using super-resolution mapping techniques. In particular, the thesis focuses on two key issues. First the accuracy with which the area of small patches is estimated. Second the accuracy with which the small patches are located geographically.

The main objective of this thesis is to improve current super-resolution mapping techniques as well as to develop a novel super-resolution mapping techniques in order to solve the two challenges listed above.

The improved or new super-resolution mapping techniques should be able to represent small land cover patches accurately. The latter will be demonstrated using a range of measures of accuracy (e.g. site specific, landscape parameter accuracy, object based accuracy, and positional accuracy) and compared with current super-resolution mapping techniques. The improved or new super-resolution mapping techniques should

help to keep the cost of acquiring remotely sensed images as low as possible. This would increase the value for the coarse spatial resolution imagery.

In order to achieve the objectives listed above, experiments reported in this thesis were undertaken using synthetic image and real image (e.g. MODIS 250 m image and a fusion of a time series MODIS 250 m images as well as Landsat ETM+ 30 m is used as a ground data for benchmark comparison). Attention is focused on a real-world application: the mapping of high latitude lakes (Smith et al., 2005). Landscape mosaic that is made up of lakes of varying shape, size and spatial configuration is used as it may contain all the four cases of the mixed pixels, which is highlighted in Figure 1.1, although the attention of the thesis is on the 'sub-pixel' sized patches case.

1.3. Thesis structure

This thesis is organised into eight chapters, including the present chapter. A brief summary of the other chapters is provided below.

Chapter 2 provides an overview of super-resolution techniques including super-resolution restitution (reconstruction) and super-resolution mapping; the differences between these two concepts will be addressed. A brief overview on soft classification techniques is included as they become pre-requisite for many super-resolution mapping techniques. This chapter also provides an overview of different assessment methods for evaluating results of super-resolution mapping techniques such as confusion matrix for site specific accuracy, landscape indices for spatial pattern analysis, object based

analyses for shape characterization and positional accuracy to determine the fitting of the boundary line between land cover patches.

Chapter 3 details the fundamental principles of two standard super-resolution mapping techniques based on a Hopfield neural network (HNN) and pixel swapping techniques. A section that details the fundamental principle of a fuzzy c-means technique will be presented as it can be used to derive soft classification from mixed pixels, which will be used as input for both of the super-resolution mapping techniques. Remote sensing images containing various spatial patterns are used. Sets of coarse spatial pattern images are derived by spatially aggregating the original images. Analyses on these techniques are focused on the site specific accuracy and spatial pattern variogram. This chapter serves as a pilot chapter, which aim to explore the standard techniques. Results of this chapter confirmed the advantages and limitations for each technique and help define the research direction.

Chapter 4 highlights the limitations of the standard HNN and pixel swapping in representing small land cover patches. The parameter setting of the HNN and pixel swapping are evaluated in a series of experiments using a single coarse spatial resolution image. In these experiments, the optimum values of the parameters that can represent small land cover patches are obtained.

Chapter 5 highlights the spatial variability of patch location from the use of the standard HNN and pixel swapping algorithms. It is demonstrated in this chapter that high spatial variability may lead to decreasing accuracy of the site specific assessment.

Using multiple sub-pixels shifted image observations, the spatial variability can be reduced, which lead to accurate localization of small land cover patches.

Chapter 6 outlines an enhanced HNN and pixel swapping methods and demonstrates their application in representing a landscape mosaic that is made up of lakes of varying shape and size from MODIS 250 m images. A fusion of time series MODIS imagery is also presented. A series of assessment such as site specific accuracy, landscape indices, object based characterization and positional accuracy are implemented in order to evaluate the representation of the lakes.

Chapter 7 presents a novel super-resolution mapping technique based on halftoning concept. This new technique provides an alternative to the current super-resolution mapping techniques in which the spatial frequency of the initial distribution of hard classifier at a sub-pixel scale of mixed pixels could be exploited.

Finally in Chapter 8, the conclusions of the research in this thesis are gathered and recommendations for future works are presented.

2. Background

This chapter reviews the background to super-resolution mapping to gain an understanding required for this thesis. Subjects reviewed include the super-resolution restitution, super-resolution mapping, soft classification, as well as accuracy assessment methods.

2.1. Super-resolution restitution

Super-resolution restitution or reconstruction is a technique to construct a fine spatial resolution image from a multiple coarse spatial resolution images by recovering the high-frequency component of image content (Yang and Huang, 2011). Super-resolution restitution consists of image registration from a set of coarse spatial resolution images and image restitution (reconstruction). During the restitution process, this technique combines non-redundant information contained in the coarse spatial resolution images and generate a fine spatial resolution image. This section reviews different approaches of the super-resolution restitution.

2.1.1. Frequency domain approach

The super-resolution concept was first introduced by Tsai and Huang (1984). Given several coarse spatial resolution images, a fine spatial resolution image is constructed in the frequency domain. The frequency domain is obtained through the transformation from the spatial domain using the Fourier transform. Their approach is based on the principles of the shifting property of the Fourier transform. The aliasing relationship between continuous Fourier transform of the original image and the discrete Fourier transform of the observed coarse spatial resolution images is considered. This technique assumes that the original fine spatial resolution is band-limited. It was assumed that the observations of the coarse spatial resolution images sequence are free from degradation and noise.

Kim et al. (1990) restored a fine spatial resolution image from noisy and blurred images. They used a recursive algorithm made up from a combination of two steps of filtering and reconstruction in the frequency domain. The filtering operation is used in the image registration to compensate the degradation and noise, and the reconstruction operation estimates the fine spatial resolution image. Every coarse spatial resolution observation image is assumed to have similar blur and noise characteristics. Later, Kim and Su (1993) made an improvement in this method by considering different amounts of blur for each coarse spatial resolution image. Tikhonov regularization (Tikhonov and Arsenin, 1977) is used to obtain a solution for inconsistent set of linear equations.

The major advantage of this approach is the theoretical simplicity in term of describing the relationship between coarse images and fine image in the frequency

domain. However, every coarse image is assumed to be affected by a translational motion and a linear space invariant blur. This is seemed as a limitation of the frequency domain approaches to handle various situations. Moreover, it is difficult to apply a priori knowledge in this domain because the data are uncorrelated in the frequency domain (Park et al., 2003).

2.1.2. Spatial domain approach

A method to reconstruct a finer spatial resolution image in the spatial domain was proposed by Stark and Oskui (1989) known as projection onto convex sets (POCS). The method is an extension of a convex projection theory used in computed tomography for one-dimensional signals (Oskui and Stark, 1988). The POCS method constructs a finer resolution image by scanning or rotating the image with respect to image-plane detector arrays. Prior information can be incorporated in this method to increase the quality of the image. This method considers the effect of noise in the data. This method requires iterative computation, thus slow convergence is one of its limitations. In addition, because POCS optimizes a purely constraint based objective, it does not converge to a unique solution (Park et al., 2003).

The concept of reconstruction of a 2-D object from its 1-D projection in computed tomography also inspired Irani and Peleg (1991) to reconstruct a fine spatial resolution image. The super-resolution problem is formulated as an Iterative Back-Projection (IBP) procedure. This method starts with an initial guess of a fine spatial resolution image. A set of coarse spatial resolution simulated images are created

corresponding to an observed coarse spatial resolution input image. The simulated images are created by shifting the pixels of the observed input image in the horizontal and vertical directions. The difference between the simulated images and the observed image is computed to improve the initial guess of a fine spatial resolution image. This algorithm projects the difference values backward and includes it while updating the desired fine spatial resolution image. This process is repeated iteratively to minimize the error function. For a single image, the super-resolution process, which is designed for sequences of images, is reduced to a problem of de-blurring an image. This technique converges quickly by fixing stable pixels. When a pixel has the same value or nearly the same value in two successive iterations, the pixel would not be considered in the next iteration, helping to accelerate the convergence process. Unlike the POCS method, the IBP procedure does not involve prior constraints. Both POCS and IBP methods are not restricted to have a specific motion characteristic. They are able to work with smooth motion, linear space variant blur, and non-homogeneous additive noise.

2.1.3. Motionless super-resolution

All the previous methods assume that there is small relative motion in the image sequences, however, Elad and Feuer (1997) demonstrated that motionless super-resolution reconstruction could be made possible from a sequence of coarse spatial resolution images which are spatially aggregated caused by a series of transformations such as geometrical warping, blurring, noisy. A hybrid algorithm is proposed from a combination of maximum likelihood (ML) estimator and the POCS algorithm. This

technique exploits the advantages of the simple ML estimator and the ability of the POCS to incorporate non-ellipsoids constraints. This technique, however, assumes a linear space variant blur, and an additive Gaussian noise.

2.1.4. Recognition based super-resolution

Baker and Kanade (2002) suggested incorporating super-resolution technique with other module in order to overcome several constraints in conventional super-resolution techniques, especially for a case of input image that is too coarse. Increasing the resolution of image containing human face could be implemented with a combination of Bayesian MAP super-resolution and a face recognition technique. This technique is known as recognition-based super-resolution or hallucination. The drawback of this algorithm is it only works with images containing a face. Results of this technique on image not containing faces showed an outline of a face, which has been hallucinated into the image even though there is no face in the input image.

2.1.5. Super-resolution restitution in remote sensing

Super resolution restitution techniques have also been applied in remote sensing applications to reconstruct a fine spatial resolution image from a set of coarse spatial observations. Examples of the application of the super-resolution restitution in remote sensing include Akgun et al. (2005), Merino and Nunez, (2007), Hu et al., (2009), and Shen et al. (2009).

2.2. Super-resolution mapping

Unlike the super-resolution restitution that only enhances the spatial resolution of imagery, super-resolution mapping is a land cover classification technique that produces thematic classifications at a sub-pixel scale (Atkinson, 2004). Soft classification may be used to estimate the class composition of image pixels but the spatial distribution of each class in these mixed pixels cannot be determined. Therefore, the attention of the super-resolution mapping is to estimate the location of the component of land cover classes within a pixel, with the proportion of the classes determined from a soft classification technique. This section first reviews soft classification techniques and then followed by a review of a variety of super-resolution mapping techniques.

2.2.1. Soft classification

The fundamental unit of a remotely sensed image is the pixel. The number of pixels in an image depends on the spatial resolution of a sensor. The pixel shows information on the spectral response of an area on the ground. The area presented in a pixel is determined by the sensor. A pixel may contain more than one thematic class. In such situation, the partitions of the thematic classes are mixed within a pixel (Fisher, 1997; Cracknell, 1998). The proportion of the mixed pixels depends on the spatial resolution of sensor and land cover mosaic on the ground (Foody 2005). The proportion of the mixed pixel increases with a coarsening of the spatial resolution and/or with increasing the fragmentation of the landscape presented in the image. Conventional hard classification method assumes that a pixel is pure, discrete and contains only one

thematic class, thus this method is not able to accurately classify mixed pixels. Therefore, soft classification methods which are able to perform classification at the sub-pixel level have been developed to un-mix the mixed pixel and to determine the composition of the pixel, which is not necessarily contain just one thematic class. This section reviews a variety of soft classification techniques, which have been used to estimate sub-pixel class composition within a mixed pixel.

2.2.1.1.   Linear mixture model

An early method to estimate the sub-pixel class composition in a mixed pixel was proposed by Settle and Drake (1993) using a linear mixture model. They determined the relative proportion of ground cover components in a mixed pixel by assuming that the spectral response of the mixed pixel is a linear weighted sum of spectral responses of its component classes. The linear spectral mixture model offers simplicity and accurate sub-pixel estimation. However, the use of the least square error criterion in this method hinders the un-mixing analysis to solve problems involving outliers. Outlier is defined as a pixel with atypical value, which does not belong to any predefined class. Instead of using a least square method, Rosin (2001) reduced the outliers' effect by using a least median square (LMedS) method. Borel and Gerstl (1994) demonstrated that linear un-mixing model was not suitable for nonlinear mixture problem. As such, non-linear mixing models were proposed (Borel and Gerstl, 1994; Foody and Arora, 1997).

2.2.1.2.   Maximum likelihood classification

The maximum likelihood (ML) classifier is a supervised statistical classification technique that is based on the Bayesian probability framework (Tso and Mather, 2009). The ML classifier calculates the probability of a pixel belonging to a predefined set of classes, and assigns a class to a pixel that has the highest posterior probability of membership. Although the classification of a pixel to one thematic class leads to the hard classification problem, the ML classifier can be adapted in the soft classification problem by assigning the procedure of the ML classifier at the sub-pixel level (Foody et al., 1992). The use of likelihood functions as estimators of mixing is valid if the classes of interest are high separable and distributions overlap only slightly (Schowengerdt, 1995).

2.2.1.3.   Fuzzy c-means

The fuzzy c-means algorithm is an unsupervised data clustering technique in which a group of data can be subdivided into c clusters or classes. Every pixel in the dataset belongs to every cluster to a certain degree of membership rather than belonging completely into just one cluster. For example, a pixel that lies close to the centre of a cluster will have a higher degree of membership than another pixel which lies far away than the centre of the cluster. This method was developed by Dunn (1973) and improved by Bezdek (1981) and Bezdek et al., (1984). Fuzzy c-means starts by assigning pixels to classes randomly. Next, every pixel is given a membership degree for each class. Fuzzy partitioning is performed iteratively with the update of membership and centre of class.

The iteration aims to minimize an objective function that represents the distance from an arbitrary pixel in an image to centre of a class weighted by the pixel's membership grade.

Fuzzy c-means has been used in remote sensing to derive sub-pixel scale thematic information (Fisher and Pathirana, 1990; Foody, 1996; Atkinson et al. 1997; Bastin, 1997). Atkinson et al. (1997) reported that fuzzy c-means was more accurate than mixture modelling but less accurate when compared with artificial neural network. In estimating sub-pixel thematic information from remotely sensed images, (Foody, 1996; Atkinson et al. 1997; Bastin, 1997; Lucas et al. 2002) the fuzzy c-means has also been used in supervised mode. The accuracy of the fuzzy c-means is subject to a value of weighting parameter which must be carefully selected by user (Foody, 1996). Fuzzy c-means generally produces accurate class composition estimates when all classes have been defined and included in the training phase of the classification. However, the presence of untrained classes would degrade the estimation accuracy of the fuzzy c-means; therefore a counterpart of this technique, namely possibilistic c-means is used for robustness towards the untrained classes (Krishnapuram and Keller, 1993; Krishnapuram and Keller, 1996; Foody, 2000).

2.2.1.4.   Feed-forward neural network

Neural network is a popular solution related to the classification problems because its ability to solve nonlinear mixture problems (Carpenter et al., 1999; Foody, 2001; Liu et al. 2004). Problems involving data classification in remote sensing have been solved

using a variety of feed-forward neural network such as multi-layer perceptron (MLP), radial basis function, and probabilistic neural network. Each of them is constructed from a fundamental unit of processing element or neuron, which is arranged in a layered network. The way the neuron is arranged in a network and the activation functions used differentiate all the three aforementioned models. Given enough training data and a priori knowledge, neural network can be an effective non-parameter solution.

Mixed pixels can be included in the feed-forward neural networks during the training stage. The trained networks can be used to predict the class membership properties for other pixels in the data set. In addition to the feed-forward neural networks, a neural network based on adaptive resonance theory (ART) has been used and known as ARTMAP. The ARTMAP learning is faster and more stable than ML classifier, MLP, or k-nearest neighbour techniques. Another advantage of the ARTMAP is that the learning process can be performed online for recognition and prediction tasks. A major drawback of neural network techniques is their lack of ability to explain physical system being modelled (Liang et al., 2008).

2.2.1.5.   Support vector machine

Support vector machine (SVM) is a supervised classification and regression methods based on statistical learning theory (Vapnik, 1995). SVM is fundamentally a binary classifier, which treats input data as two sets of vector in an n-dimensional space. SVM constructs a separating hyper-plane in that space to maximize margin between the two data sets. Large margin decreases generalization error of the classifiers. Brown et al.

(2000) showed that a constrained least squares linear spectral mixture model is equivalent to a linear SVM. Linear SVM uses linear discrimination to separate classes which are linearly separable. Linear SVM is able to select support vectors automatically from a larger database and is more appropriate for empirical mixture modelling. The accuracy of the SVM classification is not dependent on large datasets in the training and a complete description of each class in feature space but on the most useful and informative sample data. Using the MLP, Foody (1999) showed that the most informative samples lie at the edge of class distribution and between the distributions of two or more classes in feature space. These samples are known as support vectors. Mathur and Foody (2008) used an intelligent approach to identify support vectors based on ancillary information. Although SVM is generally easier to implement than neural networks, it contains no prior knowledge of the problem. To gain benefits from prior information, Tipping (2001) presented an alternative technique known as relevance vector machine (RVM), which is based on a Bayesian framework and provides posterior probabilistic outputs.

2.2.2. Super-resolution mapping

Super-resolution mapping can be divided into two main groups (Boucher, 2009). The first group exploits the spatial correlation of the fine scale attribute by assuming that observations that close together tend to be more alike than observations that further apart (Matheron, 1965). In this group, the spatial correlation is maximized by means of

several techniques. The second group utilizes knowledge based information or a priori spatial model, such as a variogram.

2.2.2.1.   Knowledge based procedure

Knowledge-based procedures depend on the accurate identification of boundary features that split the mixed pixels into pure components at fine spatial resolution. Schneider (1993) used a knowledge-based analysis to locate field boundaries down to sub-pixel scale. It comprises of pre-processing and land classification steps. In the pre-processing step, straight boundary features in Landsat Thematic Mapper (TM) were used as the knowledge in this technique. In the classification step, two classes of land cover were determined. However, the objective of this technique is only limited to localize large and homogenous fields with straight boundaries.

2.2.2.2.   Linear optimization

Sub-pixel mapping can also be formulated as a linear optimization solution (Verhoeye and De Wulf, 2002). This technique utilizes spatial dependence within and between coarse pixels where it gives priority on nearby observations more than distant observations. As such, isotropic variogram is derived from coarse resolution image. Then, the variogram results are used for spatial interpolation or kriging. This technique produces artefact, but can be eliminated by applying mode filter. However, the filtering process tends to eliminate isolated sub-pixels.

2.2.2.3.   Feed-forward neural network

Feed-forward neural network has been used as a super-resolution mapping module together with a fusion of spatial and spectral information to enhance the spatial resolution of hyperspectral images (Gu et al., 2008; Mianji et al., 2011). Further information on the possibilities and limitation of the feed-forward neural network for the derivation of super-resolution mapping is given by Nigussie et al. (2011).

2.2.2.4.   Hopfield neural network

A Hopfield neural network (HNN) technique (Hopfield, 1982) is used to design a super-resolution mapping technique by Tatem et al. (2001a). The structure of a Hopfield neural network is formulated as a 2D lattice, representing an image grid, in which one neuron of the network receives input from the corresponding sub-pixel of the image. Hopfield neural network is an optimization tool that maximizes the spatial correlation between sub-pixels while maintaining the class proportion at the pixel level. Initially, the solution of the HNN is only limited to binary classes, such as target land cover class on a background, but later is extended to multiclass applications (Tatem et al. 2001b).

The solution of the HNN for super-resolution mapping can be used to represent land cover if the size of land cover size is larger than a coarse spatial resolution image pixel. Later, Tatem et al. (2002) extended this method by including a priori information in a form of variogram in order to estimate spatial pattern of land cover patches in which the size of the patches may be larger, equal or smaller than an image pixel. The prior

information needs to be derived from a finer spatial resolution image of a same site with a coarser image.

All the previously mentioned HNN for super-resolution mapping techniques only take input from a single coarse spatial resolution image. Later, additional information, which is finer than the main coarse spatial resolution imagery, is incorporated to the input of the HNN in order to obtain higher thematic classification accuracy than by using a single image. For example, data from light detection and ranging (LIDAR) with spatial resolution of 0.8 m is incorporated into optical data at 4 m spatial resolution (Nguyen et al., 2005); multispectral (MS) bands of the IKONOS with spatial resolution of 4 m is fused with its 1 m panchromatic band (Nguyen et al., 2006); and a 2.56 m QuickBird MS image is fused with a 0.64 m PAN image (Nguyen et al., 2011).

Apart from acquiring additional information that is finer that the main imagery, time series imagery with the same spatial resolution may be fused to increase the accuracy of the HNN (Muad and Foody, 2010). This approach is applicable when the data in the time series is shifted at a sub-pixel scale. Ling et al., (2010) demonstrates that the thematic accuracy can be increased subjected to the increment of the coarse spatial resolution imagery in the time series, although their result is based on simulated coarse spatial images derived from a finer spatial resolution image.

2.2.2.5. Neural network predicted wavelet coefficients

In order to solve sub-pixel mapping problem, Mertens et al. (2004) assumed spatial dependence of image pixels among adjacent pixels. Unlike previous super-resolution mapping techniques, this technique expresses spatial dependence by neighbourhood dependence of wavelet coefficients (Daubechies, 1992; Mallat, 1989). More than one neural network is used, depending on the number of the coefficient used. Neural networks then are trained to estimate the wavelet coefficients. In this implementation, to enforce spatial dependence, a 3×3 pixels consisting centre pixel and its eight neighbours from a fraction image is fed to a feed-forward back-propagation neural network whereby each network producing an output for either horizontal, vertical, or diagonal coefficient for the Haar wavelet. Haar filter is used in the wavelet transformation since it is the simplest filter having only two coefficients. For a pixel, fraction of land cover classes needs to be determined. If the pixel is not pure, a pixel which constitutes more than one land cover class, then the three different types of networks are assigned for each class. The neural network of the diagonal coefficient tends to produce less accurate prediction than the network of the horizontal and vertical coefficients. A major disadvantage of this technique is that it requires a large datasets to be trained with neural network.

2.2.2.6. Markov random field

The Markov random field (MRF) is a technique that can be used to model contextual information (Geman and Geman, 1984). Kasetkasem et al., 2005 used the MRF to generate super-resolution for land cover mapping in remote sensing imagery. Every map

is assumed to have Markov property. This approach is based on an assumption of spatial dependence within and between pixels, in which two adjacent pixels are more likely to belong to the same land cover class. Homogeneous regions of the land cover are more likely to be mapped by this model than isolated pixels. As a result, the isolated pixels tended to be ignored. Unlike many other super-resolution mapping techniques, the MRF based super-resolution is not dependent on a soft classification technique. Therefore, the MRF based method is not affected by inaccuracy of the soft classification.

2.2.2.7.   Pixel swapping

Pixel swapping is an algorithm that calculates the attractiveness of each sub-pixel to a particular class. The algorithm was first developed by Atkinson (2005) for binary case. The algorithm starts after an image has been soft classified by a supervised fuzzy c-means algorithm (Bezdek et al., 1984; Thornton et al., 2006). The attractiveness of the pixel swapping algorithm is a function that measures the summation of weighed distance between a sub-pixel of interest and its neighbours. For a binary image case, the least attractive sub-pixel is a sub-pixel with a value "1" and surrounded mainly by sub-pixels with value "0", and the most attractive sub-pixel is a sub-pixel with a value "0" and surrounded mainly by sub-pixels with value "1". The swapping process between two sub-pixels occurs only if the spatial correlation of the sub-pixels can be increased, otherwise no swap is made. The swapping of the sub-pixels only occurs within a pixel, not between pixels. One sub-pixel within a pixel is swapped per iteration. The algorithm runs until no swaps are made or until it reach a specified number of iterations.

Mathematical morphology, a technique of analysing and processing geometric structures based on set theory, topology and random functions (Serra, 1984), was used by Thornton et al. (2006) to remove speckled pattern, which arises due to misclassification in the output of the pixel swapping method. The prediction of linear features is improved by including an anisotropic modelling component (Thornton et al. 2007). The pixel swapping increases classification accuracy compared to random allocation of sub pixels. The concept of the pixel swapping method is simpler and its computation is less extensive than the HNN method. The pixel swapping algorithm assumed that the soft classification is perfect. Therefore the classification accuracy of the pixel swapping algorithm is heavily dependent on the accuracy of the soft classification.

2.2.2.8.   Geo-statistics indicator

Boucher and Kyriakidis (2006) treated the super-resolution mapping problem as an ill-posed problem, therefore, prior information must be included in order to constrain the spatial pattern. The prior model was in the form of parameter indicator variogram models. Based on the information about the coarse resolution fractions and a sparse set of class labels at fine pixels, indicator cokriging is used to approximate the probability that a fine pixel belongs to a particular class. Unlike other previous super-resolution mapping methods that rely on single input image, this technique takes multiple images of varying degree of spatial resolution scale from the same scene. This technique is fast because no iterative procedure is involved.

2.3.   Accuracy assessment

Results of any super-resolution mapping technique should be assessed in order to determine their accuracy. In this thesis, the assessment was undertaken using site specific accuracy using the confusion matrix, texture variables, object based characterization and positional accuracy.

2.3.1. Confusion matrix

Confusion matrix is used to assess the thematic accuracy or site specific accuracy of estimated land cover mapping when compared with ground data (Congalton and Green, 2009). It may be used to provide a measure of agreement between the estimated land cover maps with the ground data. From the confusion matrix, commission and omission errors can be calculated. A commission error occurs when an area is included in an incorrect category, while an omission error occurs when an area is excluded from the category to which it belongs.

2.3.2. Texture variables

The structure of the spatial configurations of land cover mosaic can be quantified using texture measures based on gray-level co-occurrence matrix (GLCM) (Haralick, et al., 1973). Fourteen measures of texture can be derived from the GLCM. In this thesis, four texture measures were used: homogeneity, contrast, inverse difference moment, and

entropy. The four texture measures were selected because they can be used to interpret landscape heterogeneity (Benson and MacKenzie, 1995). Heterogeneous landscapes required the measurement at a fine spatial resolution scale (Nellis and Briggs, 1989), and in the case of this thesis, at a sub-pixel scale. Thus, the texture measures may be used to compare the representation of spatial configurations at a sub-pixel scale derived from different land cover mapping techniques.

Tso and Mather (2009) provide an example to compare the difference of texture measures on two different texture pattern images as shown in Figure 2.1. The texture information can be calculated at angle 0°, 45°, 90°, and 135°.

2.3.2.1.   Homogeneity

Homogeneity or the angular second moment measures spatial closeness of the distribution of the GLCM. A high value of homogeneity is produced when the distribution of the frequency $p(i, j)$ is concentrated on the diagonal of the matrix. A low value of homogeneity is produced when the value of the frequency in the matrix are almost similar, in which the distribution of the frequency in the matrix is uniform. The equation for the homogeneity is given in Equation 2.1.

$$\text{Homogeneity} = \sum_i \sum_j \left[p(i, j) \right]^2 \qquad (2.1)$$
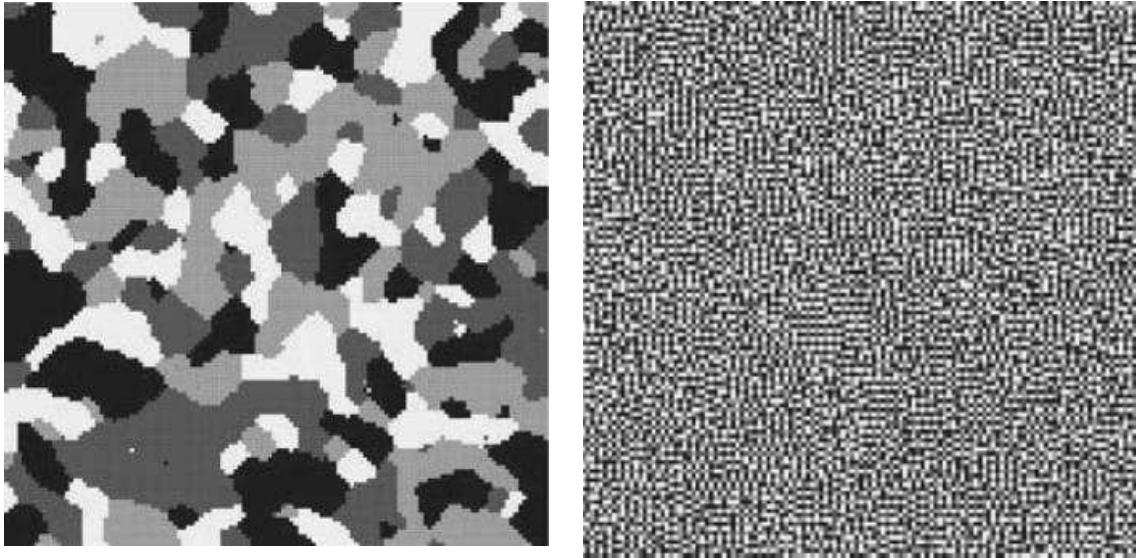
0.242	0.010	0.009	0.008
0.010	**0.230**	0.007	0.010
0.009	0.007	**0.219**	0.009
0.008	0.010	0.009	**0.195**

(a)   (b)   (c)

0.026	0.070	0.078	0.075
0.070	0.026	0.075	0.078
0.078	0.075	0.028	0.068
0.075	0.078	0.068	0.023

(d)

Figure 2-1 Illustration of two different texture patterns. (a) A coarse texture pattern. (b) A fine texture pattern. (c) GLCM computed from Figure 2.1a. (d) GLCM computed from Figure 2.1b (adapted from Tso and Mather, 2009).

2.3.2.2. Contrast

Contrast indicates local variation in the image. It measures the difference intensity between a pixel and its neighbours. More weight is assigned to the $p(i, j)$ that is away from the diagonal of the GLCM than the $p(i, j)$ on the diagonal. When the intensity

difference is large, the contrast increases. For example, the contrast for Figure 2.1a tends to be lower than the contrast of the Figure 2.1b.

$$\text{Contrast} = \sum_{n=0}^{N_g-1} n^2 \left[\sum_{\substack{i=1 \\ }}^{N_g} \sum_{\substack{j=1 \\ |i-j|=n}}^{N_g} p(i, j) \right] \qquad (2.2)$$

where N_g is the number of distinct gray levels, and n^2 is used to indicate the difference between the gray tone i and the gray tone j. This measure is suitable for images with gray-tone values rather than image containing land cover classes. For binary land cover classes, the measurement of the contrast considers the transition between two classes times two (Benson and MacKenzie, 1995).

2.3.2.3.   Inverse difference moment

Inverse difference moment (IDM) is a measurement used to indicate that an image may contain large homogeneous patches. Such image gives higher weight for the $p(i, j)$ on the diagonal of the GLCM and lower weight for the $p(i, j)$ that are distant from the diagonal. For example, the inverse difference moment for Figure 2.1a tends to be higher than that of the Figure 2.1b.

$$\text{Inverse difference moment} = \sum_{i} \sum_{j} \frac{1}{1+(i-j)^2} p(i, j) \qquad (2.3)$$

2.3.2.4. Entropy

Entropy indicates the complexity of the image by measuring the randomness of the elements of the co-occurrence GLCM. The value of the entropy is at maximum when the elements of the matrix are equal, but turn to 0 when all the elements are different. Therefore, this makes entropy and homogeneity are negatively related. For example, the entropy for Figure 2.1a is lower than the entropy for Figure 2.1b.

$$Entropy = -\sum_i \sum_j p(i, j) \log\left[p(i, j) \right] \qquad (2.4)$$

2.3.3. Object based characterization

The shape of objects may be characterized by several measures such as area, perimeter, compactness, length and orientation. Figure 2.2 illustrates an example of shape characterization for an object (shown in black). The area of an object can be determined by measuring the quantity of pixels assigned for the object, while the number of pixels at the boundary of the object determines its perimeter. Both of the measurements are in pixel units. To suit with different types of the remotely sensed imagery, the measurements in pixel unit were multiplied with the spatial resolution of the imagery used.
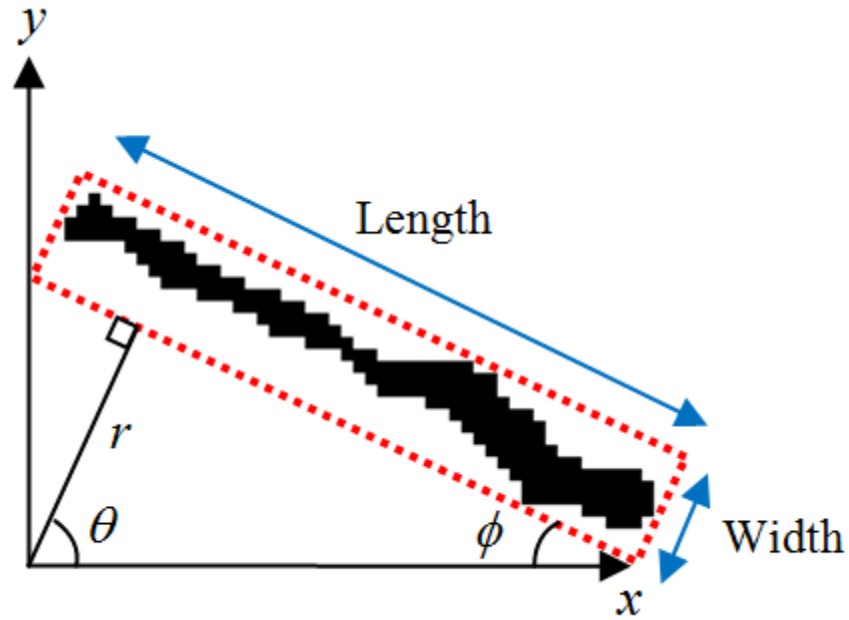
Figure 2-2 Object characterization.

The compactness of an object is calculated by

$$\omega = \frac{4\pi A}{P^2} \tag{2.5}$$

where A is area and P is perimeter. The index ranges from 0 to 1, where values approaching 1 indicate that the shape is circular while values approaching 0 are for linear shape. The orientation of an object is calculated using Hough transform (Hough, 1962; Duda and Hart, 1972).

$$r = x\cos\theta + y\sin\theta \tag{2.6}$$

$$\phi = \theta - 90^\circ \tag{2.7}$$

2.3.4. Positional accuracy

The evaluation of the positional accuracy compares the boundary of the represented land cover patches with the boundary of the corresponding patches from ground data. To generate boundary position, the boundary of the land cover patches is vectorised. The vector difference of the boundary positions between the represented land cover patches and the ground data is expressed in root mean squared error (RMSE), which provides a statistical measure of the positional accuracy of land cover patches.

2.4. Conclusions

This chapter provided a review on different approaches for super-resolution analysis. Various approaches of super-resolution techniques have been proposed in various applications to increase the spatial resolution of image. Generally, super-resolution can be divided into super-resolution restitution and super-resolution mapping. Super-resolution restitution techniques have been used widely in image processing and computer vision communities, while super-resolution mapping techniques have been used in remote sensing community. In addition, soft classification techniques, which are generally used before the processing stage of many super-resolution mapping techniques, are also presented in this chapter. Brief discussions on a series of accuracy assessments are also included as these assessments will be used to evaluate the accuracy of different super-resolution mapping techniques throughout this thesis.

In order to represent land cover mapping at a sub-pixel scale, the focus of this thesis is on the super-resolution mapping techniques rather than the super-resolution restitution. Although the mapping of land covers from the results of the super-resolution restitution can be performed using a concept of "restitution then classification" (Ling et al., 2010), there are several disadvantages using this approach. Many of the super-resolution restitution techniques only focus on enhancing the spatial appearance of the objects contained in a spatially enhanced image. Issues related with the mixed pixel problems, such as the number of land covers and their spatial location inside a mixed pixel, have not been fully addressed. In contrast, many of the super-resolution mapping techniques focus on solving the mixed pixel problems. Many of the super-resolution mapping techniques have a mechanism that can decompose the mixed pixel. With the attention of going beyond the size of a pixel, sub-pixel sized land cover patches could be represented and their location could be predicted with super-resolution mapping.

3. Super-resolution analysis for mapping patterned landscapes

This chapter presents the fundamental concepts of two standard super-resolution mapping techniques: Hopfield neural network and pixel swapping. Both techniques can use a single coarse spatial resolution image as their input to produce spatially enhanced output images. Since these two techniques rely on input from soft classification output, a section on soft classification is included. Experiments to evaluate the techniques were conducted using images of a 'shrubby' region acquired from Google Maps. This pilot chapter analyses super-resolution land cover mapping techniques applied on different spatial pattern from shrubby images.

3.1. Fuzzy c-means soft classification

Many super-resolution mapping techniques used soft classification techniques to estimate the sub-pixel level class compositions within a pixel of an image. The soft classified image is used as an input for super-resolution mapping. In this thesis, the class composition was estimated using an unsupervised fuzzy c-means clustering algorithm (Bezdek, 1984) which has been widely used in remote sensing (Foody, 1996).

The description of the fuzzy c-means algorithm is explained in this section. A set of random data $X = \{x_1, x_2, \ldots, x_n\}$ in a vector space R^d, where d is a dimension of the space, can be clustered into several classes by mapping them into a matrix U with its dimension is $c \times n$. For problems related with image classification, c is the number of clusters or classes and n is the number of pixels. Each entry of the matrix is denoted as u_{ik} with the range of its value must be between 0 and 1.

$$u_{ik} \in [0,1] \tag{3.1}$$

The u_{ik} represents the membership value of pixel k for class i. Pixel k may be assigned into several clusters, usually more than 1 and the maximum is c. Each cluster has a membership value that determines the probability of pixel k towards that cluster. The total summation of the membership values for clusters of pixel k must be 1 as specified in Equation 3.2.

$$\sum_{i=1}^{c} u_{ik} = 1, \quad \text{for all } k \tag{3.2}$$

The clustering task of the data is performed by minimizing a generalized least square error function

$$J_m(U,V) = \sum_{k=1}^{n} \sum_{i=1}^{c} (u_{ik})(x_k - v_i)^2 \tag{3.3}$$

where $V = \{v_1, v_2, \ldots, v_c\}$ is the vector of cluster centres, which often been represented as the mean of the clusters. The membership weighting exponent, m determines the fuzziness level of the clustering and its range is between $1 \leq m \leq \infty$.

Initially, a random value is assigned to the entry u_{ik}. The value of the u_{ik} is updated iteratively until the error function J_m reaches a local minimum by calculating the entry as in Equation 3.4.

$$u_{ik} = \frac{1}{\sum_{j=1}^{c} \left(\frac{x_k - v_i}{x_k - v_j} \right)^{2/(m-1)}} \qquad \text{for all k} \qquad (3.4)$$

and the mean of the ith cluster is calculated from

$$v_i = \frac{\sum_{k=1}^{n} \left(u_{ik} \right)^m \cdot x_k}{\sum_{k=1}^{n} \left(u_{ik} \right)^m} \qquad \text{for all i} \qquad (3.5)$$

Throughout this thesis, the number of clusters was set to two (i.e. $c = 2$) to differentiate between two land cover classes in the image. The algorithm's weighting parameter, m, which determines the degree of fuzziness was set, after a series of trial analyses, to 2.0. This value is widely used in many works (Foody, 2000; Foody, 1996; Krishnapuram and Keller, 1993) and within the interval between 1.5 and 2.5 as suggested by Nikhil and Bezdek (1995).

3.2. Hopfield neural network

Hopfield neural network (HNN) is a recurrent type artificial neural network which is designed for solving optimization problems (Hopfield, 1982; Hopfield 1984). The fundamental structure of the network consists of a single layer of neurons and the output

of each neuron is fed back to all other neurons input except its own input. Figure 3.1 shows an example of an HNN consisting of 3 neurons. HNN is an optimization tool defined by an energy function (Hopfield, 1984) that can be formulated to represent problems that need to be solved. The energy function often comprises goals and constraints.

The energy function of the HNN is defined as:

$$E = -\frac{1}{2}\sum_{i=1}^{N}\sum_{j=1}^{N} w_{ji} x_i x_j \qquad\qquad i \neq j \qquad (3.6)$$

where w_{ij} is the weight from neuron i to neuron j, x_i is the output of the ith neuron in the network, and N is the number of neuron. In the discrete HNN, values for j^{th} neuron x_j can be in either binary (1/0) state or in bipolar (+1/-1) state.

A set of N-dimensional vectors, denoted by $\{\xi_\mu \mid \mu = 1, 2, \ldots, M\}$ can be stored into a synaptic weight. The $\xi_{\mu,i}$ denotes the ith element of the fundamental memory ξ_μ. The synaptic weight from neuron i to neuron j is defined by

$$w_{ji} = \frac{1}{N}\sum_{\mu=1}^{M} \xi_{\mu,j}\xi_{\mu,i} \qquad\qquad (3.7)$$

To ensure convergence to a stable state, Hopfield (1984) set the weights symmetric with no-self connection between a neuron.

$$w_{ij} = w_{ji} \qquad\qquad (3.8)$$

$$w_{ii} = 0 \qquad\qquad (3.9)$$
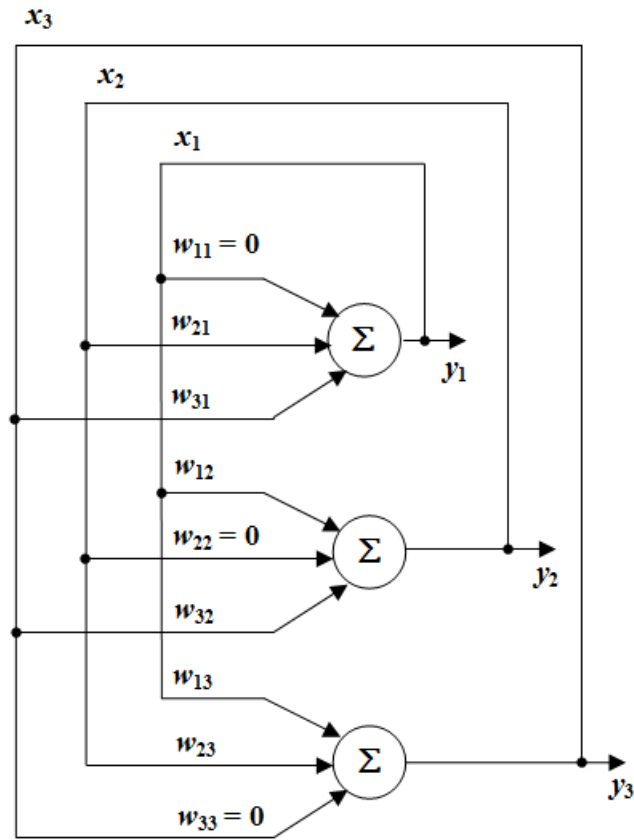
Figure 3-1 An example of an architecture of a Hopfield neural network consisting of 3 neurons (adapted from Haykin, 1999).

The Hopfield neural network updates the element of state vector x(n) into a state of x(n+1) asynchronously according to the rule

$$v_j(n) = \sum_{i=1}^{N} w_{ji} x_i(n) + b_j \qquad (3.10)$$

where v_j is an induced local field of neuron j, b_j is a bias. Neuron j updates its state x_j according to a deterministic rule

$$x_j(n+1) = \begin{cases} 1 & \text{if } v_j(n) > 0 \\ 0 & \text{if } v_j(n) < 0 \end{cases} \qquad (3.11)$$

for an unipolar case, or

$$x_j(n+1) = \begin{cases} +1 & \text{if } v_j(n) > 0 \\ -1 & \text{if } v_j(n) < 0 \end{cases} \qquad (3.12)$$

for a bipolar case. This relation may be written in the compact form as

$$x_j(n+1) = \text{sgn}\left[\sum_{i=1}^{N} w_{ji} x_i(n) + b_j\right] \qquad (3.13)$$

where "sgn" is the signum function.

As an alternative to the Equation 3.13, the state of a neuron for an input u can also be updated with a nonlinear activation function using a hyperbolic tangent, "tanh" function as formulated in Equation 3.14.

$$v_j = \frac{1}{2}\left(1 + \tanh\left(\lambda u_j\right)\right) \qquad (3.14)$$

If the value for the gain, λ is high, the activation function in Equation 3.14 approaches a step function. Figure 3.2 shows a hyperbolic tangent "tanh" function with different values for the λ. High values of the λ tend to produce a unit step function.
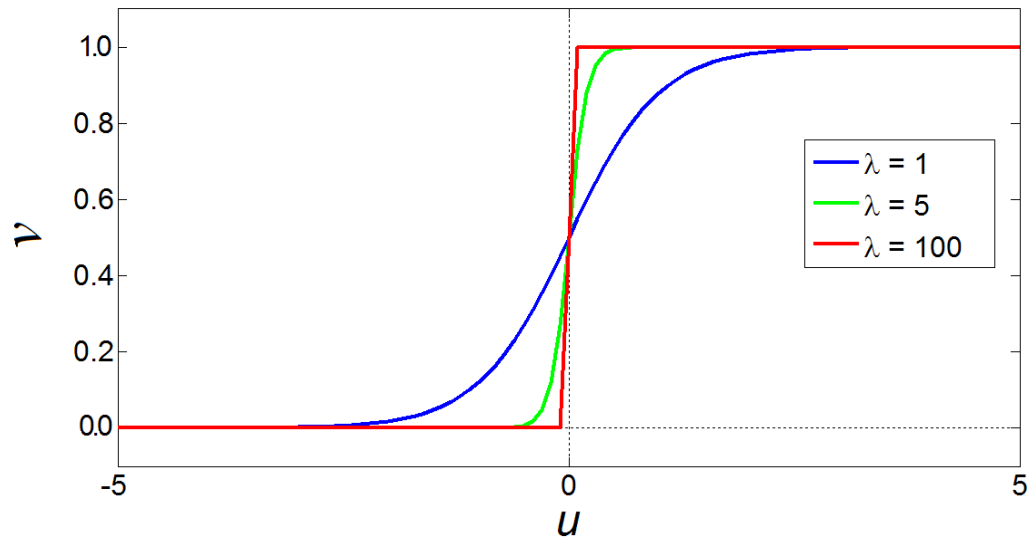
Figure 3-2 Hyperbolic tangent "tanh" function with different values of gain, $\lambda = 1$, $\lambda = 5$, and $\lambda = 100$.

Differentiating the energy function of the HNN in Equation 3.6 would derive the rate of the energy, δE

$$\frac{\delta E}{\delta x_i} = -\sum_{j=1}^{N} w_{ji} x_j \qquad (3.15)$$

And the rate of energy, δE is proportional to the rate of change of the neuron du_i.

$$\frac{du_i}{dt} = -\frac{\delta E}{\delta x_i} \qquad (3.16)$$

3.2.1. Hopfield neural network for super-resolution mapping

The optimization capability of the HNN has been used for problems that use images as the main input source, such as image restoration (Paik and Katsaggelos, 1992), feature tracking from satellite imagery (Cote and Tatnall, 1997) and image segmentation (Shen and Ip, 1997). HNN can also be used to map land covers at a sub-pixel scale accuracy from coarse spatial resolution images (Tatem et al., 2001a).

For the super-resolution mapping, each pixel of a coarse spatial resolution image is sub-divided into $z \times z$ sub-pixels, where z is the scale factor of the spatial resolution increment. Initially, sub-pixels of a pixel will take a value from their respective pixel (Fisher, 1997). The construction of the Hopfield neural network requires the consideration of the spatial resolution of the output image that will be produced. In such a case, the number of neurons and their arrangement is designed to accommodate all the sub-pixels of the image. For example Figure 3.3 shows an illustration of an arrangement of neurons of an HNN for the super-resolution mapping application. Let g be an observed coarse spatial resolution image having $P \times Q$ pixels and f be an up-sampled image from g having $zP \times zQ$ pixels. Parameter z is a zoom factor of super-resolution mapping, which determines the spatial resolution increment from the original observed image, g to the fine spatial resolution image f. Given the coarse spatial resolution image, a fine spatial resolution image, f is generated as shown in Figure 3.3. The arrangement of neurons in the HNN is corresponding to an arrangement of pixel grid in the two-dimensional fine spatial resolution image, f. Each neuron, u_{ij} will be referred to coordinate notation of its corresponding pixel in the fine resolution image, f_{ij}. The network receives an input u_{ij} and produces an output v_{ij}, where i and j represent
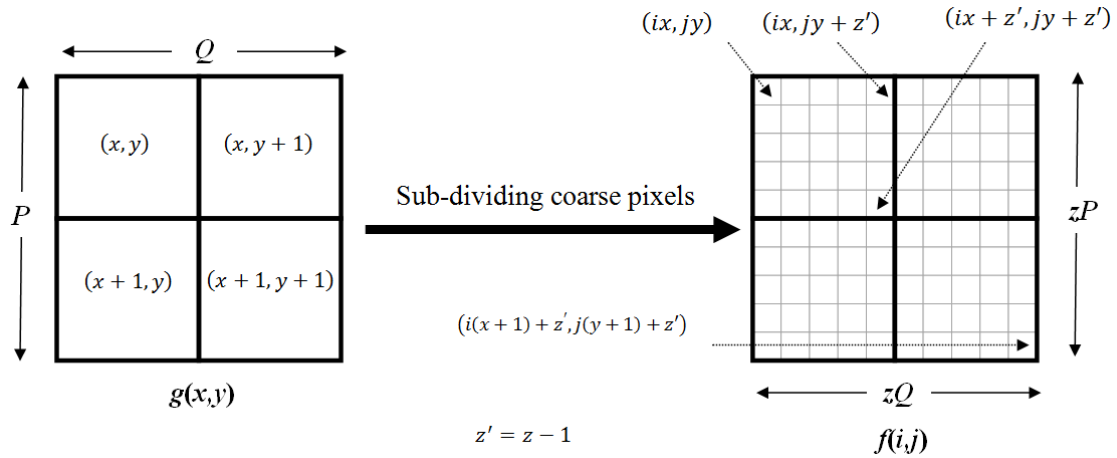
Figure 3-3 A 2×2 pixels coarse spatial resolution image and representation of input neurons arrangement for the HNN derived from the sub-dividing pixels of the coarse spatial resolution image (adapted from Tatem et al., 2001a).

coordinate of a neuron in row i and column j of the grid. Each neuron output will has either a value "1" to represent "on" or "0" to represent "off".

Careful construction of the energy function may help Hopfield neural network to converge to its targets (Tso and Mather, 2009). The energy function that represents the problem of super-resolution mapping generally comprised of two parts: a goal and a constraint (Cote and Tatnall, 1997), as defined as

$$\text{Energy} = \text{goal} + \text{constraint} \tag{3.17}$$

The goal function considers the spatial correlation between observations. The function considers a neuron together with its closest neighbours, rather than to treat a particular

neuron as an independent unit. The constraints specify the context of the available data by adding costs to the objective.

By assuming that the spatial dependence between a neuron and its adjacent neurons is higher than that of neurons that are further apart, Tatem et al. (2001a; 2001b) represented the energy function by combining spatial clustering goal function and area proportion constraint as defined by Equation 3.18.

$$\text{Energy} = \text{Goal function} + \text{Area proportion constraint} \tag{3.18}$$

The energy function can be formulated mathematically as in Equation 3.19

$$E = -\sum_i \sum_j \left(k_1 G_{ij}^{ON} + k_2 G_{ij}^{OFF} + k_P P_{ij} \right) \tag{3.19}$$

where E is the network energy, G_{ij}^{ON} and G_{ij}^{OFF} are the goal functions at a neuron (i, j), P_{ij} is the area proportion constraint, k_1, k_2, and k_P are the weight constant for the goal functions and the area proportion constraint respectively The rate of change for the energy function for a neuron at location (i, j) is defined by Equation 3.15

$$\frac{dE_{ij}}{dv_{ij}} = k_1 \frac{dG_{ij}^{ON}}{dv_{ij}} + k_2 \frac{dG_{ij}^{OFF}}{dv_{ij}} + k_P \frac{dP_{ij}}{dv_{ij}} \tag{3.20}$$

The goal functions maximize the spatial correlation of nearby neurons that have similar values. The functions receive input from neuron (i, j) and its eight surrounding

neurons. Two goal functions are required to derive the output into two binary states: on and off. In Equation 3.19, the two goal functions are denoted as G^{ON} and G^{OFF}.

The first goal function G^{ON} increases the output of the centre neuron (i, j) to 1 if the average value of its eight surrounding neurons is greater than a threshold value, T. If the average of the surrounding neurons is less than the threshold value, the goal function becomes 0. The value of the threshold value T is set to 0.5 as it is in the middle between 0 and 1. The conditions of this function can be formulated mathematically as shown in Equation 3.21.

$$\frac{dG_{ij}^{ON}}{dv_{ij}} = \frac{1}{2}\left[1 + \tanh\left(\frac{1}{8}\sum_{\substack{k=i-1 \\ k \neq i}}^{i+1}\sum_{\substack{l=j-1 \\ l \neq j}}^{j+1} v_{kl} - T\right)\lambda\right] \times \left(v_{ij} - 1\right) \qquad (3.21)$$

In this equation, the tanh function is used to activate the two conditions of the function. Gain λ determines the steepness of the tanh function. Increasing the neuron output corresponds to producing a negative gradient. The $\left(v_{ij} - 1\right)$ function controls the magnitude of the negative gradient output.

The second goal function decreases the output of the centre neuron (i, j) to 0 if the average value of its eight surrounding neurons is less than T. If the average of the surrounding neurons is greater than T, the second function increases the output of the centre neuron to 1. Decreasing the neuron output corresponds to producing a positive gradient. The v_{ij} controls the magnitude of the positive gradient output.

$$\frac{dG_{ij}^{OFF}}{dv_{ij}} = \frac{1}{2}\left[1 - \tanh\left(\frac{1}{8}\sum_{\substack{k=i-1\\k\neq i}}^{i+1}\sum_{\substack{l=j-1\\l\neq j}}^{j+1} v_{kl} - T\right)\lambda\right] \times v_{ij} \tag{3.22}$$

The area proportion constraint regulates the energy equation by retaining the pixel class proportion, a_{xy} derived from soft classification. The area proportion constraint is formulated in Equation 3.23. The threshold value of 0.5 is to define a sub-pixel belong to a class. If the area proportion of the estimate for the original pixel (x, y) is lower or greater than the target area, the output values of the neurons are increased or decreased to solve the problem. Zero gradients is produced when the P_{ij} equals zero

$$\frac{dP_{ij}}{dv_{ij}} = \left(\frac{1}{2z^2}\sum_{m=xz}^{xz+z-1}\sum_{n=yz}^{yz+z-1}\left(1 + \tanh\left(v_{mn} - T\right)\lambda\right)\right) - a_{xy} \tag{3.23}$$

The ordinary differential equation for the rate of the HNN energy in the Equation 3.20 is included into Equation 3.16 to determine the rate of change for the HNN neurons. The value for each neuron in the HNN can be updated numerically using a Euler method (Press et al., 2007) and is expressed as

$$u_{ij}\left(t + \Delta t\right) = u_{ij}\left(t\right) + \frac{du_{ij}\left(t\right)}{dt}\Delta t \tag{3.24}$$

which advances a solution from state $u_{ij}\left(t\right)$ to state $u_{ij}\left(t + \Delta t\right)$ with Δt as time step. The Equation 3.24 runs iteratively until $\sum_{ij}\left(u_{ij}\left(t + \Delta t\right) - u_{ij}\left(t\right)\right) \leq \varepsilon$, where ε is a small value.

3.2.2. Incorporating prior information into HNN

The goal functions in the HNN energy function in Equation 3.19 is only capable of solving super-resolution mapping for features larger than a size of one pixel. To estimate the pattern of features smaller than a size of pixel, Tatem et al. (2002) used semi-variance values in place of the goal functions. The semi-variance is a prior knowledge of the spatial landscape pattern derived from finer spatial resolution images. Thus, the new composition of the energy function is defined by Equation 3.25.

$$\text{Energy} = \text{Semi-variance value} + \text{Area proportion constraint} \qquad (3.25)$$

Its mathematical form is given in Equation 3.26. The energy function consists of a summation of several semi-variance values for zoom factor of z and an area proportion constraint.

$$E = -\sum_i \sum_j \left(k_1 S1_{ij} + k_2 S2_{ij} + \cdots + k_z Sz_{ij} + k_P P_{ij} \right) \qquad (3.26)$$

Constants k_1 to k_z are weighting factors for the output values for z^{th} semi-variance values, $S1_{ij}$ to Sz_{ij}, while k_P is the weighting factor the proportion constraint, P_{ij}. Accordingly, the energy change at neuron (i,j) can be written in a compact form as

$$\frac{dE_{ij}}{dv_{ij}} = \left(\sum_{n=1}^{z} k_n \frac{dSn_{ij}}{dv_{ij}} \right) + k_P \frac{dP_{ij}}{dv_{ij}} \qquad (3.27)$$

in which the first part of the equation corresponds to the semi-variance values while the second part is for the area proportion constraint.

Prior knowledge about spatial pattern in a finer spatial resolution can be modelled using a semi-variance function calculated by Equation 3.28.

$$\gamma(h) = \frac{1}{2N(h)} \sum_{i=1, j=1}^{N(h)} \left(f_{ij} - f_{i\pm h, j\pm h} \right)^2 \tag{3.28}$$

$\gamma(h)$ is the semi-variance at lag h, and N(h) is the number of pixels at lag h from the centre pixel (i,j). f_{ij} is a pixel of a fine spatial resolution image that is assumed to be available for deriving the prior information.

On one side, target centre neuron $v(c)_{ij}$ is modelled by using a quadratic equation.

$$v(c)_{ij} = \frac{-b \pm \sqrt{b^2 - 4ac}}{2a} \tag{3.29}$$

where $a = 2N(h)$, $b = \sum_{i=1, j=1}^{N(h)} v_{i\pm h, j\pm h}$, and $c = \sum_{i=1, j=1}^{N(h)} \left(v_{i\pm h, j\pm h} \right)^2 - 2N(h)\gamma(h)$. On the other side, the actual neuron output v_{ij} is compared to the target centre neuron.

The values for the actual neuron output and the target centre neuron are compared as in Equation 3.30.

$$\frac{dSn_{ij}}{dv_{ij}} = v_{ij} - v(c)_{ij} \tag{3.30}$$

In Equation 3.30, a negative gradient is produced when the output of neuron v_{ij} is lower than the target value, $v(c)_{ij}$. The declination of the gradient increases the neuron output. On contrary, when the neuron output is higher than the target value, a positive gradient

is produced, which corresponds to decreasing of the neuron output. A zero gradient occur when both the actual neuron and the target centre are identical. The calculation of the semi-variance values in Equation 3.30 is performed for lags $n = 1, \ldots, z$.

3.2.3. Multiclass land cover mapping

The goal and semi-variance values are used for mapping binary land cover classes. For multiclass land covers, an additional constraint is included in the energy function and named as a multiclass constraint (Tatem et al., 2001b). The objective of this constraint is to ensure that there is no spatial overlap between different land cover classes during the representation of land cover mapping. The multiclass constraint is used when there are more than two classes that need to be classified. For example, Figure 3.4a shows an image containing five different types of classes consisting of four different land cover patches: C_1, C_2, C_3, and C_4, and background C_5. Each of the patches in the image is segmented and separated from other patches in a binary image containing one patch as the foreground and other non-patch as the background. Figure 3.4b shows four binary images, each with particular patch, derived from the image in Figure 3.4a. Then, every binary image is arranged sequentially to construct a 3-dimensional matrix structure as shown in Figure 3.4c.

To ensure that class of patch from binary image f_1 does not map into other binary image, the multi-class function is formulated by Equation 3.31 to ensure that the
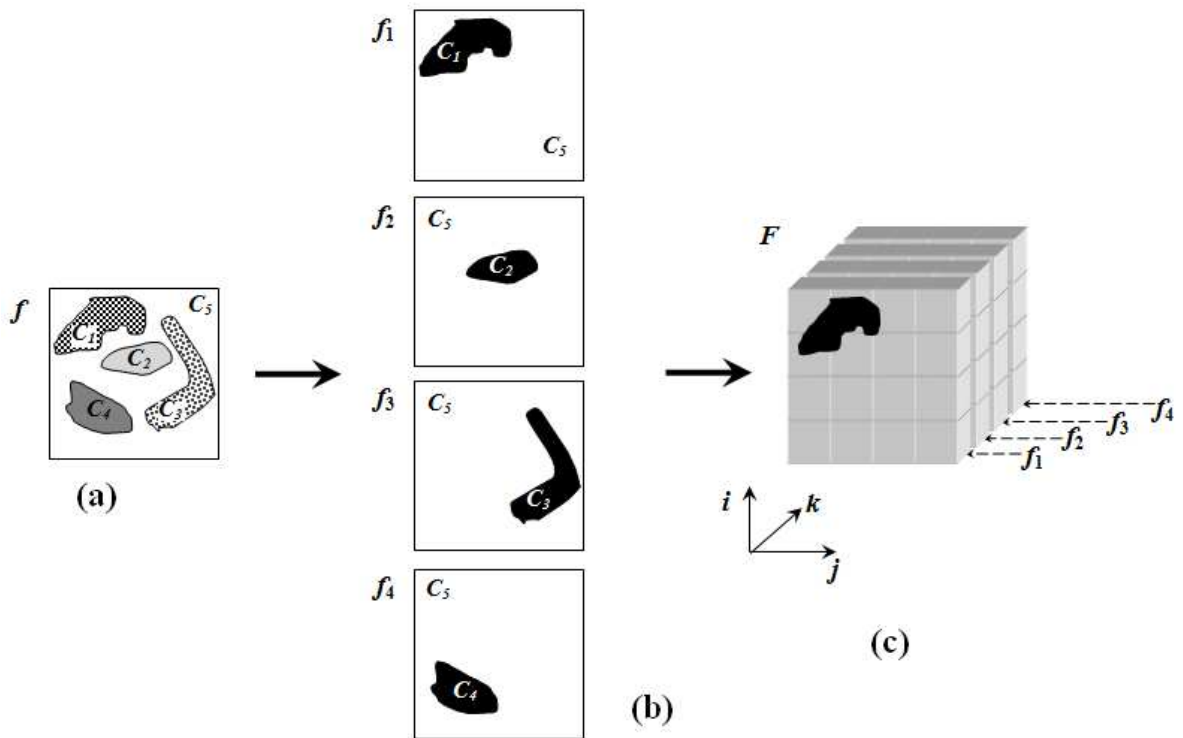
Figure 3-4 Multi-class constraint (a) an image showing five different types of classes including background, (b) Each class can be decomposed and assigned into four binary images, and (c) an arrangement of binary image of each band image creating a 3-dimensional matrix.

sum of the outputs of each set of neuron at point (i, j) equals one. This is to avoid a formation of new class resulting from overlapping process of two or more classes from different binary images.

$$\frac{dM_{kij}}{dv_{kij}} = \left(\sum_{k=1}^{C} v_{kij} \right) - 1 \qquad (3.31)$$

In the Equation 3.31, c represents the number of class to be predicted. If the output sum equals one, a zero gradient is gradient is produced. If the sum of the outputs for each classes at point (i, j) is less than 1, a negative gradient is produced which corresponds to an increase in neuron output. If the sum of the outputs for each classes at point (i, j) is greater than 1, a positive gradient occurred which corresponds to a decrease in neuron output. The energy function of the HNN for the multiclass land cover mapping is represented by Equation 3.32

$$E = -\sum_k \sum_i \sum_j \left(k_1 G_{kij}^{ON} + k_2 G_{kij}^{OFF} + k_P P_{kij} + k_M M_{kij} \right)$$

(3.32)

where k_M is a weighting constant for the multiclass constraint function.

3.3. Pixel swapping

Pixel swapping is a technique that calculates the attractiveness of each sub-pixel to a particular class of land cover. The technique was first developed by Atkinson (2005) for binary case. Contrary to its name, pixel swapping is a technique that swaps sub-pixels contained in a pixel of a coarse spatial resolution image. This technique starts after an image has been soft classified. Pixel swapping uses an attractive function to measure an attractiveness level of a sub-pixel i related to its neighbours $j = 1, \ldots, J$ as given in Equation 3.33 that measures the summation of weighed distance between a sub-pixel of interest and its neighbours.

$$A(x_i) = \sum_{j=1}^{J} \gamma_{ij} z(x_j)$$
(3.33)

where $z(x_j)$ is the binary class of the jth sub-pixel at location x_j, and γ_{ij} is a non-linear distance weighted function calculated as

$$\gamma_{ij} = \exp\left(\frac{-h_{ij}}{\alpha}\right)$$
(3.34)

where h_{ij} is the distance between sub-pixel x_i and sub-pixel x_j, and α is a parameter for the exponential function.

The attractiveness of each sub-pixel in a coarse spatial resolution pixel is measured and ranked. For a binary image case, the least attractive sub-pixel is a sub-pixel with a value "1" and surrounded mainly by sub-pixels with value "0".

$$\arg\min_{x_i} A(x_i) = \left\{ x_i \mid z(x_i) = 1 \right\}$$
(3.35)

The most attractive sub-pixel is a sub-pixel with a value "0" and surrounded mainly by sub-pixels with value "1".

$$\arg\max_{x_j} A(x_j) = \left\{ x_j \mid z(x_j) = 0 \right\}$$
(3.36)

If the attractiveness of the least attractive sub-pixel x_i is less than that of the most attractive sub-pixel x_j, then the classes of these sub-pixels are swapped.

$$\left. \begin{array}{l} z(x_i) = 0 \\ z(x_j) = 1 \end{array} \right\} \quad \text{if} \quad A_i < A_j \qquad (3.37)$$

The swapping of the sub-pixels only occurs within a pixel, not between pixels. One sub-pixel within a pixel is swapped per iteration. The algorithm runs until no swaps are made or until it reaches a specified number of iterations.

3.4. Experimental analysis

Four images of areas of different types of land cover mosaic were acquired from the Google Earth at various locations of olive farms in Granada, Spain (Figure 3.5). The four types of the spatial pattern are termed here: sparsely populated, densely populated, globally heterogeneous, and inter-grade, each is shown in order in Figure 3.6a to Figure 3.6d. The original size of each image is 256×256 pixels. To generate coarse spatial resolution image, the spatial resolution of each image in Figure 3.6 was down-sampled by factor of 8 to a size of 32×32 pixels, shown in Figure 3.7. For each coarse resolution image, the spatial resolution was increased and the spatial pattern of the land cover was estimated in order to produce estimation result as closely as its own target image as shown in Figure 3.8. The binary target or ground reference images were obtained by performing hard classification based on k-means clustering (Duda et al., 2001) on the original images. White pixels in the target images represent the olive trees in the original images, while black pixels in the target images represent the land surface in the original images.

Figure 3-5 Location of Granada, Spain.

Representation of the land cover of each site were derived and compared using a number of different types of land cover classification. For naive land cover estimation, three techniques were used: the k-means hard classification as shown in Figure 3.9, two simple interpolations: bilinear and bicubic (Keys, 1981) and the results were hardened using the k-means technique (Figure 3.10 and 3.11).

For super-resolution mapping land cover representation, another three techniques were used: HNN that used the goal function, HNN that used the semi-variance and the pixel swapping. All the super-resolution mapping techniques used inputs of proportion images derived from fuzzy c-means soft classification. An HNN consisting of goal functions and area proportion constraint was used as in Equation 3.19 to produce

estimations of land covers shown in Figure 3.12. The weighting constants for the goal functions and the area proportion constraint, k_1, k_2, and k_P were all set to 1.0 to give equal emphasis between the goal functions and the constraint. The choice of the values for the weighting constants is a standard practice in other works (Tatem et al., 2001a; Ling et al., 2010). If the strength of the goal functions is higher than that of the area proportion constraint, then the predicted shape of land cover would become too large and irregular. If the strength of the area proportion constraint is higher than that of the goal functions, then the output of the HNN would not be able to produce values of either 0 or 1, rather ranges of value between 0 and 1 would be produced, therefore, no land cover could be represented. However, by setting the equal value of the weights, the effects of the goal functions and the area proportion constrain may not be equal. For instance, the effect may be equal when a weighting of 1000000 for the area proportion constraint is paired with a weighting of 0.001 for the goal functions.

The number of the neurons in the Hopfield neural network depended on the number of the sub-pixel of the image. Since, the size of the coarse pixel was 32×32 pixels and the magnification factor required was 8, there were 256×256 sub-pixels in the image. Therefore, the arrangement of neurons in the HNN was designed to accommodate 256×256 sub-pixels in one layer. jThe value for each neuron in HNN was updated until 1000 iterations at which the energy function appear to reach its optimum level.

The other HNN used the semi-variance and the area proportion constraint and its estimation on land covers are shown in Figure 3.13. As the down-sampling factor was 8, the number of semi-variance values in the HNN was also set to 8. The weighting

constant for each of the semi-variance values in the Equation 3.26, $k_1,...,k_8$, was set equally to 1.0. The weighting constant for the area proportion constraint was also set to 1.0. The selection of these weight values would provide equal value between the semi-variance and the area proportion constraint. Again, equal value of the weights may not produce equal effect on the semi-variance and the area proportion constraint. The arrangement of neurons in this HNN was also designed to accommodate 256×256 sub-pixels in one layer. The HNN also updated iteratively until 1000 iterations, at which the energy function of the HNN reached a stable state.

For the pixel swapping super-resolution mapping technique, the iteration requires to reach a stable state was faster than that of both the HNN techniques. Here the number of iteration for pixel swapping was set to 100 iterations at which the pixel swapping appear to reach its stable state. The results of land cover estimation are shown in Figure 3.14.

Results of land cover estimations for each technique were compared in terms of thematic accuracy and spatial pattern. The site specific thematic accuracy for each technique was assessed using all 65536 (256×256) sub-pixels in each image. A confusion matrix was generated for each classification technique and its accuracy was expressed by overall proportion correct and kappa coefficient, summarized from Table 3.1 to Table 3.4 for four different land cover mosaics.

From the results, the hard classification and the interpolation technique tends to produce lower accuracy than the three super-resolution mapping techniques in all four images. Of the three super-resolution mapping techniques, the HNN that used semi-

variance produced the highest thematic accuracy in all the images, while the HNN that used goal functions was slightly higher accurate than that from the use of the pixel swapping approach.

Results in the Table 3.1 to 3.4 also indicate that the accuracy of land cover estimation was affected by the spatial configuration of land cover. All of the techniques tended to produce higher accuracy estimation for the sparsely populated pattern than the other patterns. The trend showed in the results was because the sparsely populated pattern had large land cover patches and the gap of the land surface between patches was also large. In contrast, the accuracy for all the techniques was low when estimating the densely populated pattern because the densely populated pattern had small land cover patches and the gap of the land surface between patches was also small.

To evaluate spatial pattern estimation, the semi-variance was used to measure the spatial variance between points that are spaced at a constant distance apart or lag shown in variogram in Figure 3.15 until 3.18. Each figure represents variogram plots for the various land cover estimation techniques on a particular land cover pattern. For each figure, a variogram for the particular target image was also plotted as a benchmark. Further, the sum squared error (SSE) between the variogram of the target image and the variogram of the estimated image was calculated. The SSE was calculated to provide a statistical measure of the difference between a variogram of the ground data and a variogram of land cover mapping image derived from different classification techniques. Results for the SSE for the four different spatial pattern of the land cover were presented in Table 3.5 until Table 3.8.

(a) (b) (c) (d)
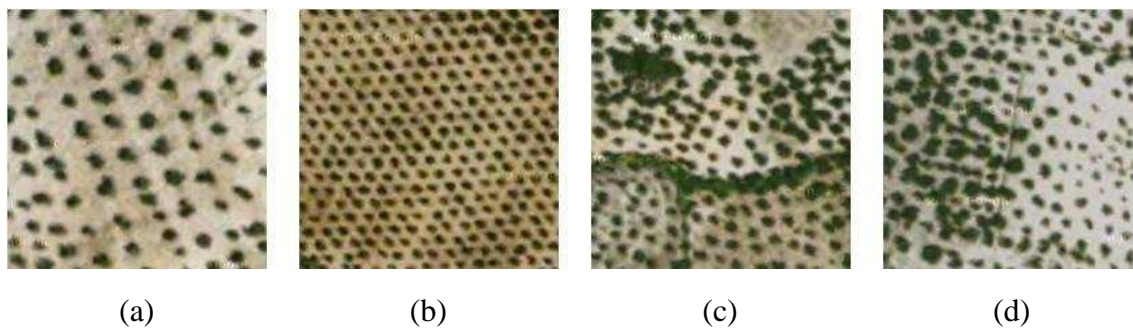
Figure 3-6 Original images of different spatial pattern of olive farms. (a) Sparsely populated, (b) densely populated, (c) globally heterogeneous, and (d) inter-grade. The size of each image is 256×256 pixels.

(a) (b) (c) (d)
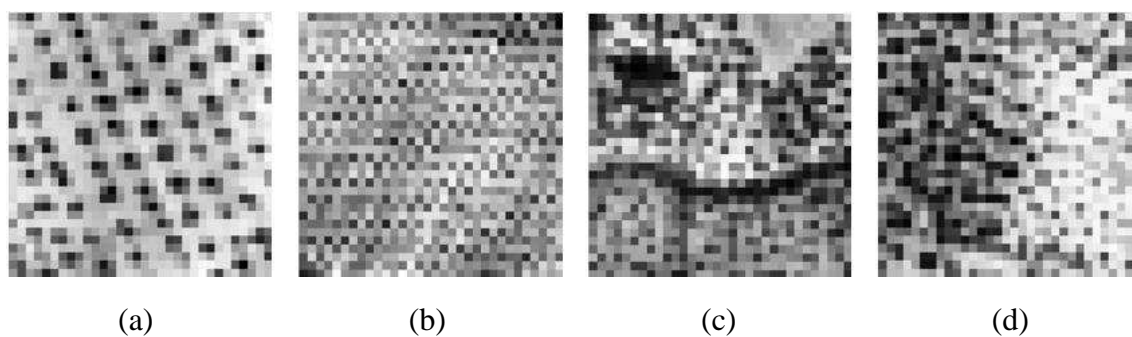
Figure 3-7 Degraded images from the original images in Figure 3.6. The size of each image is 32×32 pixels.

(a) (b) (c) (d)
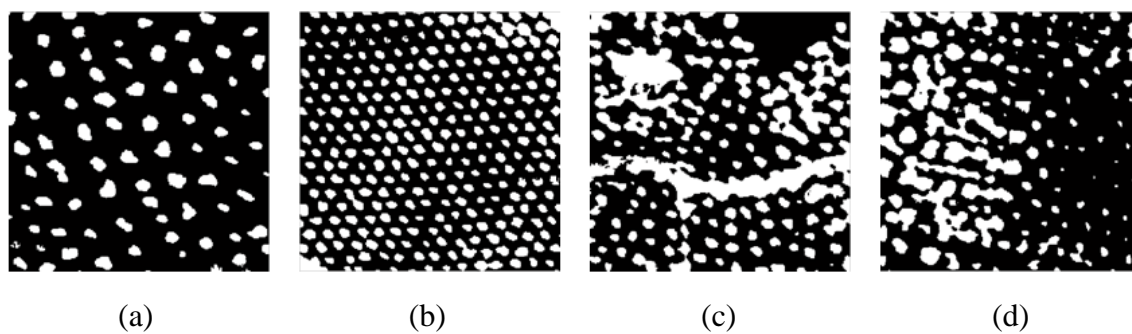
Figure 3-8 Target images.

(a)　　　　(b)　　　　(c)　　　　(d)
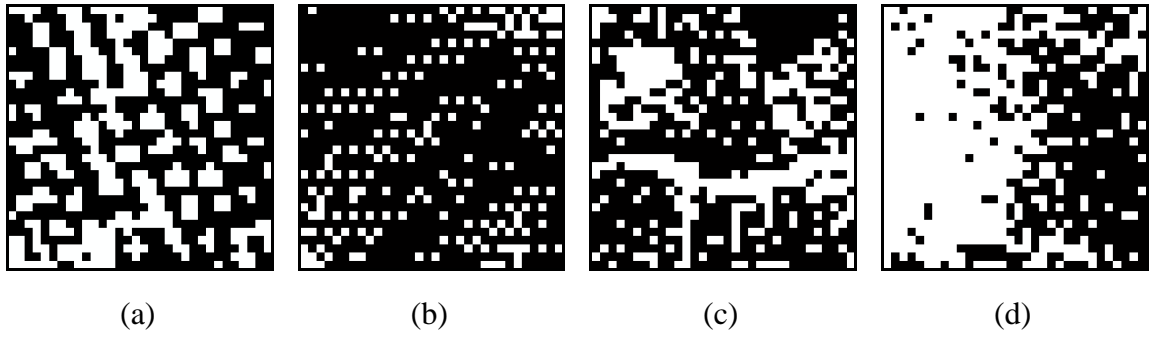
Figure 3-9 Estimation results of hard classification technique.

(a)　　　　(b)　　　　(c)　　　　(d)
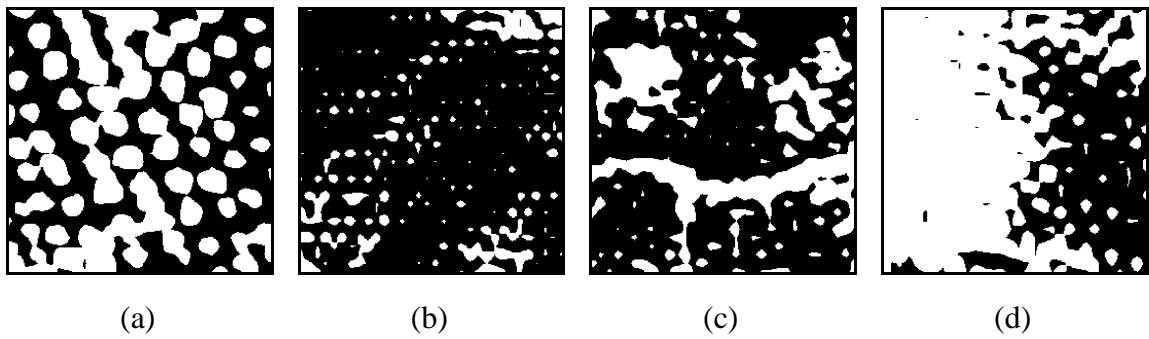
Figure 3-10 Harden classification of bilinear interpolation technique.

(a)　　　　(b)　　　　(c)　　　　(d)
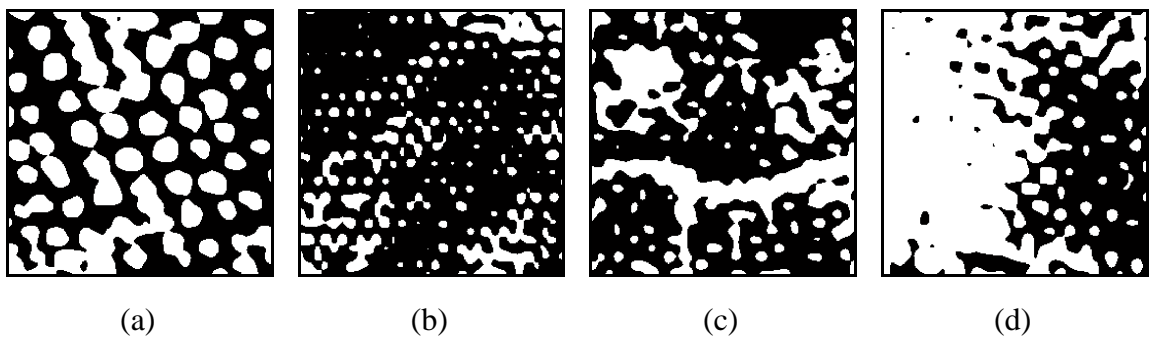
Figure 3-11 Harden classification of bicubic interpolation technique.

<div align="center">(a)   (b)   (c)   (d)</div>
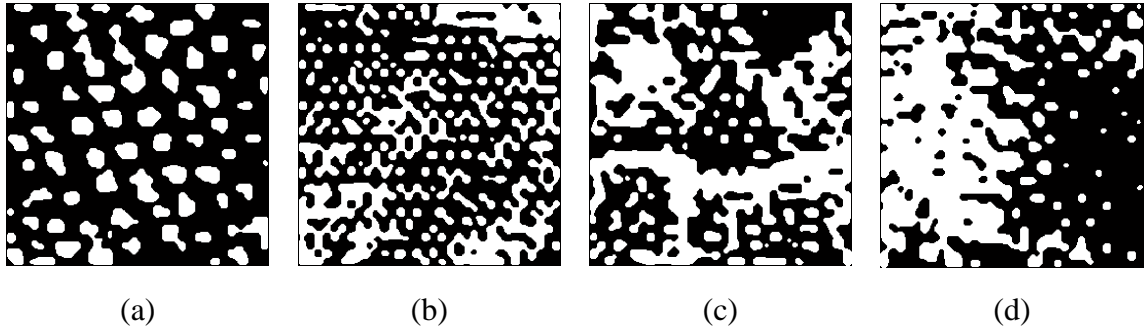
Figure 3-12 Estimation results of HNN technique that used goal functions.

<div align="center">(a)   (b)   (c)   (d)</div>
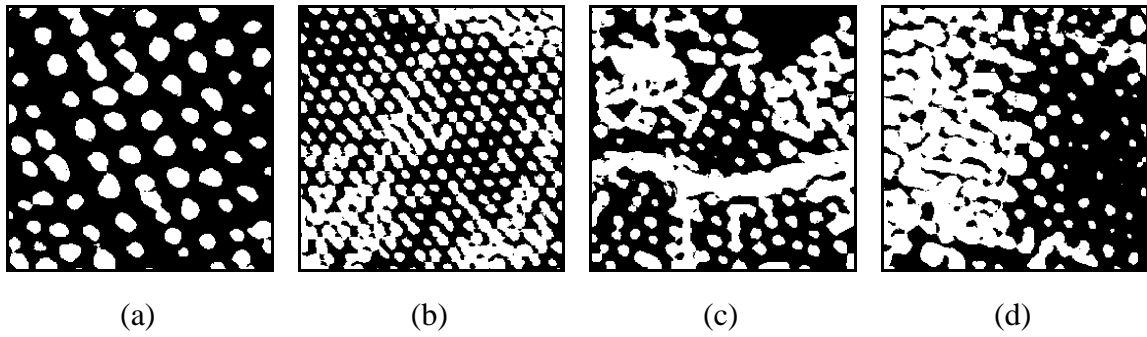
Figure 3-13 Estimation results of HNN technique that used semi-variance.

<div align="center">(a)   (b)   (c)   (d)</div>
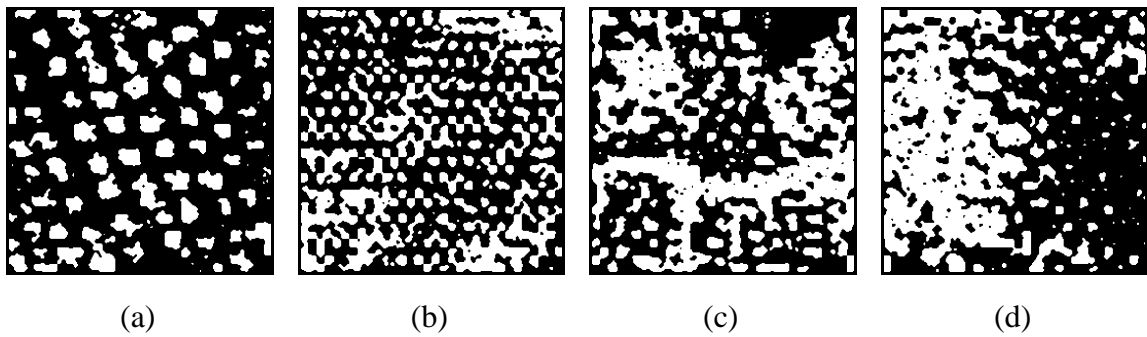
Figure 3-14 Estimation results of pixel swapping technique.

Table 3-1 Thematic accuracy comparison between different land cover mapping classification techniques for a sparsely populated land cover pattern

Classification	Proportion correct	Kappa coefficient
Hard classification	0.7986	0.5494
Bilinear	0.8817	0.7020
Bicubic	0.9005	0.7414
HNN that used goal functions	0.9179	0.7744
HNN that used semi-variance	0.9670	0.9107
Pixel swapping	0.8986	0.7249

Table 3-2 Thematic accuracy comparison between different land cover mapping classification techniques for a densely populated land cover pattern

Classification	Proportion correct	Kappa coefficient
Hard classification	0.7352	0.3596
Bilinear	0.6955	0.3711
Bicubic	0.7097	0.4022
HNN that used goal functions	0.7377	0.4408
HNN that used semi-variance	0.8873	0.7706
Pixel swapping	0.7321	0.4317

Table 3-3 Thematic accuracy comparison between different land cover mapping classification techniques for a globally heterogeneous land cover pattern

Classification	Proportion correct	Kappa coefficient
Hard classification	0.8186	0.6136
Bilinear	0.8075	0.6087
Bicubic	0.8204	0.6355
HNN that used goal functions	0.8245	0.6417
HNN that used semi-variance	0.9156	0.8284
Pixel swapping	0.8095	0.6112

Table 3-4 Thematic accuracy comparison between different land cover mapping classification techniques for an inter-grade land cover pattern

Classification	Proportion correct	Kappa coefficient
Hard classification	0.7715	0.5562
Bilinear	0.8151	0.6275
Bicubic	0.8366	0.6693
HNN that used goal functions	0.8481	0.6900
HNN that used semi-variance	0.9241	0.8471
Pixel swapping	0.8312	0.6549
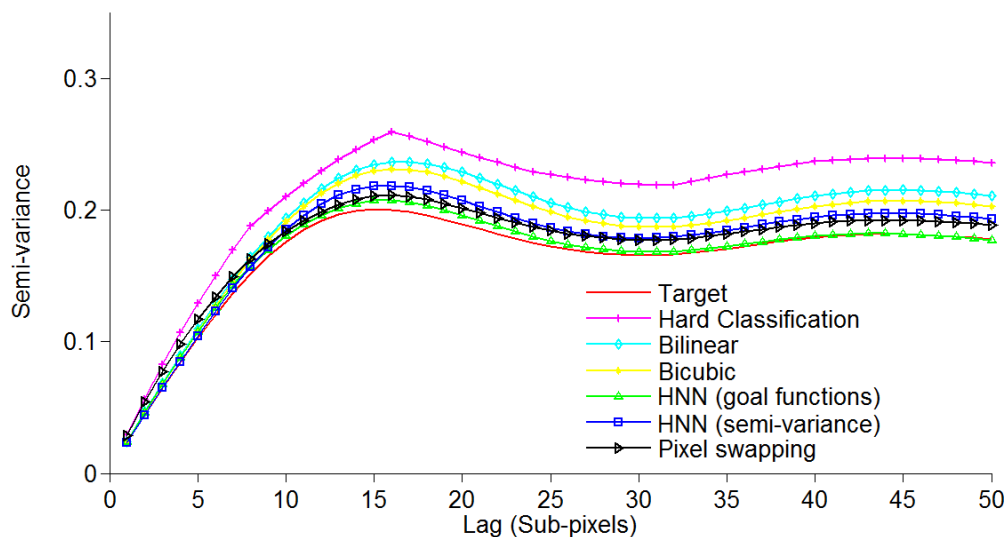
Figure 3-15 Variogram of different land cover estimation techniques for the sparsely populated land cover pattern.

Table 3-5 SSE for variogram of different land cover estimation techniques applied on a sparsely populated land cover pattern.

Classification	SSE
Hard classification	0.1264
Bilinear	0.0428
Bicubic	0.0265
HNN that used goal functions	0.0008
HNN that used semi-variance	0.0096
Pixel swapping	0.0061
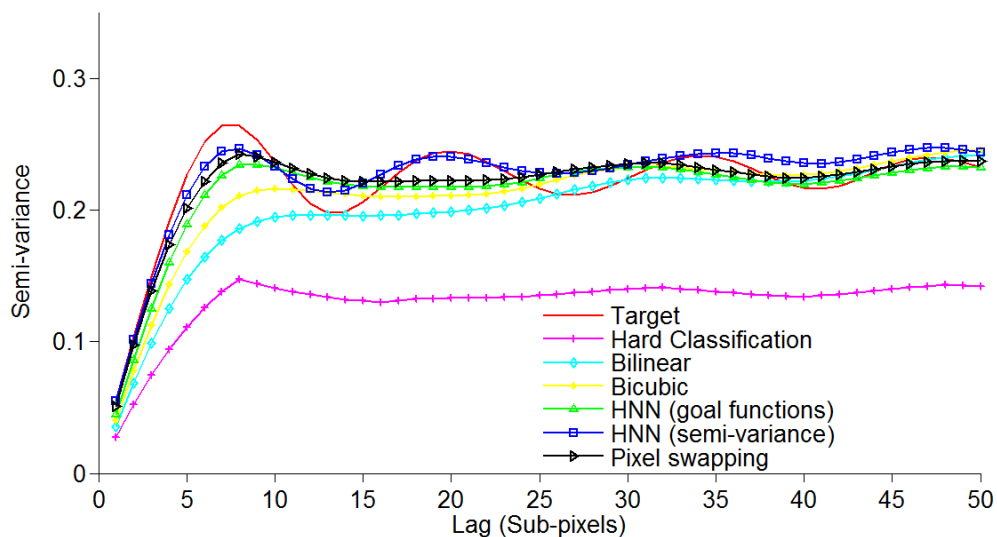
Figure 3-16 Variogram of various land cover estimation techniques on a densely populated land cover pattern.

Table 3-6 SSE for variogram of different super-resolution mapping methods applied on a densely populated land cover pattern.

Classification	SSE
Hard classification	0.4254
Bilinear	0.0558
Bicubic	0.0285
HNN that used goal functions	0.0145
HNN that used semi-variance	0.0065
Pixel swapping	0.0098
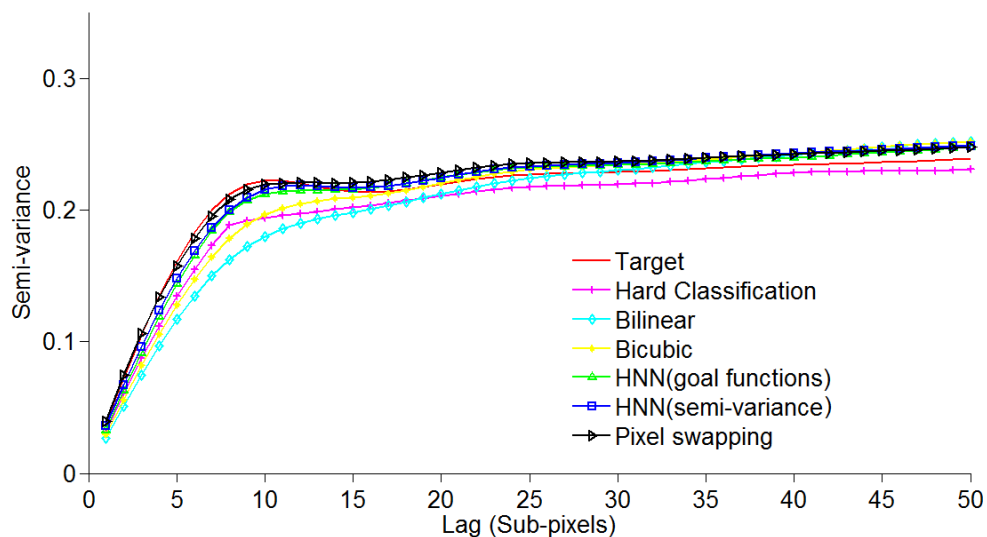
Figure 3-17 Variogram of various land cover estimation techniques on a heterogeneous land cover pattern.

Table 3-7 SSE for variogram of different super-resolution mapping methods applied on a heterogeneous land cover pattern.

Classification	SSE
Hard classification	0.0098
Bilinear	0.0219
Bicubic	0.0110
HNN that used goal functions	0.0032
HNN that used semi-variance	0.0032
Pixel swapping	0.0027
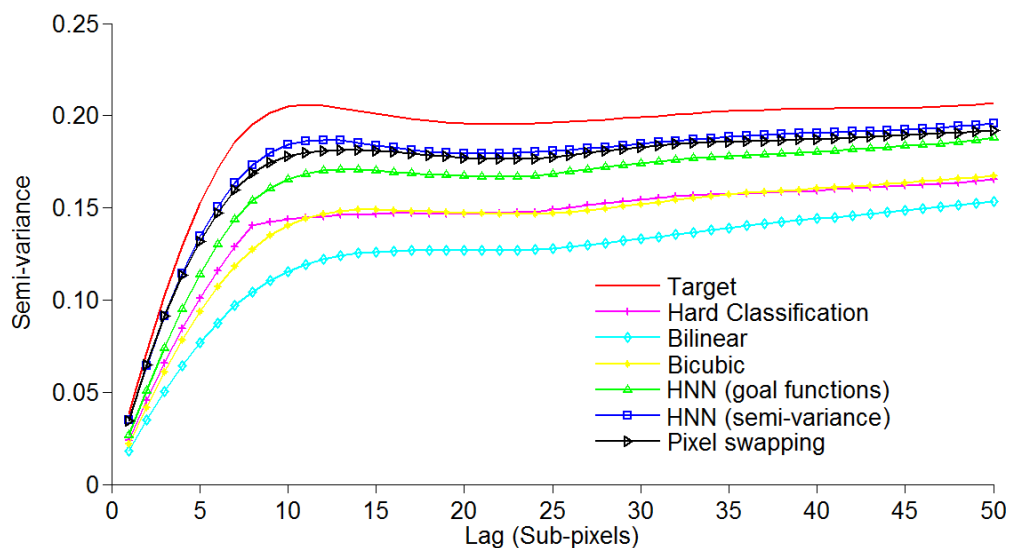
Figure 3-18 Variogram of various land cover estimation techniques on an inter-grade land cover pattern.

Table 3-8 SSE for variogram of different super-resolution mapping methods applied on an inter-grade land cover pattern.

Classification	SSE
Hard classification	0.1128
Bilinear	0.2276
Bicubic	0.1193
HNN that used goal functions	0.0399
HNN that used semi-variance	0.0117
Pixel swapping	0.0170

For the sparsely populated land cover pattern, the conventional hard classification technique produced the most error. All the three super-resolution mapping techniques produced less error compared to the two interpolation techniques. Of all the three super-resolution mapping techniques, HNN technique that used goal functions produced the least error as its variogram was closely resembled to the variogram of the target.

For densely populated land cover pattern, conventional hard classification produced the most error. All the three super-resolution mapping techniques produced less error compared to the two interpolation techniques. The HNN that used the semi-variance functions and the pixel swapping techniques tended to produce less error than that of the first HNN that used the goal functions.

For the heterogeneous land cover pattern, the two interpolation techniques produced more errors compared to other techniques. The errors produced by the two HNNs were almost identical but the error produced by the pixel swapping slightly less than that of the two HNNs.

For inter-grade land cover pattern, all the super-resolution mapping techniques produced less error than the hard classification and the interpolation techniques. The HNN that used the semi-variance produced the least error.

From the two types of accuracy analyses: the site specific thematic accuracy and the variogram, in general, the HNN that used semi-variance tended to produce higher accuracy than the other super-resolution mapping techniques in estimating land cover

(a)   (b)   (c)

Figure 3-19 'Mismatch classification' of using HNN that used semi-variance with different prior information. (a) Coarse spatial resolution of heterogeneous cover, (b) a priori knowledge from finer spatial resolution of densely populated land cover pattern, and (c) result of HNN that used semi-variance for super-resolution mapping.

and its spatial configuration of the land cover. The higher accuracy produced in the results of this HNN is contributed to the exploitation of prior knowledge in its formulation. There are advantages and disadvantages on relying on the prior knowledge. The advantages of using prior information had been demonstrated in the analyses on the site specific accuracy and variogram, which produced the most accurate results compared to the other techniques. On contrary, the disadvantages of relying on prior knowledge are that the prior information needs to be available before super-resolution mapping process begins. Prior information on one particular area also cannot be used on another area. Prior information on one area is only suitable for that particular area and not on other areas. For example, an analysis was performed on a coarse spatial resolution image of heterogeneous land cover pattern (Figure 3.19a) using this HNN

technique. A priori information was derived from a finer spatial resolution of densely populated land cover pattern (Figure 3.19b). Result produced by the HNN that used semi-variance is shown in Figure 3.19c, which demonstrates that the spatial pattern estimated appeared to be more similar to the prior information than the actual pattern.

In this chapter, shrubby images of different spatial configuration were used with different land cover mapping techniques. Apart from these images, other images can be used for various applications, such as vegetation mapping, deforestation, water bodies and land classification. From the results, it appears that one of the major limitation of the standard super-resolution mapping techniques was the low accuracy when the size of land cover patches were small than an image pixel. In addition, if the gap between the patches was also smaller than a pixel, all the standard super-resolution mapping techniques tended to produce less accurate results.

3.5. Conclusions

The fundamental concept of two standard super-resolution mapping techniques: HNN and pixel swapping were discussed in this chapter. Both techniques were formulated to map land cover at a sub-pixel scale given only a single coarse spatial resolution image. As the fuzzy c-means is an unsupervised clustering technique, it is suitable for fully automated super-resolution mapping procedure and was used here to derive the soft classification input required by the super-resolution mapping techniques.

This chapter used two sets of HNN and a pixel swapping technique to represent land cover mosaic of different spatial configurations. All of the super-resolution mapping techniques generally gave accurate representation of land cover. The use of prior information may contribute to an increase in land cover mapping accuracy, but in every super-resolution mapping process, this approach requires availability of prior information such as a finer spatial resolution of a particular area. In addition, the accuracy of land cover mapping is also affected by the different spatial configurations of land cover pattern. Generally, all of the land cover mapping techniques evaluated in this chapter produced high accuracy estimation on the sparsely populated pattern, which has large land cover patches. All of the techniques, however, tend to produce low accuracy estimation on densely populated pattern, which has small land cover patches. In Chapters 4 and 5, improvement on the HNN and pixel swapping will be discussed with particular attention on the representation of small land cover patches.

4. Super-resolution mapping for small land cover patches

In Chapter 3, the potential of the HNN and pixel swapping techniques for super-resolution mapping were demonstrated on images of different land cover mosaics. As the size of land cover patches varies, the potential value of the standard HNN and pixel swapping also varies, especially when the size of the patches is smaller than an image pixel. The difference in accuracy between the sparsely populated pattern image and the densely populated pattern image was due to the size difference of land cover patches in both images. The HNN and pixel swapping techniques generally produced high accuracy when the size of land cover patches was large, but the accuracy was low when the size of the patches was small. This chapter highlights limitations of the HNN and pixel swapping in representing various sizes of land cover patches with particular attention on small land cover patches. These limitations are tackled through appropriate parameter settings in the super-resolution mapping techniques.

4.1. Introduction

Research of the super-resolution mapping techniques that used the HNN demonstrates its flexibility more than by using the pixel swapping technique. In the HNN, additional source of information can be incorporated into the main input imagery. The additional source can be acquired from different type of imagery with different spatial or spectral resolution. For example, a priori information in the form of a semi-variance values derived from a finer spatial resolution image is incorporated with main imagery with coarser spatial resolution (Tatem et al., 2002); data from light detection and ranging (LIDAR) with spatial resolution of 0.8 m is incorporated into optical data at 4 m spatial resolution (Nguyen et al., 2005); and multispectral (MS) bands of the IKONOS with spatial resolution of 4 m are fused with its 1 m panchromatic band. In contrast, the applications of the pixel swapping (Atkinson, 2005) for super-resolution mapping are limited to a single type of image such as 2.6 m spatial resolution Quickbird imagery (Thornton et al., 2006); and 0.25 m aerial photography (Thornton et al., 2007) in which each image is used independently.

The flexibility of the HNN to use a combination of different information is facilitated by its energy function (Tatem et al., 2001a) that can be formulated in order to consider different type of resources used. Depending on the applications, the energy function can consist of different constraints. These constraints are designed to put emphasis on spatial clustering goal and area proportion (Tatem et al., 2001a); multiple land cover classification (Tatem et al., 2001b); semi-variance (Tatem et al., 2002); height constraint that is used in the LIDAR elevation data (Nguyen et al., 2005); and

panchromatic reflectance constraint (Nguyen et al., 2006). These constraints can be weighted differently to give different emphasis on the outcome of the HNN.

However, in the previous works of the HNN for super-resolution mapping, the determination of the weight constraints lack quantitative analysis that can justify the value of the weight. In Tatem et al. (2001a), the weight for the constraints is determined on the basis of a hypothetical situation. The strength of the two goal function constraints and the area proportion constraint is assumed to be equal, thus the weights for all the constraint are all set to 1.0. In Tatem et al. (2002), the weight for each of the seven semi-variance values are set to 0.2 on each one of them, while the weight for the area proportion constraint is set to 1.4. In Nguyen et al. (2005) the weights for the two goal function constraints are both set to 150 and the weight for the area proportion constraint is set to 200. In Nguyen et al. (2006) the weights for all the constraint in one experiment are all set to 70, while in another experiment, the weights for the goal function constraints are both set to 70 and the area proportion constraint weight is set to 100.

Additionally, in the previous works of the HNN, the land cover patches are generally larger than an image pixel because the spatial clustering goal function of the HNN was never intended to be applied to small land cover patches. Only in Tatem et al. (2002) that the land cover patch size is smaller than a pixel, but the method used requires a priori information derived from a fine spatial resolution image, which may increase the cost of the image acquisition.

In contrast, pixel swapping requires less complex parameter settings than the HNN (Atkinson, 2005), although research on utilizing multiple input sources for the

pixel swapping are relatively limited compared to the HNN. In addition, pixel swapping is faster than the HNN in term of iteration required to reach a stable state and so less computational time is required for the use of the pixel swapping.

In this chapter, the representation of land cover patches smaller than an image pixel using the basic HNN (Equation 3.19) and the pixel swapping (Equation 3.33) for super-resolution mapping techniques were presented. This chapter extends the application of the two techniques from Chapter 3 in order to represent small land cover patches. Simple simulated scenarios for patches were created. As the HNN requires more complex parameter settings than the pixel swapping, the attention of this chapter was focused more on the HNN, but analyses on the pixel swapping were also included. Critically, correct parameter settings may ensure that the HNN and pixel swapping can be exploited in order to represent small land cover patches. For both the HNN and pixel swapping, the representation of the land cover patches was demonstrated and compared.

4.2. Sub-pixel patches in a mixed pixel

One of the four causes of the mixed pixel problem is the existence of small land cover patches in a pixel (Fisher, 1997) as shown in Figure 1.1a. While the other three problems: boundary pixel, inter-grade and linear sub-pixel, have been solved by many super-resolution mapping techniques, there is a lack of attention focusing on the solution of the sub-pixel sized patches in a mixed pixel. As the size of the sub-pixel patches is smaller than an image pixel, inability to represent the patches also highlights the limitation of the current super-resolution mapping techniques.
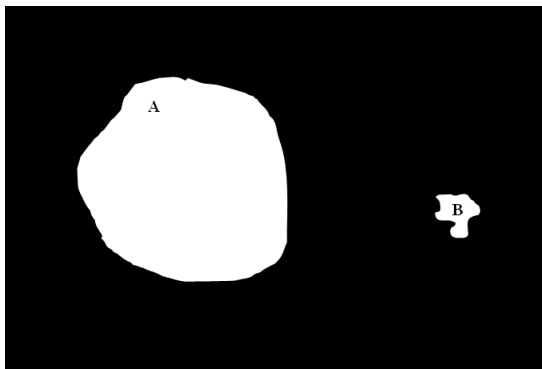
Figure 4-1 Two white land cover patches on black land cover background.
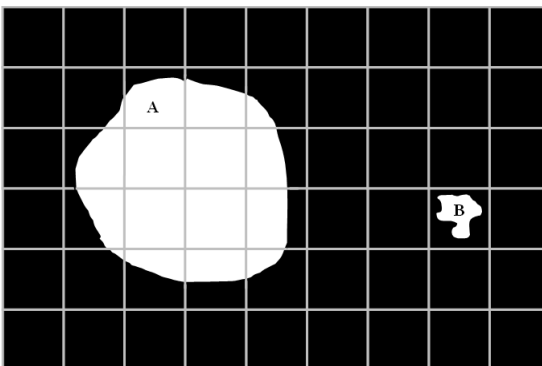
Figure 4-2 Two white land cover patches overlaid with coarse spatial resolution grid image. The size of the patch A is larger than a coarse pixel while the size of the patch B is smaller.
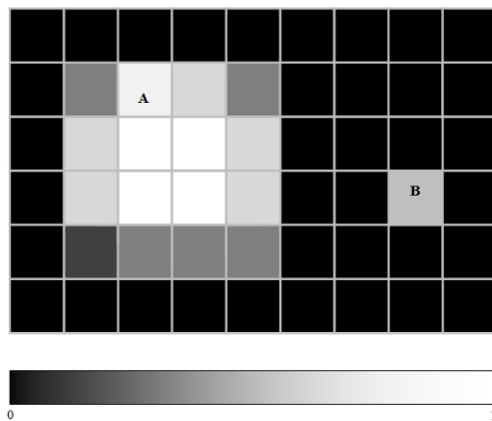
Figure 4-3 Degradation of the image in Figure 4.1 by spatial aggregation into a coarse spatial resolution image.

To evaluate the limitation of super-resolution mapping techniques, two different sizes of land cover patches were used. Figure 4.1 shows an example of a fine spatial resolution image with two identical land cover classes: white (1.0) and black (0.0); the black class can be regarded as background. The image contains two patches of the white class. Patch A is of a size larger than a pixel while patch B is smaller than a pixel. The relationship with the spatial resolution between a fine image and a coarse image is shown in Figure 4.2 in which the grid of the coarse spatial resolution image was overlaid onto the fine spatial resolution image.

The image in Figure 4.1 was degraded by spatial aggregation into a coarse spatial resolution image as shown in Figure 4.3. In the degraded image, pixels containing boundaries of the land cover patch A would appear in grey indicating that the pixels are mixed with different land cover classes and the values of these pixels are in the range of 0 and 1. Light grey indicates that the proportion of white class is greater than the proportion of black class. Dark grey indicates that the proportion of black class is greater than the proportion of white class. Other pixels that remain in either white or black indicate that the pixels are pure pixels which contain only single land cover class. In the degraded image, only one pixel represents the land cover patch B. This pixel is a mixed pixel and located in isolation because it is surrounded with black pixels. It also appears that the size of the actual land cover patch B is smaller than the size of a coarse pixel.

The solution of the HNN super-resolution mapping would employ an energy function as an optimization tool to produce the prediction of land cover mapping at a sub-pixel scale. The basic formulation of the energy function consists of two goal

functions and an area proportion constraint function as given in Equation 3.19. This formulation allows land cover to be predicted at a sub-pixel scale if the size of the land cover is larger than a coarse spatial resolution pixel. In the coarse spatial resolution image, the boundaries of the land cover will become mixed pixels. Using super-resolution mapping techniques, such as HNN and pixel swapping, at least two different land covers in the mixed pixel would present. The value of each coarse pixel was assumed to be the value of land cover proportion in that pixel and would be the input for the super-resolution mapping techniques. Examples in the following sections will demonstrate the effectiveness of the HNN to represent land cover patches when the size of the land cover patch is larger than a coarse pixel, and more importantly highlighting the limitation of the HNN when the size of the land cover patch is smaller than the size of an image pixel. For comparative purposes, representation of land cover patches using pixel swapping is also included.

4.3.   Large land cover patches

The formulation of the standard HNN (Equation 3.19) has been proven in a number of studies (e.g. Tatem et al., 2001a; Nguyen et al., 2005) to represent land cover patches that are larger than a pixel such as patch A in Figure 4.1. To illustrate the conceptual framework of the HNN for super resolution mapping, Figure 4.4a shows an example of a 3×3 block of pixels in coarse spatial resolution image. This image can be used to represent parts of the boundaries of large land cover patches. A gray pixel at the centre was a mixed pixel because it contains a mixture of two different land covers: white and

black. The mixed pixel was surrounded by pure pixels in white and pure pixels in black. The land cover proportion in the mixed pixel was expressed by soft classification. Here, the value of the soft classification in the mixed pixel was 0.50 while 1.0 for white pixels and 0.0 for black pixels. In Figure 4.4b, the spatial resolution of the coarse image was increased by a factor of eight by decomposing a pixel into 8×8 sub-pixels. For the mixed pixel, based on its soft classification value, 32 sub-pixels belong to white land cover class while the other 32 sub-pixels belong to black class. Initially, the spatial distribution of these sub-pixels was allocated randomly within region represented by the mixed pixel as shown in Figure 4.4b.

All the sub-pixels in the image were fed into input neurons of the HNN in which 24×24 neurons were used to process all the sub-pixels simultaneously. Using the hypothetical assumption that the emphasis between the goal constraint function and the area proportion constraint was equal, the weights for the goal constraint, k_1 and k_2, and the weight for the proportion constraint, k_P were all set to 1.0. The calculation of the HNN was optimized for 1000 iterations at which the energy of the HNN (Equation 3.19) became stable.

During the optimization process of the HNN, the white sub-pixels in the mixed pixel were attracted towards adjacent pure white pixels, while black sub-pixels towards adjacent pure black pixels. In the output neurons, the optimized HNN could represent a land cover and separated it with other land covers such as the background. As a result, a diagonal boundary line was created inside the mixed pixel as shown in Figure 4.4c. The

(a)   (b)   (c)
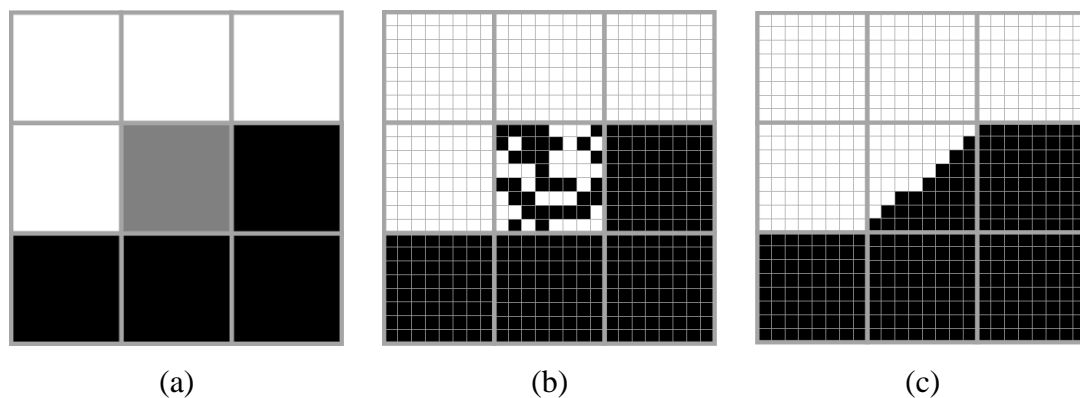
Figure 4-4 Super-resolution mapping of land cover using the standard HNN. (a) A coarse spatial resolution with 4 white pure pixels, 4 black pure pixels and 1 mixed pixel. The soft classification value in the mixed pixel is 0.5. (b) Decomposition of coarse pixel into 8×8 sub-pixels with initial random allocation of white and black sub-pixels in the mixed pixel. (c) Estimation of land cover represented from HNN showing the boundary between two land cover classes (white and black) crossing inside the mixed pixel.

(a)   (b)   (c)
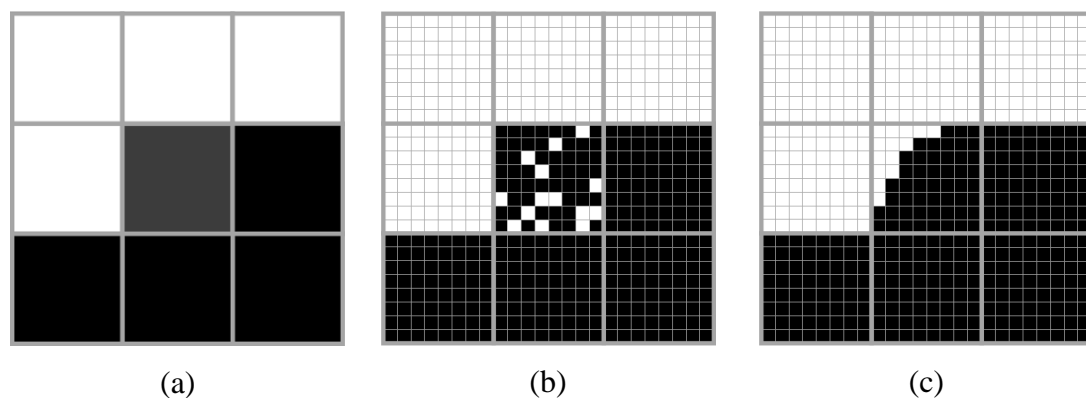
Figure 4-5 Super-resolution mapping of land cover using the standard HNN. (a) A coarse spatial resolution with 4 white pure pixels, 4 black pure pixels and 1 mixed pixel. The soft classification value in the mixed pixel is 0.2. (b) Decomposition of coarse pixel into 8×8 sub-pixels with initial random allocation of white and black sub-pixels in the mixed pixel. (c) Estimation of land cover represented from HNN showing the boundary between two land cover classes (white and black) crossing inside the mixed pixel.

number of the white sub-pixels estimated by the HNN in the mixed pixel was 33. This result suggested that the proportion of the white land cover inside the mixed pixel was 0.52 (from 33/64), making the magnitude of an error between the actual land cover proportion and the estimated land cover proportion within the mixed pixel only 0.02.

4.4.   Small land cover patches

To illustrate the capability of the HNN to represent small land cover patches, such as patch B in Figure 4.1, a simple example was demonstrated as in Figure 4.6a that shows a 3×3 block of pixels in a coarse spatial resolution image. A gray pixel at the centre is a mixed pixel because it contains a mixture of two different land cover classes: white and black; the other 8 pixels all belong fully to the black land cover class. The soft classification value of the mixed pixel in the centre was 0.50. Initial random allocation of the two land covers is shown in Figure 4.6b. Using the standard HNN, a small land cover patch was produced in Figure 4.6c, which contains 27 white sub-pixels. This result suggested that the proportion of the white land cover class inside the mixed pixel was 0.42, making the magnitude of an error between the soft classification input and the proportion of the estimated land cover to 0.08; slightly larger than the errors produced when the size of the land covers are larger than a coarse pixel.

When the value of the soft classification of the mixed pixel is low for example 0.20, the HNN may not be able to represent small land cover patch inside the mixed pixel. For example, the soft classification value of a mixed pixel in a 3×3 block of pixels

(a)   (b)   (c)
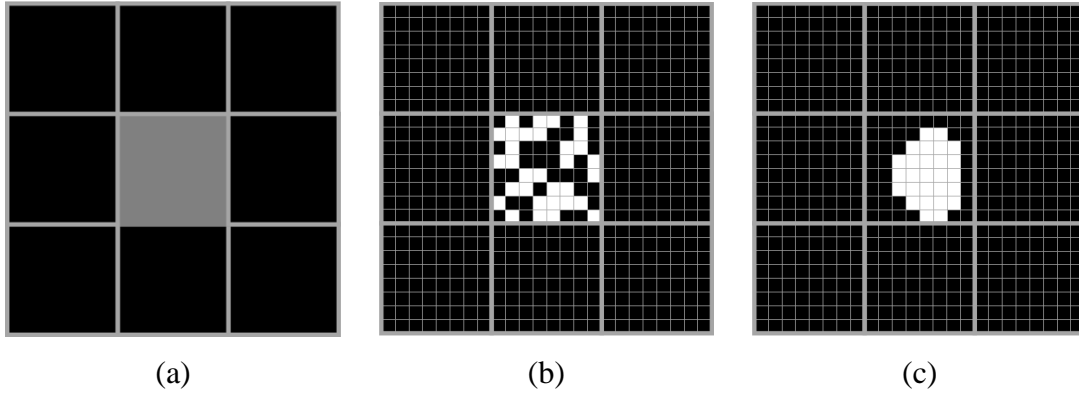
Figure 4-6 Super-resolution mapping of land cover using the standard HNN. (a) A coarse spatial resolution with 8 black pure pixels and 1 mixed pixel. The value of soft classification in the mixed pixel is 0.5. (b) Decomposition of coarse pixel into 8×8 sub-pixels with initial random allocation of white and black sub-pixels in the mixed pixel. (c) Estimation of land cover represented from HNN showing a land cover that smaller than the size of the mixed pixel.

(a)   (b)   (c)
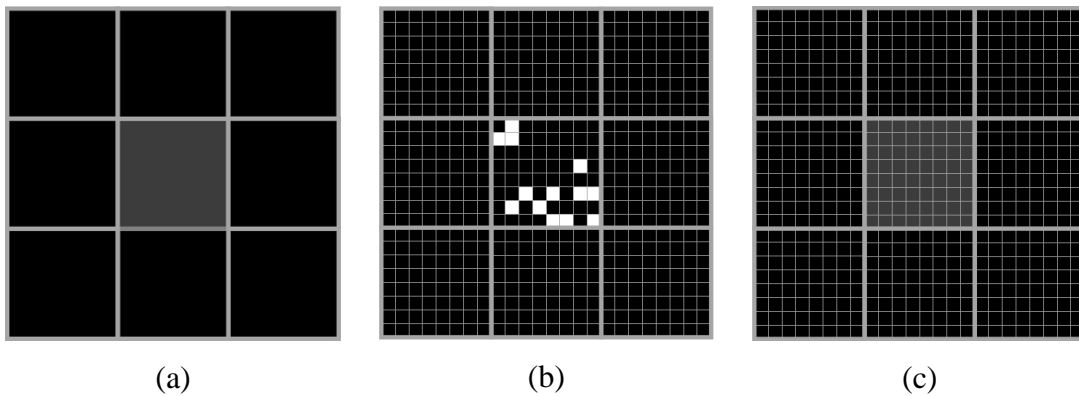
Figure 4-7 Super-resolution mapping of land cover using the standard HNN. (a) A coarse spatial resolution with 8 black pure pixels and 1 mixed pixel. The soft classification value in the mixed pixel is 0.2. (b) Decomposition of coarse pixel into 8×8 sub-pixels with initial random allocation of white and black sub-pixels in the mixed pixel. (c) Estimation of land cover derived from HNN showing that no land cover could be represented.

in a coarse spatial resolution image (Figure 4.7a) was set to 0.20. Figure 4.7b shows an initial random allocation of white and black sub-pixels. Result of the HNN was shown in Figure 4.7c. In the result, the value of each sub-pixel in the mixed pixel was 0.02. Here the HNN was unable to represent a land cover patch, which supposedly constituted from sub-pixels with each of them has a value of 1.0. Instead, all the sub-pixels were given a value of 0.2, which equivalent to the input value. This example suggested that if the value of the soft classification in isolated mixed pixel is low, no discrete land cover patch could be represented. This situation may occur in some landscapes depending on the relationship between the size of the land cover patches and the spatial configuration of the image.

4.5.   Experimental evaluation

The effectiveness of the HNN in representing land cover patches can be analysed using the two previous scenarios: patches that are larger than an image pixel and patches that are smaller than the pixel. As the value of the soft classification determines the size of the land cover patches that can be represented, the value of the soft classification in the mixed pixel was varied.

For the larger land cover patches, 20 coarse spatial resolution images were generated similar to Figure 4.4a and 4.5a. The value of the soft classification in the mixed pixel of the images was varied starting from value 0.05 until 1.00 with an increment of 0.05 on each image. For the small land cover patches, 20 coarse spatial resolution images were also generated similar to Figure 4.6a and 4.7a with the value of

the soft classification in an isolated mixed pixel of the images was varied starting from value 0.05 until 1.00. If the value of the soft classification is 1.00, the size of a patch is equal to the size of a pixel.

Each coarse spatial resolution image was used as input for HNN and was treated independently. In each image, the HNN may or may not be able to represent land cover patches at a sub-pixel scale, as these possible scenarios were already shown in the example in Figure 4.7. When the HNN managed to represent a land cover patch, the area of the represented land cover patch in each image was measured. To determine the accuracy of the HNN in retaining the proportion of land covers in mixed pixels, a ratio between output and input of the HNN was calculated. The input of the HNN was soft classification value in a mixed pixel, and the output of the HNN was the area of land cover patch represented in a mixed pixel. The ratio represented the input and output response of the HNN and used to describe the relationship between the area of the land cover patch derived from a super resolution mapping technique and the value of the soft classification in a mixed pixel. For a coarse spatial resolution image pixel with the value of the soft classification i, the ratio ψ is given by

$$\psi_i = \frac{\text{output of HNN}}{\text{input to HNN}} \tag{4.1}$$

If the value of the ratio is 0.0, it means that no land cover could be represented by the HNN. If the value of the ratio is 1.0, it indicates an exact estimation, in which the area of the represented land cover patch is equal to the actual area proportion of the land

cover in the mixed pixel. If the value of the ratio is less than 1, the area of the land cover patch is under estimated and if the ratio is larger than 1, the land cover patch is over estimated. The average of the ratios derived from all the images in the analysis was calculated to show the overall estimation of the HNN for super-resolution mapping in representing land cover patches.

4.6. Representation of large land cover patches with HNN

This section demonstrates analyses on the HNN in producing parts of large land cover patches. Results of differentiating the weights for the goal functions and the area proportion constraint, as well as the number iteration used were discussed.

4.6.1. Weight settings

Three sets of HNNs were formulated; each using different goal function weights and area proportion constrain weight as given in Equation 3.19. The first set of the HNN assumed that the strength of the goal functions and the area proportion constraints were equal. The setting of the weights what was suggested by Tatem et al., 2001a and other researchers (Nguyen et al., 2005; Ling et al., 2010). Thus, the weights for the goal functions, k_1 and k_2, and the weight for the area proportion constraint, k_P were all set to 1.0. For simplification, a notation HNN(E) was used to indicate that the HNN placed equal emphasis between the goal functions and the area proportion constraints.

To examine the different emphasis between the goal functions and the area proportion constraint, the weights for the functions and the constraint were varied. The second HNN placed more emphasis on the goal functions than the area proportion constraint. Here, the strength of the area proportion constraint was reduced to 10% of the strength of the goal functions. Thus, the weights for the goal functions, k_1 and k_2 were set to 1.0, while the weight for the area proportion constraint, k_P was set to 0.1. The notation used for this HNN was HNN(G) to indicate the emphasis on the goal functions.

Finally, the third HNN placed more emphasis on the area proportion constraint than the goal functions. The strength of the goal functions was reduced to 10% of the strength of the area proportion constraint. Thus, the weight of the area proportion constraint, k_P was set to 1.0, while the weights of the goal functions, k_1 and k_2 were set to 0.1. The notation used for this HNN was HNN(A) to indicate the emphasis on the area proportion constraint.

For the cases of the HNN(G) and the HNN(A), the values for these weights were selected as an initial attempt to examine the effects of the different emphasis between the goal functions and the area proportion constraint. The same weight values were also used in Tatem et al. (2001a) to emphasis these two cases. Later in this section, a series of different weight values for the goal functions and the area proportion constraints will be analyzed.

The number of iteration for the three HNNs was set to 10,000 to ensure that the energy of the HNN could reach an equilibrium state and the output neurons of the HNN

could produce discrete value of either 1 or 0. These discrete values were used to differentiate between land cover patches, which normally appear as white foreground (1), and the background of the image, that normally appear as black surface (0). If the iteration is low, the HNN may not reach an equilibrium state, and the output neurons could not produce discrete value of either 1 or 0. As a consequence, land cover patches may not be able to be represented. If the iteration is high, no improvement on the HNN output could be enhanced further, thus, may potentially waste the computational resources. Later in this chapter, the number of iterations that can optimize the output of the HNN will be analyzed.

Results of the three HNNs in representing large land cover patches are shown in Figure 4.8. The graph shows a relationship between input and output of the HNNs. The input of the HNN was the soft classification value inside a mixed pixel and the output of the HNN was the representation of land cover patches. The area of the represented patches was measured and used to describe the relationship of the input and output of the HNN. As a benchmark, a line illustrating an ideal relationship between input and output of the HNN is also shown in a dashed line.

For the HNN(E), the average ratio for the relationship of the output and input was 0.8265, indicating slight underestimation of patch size. The SSE for this relationship was 0.0487. The HNN(E) could recover part of the area of a land cover patch when the minimum soft classification value in a mixed pixel was 0.20.

For the HNN(G), the results tended to show a slight overestimation of patch size with its average ratio for the relationship of the output and input was 1.0066. This result
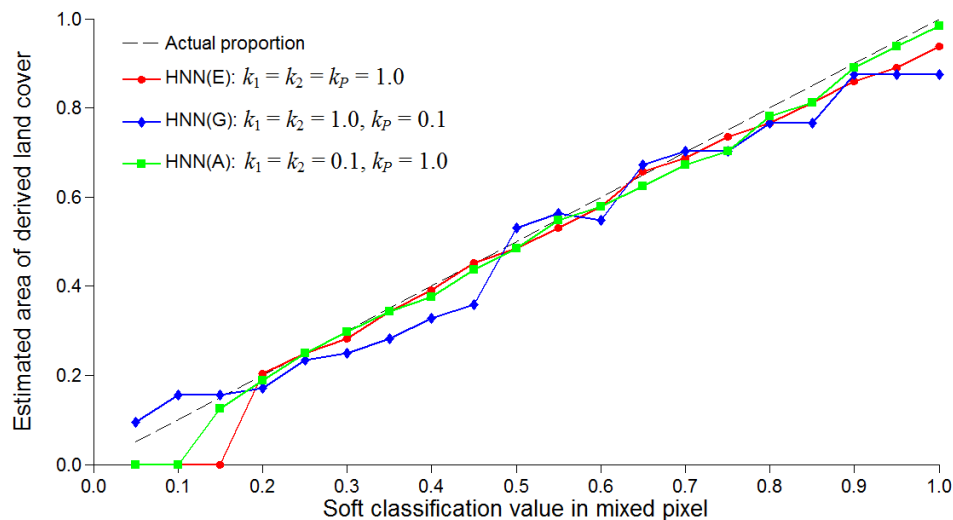
Figure 4-8 Relationship of the input and output of HNN in representing large land cover patches using HNN(E), HNN(G), and HNN(A). The number of iteration for each HNN was 10,000.

was due to the effect of the high emphasizing on the goal functions that leads to the expansion of represented land covers area larger than the actual area of the land covers (Tatem et al., 2001a). The SSE for this relationship was 0.0636, larger than the HNN(E), suggesting that the precision of the HNN(G) was low. However, the HNN(G) could recover part of the land cover patch area when the minimum value of soft classification in a mixed pixel was 0.05.

For the HNN(A), its average ratio for the relationship of the output and input was 0.8666, suggesting slight underestimation of patch size. The SSE for this relationship was 0.0207, more accurate than the results of the HNN(E). The minimum soft classification value in a mixed pixel required to recover part of the land cover patch was 0.15, slightly less accurate than the HNN(G) but more accurate than the HNN(E) in

representing part of land cover patches from mixed pixel with low soft classification values.

All the three graphs of the HNN(E), HNN(G), and HNN(A) are highly correlated with each other. This trend suggested that the effect of differentiating the emphasis between the goal functions and the area proportion constraint may not be a significant factor that could affect the representation of parts of the large patch boundaries, although slight variations may occur in the results in terms of different level of underestimation and overestimation of the size of land cover patches.

4.6.2. Number of iterations

Different number of iterations was set to each of the three HNNs. In each of the HNN, 20 coarse spatial resolution images were generated similar to Figure 4.4a and 4.5a. The value of the soft classification in the mixed pixel of the images was varied starting from value 0.05 until 1.00 with an increment of 0.05 on each image. Each of the HNN was calculated numerically for 1000, 2000, 5000, 10,000, and 15,000 iterations. Figure 4.9 to Figure 4.11 show results of the relationship between output and input of the three HNNs to represent part of large land cover patches for a series of iteration. The average of the ratio ψ for each HNN was summarized respectively in Table 4.1 until Table 4.3. The SSE was also included to provide a statistical measure of difference between output and input of the HNNs.
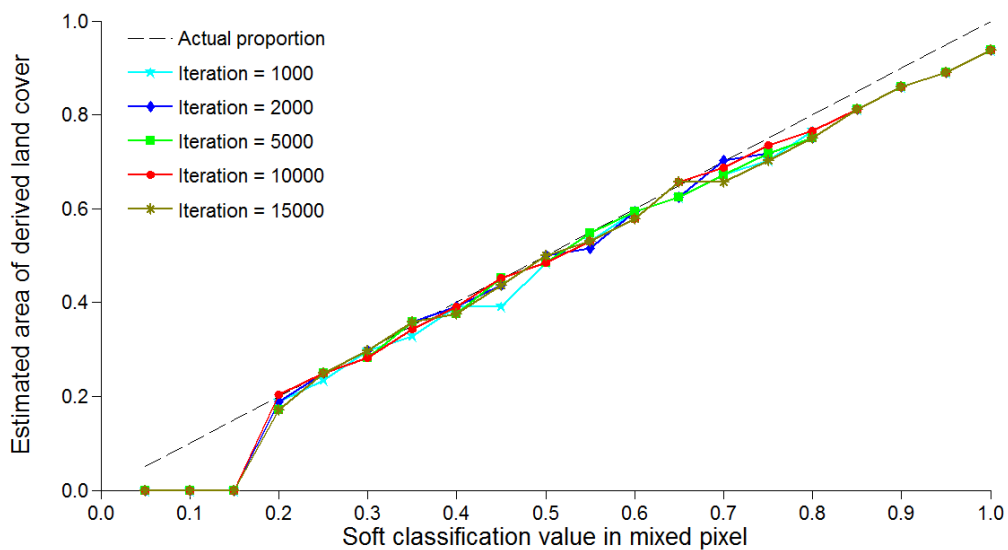
Figure 4-9 Relationship of output and input of the HNN(E) using different numbers of iteration on a large land cover patch.

Table 4-1 Average ratio of the output and input of the HNN(E) as a function of iteration on the representation of a large land cover patch from 20 coarse spatial resolution images.

Iterations	Average ψ	SSE
1000	0.8086	0.0554
2000	0.8239	0.0513
5000	0.8162	0.0525
10,000	0.8265	0.0487
15,000	0.8162	0.0546
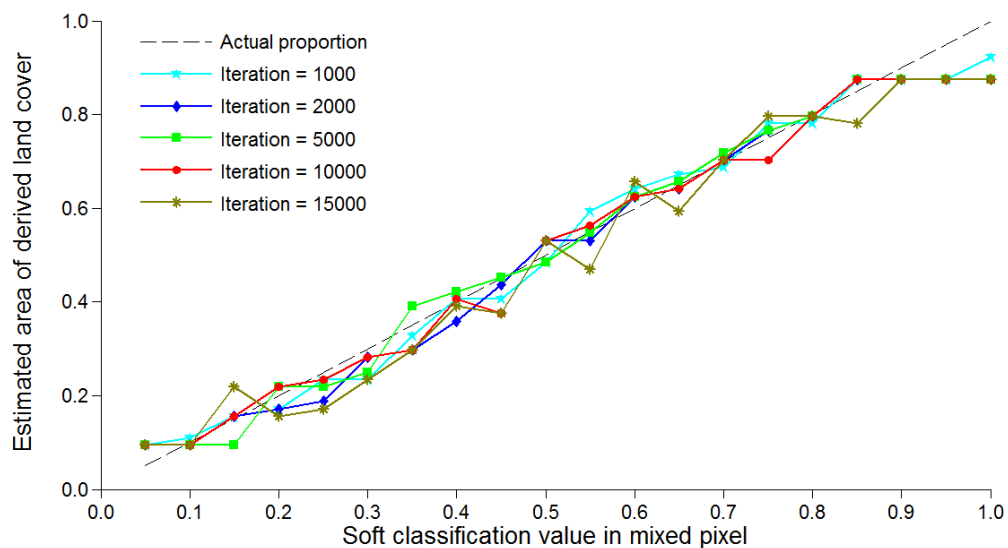
Figure 4-10 Relationship of output and input of the HNN(G) using different numbers of iteration on a large land cover patch.

Table 4-2 Average ratio of the output and input of the HNN(G) as a function of iteration on the representation of a large land cover patch from 20 coarse spatial resolution images.

Iterations	Average ψ	SSE
1000	1.0221	0.0286
2000	0.9999	0.0365
5000	1.0138	0.0351
10,000	1.0185	0.0380
15,000	0.9927	0.0703
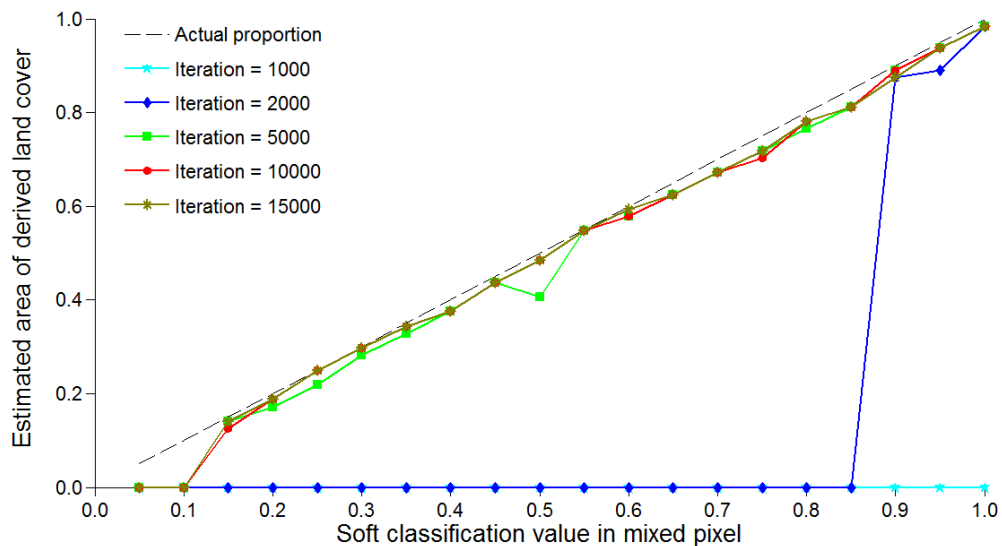
Figure 4-11 Relationship of output and input of the HNN(A) using different numbers of iteration on a large land cover patch.

Table 4-3 Average ratio of the output and input of the HNN(A) as a function of iteration on the representation of a large land cover patch from 20 coarse spatial resolution images.

Iterations	Average ψ	SSE
1000	0.000	7.1750
2000	0.1447	4.4669
5000	0.8490	0.0307
10,000	0.8666	0.0207
15,000	0.8733	0.0190

Results of the HNN(E) (Figure 4.9) underestimated the patch size as presented in Table 4.1. Increasing iteration of the numerical calculation of the HNN only produced slight changes in the results. Therefore, the number of iteration used was not a major factor that could enhance the results of the HNN.

For the HNN(G), the estimation results were mixed. From Table 4.2, at 1000, 5000 and 10,000 iterations, the results overestimated the patch area, while at 2000 and 15,000 iterations; the results underestimated the patch area. Although the graph in Figure 4.10 appeared to be unstable compare to the graph of the other two HNNs, results of the HNN(G) were more accurate. The HNN(G) was able to map the land cover even when the minimum value for the soft classification was 0.05. This value was smaller than that of the HNN(E) (0.20). Like the HNN(E), the number of iteration did not produce significant effects in the results of the HNN(G).

For the HNN(A), the number of iteration used can significantly determine the representation of land cover patches, as shown in Figure 4.11. With the low number of iterations, the HNN(E) was unable to represent land cover. At the 1000 iteration, no land cover could be represented. At the 2000 iterations, land cover could only be represented when the soft classification value inside the mixed pixel was at least 0.90. As the number of iteration increased, the effectiveness of the HNN(E) to represent land cover was also increased. Although, results at 5000, 10,000 and 15,000 iterations underestimated the patch area (Table 4.3), the errors produced were decreasing. Therefore, as the result suggested, the HNN(E) required high number of iteration in order to represent land cover patches.

For the representation of large land cover patches, the number of iteration used did not significantly improve the results of the HNN when the strength of the goal functions and the area proportion constraint were set equal such as HNN(E), or when the weight of the goal functions is stronger than the weight of the area proportion constraint such as HNN(G). The graphs that show the relationship of the output and input for both of the HNNs were highly correlated at different number of iterations. This trend suggested that a low number of iterations, such as 1000 iterations, land cover patches can sufficiently represented with the HNN(E) and HNN(G).

However, when the weight of the area proportion constraint is stronger than the weight of the goal functions, such as HNN(A), the representation of land cover patches could not be achieved at the 1000 iterations. Only when the iteration reached 2000, land cover patches could be represented. Increasing the number of iteration further could increase the accuracy of the HNN(A) to represent land cover patches.

4.7.   Representation of small land cover patches with HNN

This section demonstrates analyses on HNN in representing land cover patches smaller than an image pixel. Results of differentiating the weights for the goal functions and the area proportion constraint, as well as the number iteration used were discussed.

4.7.1. Weight settings

Similar to the example in Section 4.6, three sets of HNNs were formulated with the weights used in the three HNNs were set identical to the weights in that example. The number of iteration for the three HNNs was also set to 10,000. Results of the HNN in representing small land cover patches are shown in Figure 4.12. Although the value of the weights used in the three HNNs were identical to the setting used in the previous example, the results of the HNN on the small land cover patches produced different patterns. One noticeable difference was that all the HNNs underestimated the patch size.

For the HNN(E), the average ratio of the output and input of the HNN(E) was 0.5389. The HNN(E) required that the soft classification value inside the mixed pixel was at least 0.45 in order to represent land cover patches. Similar trend can be seen in the results produced by the HNN(G), but its estimation is lower than the estimation in the HNN(E). The average ratio of the output and input of the HNN(G) was 0.3207. The HNN(G) required that the land cover proportion inside the mixed pixel was at least 0.55 in order to represent land cover patches. For the HNN(A), its average ratio for the relationship of the output and input was 0.8489, suggesting more accurate estimation than from the other two HNNs. The HNN(E) can also map land cover even the proportion of the land cover inside the mixed pixel was as low as 0.15.

Results of differentiating the emphasis between the goal functions and the area proportion constraint for the HNN demonstrated different trends for the cases of large land cover patches representation (Figure 4.8) and small land cover patches
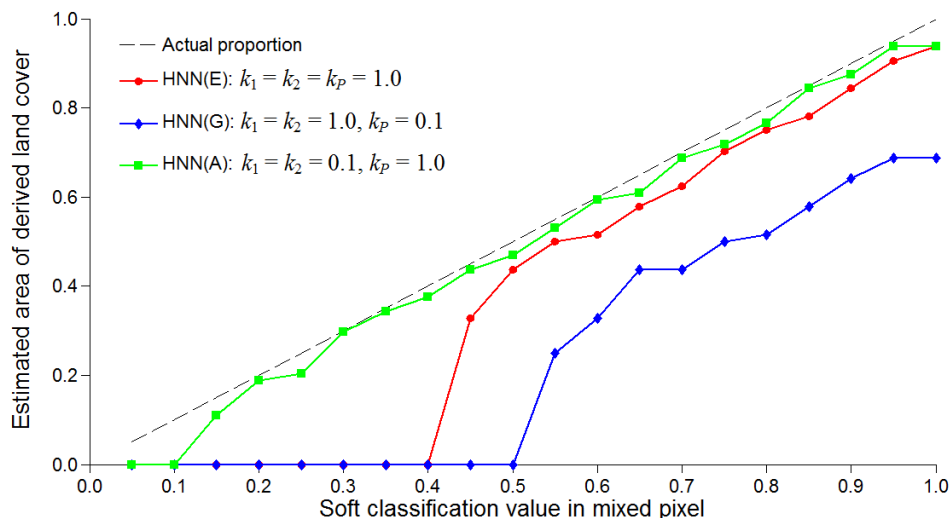
Figure 4-12 Relationship of the response of input and output of HNN in representing small land cover patches using HNN(E), HNN(G), and HNN(A). The number of iteration for each HNN was 10,000.

representation (Figure 4.12). For the large cover patches representation case, differentiating the strength of the goal functions and the area proportion constraint did not produce significant different in the results of the HNN(E), HNN(G), and HNN(A) at 10,000 iterations.

In contrast, differentiating the strength of the goal functions and the area proportion constraint of the HNN at 10,000 iterations demonstrated significant difference between HNN(E), HNN(G), and HNN(A) for the representation of small land cover patches. The trend of the graphs in Figure 4.12 suggested that emphasizing more strength on the area proportion constraint than the goal functions was more preferable for a HNN in representing small land cover patches.

4.7.2. Number of iterations

Different number of iterations was set to each of the three HNNs. In each of the HNN, 20 coarse spatial resolution images were generated similar to Figure 4.6a and 4.7a. The value of the soft classification in the mixed pixel of the images was varied starting from value 0.05 until 1.00 with an increment of 0.05 on each image. Each of the HNN was calculated numerically for 1000, 2000, 5000, 10,000, and 15,000 iterations. Figure 4.13 to Figure 4.15 show results of the relationship between output and input of the three HNNs to represent part of large land cover patches for a series of iteration. The average of the ratio ψ for each HNN was summarized respectively in Table 4.4 until Table 4.6. The SSE was also included to provide a statistical measure of difference between output and input of the HNNs.

For the HNN(E) (Figure 4.13), the results underestimated the patch size. The minimum soft classification value inside the mixed pixel that could be used to represent a small land cover patch was 0.40. Increasing the number of iteration only produced slight changes in the results. Therefore, the number of iteration used was not a major factor that could enhance the results of the HNN(E).

For the HNN(G) (Figure 4.14), the estimation results were even lower than the results produced from the HNN(E). The minimum soft classification value inside the mixed pixel that could be used to represent a small land cover patch was 0.45; that was achieved after 15,000 iterations. Similar to the HNN(E) scenario, increasing number of the iterations in the HNN(G) calculation only contributed to less significant effect in term of the representing small land cover patches.
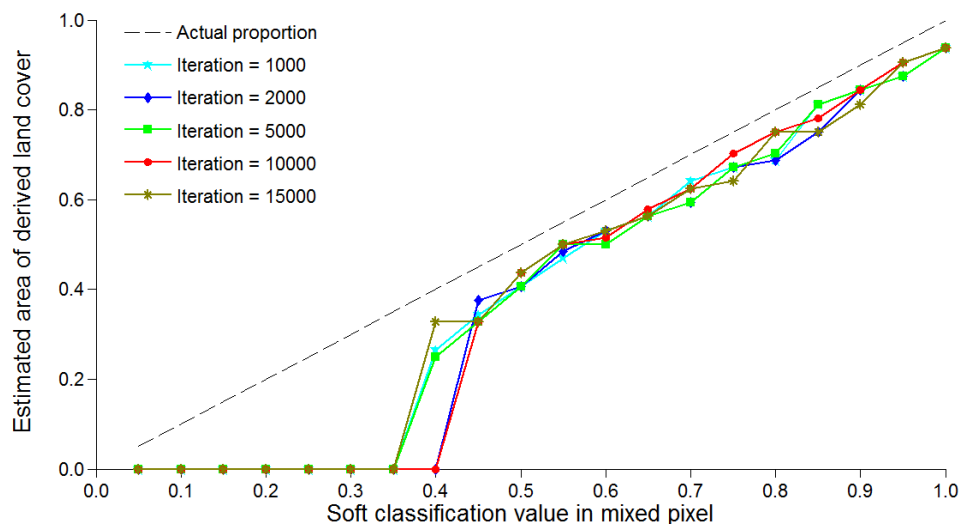
Figure 4-13 Relationship of output and input of the HNN(E) using different numbers of iteration on a small land cover patch.

Table 4-4 Average ratio of the output and input of the HNN(E) as a function of iteration on the representation of a small land cover patch from 20 coarse spatial resolution images.

Iterations	Average ψ	SSE
1000	0.5633	0.4435
2000	0.5280	0.5938
5000	0.5575	0.4572
10,000	0.5389	0.5676
15,000	0.5723	0.4324
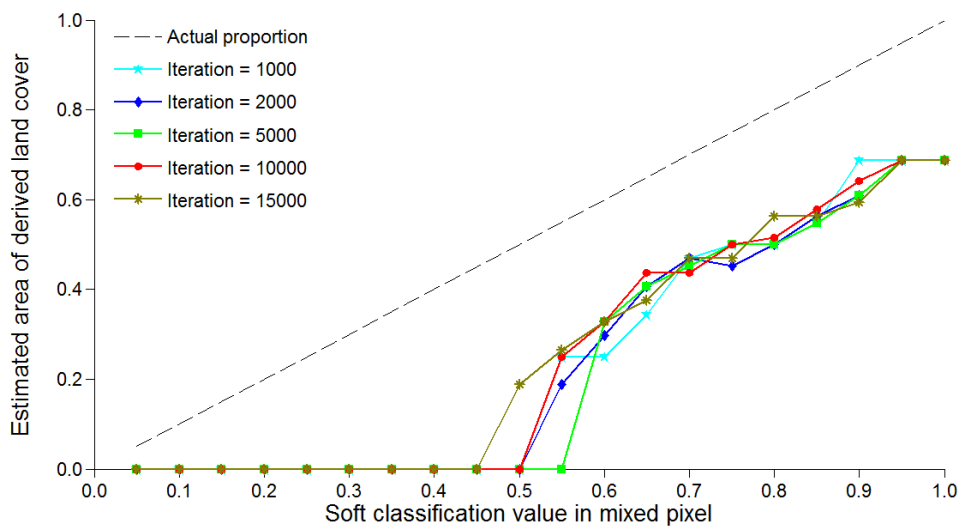
Figure 4-14 Relationship of output and input of the HNN(G) using different numbers of iteration on a small land cover patch.

Table 4-5 Average ratio of the output and input of the HNN(G) as a function of iteration on the representation of a small land cover patch from 20 coarse spatial resolution images.

Iterations	Average ψ	SSE
1000	0.3090	1.7783
2000	0.3055	1.8104
5000	0.2921	1.9547
10,000	0.3207	1.6917
15,000	0.3356	1.5725
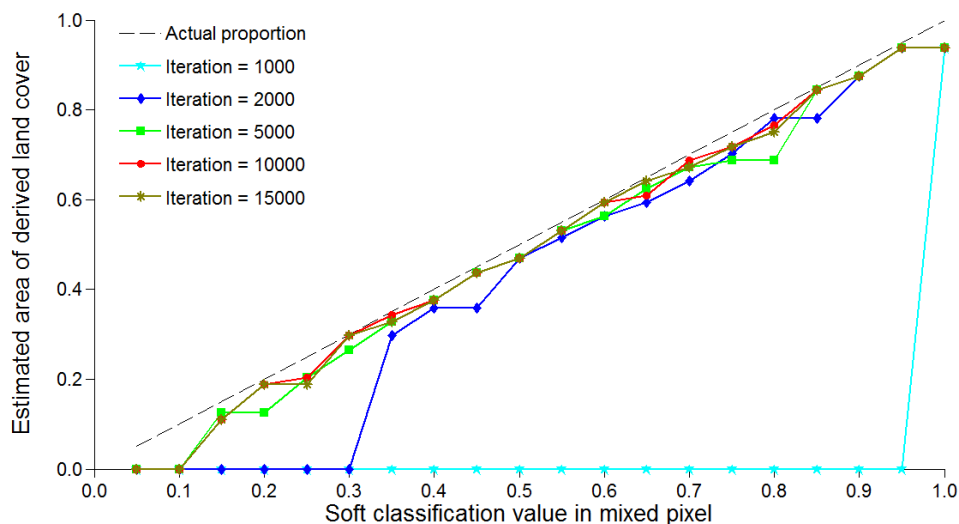
Figure 4-15 Relationship of output and input of the HNN(A) using different numbers of iteration on a small land cover patch.

Table 4-6 Average ratio of the output and input of the HNN(A) as a function of iteration on the representation of a small land cover patch from 20 coarse spatial resolution images.

Iterations	Average ψ	SSE
1000	0.0469	6.1789
2000	0.6458	0.2624
5000	0.8216	0.0488
10,000	0.8489	0.0274
15,000	0.8439	0.0299

Significant effect of the increasing number iteration was demonstrated in the results of the HNN(A) in Figure 4.15. At the 1000 iteration, a small land cover patch could only be produced if the soft classification value inside the mixed pixel was at least 1.00, in which indicate that the size of the patch was identical to an image pixel. Consequently, no land cover patch smaller than a pixel could be represented. As the number of iterations increased, small land cover patches could be represented with the decreasing values of soft classification inside the mixed pixels. The minimum soft classification value that could be used to represent a patch was as low as 0.15.

For small land cover patch applications, results produced by the HNN(A) were similar to the representation of the large land cover applications. Both applications required high number of iteration in the calculation of the HNN(A) in order to represent land cover patch although the soft classification value inside the mixed pixel was low. In contrast, increasing the number of iteration did not produce significant improvement on the results of the HNN(E) and the HNN(G).

For the representation of small land cover patches, the number of iteration used did not significantly improve the results of the HNN when the strength of the goal functions and the area proportion constraint were set equal, such as HNN(E), or when the weight of the goal functions is stronger than the weight of the area proportion constraint, such as HNN(G). The graphs that show the relationship of the output and input for both of the HNNs were highly correlated at different number of iterations. The effect of increasing the number of iterations for small land cover representation case demonstrated similar trends with the large land cover patches representation case in Section 4.6.2. For both cases, increasing the number of iterations did not improve the

result significantly. The difference between the results of both cases was that the representation of small land cover patches was severely underestimated compared to the representation of large land cover patches. This trend suggested that placing more equal emphasis between the goal functions and the area proportion constrain, or placing more emphasis on the goal functions than the area proportion constraint of a HNN would not be able to represent small land cover patches even with the increment of the number of iterations.

However, when the weight of the area proportion constraint is stronger than the weight of the goal functions, such as HNN(A), similar trend was demonstrated between the representation of small land cover patches and large land cover patches as explained in Section 4.6.2. With the HNN(A), small and large land cover patches could be represented better with the increment of the number of iterations used.

Figure 4.16 demonstrates an example of the HNN(A) in representing a small land cover patch from a mixed pixel. Figure 4.16a shows a 3×3 block of pixels in a coarse spatial resolution image with one mixed pixel at the centre of the image. The other 8 pixels are pure black pixels. The soft classification value of the mixed pixel was 0.20. The weights for the goal functions of the HNN(A) were $k_1 = k_2 = 0.1$ and for the area proportion constraint was $k_P = 1.0$. Figure 4.16b shows random initialization. Results of the land cover representation at 1000, 2000, 5000, 10,000, and 15,000 iterations are shown in Figure 4.16c-g. At least 5000 iterations was required for the HNN(A) to represent small land cover patch.

(a) (b) (c)

(d) (e) (f)

(g) (h) (i)
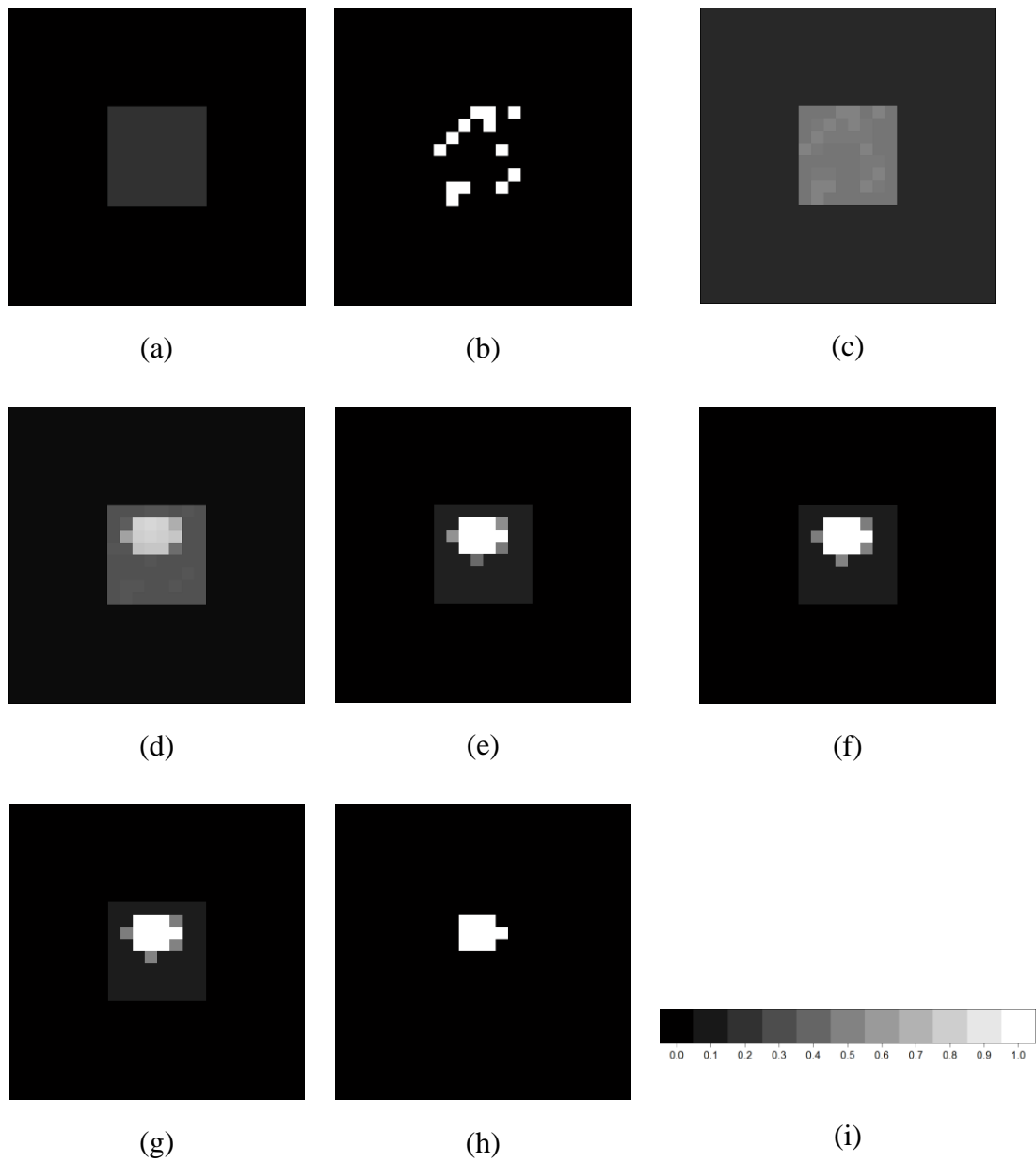
Figure 4-16 The outputs of HNN(A) with the weight settings were $k_1 = k_2 = 0.1$, $k_P = 1.0$. (a) Input from soft classification. The value of soft classification = 0.20. (b) Random initialization. Results after (c) 1000 iterations, (d) 2000 iterations, (e) 5000 iterations, (f) 10,000 iterations, (g) 15,000 iterations, and (h) final mapping. (i) Intensity scale used to represent the soft classification value in a mixed pixel.

4.8. The impact of weight settings on the HNN for the representation of small land cover patches

Two sets of HNNs were configured differently to analyse the effect of weight setting on the goal function and the area proportion constraint of the HNN for the representation of small land cover patches. Twenty coarse spatial resolution images were generated similar to images in Figure 4.6a and 4.7a with the value of the soft classification in an isolated mixed pixel of the images was varied starting from value 0.05 until 1.00. For the first HNN, the value for the goal function weights were set to constant, $k_1 = k_2 = 1.0$, while the weight for the area proportion constraint, k_P were varied from 0.1 to 1.0. For the second HNN, the weight for the area proportion constraint was constant at 1.0, while the weights for the goal function were varied from 0.1 to 1.0. The number of iteration for both of the HNN was set to 10,000.

Figure 4.17 shows relationship of the output and input of the first HNN. Table 4.7 summarized the result of the estimation and the errors. When the weight for the goal functions were set constant, varying the value of the weight for the area proportion constraint did not produce significant variation in the trend of the HNN results. Small land cover patch could only be represented when the land cover proportion inside the mixed pixel was at least 0.44. This derivation was obtained using k_P = 0.6, 0.7, and 0.8. When k_P = 0.1, 0.2, and 0.3, the minimum land cover proportion inside the mixed pixel that could be derived was 0.55. This scenario suggested that for the representation of small land cover patches, the HNN with strongly weighted goal function was slightly more accurate than the HNN with weak emphasis on the goal function.
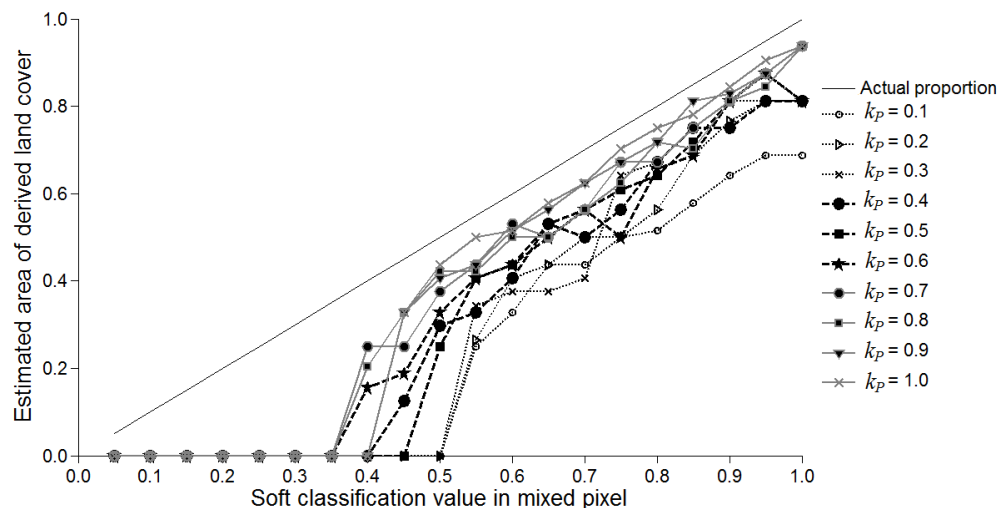
Figure 4-17 Relationship between output and input of the HNN to represent small land cover patches with the weight of the goal function was set constant at 1.0, and the weights for the area proportion constraint varied. The number for the iteration was set to 10,000.

Table 4-7 Average ratio of the output and input of the HNN as a function of varying the weight of the area proportion constrain and setting the weight of the goal functions constant at 1.0.

k_P	Average ψ	SSE
0.1	0.3207	1.6917
0.2	0.3622	1.3835
0.3	0.3777	1.3176
0.4	0.4325	0.9359
0.5	0.4342	0.9659
0.6	0.4718	0.7543
0.7	0.5282	0.5366
0.8	0.5271	0.5442
0.9	0.5242	0.5955
1.0	0.5389	0.5676
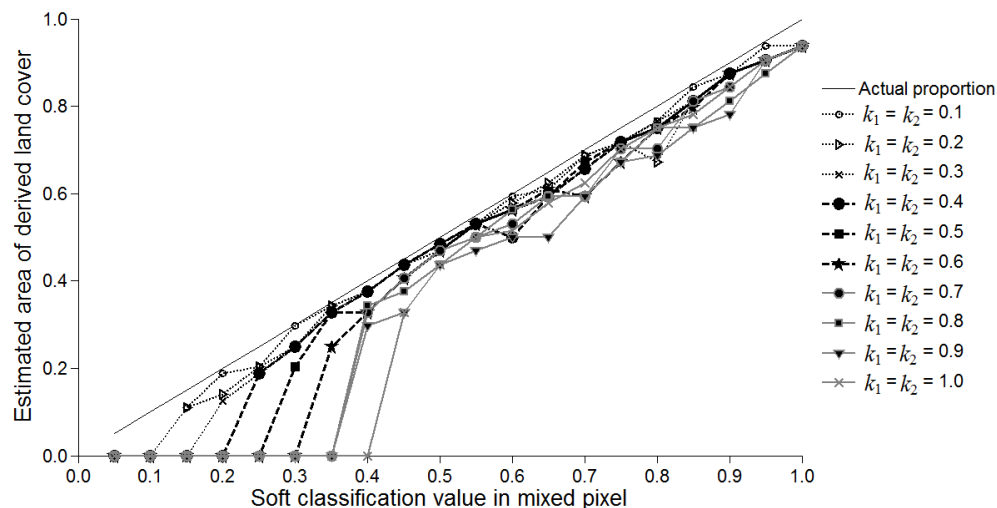
Figure 4-18 Relationship between output and input of the HNN to represent small land cover patches with the weight for the area proportion constraint was set constant at 1.0, and the weights for the goal functions varied. The number for the iteration was set to 10,000.

Table 4-8 Average ratio of the output and input of the HNN as a function of varying the weights of the goal functions and setting the weight of the area proportion constraint constant at 1.0.

k_1, k_2	Average ψ	SSE
0.1	0.8489	0.0274
0.2	0.8215	0.0503
0.3	0.7757	0.0654
0.4	0.7383	0.1096
0.5	0.6884	0.1724
0.6	0.6349	0.2781
0.7	0.5909	0.4017
0.8	0.5827	0.4168
0.9	0.5523	0.4784
1.0	0.5389	0.5676

Figure 4.18 shows relationship of the output and input of the second HNN. Table 4.8 summarized the result of the estimation and the errors. When the weight for the area proportion constraint was set constant, varying the weight of the goal function demonstrated significant variation. As the weights for the goal function decreased, the effect of the area proportion constraint was increased in the HNN calculation, leading to the accuracy increase of the HNN for the representation of small land cover patches. An optimum result was achieved when $k_p = 1.0$ and $k_1 = k_2 = 0.1$. This scenario suggested that for the strongly weighted area proportion constraint HNN, setting low values for the goal function weights would increase the accuracy of the HNN to represent small land cover patches.

The value of the weights chosen for the analyses in this section was limited from 0.1 to 1.0. From the results in this section and section 4.7, setting the value of the weights equally between the spatial clustering goal functions and the area proportion constraint may not necessarily produce equal effect. For example, when the values of the weights for the goal functions and the area proportion constraint were set equally to 1.0, small land cover patches could not be represented, as the result was appeared to be dominated by the effect of the area proportion constraint more than the effect of the goal functions. When the value of the goal functions was set lower than that of the area proportion constraint, such as $k_1 = k_2 = 0.1$ and $k_p = 1.0$, the effect seems to be equal. Different results might possibly be obtained for weights other than the value chosen.

4.9.   Representation of large land cover patches with pixel swapping

For comparative purposes, the representation of land cover patches was performed with pixel swapping technique. Although require less parameter setting than the HNN, the effect of the different number of neighbours used in the Equation 3.33 may deliver different results (Atkinson, 2005). In this section, pixel swapping was used to represent large land cover patches. The number of the neighbours was varied between 1 and 5, leading to a formation of five sets of pixel swapping. In each set, 20 coarse spatial resolution images were generated similar to Figure 4.4a and 4.5a. The value of the soft classification in the mixed pixel of the images was varied starting from value 0.05 until 1.00 with an increment of 0.05 on each image. Each coarse spatial resolution image was used as input for pixel swapping. The number of iteration for each set of pixel swapping was set to 100 as it is sufficient to achieve a stable state. The area of the represented land cover patch in each image was measured. Similar to the analysis on the HNN, a ratio ψ depicting a relationship between output and input of the pixel swapping was calculated using Equation 4.1.

Figure 4.19 shows a relationship between input and output of the pixel swapping in representing large land cover patches. As a benchmark, a line illustrating an ideal relationship between input and output of the pixel swapping is also shown in a dashed line. Only the plot of the pixel swapping with neighbour 1 is shown because pixel swapping with neighbour 2-5 produced estimation as exactly as the pixel swapping with the neighbour 1, which is confirmed in the results of the estimations and errors in Table 4.9.
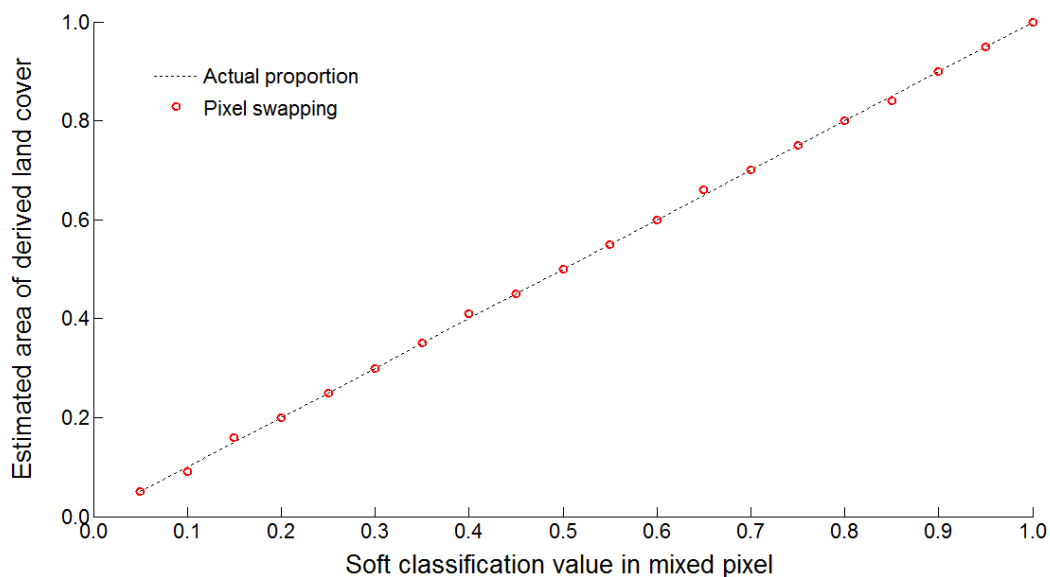
Figure 4-19 Relationship of the response of input and output of pixel swapping in representing large land cover patches.

Table 4-9 Average ratio of the output and input of the pixel swapping as a function of different number of the neighbours on the representation of a large land cover patch from 20 coarse spatial resolution images.

Neighbour	Average ψ	SSE
1	0.9963	0.0004
2	0.9963	0.0004
3	0.9963	0.0004
4	0.9963	0.0004
5	0.9963	0.0004

Overall, the average estimation of the pixel swapping was 0.9963, indicating a slight underestimation of patch size. These results suggested that the pixel swapping was more accurate than the HNN in representation large land covers. For the simple images (as in Figure 4.4a and Figure 4.5a), varying the number of neighbours of the pixel swapping did not produced any effect.

4.10. Representation of small land cover patches with pixel swapping

Analyses in Section 4.9 were repeated for the representation of small land cover patches with pixel swapping. Twenty coarse spatial resolution images were generated similar to Figure 4.6a and 4.7a.

Figure 4.20 shows a relationship between input and output of the pixel swapping in representing small land cover patches from isolated mixed pixels. As a benchmark, a line illustrating an ideal relationship between input and output of the pixel swapping is also shown in a dashed line. Only the plot of the pixel swapping with neighbour 1 is shown because pixel swapping with neighbour 2-5 produced estimation as exactly as the pixel swapping with the neighbour 1, which is confirmed in the results of the estimations and errors in Table 4.10.

Results of the representation of small land cover patches in this section were similar with the results of the representation of large land cover patches in Section 4.9. For the both cases: large and small land cover patches, the accuracy of the pixel
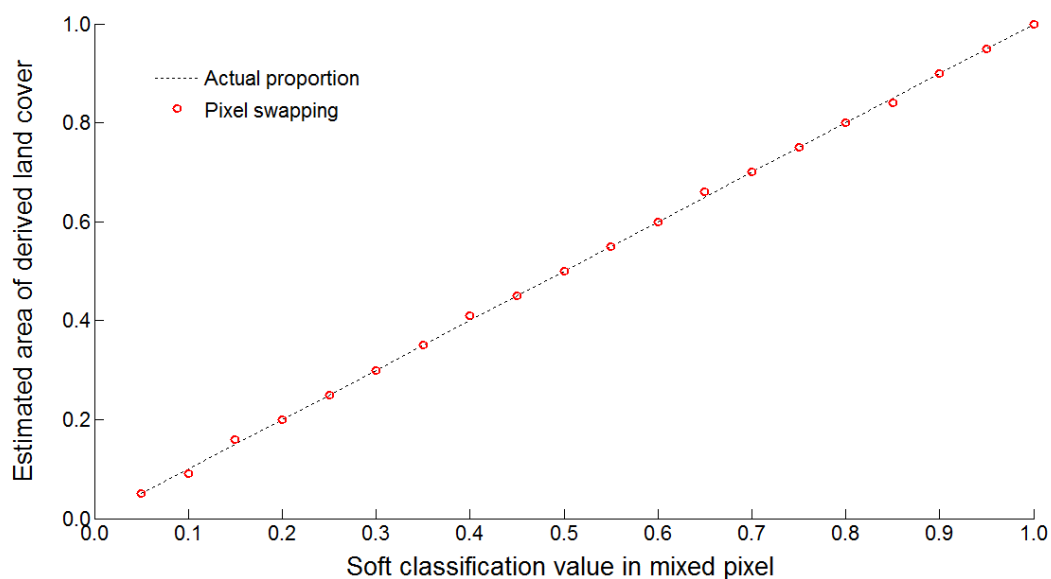
Figure 4-20 Relationship of the response of input and output of pixel swapping in representing small land cover patches.

Table 4-10 Average ratio of the output and input of the pixel swapping as a function of different number of the neighbours on the representation of a small land cover patch from 20 coarse spatial resolution images.

Neighbour	Average ψ	SSE
1	0.9963	0.0004
2	0.9963	0.0004
3	0.9963	0.0004
4	0.9963	0.0004
5	0.9963	0.0004

swapping was higher than that of the HNN in retaining the proportion of the area of a land cover inside a mixed pixel.

These results also suggested that the pixel swapping was better than HNN in representation land covers smaller than the size of coarse spatial resolution pixel. Using the HNN(A), the minimum soft classification value that could be used to represent a land cover patch was 0.15 (Figure 4.15), whereas using the pixel swapping, the minimum soft classification value was only 0.05. Therefore, smaller size of land cover patches could be represented using pixel swapping than by using the HNN(A).

4.11. Representation of different mixed pixel scenarios

Further evaluation of the HNN and pixel swapping in representing land cover patches was performed using images that represent the mixed pixel problem as highlighted by Fisher (1997). Three problems were evaluated: (1) boundaries of the patches at a sub-pixel scale (Figure 4.21); (2) linear patch at a sub-pixel scale (Figure 4.22); and (3) small patches at a sub-pixel scale (Figure 4.23).

Images in Figure 4.21a, 4.22a, and 4.23a are fine spatial resolution images with a size of each of them is 80×80 fine resolution pixels. Image in Figure 4.21a contains two patches touching one another. Image in Figure 4.22a contains a diagonal patch. Image in Figure 4.23a contains a cluster of small patches. All the three images were degraded by spatial aggregation into 10×10 coarse resolution pixels images as shown in Figure 4.21b, 4.22b, and 4.23b.

Two sets of HNN were used. First, HNN(E) with the weights for the goal functions and the area proportion constraint were all set to 1.0. Second, HNN(A) with the weights for the goal functions, k_1 and k_2 were set to 0.1 and the weight for the area proportion constraint, k_P was set to 1.0. The number of neurons in each HNN was set to 80×80, identical to a size of the fine spatial resolution image. Each of the HNN was calculated numerically for 10,000 iterations. HNN(G) was not used because this technique produced the least accuracy estimation than the other two HNNs in representing small land cover patches (Figure 4.12).

Two sets of pixel swapping were also used. First, pixel swapping with the number of neighbour used was 1. For simplification, a notation used for the first pixel swapping was PS(1). Second, pixel swapping with the number of neighbours used was 5 and the notation used was PS(5). Each pixel swapping technique was calculated numerically for 100 iterations.

Results of the land cover patches representation using the HNN(E) are shown in Figure 4.21c, 4.22c, and 4.23c. Results of the land cover patches representation using the HNN(A) are shown in Figure 4.21d, 4.22d, and 4.23d. Results of the land cover patches representation using the PS(1) are shown in Figure 4.21e, 4.22e, and 4.23e. Results of the land cover patches representation using the PS(5) are shown in Figure 4.21f, 4.22f, and 4.23f.
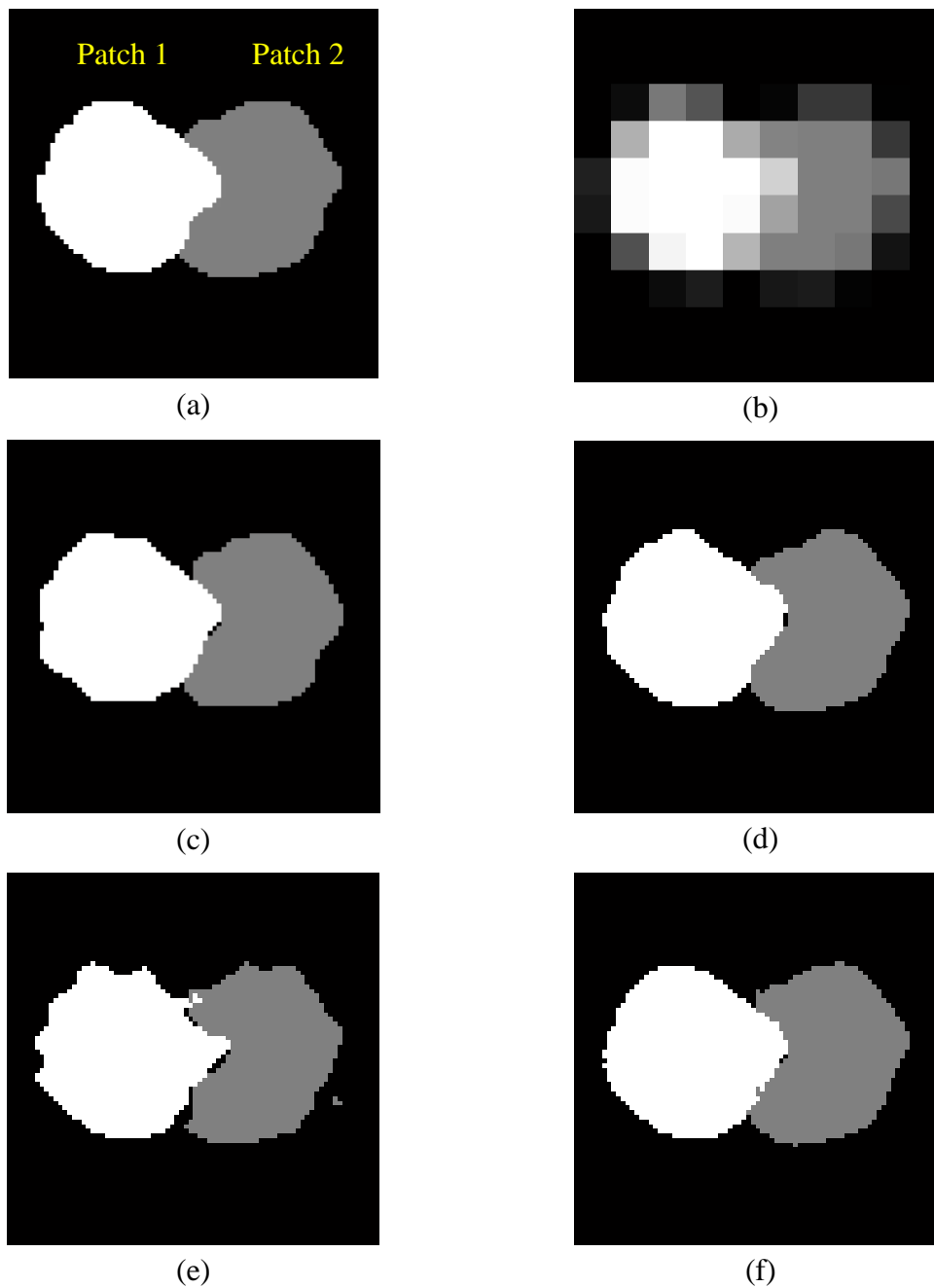
Figure 4-21 Representation of land cover patches concerning on a problem of boundary of the patches at a sub-pixel scale. (a) Original fine spatial resolution image. (b) Degraded image. Super-resolution mapping using (c) HNN(E), (d) HNN(A), (e) PS(1), and (f) PS(5).
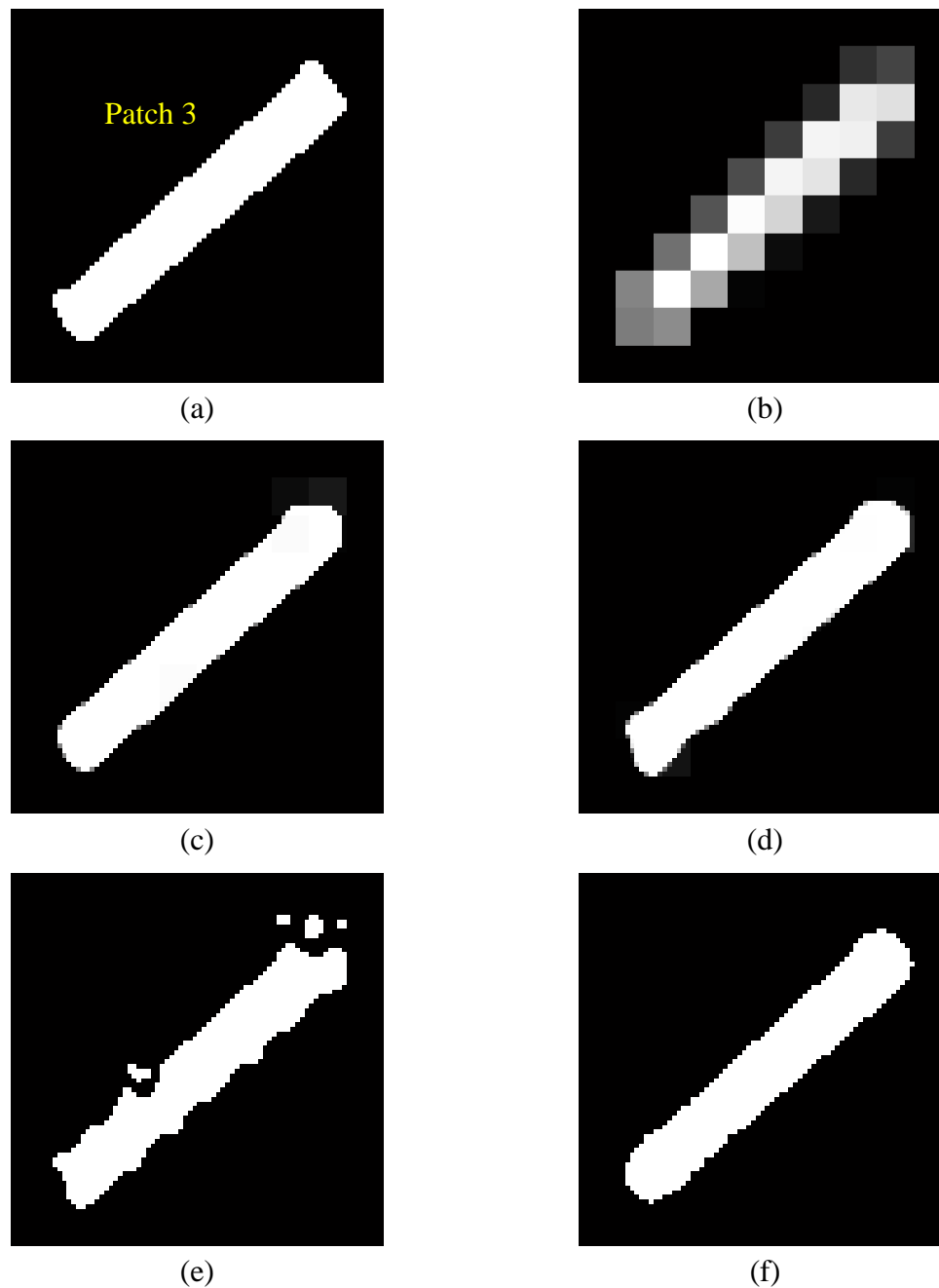
Figure 4-22 Representation of land cover patches concerning on a problem of a linear patch at sub-pixel scale. (a) Original fine spatial resolution image. (b) Degraded image. Super-resolution mapping using (c) HNN(E), (d) HNN(A), (e) PS(1), and (f) PS(5).
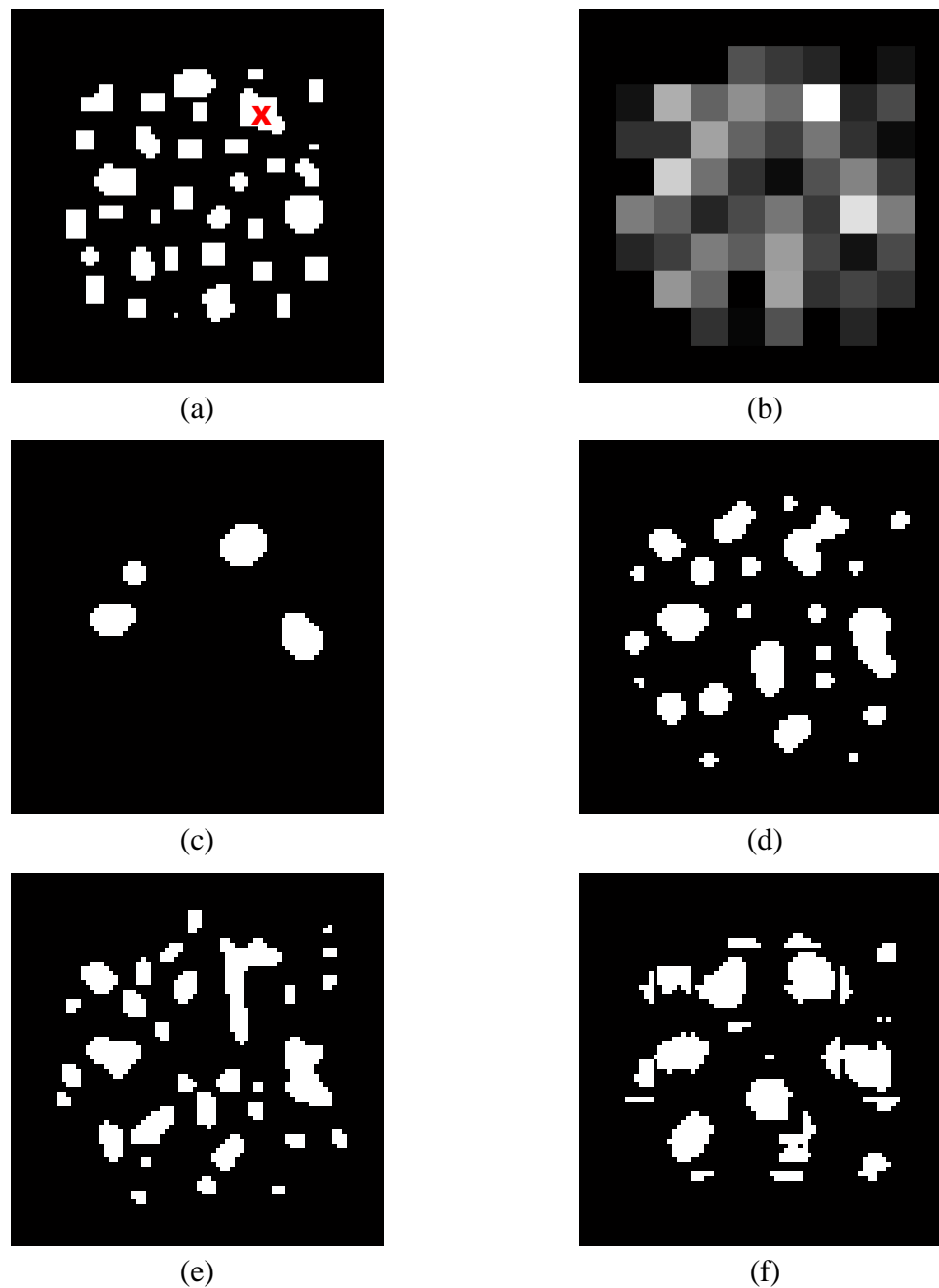
Figure 4-23 Representation of land cover patches concerning on a problem of small patches at a sub-pixel scale. (a) Original fine spatial resolution image. (b) Degraded image. Super-resolution mapping using (c) HNN(E), (d) HNN(A), (e) PS(1), and (f) PS(5).

Table 4-11 Area measurement on patches (unit sub-pixels)

Patch	Ground data	HNN(E)	HNN(A)	PS(1)	PS(5)
1	1049	1042 (-7)	1051 (2)	1047 (-2)	1050 (1)
2	953	930 (-23)	953 (0)	938 (-15)	952 (-1)
3	957	950 (-7)	952 (-5)	914 (-43)	955 (-2)
Total error		37	7	60	4

Table 4-12 Perimeter measurement on patches (unit sub-pixels)

Patch	Ground data	HNN(E)	HNN(A)	PS(1)	PS(5)
1	123.71	120.30 (-3.41)	122.37 (-1.34)	138.85 (15.14)	128.47 (4.76)
2	134.85	124.88 (-9.97)	131.85 (-3.00)	145.12 (10.27)	139.02 (4.17)
3	178.56	174.25 (-4.31)	179.84 (1.28)	191.94 (13.38)	184.42 (5.86)
Total error		17.69	5.62	38.79	14.79

Table 4-13 Positional accuracy of the boundary of the land cover patches (unit sub-pixels)

Patch	HNN(E)	HNN(A)	PS(1)	PS(5)
1	13.43	7.45	15.61	5.19
2	9.92	8.36	14.01	6.83
3	3.78	5.31	14.89	4.84
Total error	27.13	21.12	44.51	16.86

Table 4-14 Number of patches.

Ground data	34
HNN(E)	4
HNN(A)	24
PS(1)	31
PS(5)	22

The shape of the land cover patches was characterized in order to evaluate the results of land cover patch representation from different super-resolution mapping techniques. The measurements of the area and perimeter for patches represented by the super-resolution mapping techniques were presented in Table 4.11 and Table 4.12. As a benchmark, the measurements of the area and perimeter of patches from the original fine spatial resolution image were also provided as ground data. Numbers in the bracket indicate the difference of the area and perimeter measurements between the patches represented by the super-resolution mapping techniques and the patches in the ground data. Positive values indicate overestimation, while negative values indicate underestimation of patch proportion.

For the area measurement, in average, the PS(5) and HNN(A) produced better area estimation compared with the HNN(E) and PS(1). For the perimeter measurement, in average the HNN(A) produced the smallest error while the PS(1) produced the largest error.

The boundary of the land cover patches was vectorised in order to evaluate the positional accuracy of the land cover patches. As a benchmark, the boundary of the

patches from the original fine spatial resolution image was also vectorised. The difference between these boundaries was expressed in RMSE as presented in Table 4.13.

In average, the PS(5) produced the lowest positional error with the RMSE 16.86 sub-pixel, while the PS(1) produced the highest error (44.51 sub-pixels). Comparison between the HNN demonstrated that the HNN(A) produced RMSE 21.12 sub-pixels, which is smaller than that of the HNN(E) (27.13 sub-pixels).

Table 4.14 provides information about the number of patches in images in Figure 4.23. In the original fine spatial resolution image, there are 34 patches of varying size, but only one of them is larger than a coarse spatial resolution image pixel as annotated with symbol 'x'. The rest of the patches are smaller than the coarse pixel. Comparison between the two HNNs demonstrated that the HNN(A) represented 24 patches, which is more than that of the HNN(E) (4 patches). Comparison between the two pixel swapping demonstrated that the PS(1) represented 31 patches, which is more than that of the PS(5) (22 patches).

Apart from the patch representation using the HNN(E) in Figure 4.23c, visual comparison between results of the small land cover patches representation in Figure 4.23d-f demonstrate that the patch representation using the PS(5) is tended to be bigger than the patch representation using HNN(A) and PS(1). The existence of a number of small features may or may not be regarded as land cover patches, because pixel swapping may produce speckled pattern in its results (Thornton et al., 2006). Using the PS(1) and the HNN(A) more small land cover patches could be represented.

The application of the PS(1) on large land cover patches demonstrated poor estimation on the area, perimeter and positional accuracy. This technique produced the highest errors compared with other techniques in the three measures: area, perimeter, and positional accuracy (Table 4.11-12). Contrast trends were demonstrated by the PS(5) when it produced the lowest errors compared with other techniques.

The HNN(A) demonstrated more accurate representation of small and large land cover patches than the HNN(E) when producing lower errors in the estimations of area, perimeter, and positional accuracy. Also, more small land cover patches were presented in the result of the HNN(A) than in the result of the HNN(E). However, when the patches contain high proportion of mixed pixel, such as diagonal shape in Figure 4.22, the RMSE of the positional accuracy for the patch represented by the HNN(A) was higher than that of the patch represented by the HNN(E), as given in Table 4.13. This scenario demonstrated that, for a case of high proportion of mixed pixel, the shape of land cover patches representation using HNN(E) was more compact when compared with the patches represented by the HNN(A), PS(1), and PS(5) which tended to be irregular at the boundary of the patch.

In general, results in this section demonstrated that both the HNN and pixel swapping can be used to represent land cover of different sizes from different mixed pixel scenarios. The representation of land cover patches with the HNN(A) was more accurate than the other techniques in all of the scenarios. For the pixel swapping, the representation of small land cover patches with the PS(1) was more accurate than the PS(5), but the PS(5) was more accurate than the PS(1) in representation of large land cover patches.

4.12. Conclusions

Analyses in this chapter focus on the optimum parameter setting for the HNN and pixel swapping for super-resolution mapping of large and small land cover patches. The attention focused more on the HNN because it requires more complex setting than that of the pixel swapping. Placing more strength on the area proportion constraint than the goal functions of the HNN, and with the high number of iterations on the HNN numerical calculation, different sizes of the land cover patches could be more accurately represented. Analyses in this chapter suggested that with the correct setting of the HNN parameters, the applications of the HNN could be extended and not limited to the size of the land cover especially when the size is smaller than an image pixel.

In this chapter, results of the representation of the small land cover patches suggested a requirement of increasing the number of iterations of the HNN. Further work in this research need to consider of reducing the number of iterations as it would lead to the reducing of processing time, especially for remote sensing imagery, in which the size of the images are normally large.

In summary, pixel swapping was better than HNN in retaining the proportion of land cover from mixed pixels. Large land cover patches could be represented using the HNN(E), HNN(G), and HNN(A). For the pixel swapping, large land cover patches could be represented by the PS(1) and the PS(5), but the boundary of the patches represented by the PS(1) tended to be irregular and not as compact as the boundary of the patches represented by the PS(5). For the small land cover patches, the representation of the HNN(A) was more accurate than that of the HNN(E) and the

HNN(G). More small land cover patches could be represented with the PS(1) than the PS(5). In Chapter 5, issues related with the prediction of spatial location of the small land cover patches will be addressed.

5. Increasing the accuracy of land cover patch location

In Chapter 4, the representation of small land cover patches by super-resolution mapping with the HNN and pixel swapping was demonstrated. Attention focused on the accuracy of patch representation, notably in term of patch area and perimeter. The limitations of these techniques regarding the spatial location of the patches were not addressed. The focus of this chapter is to highlight the limitation of the super-resolution mapping techniques in predicting the spatial location of the land cover patches. An approach that exploits the sub-pixel shifts from multiple observations was used to increase the accuracy of patch location.

5.1. Introduction

As shown in Chapter 4, using the appropriate parameter setting for both the HNN and pixel swapping techniques may ensure the representation of small land cover patches. The effectiveness of these super-resolution mapping techniques in representing small patches may produce highly accurate land cover mapping. However, the accuracy of the land cover mapping is also a function of the positional accuracy of land cover patch prediction. If the small patches can be represented but not allocated accurately, the

accuracy of the non-specific accuracy assessment may increase but not necessarily if assessed on a site specific basis (Congalton and Green, 2009).

A conceptual example that demonstrates the shortcoming of mis-location of the small patches of land cover mapping can be illustrated graphically in this section using synthetic images and not necessarily based on real data. Figure 5.1a shows a 531×522 pixels synthetic image of a reference image with a large patch and 5 small patches. The reference image shows a total of 15556 pixels unit of the patches. Figure 5.1b is a synthetic image that shows an example of a land cover mapping result when only the large path that can be represented. The total area of the patch in Figure 5.1b is 14063 in pixel unit. The total area differs by 1493 pixels unit with the reference image. Figure 5.1c is a synthetic image that shows an example of a land cover mapping result containing a representation of a large patch and 4 small patches. The allocation of the small patches is slightly off position than the location of their corresponding patches in Figure 5.1a. The total area of the patches in Figure 5.1c is 15842 in pixels unit, and differs only by 286 pixels unit. All the images in the Figure 5.1 contained land cover class of the same category, although the land cover patches in Figure 5.1a were shown in red while the land cover patches in Figure 5.1b and 5.1c were shown in green. The difference in the colour scheme was only intended for a comparison purpose between land cover patches in the reference image and the land cover patches in the other images. Figure 5.2 shows spatial correspondence between patches in Figure 5.1b and 5.1c with the reference image in Figure 5.1a.

Table 5.1 and 5.2 provide site specific assessment in a form of confusion matrix for land cover mapping in Figure 5.1b and 5.1c, respectively. Using the site specific assessment, the accuracy of the land cover mapping in Figure 5.1b is 98.20%, which is higher than that of the mapping in Figure 5.1c (96.91%). It is noticeable that the results of the site specific assessment are not parallel with the results of the non-site specific assessment that calculate the number of patches and measure the total area of the patches. Although the accuracy of the non-site specific assessment of land cover mapping in Figure 5.1c is higher than that of the mapping in Figure 5.1b, the mis-location of the small patches in Figure 5.1c could give misleading information about the representation of the land cover mapping if one is only relying on the site specific assessment. Furthermore, the representation of the land cover mapping might get different results if assessed in an object basis.

The commission and omission errors in Table 5.1 and 5.2 also confirmed that the mis-location of the small patches could reduce the site-specific accuracy. In Table 5.1 only the omission error of the patch produces substantial amount of errors with 10.6752% compared with other errors. This omission error of the patch indicates that the small patches are omitted from the representation of land cover mapping in Figure 5.1b. In Table 5.2 the omission and commission errors of the patch produce substantial amount of errors with 9.2063% and 10.832 %, respectively. These errors rise due to the mis-location of the small patches in Figure 5.1c. The representation of the small patches at the wrong locations give rise to the commission error, while the location that the patches missed give rise to the omission error.

(a) (b) (c)
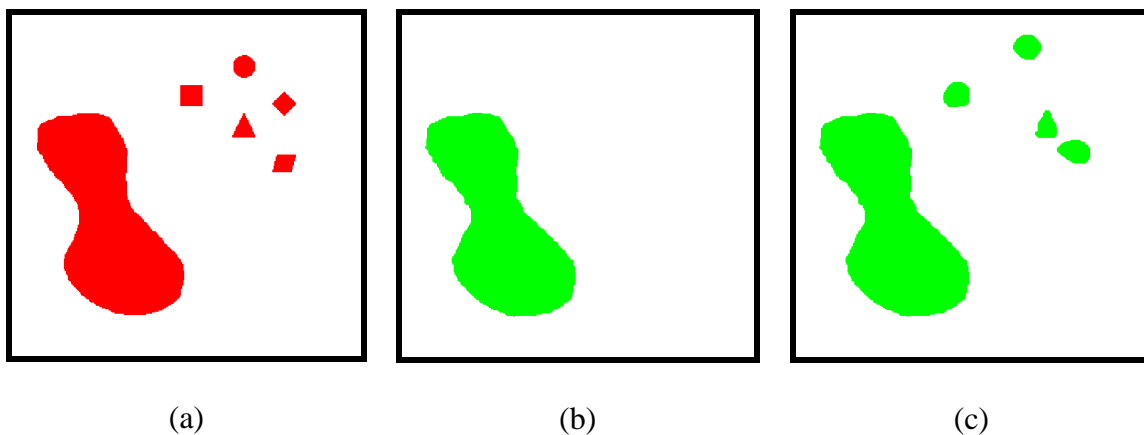
Figure 5-1 Illustration of the effect of mis-location of small patches in land cover mapping. (a) Reference image. (b) Land cover mapping with only a large patch represented. (c) Land cover mapping with a large patch and only four small patches represented. The locations of the small patches are slightly offset from the location in the reference image.

(a) (b)
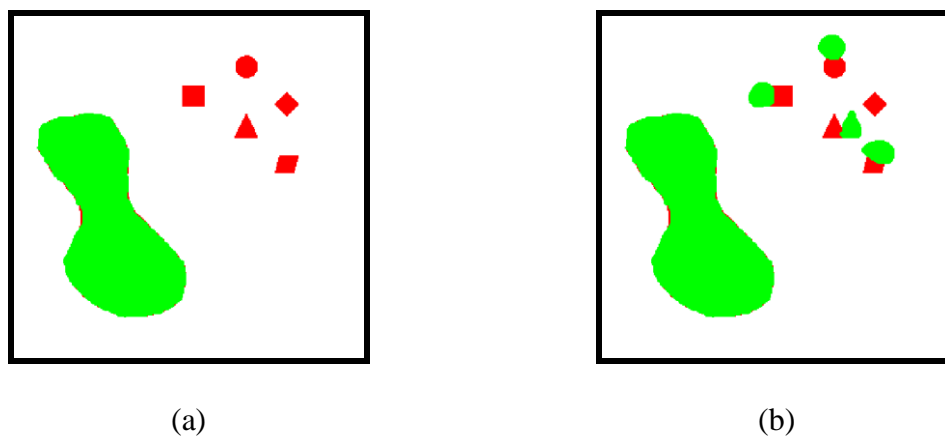
Figure 5-2 Spatial correspondences between patches in (a) Figure 5.1b with the reference image, and (b) Figure 5.1c with the reference image.

127

Table 5-1 Confusion matrix for land cover mapping in Figure 5.1b

| Estimated Class | Reference Class | | | |
	Patch	Background	∑	Error (C)
Patch	**13865**	174	14039	1.2394%
Background	1657	**86056**	87713	1.8891%
∑	15522	86230	**101752**	
Error (O)	10.6752%	0.20179%		
Kappa = 0. 92756		Overall accuracy = 98.20%		

Table 5-2 Confusion matrix for land cover mapping in Figure 5.1c

| Estimated Class | Reference Class | | | |
	Patch	Background	∑	Error (C)
Patch	**14093**	1712	15805	10.8320%
Background	1429	**84518**	85947	1.6627%
∑	15522	86230	**101752**	
Error (O)	9.2063%	1.9854%		
Kappa = 0.8815		Overall accuracy = 96.9131%		

Figure 5.3a is a synthetic image that shows an example of a land cover mapping result containing a representation of a large patch and 4 small patches. The spatial correspondence between patches in Figure 5.3a with the reference image is shown in Figure 5.3b. The degree of the mis-location of the small patches in Figure 5.3a was low; therefore provide high agreement of the spatial correspondence between patches in Figure 5.3a and patches in the reference image. The total area of the patch in Figure 5.3a is 15539 pixels unit. The total area differs only by 17 pixels unit with the reference image. Similar to the Figure 5.1c, the accuracy of the non-site specific assessment of the land cover mapping in Figure 5.3a was higher than that of the Figure 5.1b.

(a)   (b)
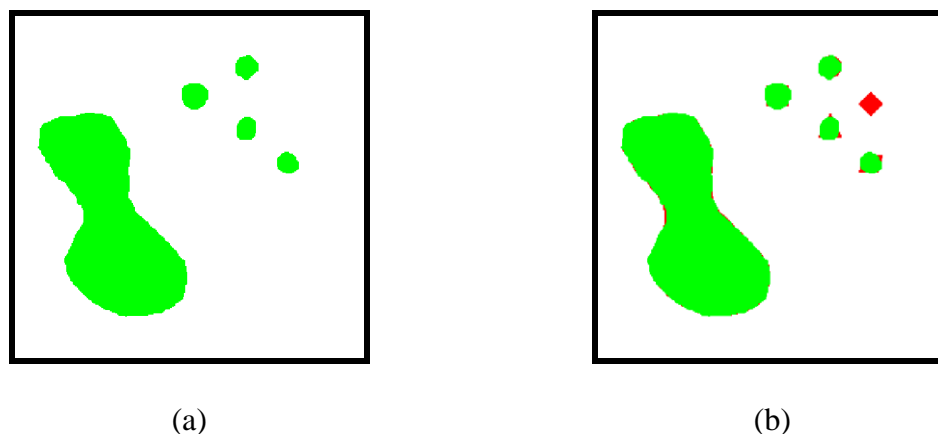
Figure 5-3 (a) Land cover mapping with a large patch and small patches represented.

(b) Spatial correspondences between patches in Figure 5.3a with the reference image.

Table 5-3 Confusion matrix for land cover mapping in Figure 5.3a

| Estimated Class | Reference Class | | | |
	Patch	Background	∑	Error (C)
Patch	**15065**	439	15504	2.8315%
Background	457	**85791**	86248	0.5299%
∑	15522	86230	**101752**	
Error (O)	2.9442%	0.5091%		
Kappa = 0.9659	Overall accuracy = 99.1194%			

Site specific assessment for land cover mapping in Figure 5.3a is summarized in Table 5.3, which demonstrated that the overall accuracy (99.1194%) is higher than that of the accuracy of land cover mapping in Figure 5.1b as given in Table 5.1. The omission and commission errors of the patches were low because the agreement of the spatial correspondence between the represented patches and the patches in the reference image was high.

The scenarios presented in this section suggested that mis-location of the represented small land over patches could affect the accuracy of the site specific assessment although producing high accuracy for the non-site specific assessment. Improving the accuracy with which the small patches are located could increase both of the site and no-site specific assessments. Therefore, in this chapter, the improvement of the small land cover patches location will be discussed.

5.2. Mis-location of small land cover patches

The problem of mis-location of small land cover patches represented by super-resolution mapping techniques can be illustrated in a simple example in Figure 5.4. Figure 5.4a shows a 24×24 pixels fine spatial resolution image. The image was a synthetic image that did not represent real data, but used to provide a graphical explanation. The image contains a land cover patch with an area of 9 white fine pixel units. Figure 5.4b is a 3×3 pixels coarse spatial resolution aggregated from the fine image in Figure 5.4a by a factor of eight. It makes a coarse spatial resolution pixel constituted by 8×8 sub-pixels. Since the area of the land cover in Figure 5.4a is less than 64 sub-pixels unit, the aggregation process would produce a mixed pixel at the centre of the coarse spatial resolution image (Figure 5.4b) with the value of the soft classification in the mixed pixel is $9/64 = 0.14$. Figure 5.4c shows an example of super-resolution mapping land cover representation, which mis-locates the patch inside the mixed pixel. Here, the centre of the represented patch is denoted by a red star symbol, while the centre of the actual patch in Figure 5.4a

(a)   (b)   (c)

(d)   (e)   (f)
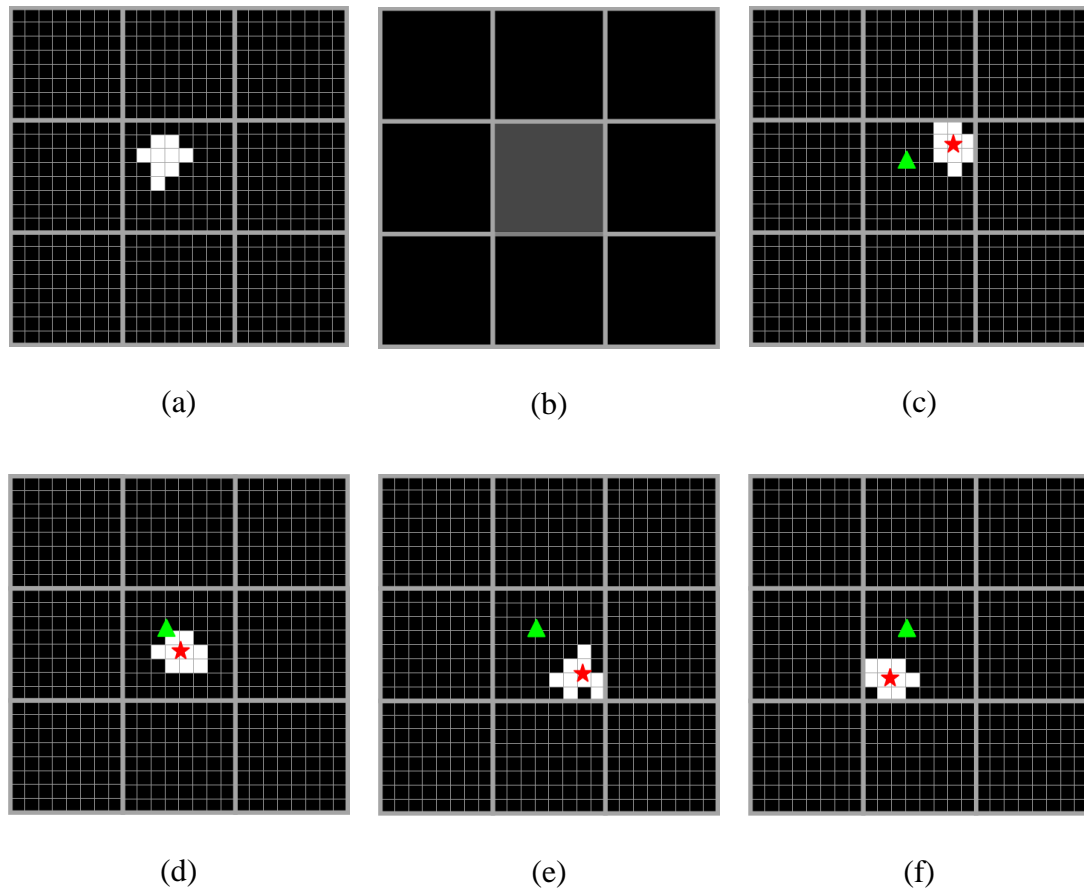
Figure 5-4 Mis-location of small land cover patch representation inside a mixed pixel. (a) Land cover patch in a fine spatial resolution image. (b) A 3×3 pixels coarse spatial resolution image with a mixed pixel at the centre. The soft classification value = 0.14. (c) An example of land cover patch representation. The red star symbol is the centre of the land cover, while the green triangle is the centre for the corresponding land cover in Figure 5.4a. The displacement vector between the two centres of gravity is 3.5573 unit pixels. (d)-(f) Possible locations of the patch.

is highlighted by a green triangle symbol. The displacement vector between the two centres of the patches was measured to determine the displacement resulted from the mis-location of the represented patch. In Figure 5.4c, the displacement vector was approximately 3.5573 in sub-pixels unit. The mis-location of the patch could occur anywhere inside the mixed pixel, such as images in Figure 5.4d-f, resulting in different displacement values. Consequently, the mis-location of the patches could contribute to the increasing spatial variability of super-resolution mapping.

5.3.   Image fusion from multiple observations

The predicted location of a sub-pixel sized land cover patches may vary greatly. In order to reduce the spatial variability of the represented land cover patches, multiple observations of the remote sensed imagery could be exploited by fusing them together to help locate patch accurately. This approach could potentially be useful because of the availability of the coarse but fine temporal resolution of several remote sensing systems such as AVHRR, MODIS and MERIS.

Due to the Earth's rotation and slight orbital position of remote sensing satellites, shifts at a fraction of a pixel between images may occur in the time series data. These images may look similar but they are different. In detail the contents of the images may look translated from one image to another, assuming that there are no significant changes that occur on the land. The sub-pixel shift could be inversely shifted to the exact position as the position of a reference image in the time series using image registration techniques (Zitova and Flusser, 2003).

(a)

(b)

(c)
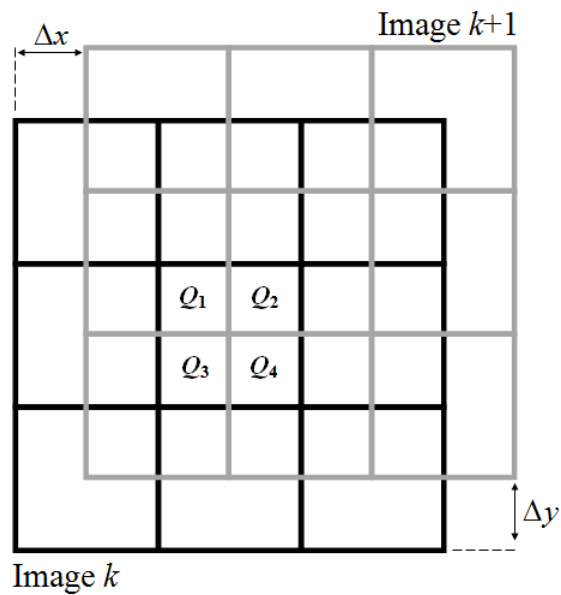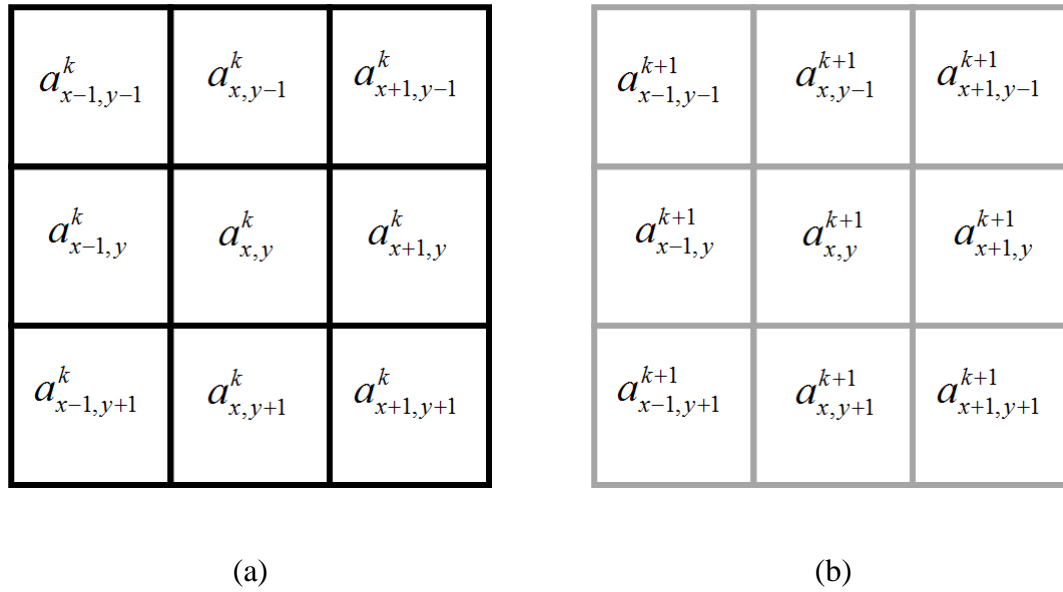
Figure 5-5 Decomposition of a coarse pixel into quadrants. (a) A coarse spatial resolution image of the k-th frame of a time series data. (b) A coarse spatial resolution of the k+1 –th frame. (c) Overlaying the image k and k+1 resulted in partitions Q_1, Q_2, Q_3, and Q_4 in a pixel (adapted from Ling et al., 2010).

At the pixel level, the corresponding pixels from different images can be combined into a fused pixel. With the sub-pixel shift normally occur in the time series images, overlaying all the corresponding pixels tend to produce several partitions, with the scale of each partition are usually smaller than a size of the fused pixel (Ling et al., 2010). Figure 5.5 shows a simple graphical representation of sub-pixel shift between pixels of two synthetic coarse spatial resolution images in the k-th frame (Figure 5.5a) and k+1-frame (Figure 5.5b). These two images were assumed to be translated linearly at horizontal, Δx and vertical, Δx positions. Both Δx and Δy were smaller than a size of a coarse spatial resolution pixel. Figure 5.5c shows that the two images were overlaid. The overlaying process can be performed when one image is registered to another image. Pixel $a_{x,y}$ of image k is overlaid with parts of pixels $a_{x-1,y}$, $a_{x,y}$, $a_{x-1,y+1}$, and $a_{x,y+1}$ of image k+1. The four partitions derived from the overlaying are called quadrants.

The size of a quadrant was smaller than a pixel but bigger than a sub-pixel. Example in Figure 5.5c shows four quadrants were created. Each quadrant may have different value depending on the combination of the images. For example, soft classification values of the two corresponding pixels from the two coarse spatial resolution images could be combined and assigned into the quadrants as given by

$$p(Q_1) = \frac{a_{x,y}^{k} + a_{x-1,y}^{k+1}}{2} \tag{5.1}$$

$$p(Q_2) = \frac{a_{x,y}^{k} + a_{x,y}^{k+1}}{2} \tag{5.2}$$

$$p(Q_3) = \frac{a_{x,y}^{k} + a_{x-1,y+1}^{k+1}}{2} \qquad (5.3)$$

$$p(Q_4) = \frac{a_{x,y}^{k} + a_{x,y+1}^{k+1}}{2} \qquad (5.4)$$

If there is K number of images, a quadrant i derived from a combination of the images was given by

$$p(Q_i) = \frac{a_{x,y}^{k} + a_{x',y'}^{k+1} + \ldots + a_{x',y'}^{K}}{K} \qquad (5.5)$$

where (x', y') is a coordinate of a pixel for image k+1, k+2, ..., or K that overlaid with a pixel (x, y) of a reference image k. p is an average value of soft classification from pixel of several images that overlaid on a quadrant. The difference in the p values was used to rank the quadrant. Quadrant with the highest p value indicates that the quadrant has the highest possible location of the small land cover patches.   If there are four quadrants in a pixel, a set the quadrants in the pixel was given by $\{p(Q_1), p(Q_2), p(Q_3), p(Q_4)\}$. In this set, the rank of the quadrant was sorted in a descending order. To simplify the explanation, it was assumed that the rank of the quadrant was $p(Q_1) > p(Q_2) > p(Q_3) > p(Q_4)$. It was also assumed that the size and shape of the quadrants in a pixel are equal.

Based on the rank of the quadrant, a soft classification value of a reference image in a time series images was divided among the four quadrants based upon the rank of each quadrant that contain the location of small land cover patches. For the quadrant with the highest rank, the soft classification value in the quadrant was

$$Q_l = \frac{\min\left[(a \times z \times z), (z_Q \times z_Q)\right]}{z_Q \times z_Q} \qquad (5.6)$$

Here, the spatial resolution of the pixel was increased by decomposing it into $z \times z$ sub-pixels. The size of a sub-pixel is given by $z_{SP} \times z_{SP}$. The size of a quadrant was constituted from $z_Q \times z_Q$ number of sub-pixels, where $z > z_Q > z_{SP}$.

It was assumed that the value of soft classification in the coarse pixel is a proportion of the number of two hard binary classes (e.g. white and black) at a sub-pixel level. Therefore, the number of white sub-pixels in the coarse pixel was $a \times z \times z$, where a is the soft classification value of the pixel in the range between 0 and 1. Equation 5.6 describes a filling process of the white sub-pixels into quadrant, Q_1 by assuming that the quadrant Q_1 posed the highest possible location of the small land covers. The maximum number of white sub-pixel that can be filled in the quadrant Q_1 was $(z_Q)^2$ number of sub-pixels.

In the quadrant Q_1, if the number of the white sub-pixel is less or equal than the maximum allocation, $(z_Q)^2$, then the total number of white sub-pixel in the quadrant equals to the total number of white sub-pixel in the coarse pixel, which is given by $a \times z \times z$. The value of the soft classification in the quadrant was normalized to ensure the range of the soft classification is in between 0 and 1. Since the value of the soft classification in the first quadrant is equal to the value of the soft classification in the pixel, then the values of the soft classification in other remaining quadrant Q_2, Q_3 and Q_4 were zero.

However, if the number of white sub-pixel allocated in the quadrant Q_1 was greater than the maximum number of sub-pixels that can be assigned into the quadrant, then the first quadrant, Q_1 would only take $z_Q \times z_Q$ number of white pixels. The allocation of remaining white sub-pixels would be concentrated on the second quadrant, Q_2, which has the second highest rank from the set. In the second quadrant, the number of white sub-pixel that can be allocated is the minimum value of either the remaining between the number of white sub-pixel in the first quadrant, or the maximum allocation space for sub-pixels in the second quadrant as given by

$$Q_2 = \frac{\min\left[\left\{(a \times z \times z) - Q_1\right\}, \left(z_Q \times z_Q\right)\right]}{z_Q \times z_Q} \tag{5.7}$$

Likewise, the number of white sub-pixel in the third quadrant or fourth quadrant would take the minimum value of either the remaining between the number of white sub-pixel in the previous quadrants, or the maximum allocation space in the third quadrant or fourth quadrant as given by

$$Q_3 = \frac{\min\left[\left\{(a \times z \times z) - (Q_1 + Q_2)\right\}, \left(z_Q \times z_Q\right)\right]}{z_Q \times z_Q} \tag{5.8}$$

$$Q_4 = \frac{\min\left[\left\{(a \times z \times z) - (Q_1 + Q_2 + Q_3)\right\}, \left(z_Q \times z_Q\right)\right]}{z_Q \times z_Q} \tag{5.9}$$

To simplify the description of the algorithm, suppose that the value of soft classification in a coarse spatial resolution image pixel was 0.56. If there were two classes in the
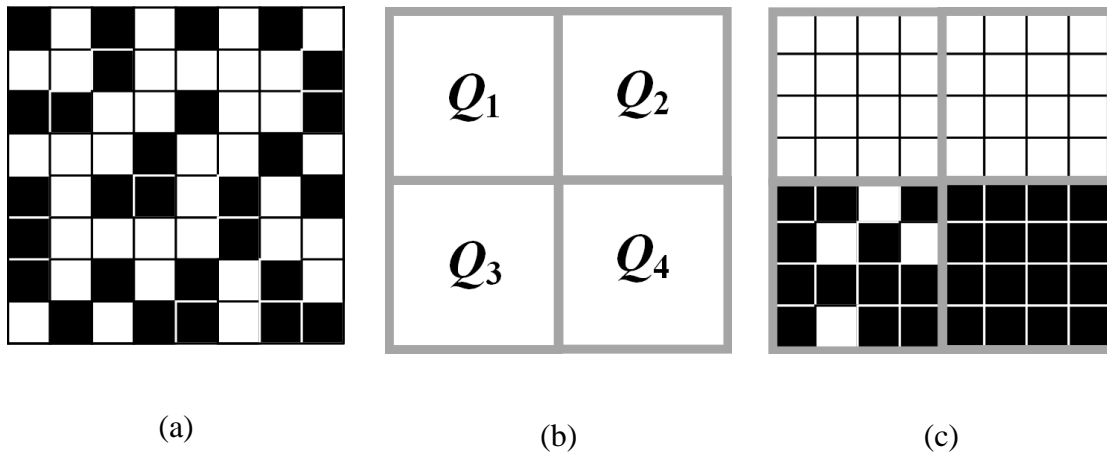
Figure 5-6 The assignment of sub-pixels within a coarse spatial resolution pixel based upon the rank of quadrants. (a) Random allocation of the sub-pixels within a coarse spatial resolution pixel. (b) Four quadrants inside a pixel with the rank is $p(Q_1) \geq p(Q_2)$ $\geq p(Q_3) \geq p(Q_4)$. (c) An example of the assignment of four quadrants inside the pixel.

coarse pixel, 56% of the area in the pixel belongs to class white and the remaining 44% belongs to class black. The spatial resolution of the coarse pixel was increased by decomposing it into $z \times z$ sub-pixels. The value of z was set to 8. Of the 64 sub-pixels in the coarse pixel, 36 sub-pixels were classified as white while the other remaining 28 sub-pixels were black. Using only single coarse image, the location of these sub-pixels was merely distributed randomly as shown graphically using synthetic image in Figure 5.6a. For simplicity, the rank of quadrant was assumed to be $p(Q_1) \geq p(Q_2) \geq p(Q_3) \geq p(Q_4)$ as show in Figure 5.6b. Therefore, the first 16 white sub-pixels were allocated in the first quadrant, Q_1. The other 16 white sub-pixels were allocated in the second quadrant, Q_2. The remaining four white sub-pixels were allocated randomly in the third

quadrant, Q_3. Figure 5.6c shows an example of the allocation of sub-pixels according to the rank of quadrants.

5.4. Sub-pixel shift estimation

To determine the sub-pixel shift between images, an image registration technique based on a phase correlation (Reddy and Chatterji, 1996) was used. This technique allows linear transformation such as translation and rotation to be detected even under different radiometric conditions and corrected in a new registered image. For many of the popular coarse spatial resolution imagery systems, such as AVHRR, MODIS, and MERIS, the degree of deformation in one image to another in one system is relatively low. Moreover, the translation between images is also linear. Therefore, this image registration technique for 2D rigid translation is typically sufficient for a time-series remote sensing images.

For the case of a translation between two coarse spatial resolution images, the relationship between these images can be written as

$$g_1(x, y) = g_2(x - \hat{x}, y - \hat{y})$$

(5.9)

where $\hat{x}$ and $\hat{y}$ are the shifts at a pixel scale.

Similarly, the relationship between these two images can be described in the frequency domain using Fourier shift theorem (Barrett and Myers, 2004).

$$G_1(u,v) = G_2^*(u,v)\exp\left[i2\pi\left(\frac{u\hat{x}}{M}+\frac{v\hat{y}}{N}\right)\right] \tag{5.10}$$

where N and M are the image dimensions and (*) indicates complex conjugate. The cross correlation between the images is the summation of all image pixels.

$$
\begin{aligned}
r_{g_1g_2}(\hat{x},\hat{y}) &= \sum_{x,y} G_1(x,y)G_2^*(x-\hat{x},y-\hat{y}) \\
&= \sum_{u,v} G_1(u,v)G_2^*(u,v)\exp\left[i2\pi\left(\frac{u\hat{x}}{M}+\frac{v\hat{y}}{N}\right)\right]
\end{aligned}
\tag{5.11}
$$

The magnitude of relative shift between the two images can be determined by locating the maximum point of an impulse peak in the cross correlation spectrum, $r_{g_1g_2}$. Up-sampling the spectrum allows the determination of the impulse peak's location at a sub-pixel scale for both the Δx and Δy (Sicairos et al., 2008; Soummer et al., 2007).

The approach of sub-pixel registration of image pairs can be extended to a time series of multiple coarse spatial resolution images by using one image as a reference for each of the other images in the time series.

$$g_1(x,y) = g_2\left(x-\hat{x}_{1,2},y-\hat{y}_{1,2}\right) = \ldots = g_k\left(x-\hat{x}_{1,k},y-\hat{y}_{1,k}\right) \tag{5.12}$$

where $\hat{x}_{1,2}$ and $\hat{y}_{1,2}$ are the pixel shifts between a reference image, g_1 and image g_2, while the $\hat{x}_{1,k}$ and $\hat{y}_{1,k}$ are the pixel shifts between the reference image and image g_k.

Up-sampling of all the coarse spatial resolution images in the time series would produce finer spatial resolution images as give by

$$f_1(i, j) = f_2\left(i - \hat{i}_{1,2}, j - \hat{j}_{1,2}\right) = \cdots = f_k\left(i - \hat{i}_{1,k}, j - \hat{j}_{1,k}\right) \tag{5.13}$$

where $\hat{i}_{1,2}$ and $\hat{j}_{1,2}$ are the sub-pixel shifts between a reference image, f_1 and image f_2, while the $\hat{i}_{1,k}$ and $\hat{j}_{1,k}$ are the pixel shifts between the reference image and image f_k; and $i = xz$, $j = yz$ where z is an up-sampling factor.

Because the image registration technique is able to measure the relative translation between two images at sub-pixel accuracy, the correction of an image's translation towards the reference image can be made at a fraction of a pixel. This would allow the proportion image derived from a soft classification of each image in the time series to be fused at a scale smaller than a pixel (Ling et al., 2010) and was normalized by the total number of imagery used.

$$f_{\text{Fused}}(i, j) = \frac{1}{K}\sum_{k=1}^{K} f_k\left(i - \hat{i}_{1,k}, j - \hat{j}_{1,k}\right) \tag{5.14}$$

where f_k is the kth registered image in the sequence of the time series, f_{Fused} is the result of the image fusion, and K is the number of the images in the time series. For a reference image, f_1, $\hat{i}_{1,1} = \hat{j}_{1,1} = 0$.

5.5. Incorporating a fusion of multiple observations into super-resolution mapping

The algorithm that exploited the fusion of sub-pixel shift multiple observations between one image and another can be implemented in the HNN and pixel swapping for super-

resolution mapping. For the HNN, a modification of the standard algorithm in Equation 3.19 was on the area proportion constraint component. Instead of retaining the class proportion inside a coarse pixel (Equation 3.23), Equation 5.15 retains the class proportion inside a quadrant. Here the size of the quadrant Q is less than a coarse spatial resolution pixel, a .

$$\frac{dP_{ij}}{dv_{ij}} = \frac{1}{2z_Q^2} \sum_{m=xz_Q}^{(x_Q z_Q + z_Q - 1)} \sum_{n=yz_Q}^{(y_Q z_Q + z_Q - 1)} \left(1 + \tanh\left(v_{mn} - 0.5\right)\lambda\right) - Q_{x_Q, y_Q} \qquad (5.15)$$

For the pixel swapping, instead of performing the swapping process within a coarse pixel as in Equation 3.33 until Equation 3.36, the pixel swapping was executed within a quadrant.

5.6.   Spatial variability analysis

Two analyses were performed for the representation of land cover patches using the modified HNN and the pixel swapping. The images used for the evaluation were similar to the images in Figure 5.4a. The proportion of the area of the patch inside the grid of a coarse pixel at the centre of the image was measured as a soft classification value. The size of the patch was gradually increased. The increment of the size of the patch was equal to the increment of the soft classification values from 0.10 to 0.90, which increase by 0.10 in each increment. Soft classification value at 1.00 was not used because the size of the represented land cover patch would equal to the size of a pixel, thus the centre of the patch is highly likely identical or close to the centre of the pixel, thus, the

displacement between the two centres is very small. Moreover, the attention of the analysis is on the location prediction of small land cover patches, which are derived from pixels with low soft classification values.

In each increment of the patch size, the location of the patch was randomly assigned inside the coarse pixel. The allocation of the patch inside the pixel was repeated 10 times, thus, generating 10 fine spatial resolution images in each path size increment. The size of these images was 24×24 fine spatial resolution pixels. Each of the fine spatial resolution images was degraded by spatial aggregation into a 3×3 pixels coarse spatial resolution image, similar to the image in Figure 5.4b. These images were used as input images for the HNN and pixel swapping techniques.

As explained in Chapter 4, small patches can be represented when the area proportion constraint of the HNN is weighted stronger than the goal functions (Equation 3.19). The weight of the area proportion constraint, k_P was set to 1.0, while the weights for the goal functions, k_1 and k_2, were all set to 0.1. In each of the patch representation, the number of iteration for the HNN was set to 10,000, in which the HNN would become stable and small patches could be represented. The input of the HNN was constituted of 24×24 neurons to accommodate all the sub-pixels of a coarse spatial resolution image. The displacement between the centres of the represented patches and the actual patch was acquired. The displacements from the 10 analyses were used to derive the spatial variability of the HNN in representing small land cover patches. For each of the patch representation process, the HNN only received a single coarse spatial resolution image. The procedure here was to evaluate the spatial variability of the HNN when using only a single coarse spatial resolution image.

For the pixel swapping, the number of neighbour (Equation 3.33) was set to 1 as this setting was more able to represent small patches than higher number of neighbour (Section 4.11). The number of iterations of the pixel swapping approach was set to 100 as this value was sufficient for the pixel swapping to reach a stable state in representing the patches. Similar to the HNN analysis, the displacement between the centres of the represented patches and the actual patch was taken to derive the spatial variability of the pixel swapping.

The spatial variability of the HNN using a single coarse spatial resolution image is shown in Figure 5.7. The spatial variability of the predicted patch location from the HNN depended on the value of the soft classification inside the mixed pixel. When the value of the soft classification was low, the spatial variability of the patches was high. With the low soft classification values, the size of the patches that could be represented by the HNN was smaller as compared when the values of the soft classification were high. The displacement of the small patches tended to be larger than the displacement of the bigger patches. Table 5.4 summarized the mean and variance of the spatial variability of the HNN for the soft classification values ranging from 0.10 to 0.90. The total variance was 5.3709.

Figure 5.8 shows the spatial variability of the predicted patch location from the pixel swapping using only a single coarse spatial resolution image. Table 5.5 summarized the mean and variance of the spatial variability of the pixel swapping for the soft classification values ranging from 0.10 to 0.90. The total variance was 9.4966. In general, the spatial variability for the HNN was lower than that of the pixel swapping when using only single coarse spatial resolution image.
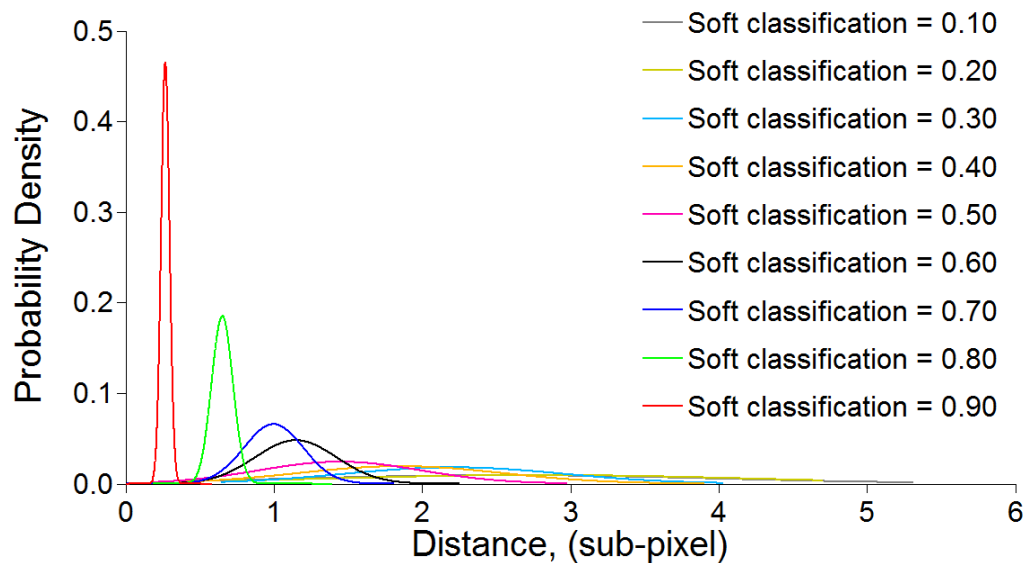
Figure 5-7 Spatial variability of the HNN using only a single coarse spatial resolution image.

Table 5-4 Statistics of the spatial variability of the HNN using only a single coarse spatial resolution image. Mean and variance were measured from 10 displacements of a patch in every increment of soft classification value in a mixed pixel.

Soft classification value in a mixed pixel	Mean	Variance
0.10	2.5659	1.4223
0.20	2.7923	1.3961
0.30	2.2159	0.7362
0.40	1.8540	0.6891
0.50	1.4451	0.5484
0.60	1.1485	0.2767
0.70	0.9979	0.2018
0.80	0.6525	0.0717
0.90	0.2684	0.0286
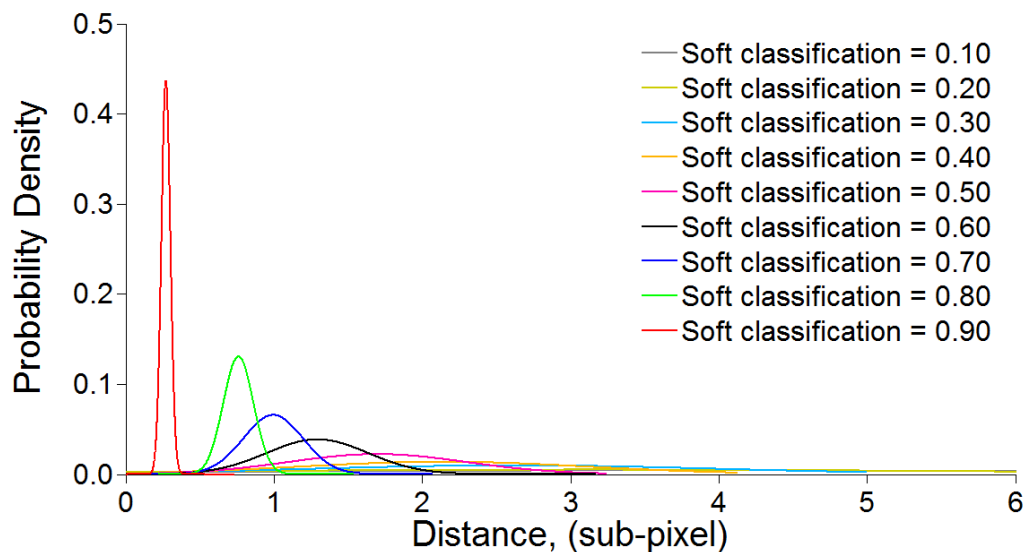
Figure 5-8 Spatial variability of the pixel swapping using only a single coarse spatial resolution image.

Table 5-5 Statistics of the spatial variability of the pixel swapping using only a single coarse spatial resolution image. Mean and variance were measured from 10 displacements of a patch in every increment of soft classification value in a mixed pixel.

Soft classification value in a mixed pixel	Mean	Variance
0.10	3.6432	3.2124
0.20	3.1580	2.6678
0.30	2.6292	1.3698
0.40	2.1456	0.9691
0.50	1.6977	0.5984
0.60	1.2941	0.3447
0.70	0.9951	0.2021
0.80	0.7608	0.1018
0.90	0.2722	0.0305
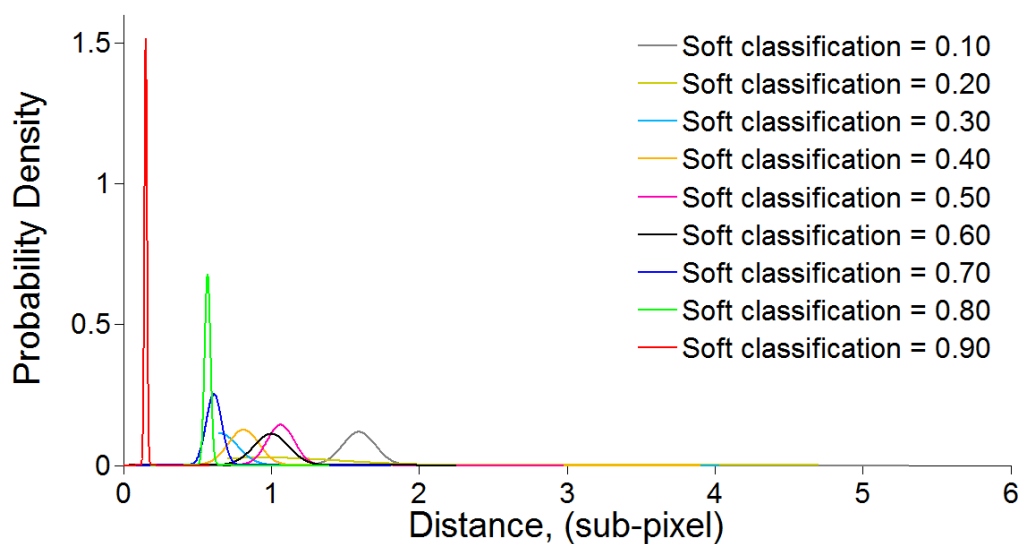
Figure 5-9 Spatial variability of the HNN using multiple coarse spatial resolution images.

Table 5-6 Statistics of the spatial variability of the HNN using multiple coarse spatial resolution images. Mean and variance were measured from 10 displacements of a patch in every increment of soft classification value in a mixed pixel.

Soft classification value in a mixed pixel	Mean	Variance
0.10	1.5943	0.1122
0.20	0.9333	0.4524
0.30	0.6578	0.1179
0.40	0.8134	0.1054
0.50	1.0633	0.0925
0.60	1.0020	0.1193
0.70	0.6139	0.0525
0.80	0.5714	0.0196
0.90	0.1531	0.0088
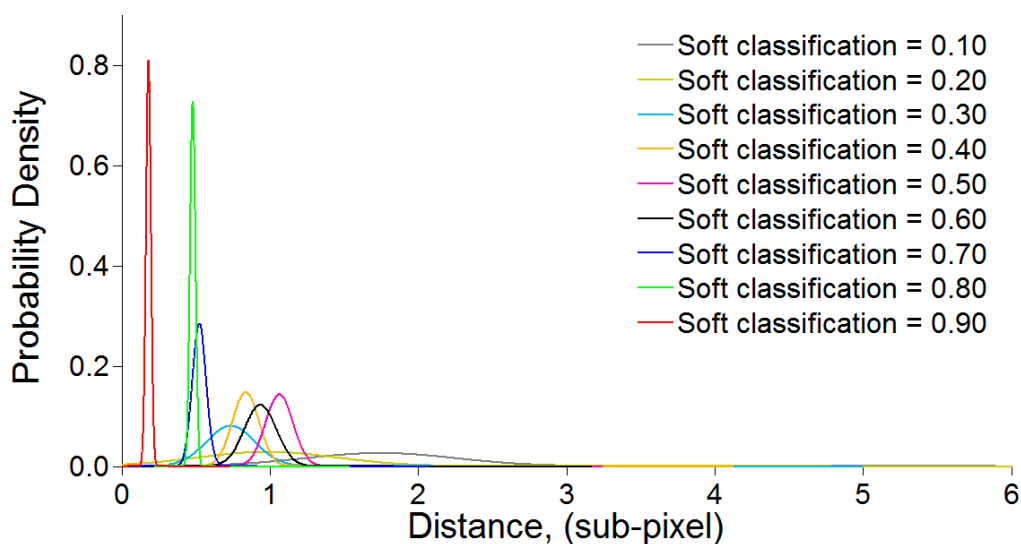
Figure 5-10 Spatial variability of the pixel swapping using multiple coarse spatial resolution images.

Table 5-7 Statistics of the spatial variability of the pixel swapping using multiple coarse spatial resolution images. Mean and variance were measured from 10 displacements of a patch in every increment of soft classification value in a mixed pixel.

Soft classification value in a mixed pixel	Mean	Variance
0.10	1.7473	0.5090
0.20	0.9833	0.4666
0.30	0.7367	0.1648
0.40	0.8368	0.0898
0.50	1.0633	0.0925
0.60	0.9348	0.1082
0.70	0.5242	0.0465
0.80	0.4803	0.0182
0.90	0.1818	0.0164

To evaluate the effectiveness of the incorporation of sub-pixel shifted multiple observations into super-resolution mapping techniques, procedure similar to the HNN and pixel swapping using only single coarse spatial resolution image was repeated. However, the degradation of a fine spatial resolution image produced several coarse spatial resolution images, which were translated randomly at a sub-pixel scale between one another. Five coarse spatial resolution images were generated. One image was generated without shifting from the fine spatial resolution image. The other four images were generated from the fine spatial resolution image by shifting at the up, bottom, left and right directions at a sub-pixel scale. The sub-pixel shifts between images were determined using Equation 5.9-5.11. All the coarse spatial resolution images were combined using Equation 5.14 to produce a fused image.

For the HNN, the fused image was fed into a HNN that employed a modified area proportion constraint as in Equation 5.15. In the modified constraint, instead of placing the area constraint within a pixel, the constraint was focused within a quadrant. For the pixel swapping, the fused image was used as an input for this technique, in which the operational of this technique was performed using Equation 3.23-3.36 but instead of performing the operation within a pixel, the pixel swapping algorithm was performed within a quadrant.

The spatial variability of the HNN using multiple coarse spatial resolution images is shown in Figure 5.9. Table 5.6 summarized the mean and variance of the spatial variability of the HNN for the soft classification values ranging from 0.10 to 0.90. The total variance was 1.0806. Figure 5.10 shows the spatial variability of the pixel swapping using multiple coarse spatial resolution images. Table 5.7 summarized the

mean and variance of the spatial variability of the pixel swapping for the soft classification values ranging from 0.10 to 0.90. The total variance was 1.5120.

The incorporation of the multiple sub-pixel shifted coarse spatial resolution images into the HNN and pixel swapping demonstrated the decreasing of the spatial variability for both technique especially when the values of the soft classification were low. Critically, at the low soft classification values, the spatial variability of the predicted patch location from the HNN and pixel swapping tended to be high as the size of the represented patches were generally small, thus making the displacement vector between the centre of the represented patch with the centre of the actual patch appear to be high. At high soft classification values, the size of the represented patches were slightly big, making the displacement vector appears to be low.

5.7. Land cover patches representation using multiple coarse spatial resolution images

Further evaluation of an approach that used multiple sub-pixel shifted coarse spatial resolution images was performed using the HNN and pixel swapping. The image in Figure 5.11a is a fine spatial resolution image with its size was 96×96 fine resolution pixels. The image contains a cluster of small patches. The image was degraded by spatial aggregation into a 12×12 coarse resolution pixels image as shown in Figure 5.11b.

Using only the coarse spatial resolution image, the representation of the patches was evaluated with the HNN and pixel swapping techniques. To represent the small patches, a HNN with weights for the goal functions, k_1 and k_2 were set to 0.1 and the weight for the area proportion constraint, k_P was set to 1.0 (Equation 3.19). The justification of the value of the weights was provided in Chapter 4. The number of neurons in each HNN was set to 96×96, identical to a size of the fine spatial resolution image. Each of the HNN was calculated numerically for 10,000 iterations. For the pixel swapping, the number of neighbour used was set to 1 (Equation 3.33). The pixel swapping technique was run for 100 iterations.

Result of the HNN using only a single coarse spatial resolution image is shown in Figure 5.11c and the site specific assessment is summarized in a confusion matrix in Table 5.8. The site specific accuracy was assessed using all 9216 (96×96) sub-pixels in the image represented by the HNN. Overall, the accuracy of the site specific assessment was 92.7843%. Result of the pixel swapping using only a single coarse spatial resolution image is shown in Figure 5.11d and the site specific assessment is summarized in a confusion matrix in Table 5.9. Overall, the accuracy of the site specific assessment was 91.8403%.

The analyses of the HNN and pixel swapping that used only a single image were repeated using multiple sub-pixel shifted coarse spatial resolution images. These images were fused and fed into the input of the HNN and pixel swapping. Result of the HNN is shown in Figure 5.11e and the site specific assessment is summarized in a confusion matrix in Table 5.10. Overall, the accuracy of the site specific assessment was
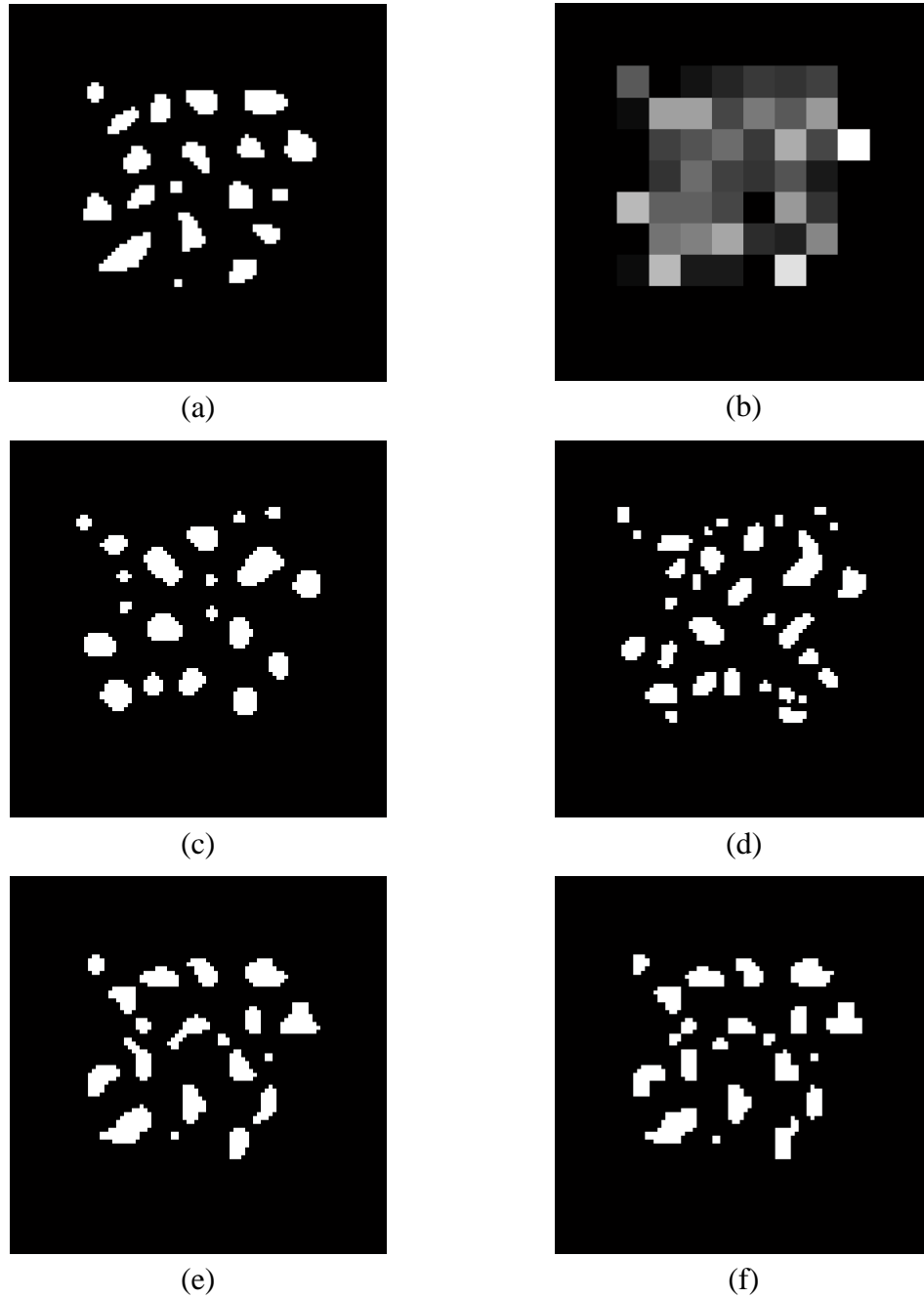
Figure 5-11 Small patches representation. (a) Original fine spatial resolution image. (b) Degraded image. Super-resolution mapping (c) HNN using a single coarse spatial resolution image, (d) pixel swapping using a single coarse spatial resolution image, (e) HNN using multiple coarse spatial resolution images, and (f) pixel swapping using multiple coarse spatial resolution images.

Table 5-8 Confusion matrix for land cover mapping represented by HNN using a single coarse spatial resolution image.

Estimated Class	Reference Class			
	Patch	Background	∑	**Error (C)**
Patch	**284**	319	603	52.9022%
Background	346	**8267**	8613	4.0172%
∑	630	8586	**9216**	
Error (O)	54.9206%	3.7154%		
Kappa = 0.4220		Overall accuracy = 92.7843%		

Table 5-9 Confusion matrix for land cover mapping by pixel swapping using a single coarse spatial resolution image.

Estimated Class	Reference Class			
	Patch	Background	∑	**Error (C)**
Patch	**254**	376	630	59.6825%
Background	376	**8210**	8586	4.3792%
∑	630	8586	**9216**	
Error (O)	59.6825%	4.3792%		
Kappa = 0.3594		Overall accuracy = 91.8403%		

Table 5-10 Confusion matrix for land cover mapping represented by HNN using a time series coarse spatial resolution images.

Estimated Class	Reference Class			
	Patch	Background	∑	**Error (C)**
Patch	**461**	166	627	26.4753%
Background	169	**8420**	8589	1.9676%
∑	630	8586	**9216**	
Error (O)	26.8254%	1.9334%		
Kappa = 0.7140		Overall accuracy = 96.3650%		

Table 5-11 Confusion matrix for land cover mapping by pixel swapping using a time series coarse spatial resolution images.

Estimated Class	Reference Class			
	Patch	Background	∑	**Error (C)**
Patch	**459**	169	628	26.9108%
Background	171	**8417**	8588	1.9912%
∑	630	8586	**9216**	
Error (O)	27.1429%	1.9683%		
Kappa = 0.7099		Overall accuracy = 96.3108%		

96.3650%. Result of the pixel swapping is shown in Figure 5.11f and the site specific assessment is summarized in a confusion matrix in Table 5.11. Overall, the accuracy of the site specific assessment was 96.3108%. This analysis demonstrated that by using the multiple sub-pixel shifted coarse spatial resolution images, the site specific accuracy of the HNN increased by 3.5807% and for the pixel swapping, the accuracy increased by 4.4705% compared to using a single coarse spatial resolution image.

High omission and commission errors in Table 5.8 and 5.9 were due to the mis-location of the represented of the small patches. As explain in Section 5.1, the representation of the small patches at the wrong locations could increase the commission error; in turn the location that the patches missed could increase the omission error. For the HNN, using only a single coarse spatial resolution image, the omission error of the patches was 54.9206% and the commission error of the patches was 52.9022% (Table 5.8). Using multiple sub-pixel shifted coarse spatial resolution images, these errors were reduced to 26.8254% for the omission error and 26.4753% for the commission error

(Table 5.10). For the pixel swapping, using only a single coarse spatial resolution image, the omission error of the patches was 59.6825% and the commission error of the patches was 59.6825% (Table 5.9). Using multiple sub-pixel shifted coarse spatial resolution images, these errors were reduced to 27.1429% for the omission error and 26.9108% for the commission error (Table 5.11).

Analyses in this section demonstrated that the spatial variability of the represented patches could contribute to the uncertainty of the HNN and pixel swapping in predicting the location of small land patches. The uncertainty was related with the accuracy of the site specific thematic assessment. Using a fusion of multiple coarse spatial resolution images, could potentially increase the accuracy of the prediction of the small patch location, thus improving the accuracy of the site specific thematic assessment.

The limitations of the algorithm were that the size of all the quadrants was assumed to be equal, and the shape of each quadrant was square, with the sub-pixel shifts at the horizontal, Δx and vertical, Δx are equal. Future works will be focused on different sizes and shapes (e.g. rectangle) of the quadrant.

5.8. Conclusions

Super-resolution mapping aims to locate sub-pixel land cover fractions within the area represented by a pixel. One problem that has been highlighted for small land cover patches is that the predicted location is very uncertain. As a result if an analysis was

repeated, for example, there would be great variability in the predicted location of small land cover patches.

Analyses in this chapter focus on reducing the spatial variability of the predicted location of land cover patches from the use of the HNN and pixel swapping approaches for super-resolution mapping. This chapter presents an algorithm that fused multiple sub-pixel shifted coarse spatial resolution image. Multiple coarse spatial resolution images could be acquired from time series remotely sensed imagery. At a pixel level, four quadrants were generated resulted from the overlaying of the multiple images. Each quadrant has rank order of containing the location of small land cover patches. The operational of the HNN and pixel swapping was performed at a quadrant scale. The accuracy of the image registration techniques is also essential in order to ensure the success of this approach.

Using a fusion of time series data of the coarse spatial resolution images, the spatial variability of land cover patches can be reduced compared when using only single coarse spatial resolution image. Consequently, the location of the small land cover patches can be accurately predicted. Several issues associated with the statistical significance of the results will be considered in the future. The algorithm proposed in this chapter will be used to improve the super-resolution mapping techniques for use with real coarse spatial resolution images, which will be discussed in Chapter 6.

6. Super-resolution mapping for landscape patches using a fusion of time series imagery

Having investigated the effect of variation on the parameters settings of the HNN and pixel swapping and improving the location with which small land cover patches are predicted, attention is now focused on the representation of real landscape patches (lakes) from popular coarse spatial resolution remotely sensed imagery. In this chapter, brief reviews on the MODIS and Landsat ETM+ imagery are presented, before a novel, two step HNN technique that exploits the best features of two HNNs with different parameters settings was implemented on a time series MODIS images.

6.1. Introduction

Remote sensing systems acquire observations of the Earth's surface while orbiting the Earth. The frequency of the observation on a same site depends upon the revisit interval characteristic of satellites. Often, the revisit interval is inversely proportional with the spatial resolution of remotely sensed images (Toutin, 2009; Goward et al., 2009; Justice and Tucker, 2009). Moreover, the relationship between the sensor spatial resolution and

the cost of the sensor is also often proportional. So, there is possibility to acquire multiple spatial resolution images inexpensively.

Additional information, normally at a finer spatial resolution image can be incorporated into the super-resolution mapping to increase the accuracy of land cover mapping and to decrease the uncertainty of locating the land cover. Amongst the additional information that have been used in the super-resolution mapping are LIDAR (Nguyen et al., 2005), geo-statistical data (Boucher and Kyriakidis, 2006), fused images (Nguyen et al., 2006) and panchromatic (PAN) imagery (Atkinson, 2008: Nguyen et al., 2011). Fine spatial resolution remote sensing systems such as SPOT HRG, IKONOS and QuickBird provide both multispectral and panchromatic imagery. The panchromatic images usually have finer spatial resolution than the multispectral images, which often used as main imagery.

However, not all remote sensing systems are able to acquire finer spatial resolution image along with the main imagery. Coarse spatial resolution remote sensing systems such as the Moderate-resolution Imaging Spectroradiometer (MODIS), Medium Resolution Imaging Spectrometer (MERIS) and Advanced Very High Resolution Radiometer (AVHRR) are not designed to capture panchromatic images. One of the aspects from these systems that could be utilized is their fine temporal resolution as the revisit interval of these systems is normally on a daily basis (Justice and Tucker, 2009). Exploiting the fine temporal resolution of these systems may solve the problem of acquiring additional information for the image fusion.

During remote sensing observations, a sample-scene phase scenario may occur (Park and Schowengerdt, 1982), which may be perceived as a limitation during the observation. However, this discrepancy can be exploited as the imagery of a site acquired on different dates typically differs in subtle ways, with the location of pixels varying slightly due to, for example, minor orbital translations of remote sensing satellites. The slight differences between images can be exploited by combining a time-series coarse spatial resolution images into an integrated image, which may contain more information than a single coarse spatial resolution image (Packalen et al., 2006; Shen et al., 2009). Acquisition of several coarse spatial resolution images is also a basic premise for spatial resolution enhancement in many super-resolution image restitution techniques (Park et al., 2003; Yang and Huang, 2011) but quite unexplored in the context of super-resolution mapping (Ling et al. 2010).

Although some papers in the literature provided the application of super-resolution mapping technique that used several coarse spatial resolution images (Lu and Inamura, 2003; Ling et al. 2010)., the imagery used were not real, rather generated by spatial degradation from finer spatial resolution images. Therefore, in this chapter, the application of super-resolution mapping using time-series MODIS images will be investigated.

6.2.   Moderate Resolution Imaging Spectroradiometer

The Moderate Resolution Imaging Spectroradiometer (MODIS) is a sensor designed for NASA's Earth Observing System (EOS) on board the Terra and Aqua satellites (Justice

and Tucker, 2009). The applications of MODIS include land, ocean, and atmospheres observations and provide understanding of the Earth system processes at global, continental, and regional scales. The Terra and Aqua orbit is approximately at 705 km, and gives a swath width as wide as 2330 km and global near-daily coverage. There are 36 spectral bands in the MODIS allowing it to cover wavelengths from the visible (0.415 μm) to infrared (14.235 μm) spectrum. Two bands are at 250 m spatial resolution, five bands are at 500 m resolution and 29 bands are at 1 km resolution. The first seven bands are designed explicitly for land surface applications (Friedl et al., 2002) with the spatial resolution of 250 m for band 1 (red, 0.620-0.670 μm), and band 2 (near infrared, 0.841-0.876 μm), and 500 m for bands 3 to 7 (0.459-0.479, 0.545-0.565, 1.230-1.250, 1.628-1.652, 2.105-2.155 μm, respectively).

6.3.   Landsat ETM+

The main instrument carried by Landsat 7 is the Enhanced Thematic Mapper Plus (ETM+). This instrument maintains the essential characteristics of Thematic Mapper carried by Landsats 4 and 5. Ground resolution for ETM+ data remains unchanged at a spatial resolution of 30 m, except for the thermal band in which the resolution increased from 120 to 60 m. A panchromatic band with 15 m resolution is also added for rectification and image sharpening. Landsat 7 provides data with a swath width of 185 km and a repeat coverage interval of 16 days (Goward et al., 2009).

Table 6-1 Landsat 7 ETM+ bands

Band number	Spectral range (µm)	Ground resolution (m)
1	0.450 – 0.515	30
2	0.525 – 0.605	30
3	0.630 – 0.690	30
4	0.750 – 0.900	30
5	1.550 – 1.750	30
6	10.400 – 12.500	60
7	2.090 – 2.350	30
Panchromatic	0.520 – 0.900	15

6.4. Test site and data

The study area covers approximately a 26 km × 28 km area located in Quebec province, Canada. It is situated between latitudes $54^{o}26'24"N$ and $54^{o}12'10"N$ and between longitudes $85^{o}26'15"W$ and $85^{o}01'22"W$. The area contains a landscape mosaic that is made up of lakes of varying size and shape. Figure 6.1 shows the location of the study area. Not only do the lakes provide a challenge for super-resolution mapping there is a desire for more information on such features in high latitude regions as they appear to be disappearing (Smith et al., 2005). The disappearing of the lakes may be caused by the shrinking of the size of the lakes until they vanished and converted the land cover into vegetation. The disappearing of the lakes may also have impacts on the ecological and environmental systems on that region.
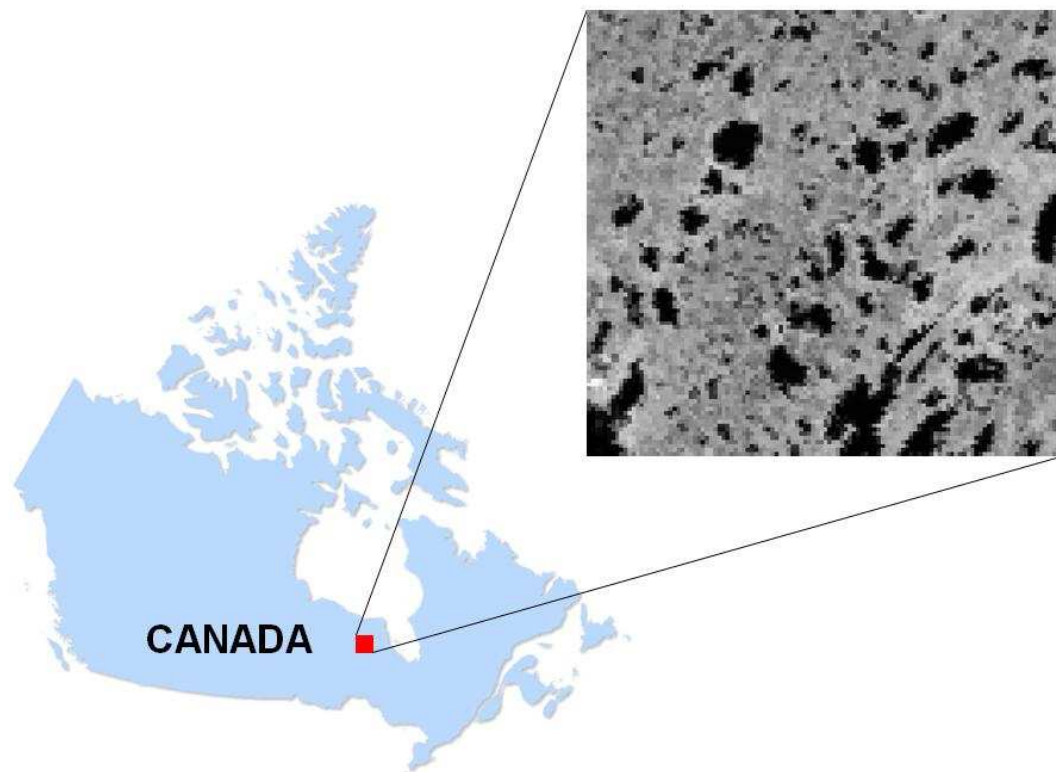
Figure 6-1 Test site

(a)   (b)
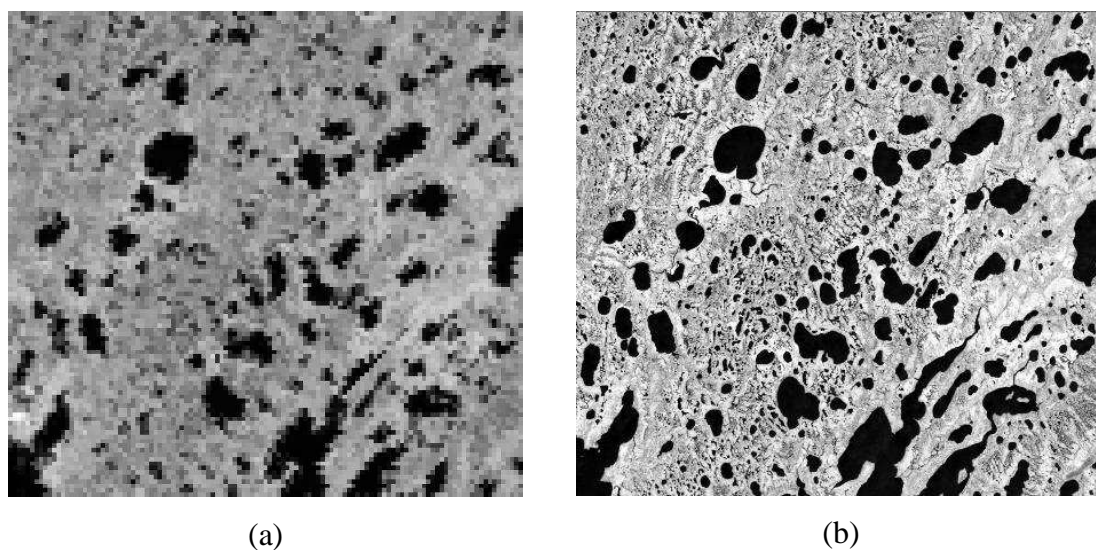
Figure 6-2 Datasets (a) one of the MODIS 250 m near IR images acquired on 5 July 2002 and (b) Landsat ETM+ 30 m near IR image taken on 10 July 2002 that was used as ground data.
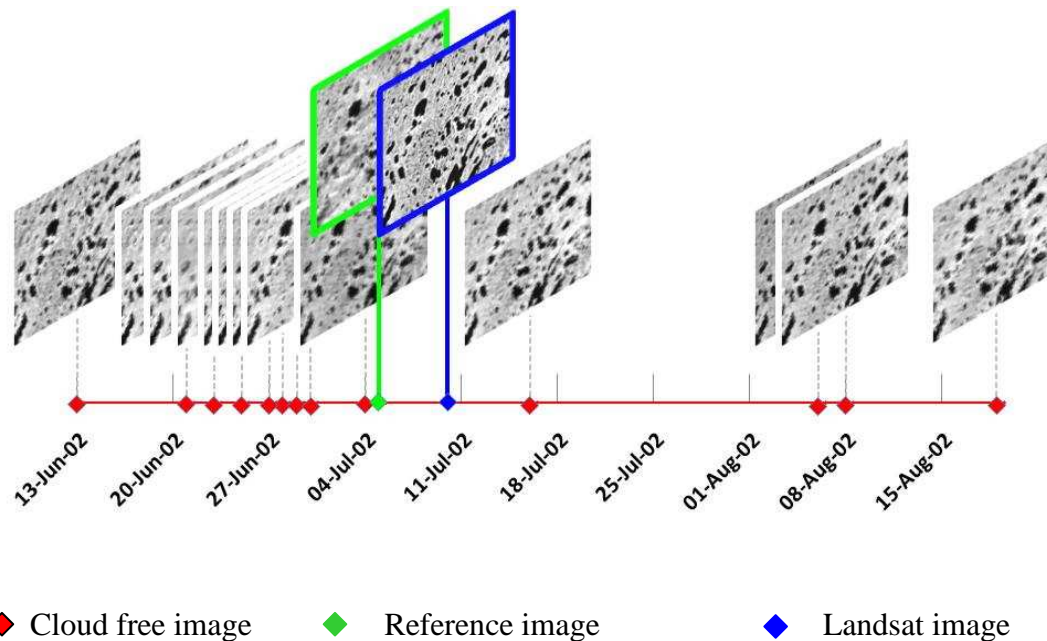
Figure 6-3 Temporal coverage of a time-series daily MODIS 250 m. A MODIS image acquired on 5 July 2002 was used as a reference image for a time series image registration. Landsat image acquired on 10 July 2002 was used as a ground data as a means to set the orientation of the MODIS image correctly.

Two sets of image data were used. First, a time series of coarse spatial resolution imagery acquired by the MOD09GQ (MODIS surface reflectance product) MODIS 250 m spatial resolution sensor onboard Terra was acquired between 13 June 2002 and 19 August 2002 because land cover is largely static at this time scale. During this period, the site was clear from cloud, snow and haze. Only the data acquired in the near infrared band (0.841-0.876 µm) were used because land and water are highly separable in this part of the spectrum. MOD09GQ is a level 2 data of MODIS which has not been

gridded into a map projection as in Level 3 data of composite MODIS images (Vermote et al. 2002), thus allowing further processing to be determined by users, such as sub-pixel shifts measurement. The MODIS images were projected from Sinusoidal projection into a Landsat Universal Transverse Mercator (UTM) projection at zone 16. The MODIS images were provided by the USGS Land Processes Distributed Active Archive Center (LP DAAC) website (https://lpdaac.usgs.gov/). An example of a MODIS image acquired on 5 July 2002 is shown in Figure 6.2a.

Second, a Landsat ETM+ of the region acquired on 10 July 2002 was used to provide ground data on lakes. These data have a spatial resolution of 30 m and the mosaic of lakes is visually evident in the image (Figure 6.2b). Only the near infrared band image (0.750-0.900 µm) was used because land and water are very separable within this band. The Landsat image was provided by the U.S Geological Survey (USGS) Global Visualization Viewer website (http://glovis.usgs.gov/). The Landsat image lies in the middle of the set of dates over which the MODIS data set was acquired. The MODIS image acquired on 5 July 2002 was used as a reference image for time series image registration because its date of acquisition is the closest temporally to that of the Landsat ETM+ image and lies in the middle of the set of dates over which the MODIS data set was acquired. Figure 6.3 illustrates graphically the position of the reference and ground data images relating to the temporal coverage of the time series MODIS images.

6.5.   Sub-pixel shift estimation in the time series MODIS images

In the daily MODIS time series images, the level of change in one image to another is relatively low because they are acquired on a same site and the duration of the acquisition is only two months, thus no significant changes that occur to the shape of the lakes. As explained in Section 5.4, the sub-pixel shifted between images in a time series can be estimated provided that the relative translation between one image to another is linear. The sub-pixel shift between images in the MODIS time series was measured using a phase correlation technique (Sicairos et al., 2008; Soummer et al., 2007; Reddy and Chatterji, 1996). The phase correlation technique is based on fast Fourier transform (FFT), which allows linear transformation between one image to another such as translation and rotation to be detected even under different radiometric conditions and corrected to produce a new registered image.

Table 6.2 shows relative translation between the MODIS reference image and the rest of the MODIS images in the time series. The measurement was taken at the x and y directions. Measurement of the relative translation below 100% indicates that the translation occurred at a fraction of a pixel. Note that the scale of the translation at the x direction was larger than that at the y direction. This situation can be related with the whiskbroom scanning mechanism of the Terra on-board MODIS sensor whereby the x direction refers to cross-track while the y direction refers to in-track (Schowengerdt, 2007). Here, based on the Table 6.2, the movement of the Terra satellite along the cross-track is more apparent compared to the movement along the in-track.

Table 6-2 Relative translations at sub-pixel scales between a reference MODIS image acquired on 5 July 2002 and the rest of the images in the time series daily MODIS images.

No.	MODIS image (Time of acquisition)	Δx (%)	Δy (%)
1	13 June 2002	87.5	-25.0
2	21 June 2002	62.5	-75.0
3	23 June 2002	75.0	-100.0
4	25 June 2002	-12.5	-87.50
5	27 June 2002	137.5	-62.5
6	28 June 2002	37.5	12.5
7	29 June 2002	112.5	-50.0
8	30 June 2002	50.0	-87.5
9	4 July 2002	187.5	-12.5
10	16 July 2002	100	-12.5
11	6 August 2002	12.5	-62.5
12	8 August 2002	12.5	-25.0
13	19 August 2002	25.0	-62.5
	Average translations	68.3	-50.0

6.6. A two-step HNN for super-resolution mapping

A new technique for super-resolution mapping is proposed that combines two HNN super-resolution mapping techniques: a HNN that placed equal emphasis between the goal function and the area proportion constraint (HNN(E)), and a HNN that placed emphasis on the area proportion constraint over the goal functions (HNN(A)). Results in Chapter 4 demonstrated that the HNN(A) was more accurate than the HNN(E) to represent small land cover patches (Section 4.7). However, when the proportion of

mixed is high, the boundary of the patch represented with the HNN(A) tended to be irregular and not smooth, leading to the increasing of the RMSE value for the boundary fitting (Section 4.11).

In contrast, the patch representation using the HNN(E) tended to have smooth boundary representation when the proportion of mixed pixel is high, leading to the low value of the RMSE (Section 4.11). However, the HNN(E) was less accurate than the HNN(A) to represent small land cover patches (Section 4.7 and 4.11).

The aim of the proposed technique was to combine the best features of the HNN(E) and HNN(A). The first HNN was based on HNN(A) used to represent small land cover patches, while ignoring large patches by using morphology filter. The second HNN was based on HNN(E) used to represent large land cover patches, and ignoring small patches. Therefore, this approach is called 2-step HNN and a notation used for simplicity was HNN_2.

The proposed technique only considered the HNN technique and not the pixel swapping. Although pixel swapping was effective in retaining the proportion of land cover from mixed pixels (Section 4.9 and 4.10), results of the pixel swapping tended to be dominated by speckled pattern (Thornton et al., 2006). This pattern may wrongly be classified as land cover patches. The removal of the speckled pattern may also eliminate small land cover patches.

6.7. Experimental analysis

Two types of images were used to evaluate the HNN, pixel swapping, and the proposed techniques in representing lakes. First, a single MODIS image was used. Second, a fusion of a time series MODIS images was used as Chapter 5 (Equation 5.14) illustrated the potential of such an approach for land cover mapping.

6.7.1. Single MODIS image

The MODIS image acquired on 5 July 2002, which consist of 109×117 pixels, was used as an input image to produce thematic map of land cover classification using several different techniques. A conventional k-means hard classification (Duda et al., 2001) was applied to the input image. Using the same input image, a proportional image was produced by fuzzy c-means soft classification (Bezdek et al., 1984). The fuzzy c-means algorithm was explained in Section 3.1. The number of cluster, c was set to 2 to differentiate between lakes and land surface, while the weighting parameter that determines the degree of fuzziness, m, was set to 2.0. The spatial resolution of the proportional image was increased by magnification factor of eight. Specifically, a pixel of the proportional image was sub-divided into 8×8 repetitive sub-pixels, making 872×936 sub-pixels in the image. Each sub-pixel then was rescaled to a spatial resolution of 30 m, which is equal to the spatial resolution of a Landsat ETM+ pixel.

Two pixel swapping techniques were implemented on the proportional image. First the number of neighbours (Equation 3.33) was set to 1. Second the number of neighbours was set 5. The choice of the number of neighbours for the pixel swapping

may determine the size of the lake that can be represented. These two pixel swapping were calculated for 100 iterations, at which a stable state of estimation should be reached.

Three types of the standard HNN (Equation 3.19) were used. First the HNN with the equal strength of the goal function and area proportion constraints (HNN(E)). The weights, k_1, k_2 and k_P were all set to 1.0. Second, the strength of the area proportion constraint was emphasized more than the goal function constraint (HNN(A)). Thus, the weights for the goal function k_1 and k_2 were set to 0.1, while the weight for the area proportion constraint, k_P was set to 1.0. These weight values were chosen because as they give the best result for the HNN in representing small patches, as demonstrated in Chapter 4. The two HNNs were calculated numerically for 10,000 iterations each to enabling representation of small patches. Third, a combination of the two earlier HNNs, the HNN_2, as described in Section 6.6, was used. Each of the HNN comprised of 872×936 neurons to support the number of sub-pixels of the proportional image that was used as an input image. The HNN that placed more emphasis on the goal functions than the area proportion constraints, HNN(G), was not used because this technique produced the least accurate estimation than the HNN(E) and HNN(A) in representing small land cover patches (Figure 4.12).

6.7.2. Time series MODIS images

A proportional image for each image in a time series MODIS image was derived using the fuzzy c-means soft classification technique. All the proportion images derived from the time series were fused using Equation 5.14. Experiments similar to the analyses of the HNN and pixel swapping in Section 6.7.1 were repeated using the fused image.

6.7.3. Notations

To simplify the explanation throughout this chapter, notation for each super-resolution mapping techniques were used as shown in Table 6.3.

Table 6-3 Notations for different super-resolution mapping techniques.

Super-resolution mapping technique	Description
PS(1)	Pixel swapping with 1 neighbour
PS(5)	Pixel swapping with 5 neighbours
HNN(E)	HNN with equal emphasis between the goal function constraint and the area proportion constraint
HNN(A)	HNN with emphasis on the area proportion constraint
HNN_2	A combination of HNN(E) and HNN(A)

6.8. Results and discussions

The 5 different techniques (Table 6.3) were used to map land cover for a single MODIS image and a fusion of time-series MODIS images. Figure 6.4 shows the classification of

the Landsat data that was used as ground data. The image shows binary land cover mapping classification showing land (white) and lakes (black). The image was used as a comparison benchmark against outputs of different land cover mapping techniques. Results of the land cover mapping were evaluated using visual assessment, site specific thematic accuracy assessment, landscape parameters, texture variables, characterization of the shape of the lakes, and positional accuracy.

6.8.1. Single MODIS image

Result of the hard classification on a MODIS image is shown in Figure 6.5. It provided a very blocky and unrealistic representation of the lakes and failed to represent many of the small lakes. Result of the soft classification is shown in Figure 6.6. The soft classification provided a richer representation but was also unable to provide a realistic representation of the actual distribution of the land and lakes.

Results of the two pixel swapping, PS(1) and PS(5) are shown in Figure 6.7a and 6.7b, respectively. The two pixel swapping outputs were appeared to be dominated by a speckled pattern, which existed in black and white colours. The presence of the speckled features may arise due to misclassification in the soft proportion image (Thornton et al., 2006). This error was suppressed using median filter (Pitas, 2000) with a 3×3 operator and the results are shown in Figure 6.8a and 6.8b. The 3×3 operator is the smallest operator for the filter, which can remove a considerable amount of small speckled features while leaving the large lakes mainly intact.
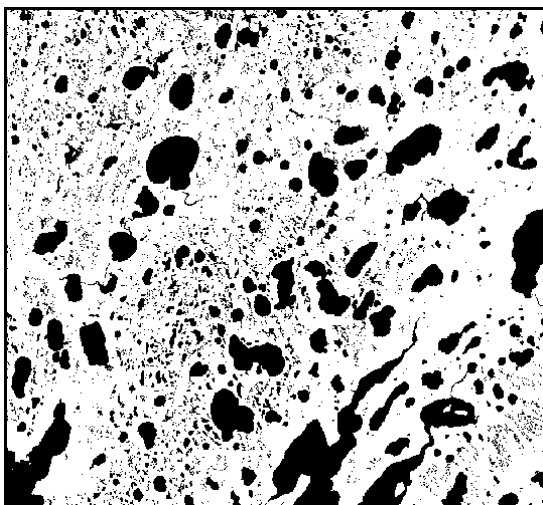
Figure 6-4 Ground data.
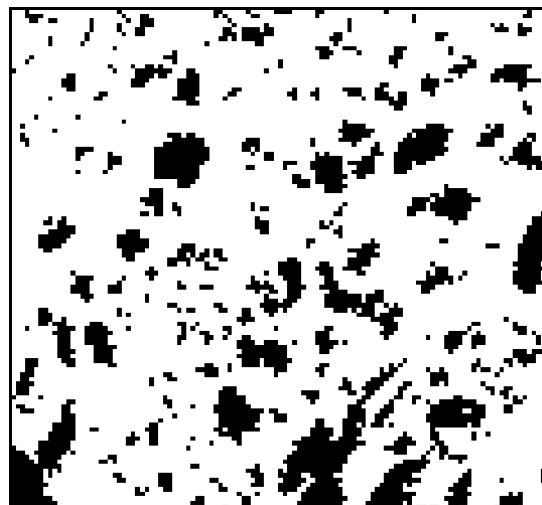
Figure 6-5 Hard classifier.
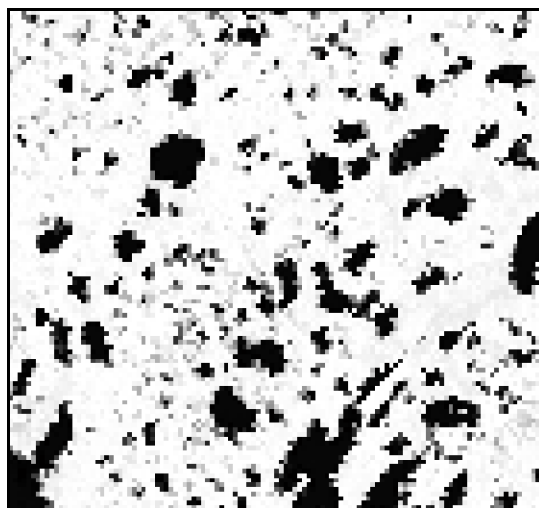
Figure 6-6 Proportional image derived from fuzzy c-means soft classification.

(a)   (b)
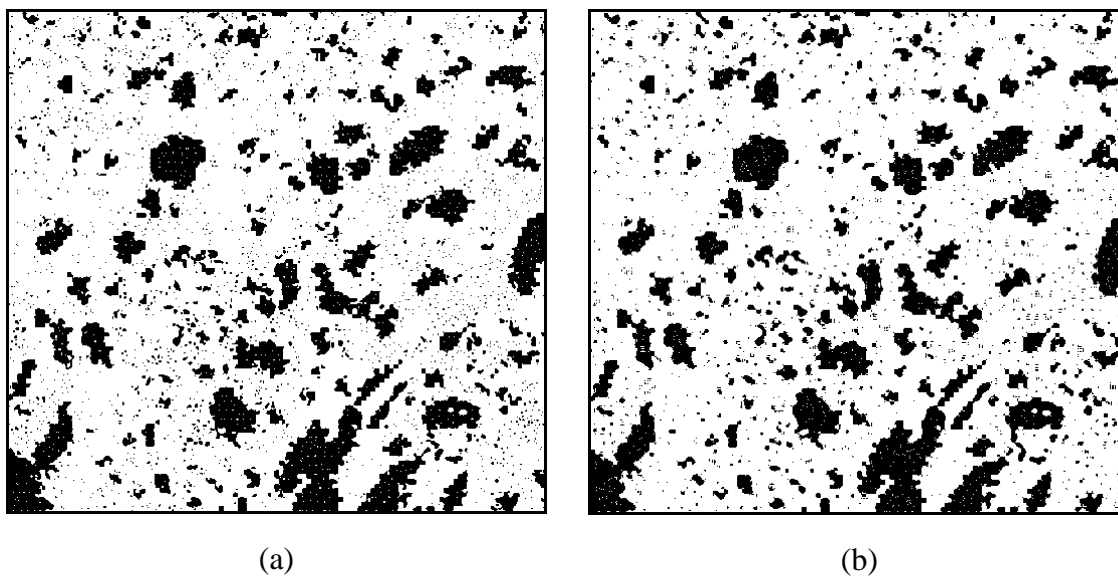
Figure 6-7 Application of a MODIS image into (a) PS(1) and (b) PS(5).

(a)   (b)
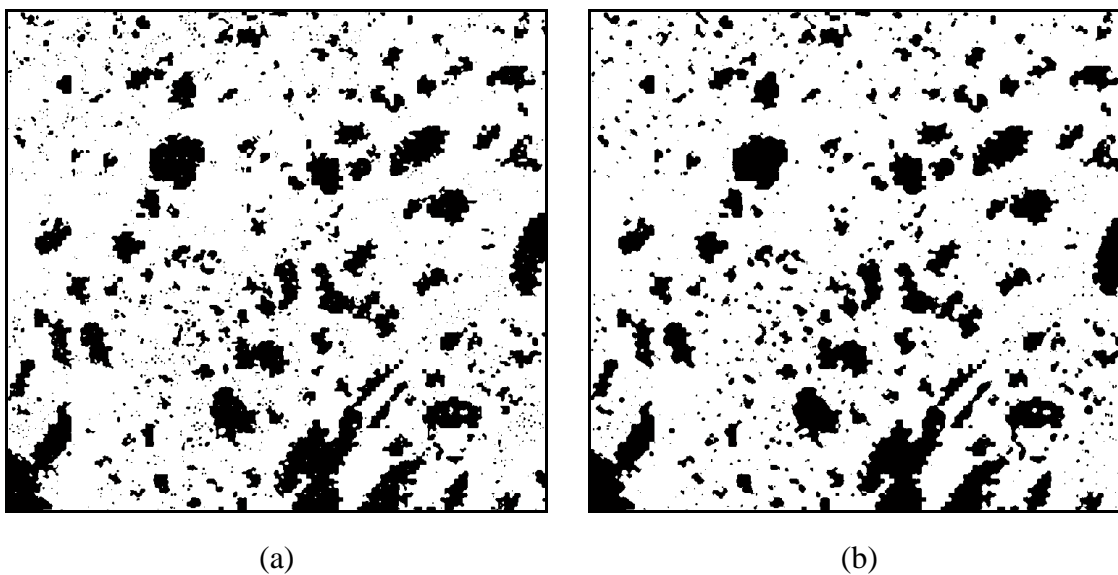
Figure 6-8 Application of a MODIS image into (a) PS(1) and (b) PS(5). Results of both techniques were filtered with a 3×3 median filter.

(a) (b)
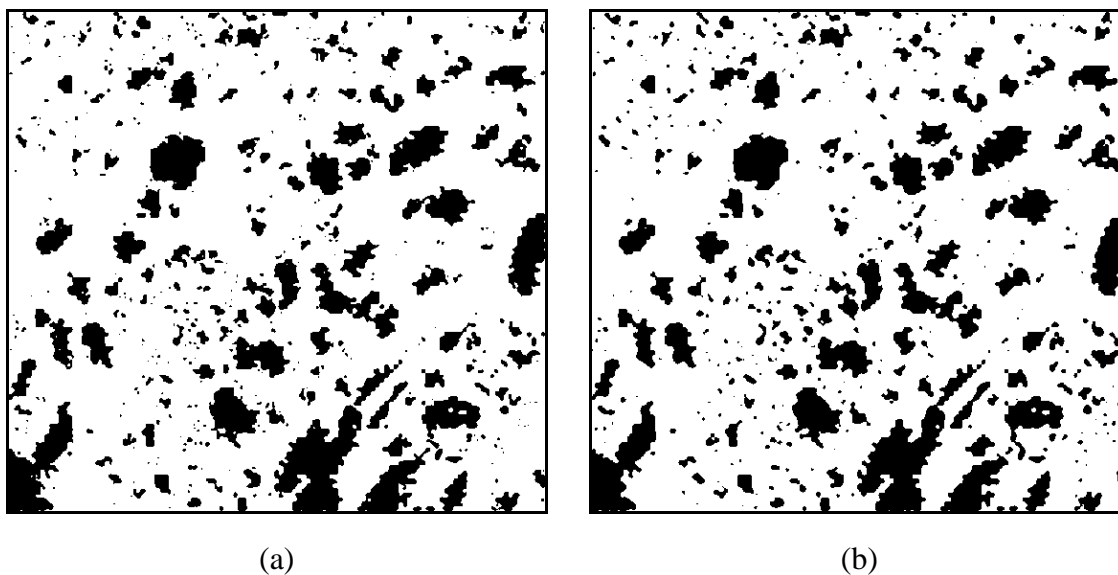
Figure 6-9 Application of a MODIS image into (a) PS(1) and (b) PS(5). Results of both techniques were filtered with a 5×5 median filter.

(a) (b)
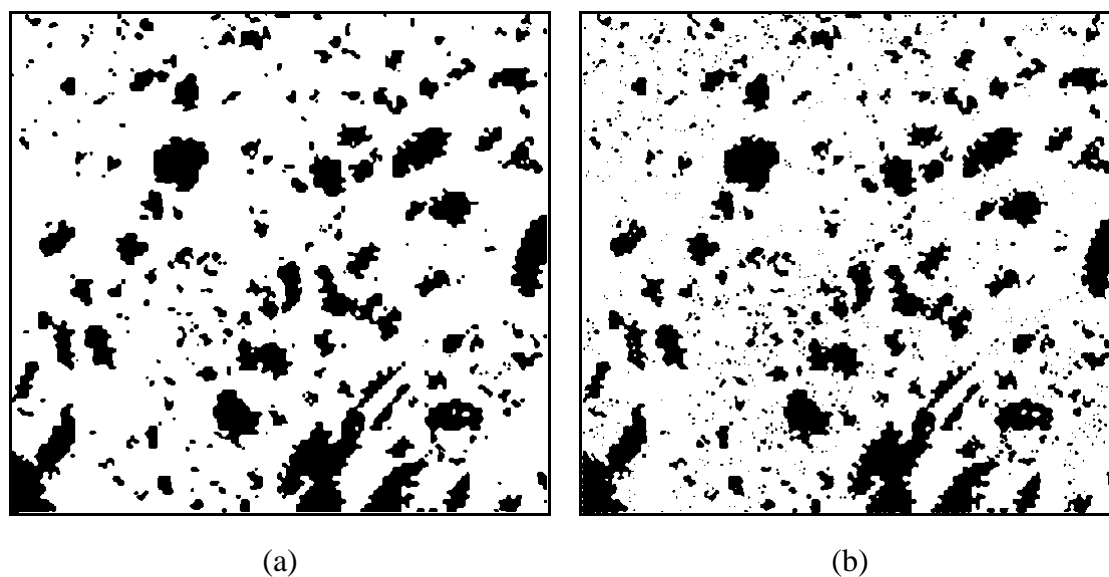
Figure 6-10 Application of a MODIS image into (a) HNN(E) and (b) HNN(A).
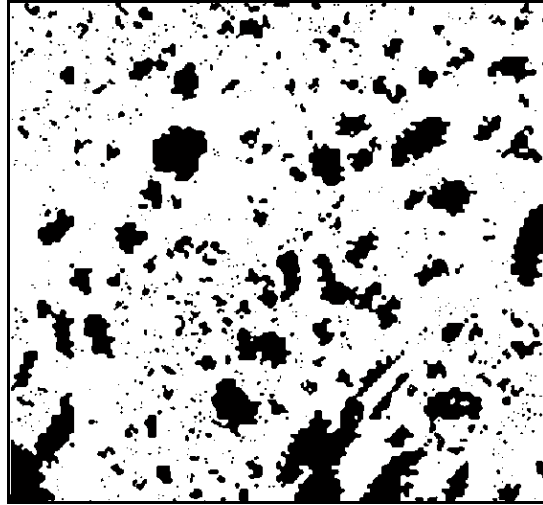
Figure 6-11 Application of a MODIS image into HNN$_2$ approach.

As the speckled features were still present, as can be seen in lakes in Figure 6.8a and 6.8b, a 5×5 operator was applied to the outputs of the pixel swapping as shown in Figure 6.9a and 6.9b. The implementation of the larger median filter operator removed the speckle features but a considerable number of small lakes were also eliminated. From the Figure 6.9a and 6.9b, the number of lakes is less than that of the number of lakes in the ground data. It also appeared that the boundary of lakes is irregular and serrated as compared to the boundary of lakes depicted in the ground data.

Results of the three HNN are presented in Figure 6.10 and Figure 6.11. It appears that the number of small lakes in the HNN(A) and the HNN$_2$ was higher than that of the HNN(E). Unlike the pixel swapping, the speckled pattern is not apparent in the images produced by the three HNNs. Therefore, pre-processing steps, such as median filtering, were unnecessary. The avoidance of the pre-processing steps was vital in order to ensure that small lakes remain intact and not to be misclassified as the speckled pattern and eliminated. Similar to the pixel swapping, the number of lakes

detected in all the HNN techniques is less that the number of lakes in the ground data, while the boundary of the lakes is also appeared to be irregular, serrated and not smooth.

6.8.1.1.   Site specific thematic accuracy assessment

The site specific thematic accuracy for each technique was assessed using all 816192 (872×936) sub-pixels in each image. A confusion matrix was generated for each classification technique and its accuracy was expressed by overall proportion correct, kappa coefficient, and per-class commission and omission errors. Results of the land cover mapping using different techniques are presented in confusion matrices in Table 6.4 until Table 6.13. In general, certain super-resolution mapping techniques produced slightly higher accuracy than the conventional hard classifier, but there were also certain techniques that produced less accurate results. Both the PS(1) and PS(5) that used a 5×5 median filter operator and the HNN(E) were of higher accuracy than the hard classifier. The PS(1) and PS(5) techniques that applied without the median filter and, the PS(1) and PS(5) that used a 3×3 median filter, HNN(A), and HNN_2 produced less accurate results than that of the hard classifier. Overall, the differences of the accuracy produced from various super-resolution mapping techniques were marginal to approximately less than 2%.

For the pixel swapping, when the number of the neighbour was set to 1, the overall accuracy was increased with the increment of the median filter operator. However, only when the size of the operator set to 5×5 (Table 6.7) did the pixel swapping produces accuracy higher than that of the hard classifier (0.29% more).

Similar trend was demonstrated when the number of the neighbour of the pixel swapping was set to 5. Only the pixel swapping with the median filter operator set to 5×5, the overall accuracy of the pixel swapping was higher than that of the hard classifier with 0.33% increment as presented in Table 6.10.

Detailed analyses on the implementation of the median filter can be observed in the commission errors of the lakes and the omission errors of the land in confusion matrices in Table 6.5 until Table 6.7 for the PS(1), and Table 6.8 until Table 6.10 for the PS(5). Here, the white speckled features may be misclassified as land and falsely located in the lakes. As the size of the median filter increased, a considerably amount of the white speckle features decreased, leading to the decreasing of the commission errors of the lakes, suggesting better representation of the lakes at the right locations.

The usage of the number of neighbour used in the pixel swapping demonstrated a marginal difference in the site specific accuracy between the PS(1) and the PS(5) with the PS(5) tended to be more accurate. The implementation of the median filter also may remove a considerably number of lakes, which may be misclassified as speckled features. This scenario is shown by a decreasing number of total sub-pixels that were estimated as lakes from Table 6.5 to 6.7 for the PS(1) and from Table 6.8 to 6.10 for the PS(5).

For the HNN techniques, only the HNN(E) produced higher accuracy than that of the hard classifier with 85.34% as presented in Table 6.11. The other two HNN techniques, however produced less accurate results compare to the accuracy of the hard classifier as presented in Table 6.12 for the HNN(A) and Table 6.13 for the HNN_2.

The commission error of the lakes for the HNN(E) (Table 6.11) was lower than the commission error of the lakes for the HNN(A) (Table 6.12) and the HNN_2 (Table 6.13) because in the HNN(E), a considerable number of lakes were not represented, especially small lakes. This scenario was confirmed by the lower number of total sub-pixels that were estimated as lakes in HNN(E) compared to the number of sub-pixels in the HNN(A) and the HNN_2.

Results from the confusion matrices also highlighted that, in general, all the techniques were not able to represent the lakes at all rather than to represent the lakes at the wrong locations. From all the confusion matrices (Table 6.4 to 6.13), the omission errors of the lakes were higher than the commission errors of the lakes. This scenario suggested that many lakes were not represented at all as they may be too small (~0.03 km^2); instead the location of these lakes was represented by land surface. This scenario was more apparent than the representation of the small lakes at the wrong locations. In addition, the uncertainty in term of the accuracy of the soft classification may affect this scenario.

Table 6-4 Confusion matrix for hard classifier applied on a MODIS image

Estimated Class	Reference Class			
	Water	Land	∑	**Error (C)**
Water	**124047**	40561	164608	24.64%
Land	82908	**568676**	651584	12.72%
∑	206955	609237	**816192**	
Error (O)	40.06%	6.66%		
Kappa = 0.5714		Overall accuracy = 84.87%		

Table 6-5 Confusion matrix for PS(1) without median filter applied on a MODIS image

Estimated Class	Reference Class			
	Lake	Land	∑	**Error (C)**
Lake	**122039**	47609	169648	28.06%
Land	84916	**561628**	646544	13.13%
∑	206955	609237	**816192**	
Error (O)	41.03%	7.81%		
Kappa = 0.5439		Overall accuracy = 83.76 %		

Table 6-6 Confusion matrix for PS(1) with a 3×3 median filter applied on a MODIS image

Estimated Class	Reference Class			
	Lake	Land	∑	**Error (C)**
Lake	**122699**	41623	164322	25.33 %
Land	84256	**567614**	651870	12.93 %
∑	206955	609237	**816192**	
Error (O)	40.71%	6.83 %		
Kappa = 0.5628		Overall accuracy = 84.56 %		

Table 6-7 Confusion matrix for PS(1) with a 5×5 median filter applied on a MODIS image

	Reference Class			
Estimated Class	Lake	Land	∑	**Error (C)**
Lake	**121971**	36138	158109	22.86 %
Land	84984	**573099**	658083	12.91 %
∑	206955	609237	**816192**	
Error (O)	41.06%	5.93 %		
Kappa = 0.5748		Overall accuracy = 85.16 %		

Table 6-8 Confusion matrix for PS(5) without median filter applied on a MODIS image

	Reference Class			
Estimated Class	Lake	Land	∑	**Error (C)**
Lake	**123350**	46292	169642	27.29 %
Land	83605	**562945**	646550	12.93 %
∑	206955	609237	**816192**	
Error (O)	40.40 %	7.60 %		
Kappa = 0.5530		Overall accuracy = 84.09 %		

Table 6-9 Confusion matrix for PS(5) with a 3×3 median filter applied on a MODIS image

	Reference Class			
Estimated Class	Lake	Land	∑	**Error (C)**
Lake	**124131**	41166	165297	24.90 %
Land	82824	**568071**	650895	12.72 %
∑	206955	609237	**816192**	
Error (O)	40.02 %	6.76 %		
Kappa = 0.5701		Overall accuracy = 84.81 %		

Table 6-10 Confusion matrix for PS(5) with a 5×5 median filter applied on a MODIS image

| | Reference Class | | | |
Estimated Class	Lake	Land	∑	Error (C)
Lake	**123437**	37301	160738	23.21 %
Land	83518	**571936**	655454	12.74 %
∑	206955	609237	**816192**	
Error (O)	40.36 %	6.12 %		
Kappa = 0.5778		Overall accuracy = 85.20 %		

Table 6-11 Confusion matrix for HNN(E) applied on a MODIS image

| | Reference Class | | | |
Estimated Class	Lake	Land	∑	Error (C)
Lake	**121423**	34123	155546	21.94 %
Land	85532	**575114**	660646	12.95 %
∑	206955	609237	**816192**	
Error (O)	41.33 %	5.60 %		
Kappa = 0.5781		Overall accuracy = 85.34%		

Table 6-12 Confusion matrix for HNN(A) applied on a MODIS image

| | Reference Class | | | |
Estimated Class	Lake	Land	∑	Error (C)
Lake	**123795**	42045	165840	25.35 %
Land	83160	**567192**	650352	12.77 %
∑	206955	609237	**816192**	
Error (O)	40.18 %	6.90 %		
Kappa = 0.5663		Overall accuracy = 84.66%		

Table 6-13 Confusion matrix for HNN_2 applied on a MODIS image

Estimated Class	Reference Class			
	Lake	Land	Σ	Error (C)
Lake	**124695**	42121	166816	25.25 %
Land	82260	**567116**	649376	12.67 %
Σ	206955	609237	**816192**	
Error (O)	39.75 %	6.92 %		
Kappa = 0.5699		Overall accuracy = 84.76 %		

6.8.2. Time series MODIS images

A proportional image derived from a fusion of a time series MODIS images is shown in Figure 6.12. Results of the two pixel swapping, PS(1) and PS(5) are shown in Figure 6.13a and 6.13b, respectively. Similar to the case of using a single MODIS image, the implementation of the pixel swapping produced the speckled pattern which arises due to mis-classification in the soft proportion images (Thornton et al., 2006). With a 5×5 median filter, both images in Figure 6.13a and 6.13b were filtered and the results are shown in Figure 6.14a and 6.14b, respectively. Visual comparison on the two filtered images shows that the lake boundaries in PS(1) are irregular, serrated and not as smooth as the lake boundaries in the PS(5).

Results of the three HNN techniques are shown in Figure 6.15 and Figure 6.16. Similar to the case of a single MODIS image, the number of small lakes in the HNN(E) is less than that of the HNN(A) and the HNN_2. However, the application of the time series MODIS images produced different results than by using a single MODIS image. For the time-series MODIS images, the lake boundaries in the HNN(E) tended to be

smoother and less irregular when compared to the lake boundaries in the HNN(A). This trend is not apparent in the single MODIS image case in which both the HNN(E) and the HNN(A) produced irregular lake boundaries. The advantage of the HNN(E) in retaining the smoothness of lake boundaries and the advantage of the HNN(A) in representing small lakes were exploited by combining the these two techniques in the proposed HNN_2 technique as shown in Figure 6.16.

The number of lakes represented by all the super-resolution mapping techniques from either the single MODIS image or the fusion of the MODIS images appears to be less than the number of lakes in the ground data. Although some techniques, such as PS(1) , HNN(A) , and HNN_2 were suitable to represent small lakes, the number of lakes in those images were far less than that in the ground data. In addition, the complexity of the spatial distribution of the lakes in the results of super-resolution mapping techniques was less than that in the ground data. These scenarios may be because the coherence between the MODIS images and the Landsat image, which was used as a ground data, was not perfect. Therefore, there were tendency of mismatch between the results derived from the MODIS images and the ground data.
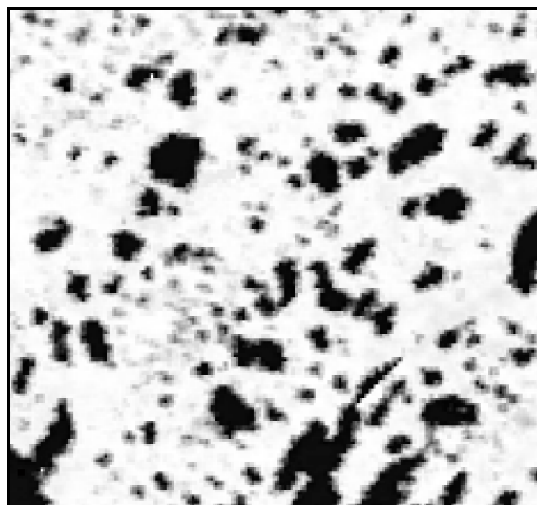
Figure 6-12 Proportional image derived from a fusion of proportional images of a MODIS time series.
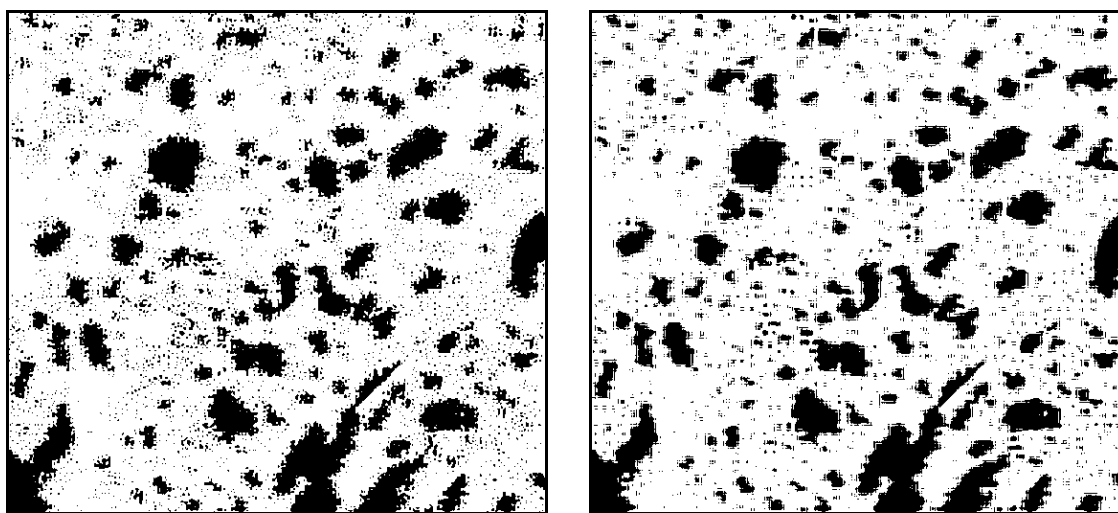
(a)　　　　　　　　　　　　　　(b)

Figure 6-13 Application of a fused time series MODIS images into (a) PS(1) and (b) PS(5).
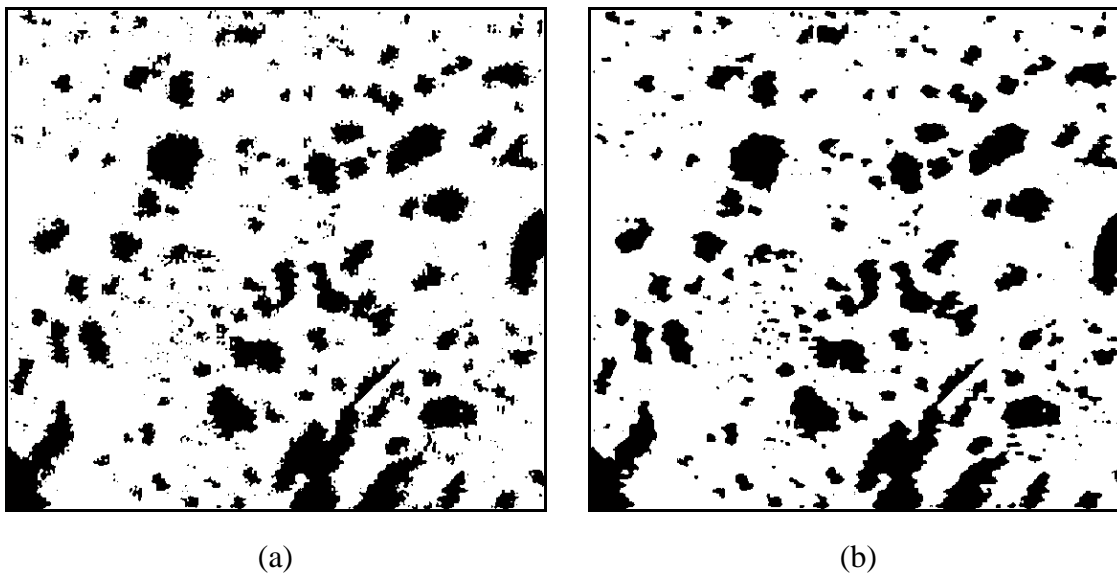
Figure 6-14 Application of a fused time series MODIS images into (a) PS(1) and (b) PS(5). Results of both techniques were filtered with a 5×5 median filter.
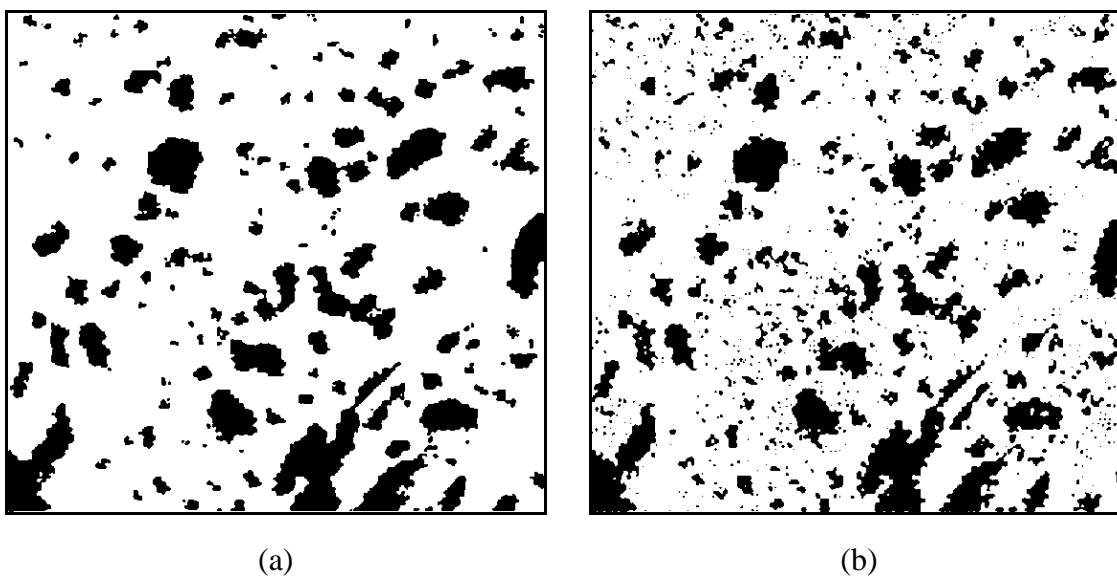
**Figure 6-15** Application of a fused time series MODIS images into (a) HNN(E) and (b) HNN(A).
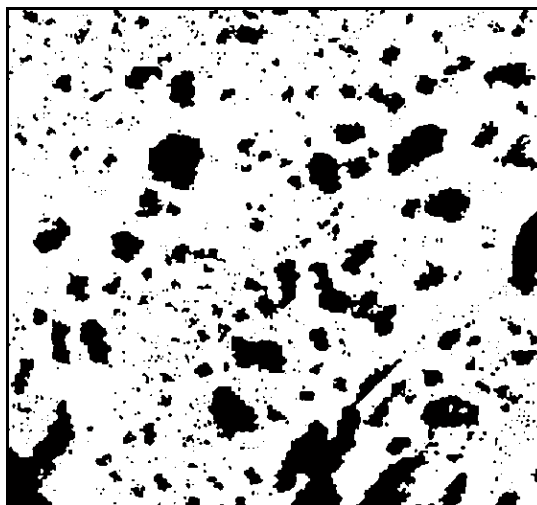
Figure 6-16 Application of a fused time series MODIS images into HNN_2 approach.

6.8.2.1.   Site specific thematic accuracy assessment

The site specific thematic accuracy for each technique on a fusion of time series MODIS images was assessed using all 816192 (872×936) sub-pixels in each image. A confusion matrix was generated for each classification technique and its accuracy was expressed by overall proportion correct, kappa coefficient, and per-class commission and omission errors. The results are presented in confusion matrices in Table 6.14 until Table 6.18. All the super-resolution mapping techniques produced more accurate results than the conventional hard classifier.

For the pixel swapping technique, only results that were filtered with the 5×5 median filter operator were assessed in confusion matrices in Table 6.14 and 6.15. The difference of the overall accuracy between the two pixel swapping techniques was marginal with the accuracy of the PS(1) was 86.66 % and PS(5) was 86.95 %.

Table 6-14 Confusion matrix for PS(1) with a 5×5 median filter applied on a fused time series MODIS images

	Reference Class			
Estimated Class	Lake	Land	∑	**Error (C)**
Lake	**128625**	30554	159179	19.20 %
Land	78330	**578683**	657013	11.92 %
∑	206955	609237	**816192**	
Error (O)	37.85 %	5.02 %		
Kappa = 0.6185			Overall accuracy = 86.66 %	

Table 6-15 Confusion matrix for PS(5) with a 5×5 median filter applied on a fused time series MODIS images

	Reference Class			
Estimated Class	Lake	Land	∑	**Error (C)**
Lake	**130672**	30223	160895	18.78 %
Land	76283	**579014**	655297	11.64 %
∑	206955	609237	**816192**	
Error (O)	36.86 %	4.961 %		
Kappa = 0.6279			Overall accuracy = 86.95 %	

Table 6-16 Confusion matrix for HNN(E) applied on a fused time series MODIS images

	Reference Class			
Estimated Class	Lake	Land	∑	**Error (C)**
Lake	**126887**	25280	152167	16.61 %
Land	80068	**583957**	664025	12.06 %
∑	206955	609237	**816192**	
Error (O)	38.69 %	4.15 %		
Kappa = 0.6264			Overall accuracy = 87.09 %	

Table 6-17 Confusion matrix for HNN(A) applied on a fused time series MODIS images

Estimated Class	Reference Class			
	Lake	Land	$\sum$	**Error (C)**
Lake	**124722**	41255	165977	24.86 %
Land	82233	**567982**	650215	12.65 %
$\sum$	206955	609237	**816192**	
Error (O)	39.76 %	6.77 %		
Kappa = 0.6264		Overall accuracy = 87.09 %		

Table 6-18 Confusion matrix for HNN_2 applied on a fused time series MODIS images

Estimated Class	Reference Class			
	Lake	Land	$\sum$	**Error (C)**
Lake	**133075**	37549	170624	22.07 %
Land	73880	**571688**	645568	11.44 %
$\sum$	206955	609237	**816192**	
Error (O)	35.70 %	6.16 %		
Kappa = 0.6172		Overall accuracy = 86.35 %		

For the HNN technique, the accuracy produced by the HNN(E) and the HNN(A) were equal and they were slightly more accurate than the pixel swapping techniques. Although the overall accuracy produced by the HNN_2 was the least, the omission error for the lakes representation with this technique was the lowest among all the super-resolution mapping techniques. This trend suggested that the HNN_2 was more accurate than the other techniques in representing small lakes. Mis-location of those lakes may contribute to the higher commission error of the lake when compared with commission errors of other techniques. Moreover, the total number of sub-pixels that was estimated

as lakes in Table 6.18 was higher compared to the total number of those sub-pixels in Table 6.14 until 6.17.

Results from all the confusion matrices in this section also demonstrated higher overall accuracy compared with the overall accuracy from confusion matrices in Section 6.8.1.1. These results suggested that by fusing a time series MODIS images, the overall accuracy of site specific assessment could be increased compared when using only a single MODIS image regardless of super-resolution mapping techniques being used.

6.8.3. Texture variables

Analyses on the landscape parameters considered the results of different super-resolution mapping techniques on a single MODIS image and a fused time series MODIS images. Table 6.19 provides comparison of several texture variables. Values of the texture measures such as homogeneity, contrast, inverse difference moment (IDM), and entropy were derived from the gray-level co-occurrence matrix (GLCM). At the 0°, 45°, 90°, and 135° degrees, the values of each of the texture variables were derived. The average value from those angles of each texture measure was presented in Table 6.19. Numbers in the brackets indicate the difference of the texture variables with the ground data. Positive values indicate overestimation, while negative values indicate underestimation. The measurements of the texture variables at 0°, 45°, 90°, and 135° degrees are shown in Figure 6.17 until Figure 6.20.

From analyses on both the single MODIS image and the fused time series MODIS images, results produced by the HNN_2 provide the least difference error for estimating the percentage of the water when compared to the other techniques. The differences of the percentage of water were -4.92% for the single MODIS image and the differences of the percentage of water were -4.46% for the fused time series MODIS images.

On landscape parameter assessment, the HNN(A) applied on a single MODIS image was more accurate than the other techniques in estimating the number of lakes and the average area of the lakes. However, the HNN_2 technique applied on a single MODIS image was more accurate than the other techniques in estimating the average perimeter of lakes.

Assessment on the homogeneity measurement demonstrated that the difference percentage of all the techniques ranges from 15.29 % to 21.89 %. The proposed HNN_2 applied on a fused image produced the least error while the HNN(E) on a fused image produced the largest error. Assessment on the homogeneity illustrated that the homogeneity differences between the HNN_2 on the single MODIS image was 0.0896, while on the time series MODIS images was 0.0853. Figure 6.17 shows that at 0°, 45°, 90°, and 135° degrees, homogeneity results produced by the HNN_2 using the fused time series MODIS images were closer to the homogeneity of the ground data than that of the other techniques. This situation occurred because a considerable amount of small lakes are apparent in the output images derived from the proposed technique. The presence of the small lakes in the output images tended to decrease the homogeneity values. In contrast, the homogeneity of the HNN(E) using both the single MODIS image and the

fused time-series MODIS images tended to be high because of the decreasing amount of small lakes in those images. The homogeneity measurements for all the techniques demonstrated that at the angle 0° and 90°, the measurements were slightly higher that the measurement at the 45° and 135°.

Assessment on the contrast measurement demonstrated that the difference percentage of all the techniques ranges from 57.89 % to 75.58 %. The use of the HNN(A) on a fused image produced the least error while the HNN(E) on a fused image produced the largest error. All the techniques produced lower contrast measurement than that of the ground data because they contain relatively large lakes compare to the lakes in the ground data. Because many of the small lakes in the images produced by all the techniques were missing, the difference between neighbouring pairs of the GLCM becomes small, leading to the decreasing of the contrast measurement. The HNN(A) tended to produce higher contrast measurement than that of the other techniques because more small lakes were presented. Although the HNN_2 also presented a considerable amount of small lakes, the boundary of the lakes appeared to be less irregular when compare with the boundary of the lakes in the HNN(A) images. This factor may be contributed to the slightly higher contrast measurement in the HNN(A) images than the measurement in the HNN_2 images. Figure 6.18 shows that the contrast measurements at 0°, 45°, 90°, and 135° degrees. For all the techniques, the contrast measurements at the angle 45° and 135° were slightly higher than the measurements at the 0° and 90°.

Table 6-19 Comparison of landscape parameters and texture variables from various super-resolution mapping techniques. Results shown in bold indicate that the prediction is the closest to the ground data.

Parameter	GD	Single image						Fused image				
		HC	PS (1)	PS (5)	HNN (E)	HNN (A)	HNN$_2$	PS (1)	PS (5)	HNN (E)	HNN (A)	HNN$_2$
Percent water	25.36	20.17	19.37	19.69	19.06	20.32	20.44	19.50	19.71	18.64	20.34	**20.90**
		(-5.19)	(-5.99)	(-5.67)	(-6.30)	(-5.04)	(-4.92)	(-5.86)	(-5.65)	(-6.72)	(-5.02)	**(-4.46)**
Number of lakes	5016	183	484	428	273	**966**	941	566	350	164	899	879
		(-4833)	(-4532)	(-4588)	(-4743)	**(-4050)**	(-4075)	(-4450)	(-4666)	(-4852)	(-4117)	(-4137)
Average lake area (km2)	0.0371	0.8095	0.2940	0.3380	0.5128	**0.1545**	0.1596	0.2531	0.4137	0.8351	0.1662	0.1747
		(0.7724)	(0.2569)	(0.3009)	(0.4757)	**(0.1174)**	(0.1225)	(0.2160)	(0.3766)	(0.798)	(0.1291)	(0.1376)
Average lake perimeter (m)	235.63	2583.10	1209.8	1339.90	1656.70	630.34	**576.48**	1130.70	1541.40	2608.00	711.41	616.74
		(2347.50)	(974.17)	(1104.30)	(1421.10)	(394.71)	**(340.85)**	(895.07)	(1305.80)	(2372.4)	(475.78)	(381.11)
Homogeneity	0.5578	0.6559	0.6644	0.6610	0.6712	0.6482	0.6474	0.6620	0.6633	0.6799	0.6479	**0.6431**
		(0.0981)	(0.1066)	(0.1032)	(0.1134)	(0.0904)	(0.0896)	(0.1042)	(0.1055)	(0.1221)	(0.0901)	**(0.0853)**
Contrast	0.0684	0.0226	0.0237	0.0231	0.0203	0.0287	0.0278	0.0245	0.0205	0.0167	**0.0288**	0.0266
		(-0.0458)	(-0.0447)	(-0.0453)	(-0.0481)	(-0.0397)	(-0.0406)	(-0.0439)	(-0.0479)	(-0.0517)	**(-0.0396)**	(-0.0418)
IDM	0.9658	0.9887	0.9881	0.9884	0.9898	0.9857	0.9861	0.9877	0.9898	0.9916	**0.9856**	0.9867
		(0.0229)	(0.0223)	(0.0226)	(0.0240)	(0.0199)	(0.0203)	(0.0219)	(0.0240)	(0.0258)	**(0.0198)**	(0.0209)
Entropy	1.1608	0.8722	0.8624	0.8662	0.8388	0.9062	0.9048	0.8692	0.8529	0.8106	0.9072	**0.9083**
		(-0.2886)	(-0.2984)	(-0.2946)	(-0.3220)	(-0.2546)	(-0.2560)	(-0.2916)	(-0.3079)	(-0.3502)	(-0.2536)	**(-0.2525)**

HC = hard classifier; GD = ground data
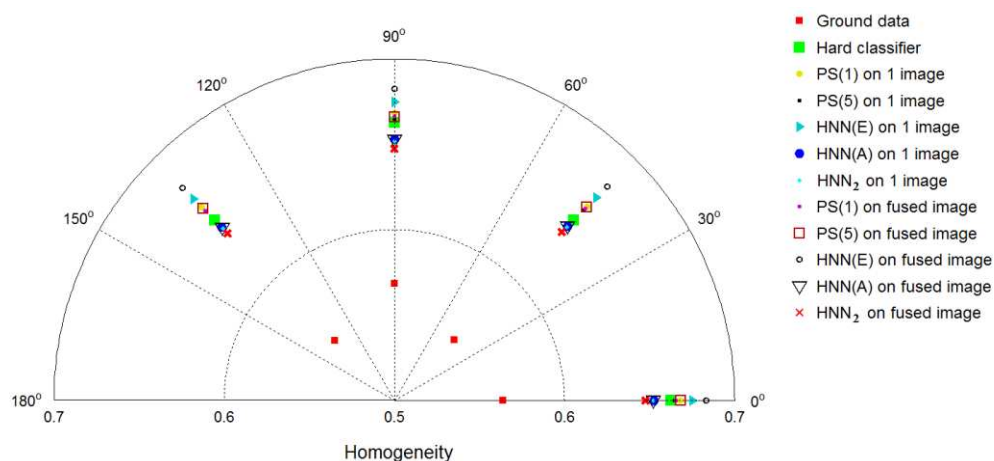
Figure 6-17 Texture values for different land cover mapping techniques as a function of angle for homogeneity. Low homogeneity indicates high number of small lakes presented in an image, such as image in the ground data.
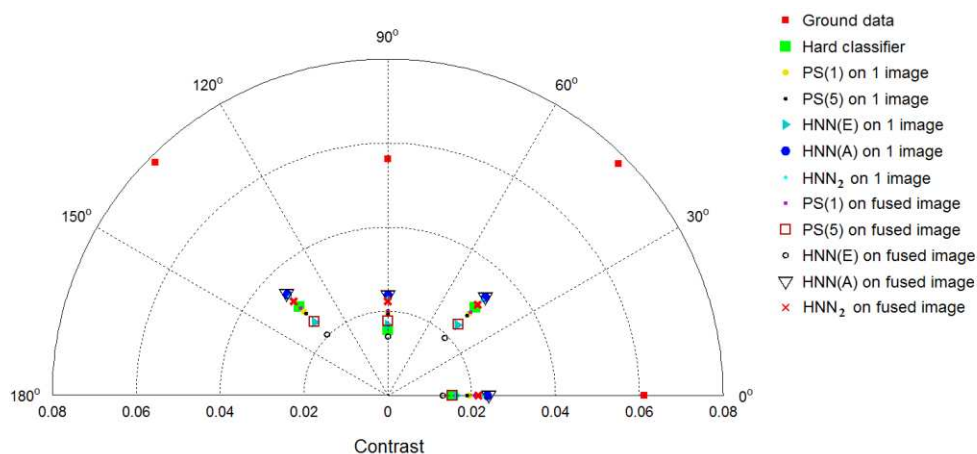
Figure 6-18 Texture values for different land cover mapping techniques as a function of angle for contrast. High contrast indicates high number of small lakes presented in an image, such as image in the ground data.
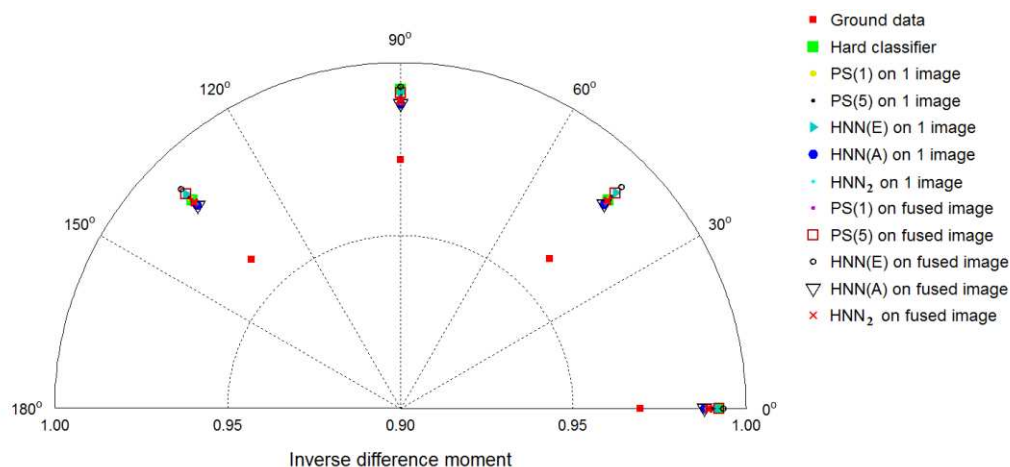
Figure 6-19 Texture values for different land cover mapping techniques as a function of angle for inverse difference moment (IDM). High IDM indicates that more large lakes are presented in an image than small lakes. The high number of small lakes in the ground data decreases the IDM value as in the ground data.
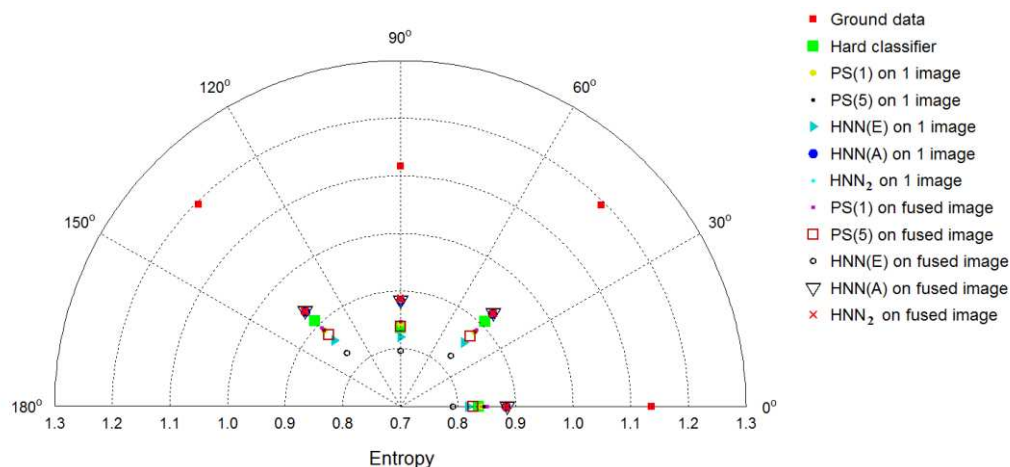
Figure 6-20 Texture values for different land cover mapping techniques as a function of angle for entropy. High entropy indicates that the complexity of the spatial distribution of lakes is high in an image, such as image in the ground data.

Assessment on the IDM measurement demonstrated that the difference percentage of all the techniques ranges from 2.05 % to 2.67 %. The HNN(A) on a fused image produced the least error while the HNN(E) on a fused image produced the largest error. All the techniques produced higher IDM measurement than that of the ground data because they contain relatively large lakes compared to the lakes in the ground data. The presence of the large lakes in the images tended to generate high values on the main diagonal of the GLCM, leading to the increasing of the IDM measurement. The HNN(A) on a fused image produced the least error because of its ability to represent small lakes compared to the limitation of the HNN(E) that to tended to miss those lakes. Figure 6.19 shows that the IDM measurements at 0°, 45°, 90°, and 135° degrees. It appeared that angle did not have significant effect on the value of the IDM measurements for all the techniques.

Assessment on the entropy measurement demonstrated that the difference percentage of all the techniques ranges from 21.75 % to 30.17 %. All the techniques produced lower entropy measurement than that of the ground data because the complexity of the spatial distribution of lakes they presented was less than the complexity of the spatial distribution of lakes in the ground data. The proposed HNN_2 on a fused image produced the least error while the HNN(E) on a fused image produced the largest error. Figure 6.20 shows that the entropy measurements at 0°, 45°, 90°, and 135° degrees. For all the techniques, the entropy measurements at the angle 45° and 135° were slightly higher than the measurements at the 0° and 90°.

6.8.4. Characterization of the shape of lakes

The shape of the lakes was characterized using standard measures: area, perimeter and compactness. The compactness is a ratio of the area and the perimeter (Equation 2.5). Here the lakes were treated as objects. Figure 6.21 shows 30 lakes of varying sizes and shapes were selected and annotated from the ground data. Corresponding lakes in the images of land cover mapping derived from different techniques were compared with the ground data. Table 6.20 summarized the comparison for area. Table 6.21 summarized the comparison for perimeter, and Table 6.22 summarized the comparison for compactness.

As the HNN_2 technique was a combination of the HNN(E) and HNN(A), several results of the HNN_2 technique in the Table 6.20 until 6.22 may identical or close to the results of the HNN(E) and HNN(A). The HNN(A) technique was used to represent lakes $\leq 0.0625km^2$, which is a size of an area of a MODIS 250 m pixel, while the HNN(E) was used for lakes $> 0.0625km^2$. Since the 30 selected lakes were bigger than the size of the MODIS pixel, most of the results of the HNN_2 were identical or close to the results of the HNN(E).

Overall, the proposed HNN_2 applied on the fused MODIS time series images produced the lowest error for the area measurement with the average error was 0.1290 km^2, while the PS(5) applied on a single MODIS image produced the highest error with 0.2009 km^2. By using the fused image, all the techniques demonstrated decreasing in the error for the area measurement of the lakes.
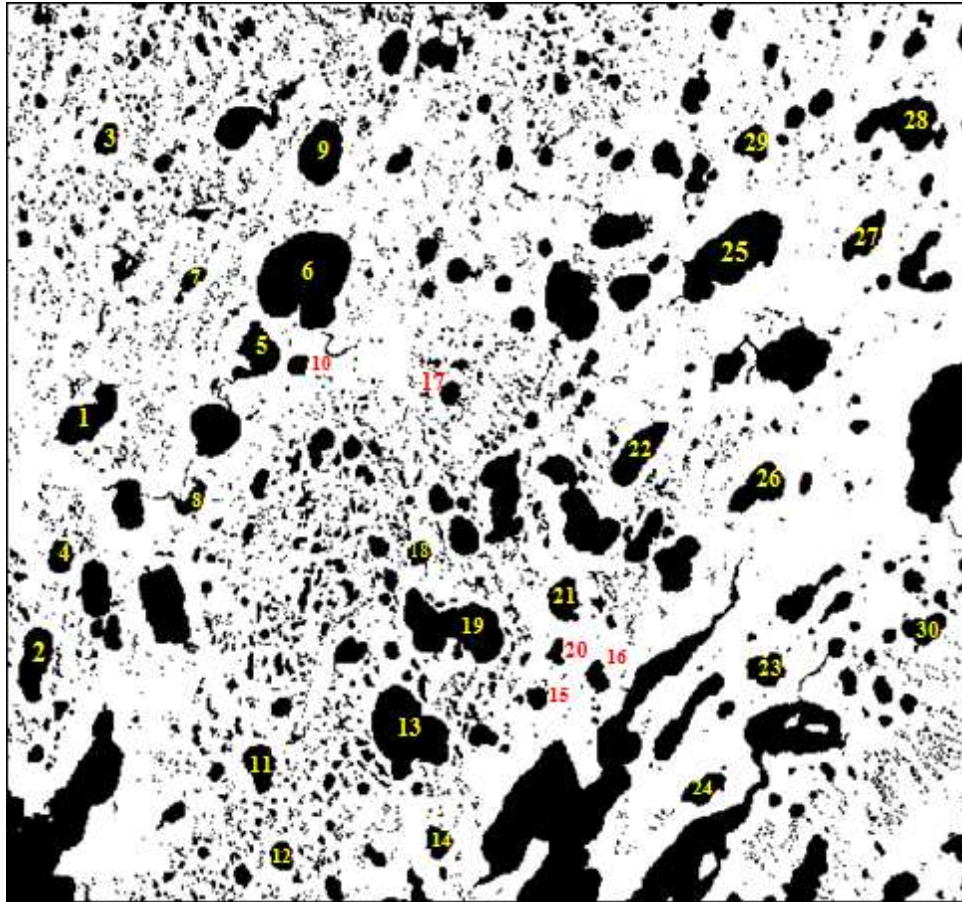
Figure 6-21 Selected lakes used for object based analysis.

For small lakes, such as lakes 10, 15, 17, and 20, in which the size of the lakes are ~0.3 km^2 , the HNN$_2$ applied on the fused image produced the lowest error on the area measurement with the average error was 0.0379 km^2. Other technique that produced the second lowest error was the HNN(E) technique that was applied on the fused image with the average error was 0.0641 km^2. The hard classification technique produced the highest error with the average error was 0.1025 km^2.

For big lakes, such as lakes 6, 13, 19, 25, and 28, in which the size of the lakes are > 2.6 km^2, the HNN(E) applied on the fused image produced the lowest error on the

area measurement with the average error was 0.3319 km^2. The HNN$_2$ that was applied on the fused image produced an average error of 0.3417 km^2. The hard classification technique produced the highest error with the average error was 0.4327 km^2.

For the perimeter measurement, the PS(5) applied on the fused image produce the lowest error with 0.6732 m, while the HNN$_2$ applied on the fused image produced 0.7218 m error. The HNN(A) that was applied on a fused image produced the highest error with 1.4164 m. For both cases of the single MODIS image and the fused image, the HNN(A) tended to produce high error because the representation of the boundary of the lakes appear to be irregular, serrated and not smooth.

For the small lakes (lakes 10, 15, 17, and 20), the HNN$_2$ applied on the fused image produced the lowest error on the perimeter measurement with the average error was 0.1127 m. Other technique that produced the second lowest error was the HNN(E) technique that was applied on the fused image with the average error was 0.3230 m. The HNN(A) technique that was applied on the fused image produced the highest error with the average error was 0.7020 m.

For the big lakes (lakes 6, 13, 19, 25, and 28), the PS(5) applied on the fused image produced the lowest error on the perimeter measurement with the average error was 0.9782 m, while the HNN$_2$ applied on the fused image produced 1.5248 m error. The PS(1) technique that was applied on the fused image produced the highest error with the average error was 2.3963 m.

Table 6-20 Comparison of area, (km^2). Bold and underlined results indicate predictions closest to the ground data.

Lake	GD	Single image						Fused Image				
		HC	PS (1)	PS (5)	HNN (E)	HNN (A)	HNN$_2$	PS (1)	PS (5)	HNN (E)	HNN (A)	HNN$_2$
1	1.8440	**1.9018**	1.9627	1.9488	1.9663	1.9468	1.9663	2.0336	2.0705	2.0117	1.9607	2.0117
2	1.5986	1.3833	1.3726	1.3807	1.3653	1.3889	1.3653	1.3010	1.3115	1.2464	**1.3917**	1.2464
3	0.5352	**0.5762**	0.5919	0.5966	0.5930	0.6056	0.5930	0.6658	0.6776	0.6370	0.6056	0.6370
4	0.5774	**0.5762**	0.5996	2.4824	2.4943	2.4840	2.4943	0.5556	0.5726	0.5416	2.4831	0.5416
5	1.4457	1.0947	1.1269	1.1440	1.1376	1.1430	1.1376	1.4564	1.5011	1.4177	1.1424	**1.4365**
6	5.9101	6.0493	6.0531	6.0720	**6.0465**	6.0913	6.0465	6.3018	6.3529	6.2614	6.0629	6.2614
7	0.4299	0.4610	0.4201	0.4307	0.4223	0.4429	0.4223	0.3314	0.3410	0.3122	**0.4292**	0.3122
8	0.5914	0.4033	0.3736	0.4437	0.3738	0.4524	0.3738	**0.5744**	0.5718	0.5466	0.4499	0.5466
9	1.9056	1.9015	1.9160	**1.9061**	1.9116	1.9119	1.9116	2.0124	2.0780	2.0633	1.9151	2.0725
10	0.3129	0.2306	0.2491	0.2594	0.2474	0.2607	0.2708	0.2628	**0.2800**	0.2577	0.2579	0.3480
11	0.9788	0.6338	0.6040	0.6477	0.6111	0.6154	0.6111	0.6767	**0.6922**	0.6558	0.6141	0.6558
12	0.4754	0.6337	0.6586	0.6621	0.6416	0.6665	0.6416	0.5429	0.5482	0.5145	0.6685	**0.5145**
13	4.0832	4.6676	4.6482	4.6379	4.5882	4.5872	4.6113	4.7279	4.7588	4.6449	**4.5745**	4.6692
14	0.5535	0.6918	0.5453	0.5712	**0.5505**	0.5621	0.5505	0.5400	0.5376	0.5212	0.5841	0.5212
15	0.3260	0.4611	0.2350	0.3765	**0.3485**	0.3544	0.3958	0.3592	0.3842	0.3717	0.3660	0.3717
16	0.4480	**0.4612**	0.4710	0.4851	0.4627	0.4968	0.4627	0.4309	0.4295	0.4218	0.4979	0.4218
17	0.3407	0.5186	0.4691	0.4723	0.4751	0.4860	0.4751	0.4199	0.4441	**0.3984**	0.4847	**0.3984**
18	0.4236	0.5189	0.3656	0.4065	0.3731	0.3377	0.3887	0.4068	**0.4218**	0.4066	0.4055	0.4066
19	3.9584	3.6880	3.7010	3.7262	3.7403	3.7203	3.7673	4.0006	4.0160	**3.9615**	3.7399	3.9858
20	0.2738	0.2883	0.1555	0.2000	0.2043	0.2067	0.2160	0.1716	0.1908	0.1758	0.2070	**0.2606**
21	0.9444	1.0375	0.9702	0.9713	0.9752	0.9713	0.9752	0.9794	1.0101	**0.9677**	0.9730	**0.9677**
22	1.6112	1.8445	1.7565	1.7580	1.7208	1.7664	**1.7208**	1.8334	1.8818	1.8785	1.7667	1.8785
23	0.8553	0.6916	0.6764	0.6794	0.7419	0.7543	0.7419	0.7653	0.7722	**0.7731**	0.7536	**0.7731**
24	0.7880	0.9800	0.9042	0.9154	0.9189	0.9125	0.9189	0.8955	0.8892	**0.8649**	0.9118	**0.8649**
25	4.3698	4.8981	4.6351	**4.6338**	4.6682	4.6479	4.6682	4.8198	4.7982	4.8058	4.6536	4.8058
26	1.4145	1.4410	1.3761	1.3494	1.3563	1.3646	1.3563	**1.4117**	1.4754	1.3782	1.3687	1.4067
27	1.0543	0.9797	0.9996	1.0035	1.0673	1.0169	1.0735	1.0814	1.1102	**1.0504**	1.0095	1.0824
28	2.6006	1.9594	2.0331	2.0476	2.0328	2.0559	2.0328	2.2671	**2.3279**	2.2930	2.0773	2.2930
29	0.7855	0.7492	**0.7853**	0.7906	0.7871	0.8051	0.7871	0.8743	0.8710	0.8558	0.7971	0.8558
30	0.8674	0.9223	0.8406	0.8428	0.8398	0.8513	0.8398	0.8504	**0.8710**	0.8484	0.8484	0.8484
Average error		0.1696	0.1471	0.2009	0.1992	0.2006	0.1991	0.1336	0.1425	0.1313	0.1973	0.1290

Table 6-21 Comparison of Perimeter, (m). Bold and underlined results indicate predictions closest to the ground data.

Lake	GD	Single image						Fused image				
		HC	PS (1)	PS (5)	HNN (E)	HNN (A)	HNN₂	PS (1)	PS (5)	HNN (E)	HNN (A)	HNN₂
1	7.8765	7.7546	7.7544	7.1523	6.4623	**7.8290**	6.4623	9.8196	7.7493	6.9362	8.4560	6.9362
2	6.1207	7.7173	7.2277	6.9898	6.5801	7.3301	6.5801	7.3344	6.6440	**6.0110**	7.2196	**6.0110**
3	3.0076	3.3849	3.1028	3.1452	**3.0179**	3.2507	**3.0179**	3.9325	3.7071	3.3874	3.2507	3.3874
4	3.0574	3.3600	3.1752	11.171	10.6710	13.634	10.6710	3.2922	**3.0801**	2.7728	13.5764	2.7728
5	7.1720	5.3173	5.2259	4.9092	4.7592	5.0540	4.7592	7.9511	**7.2804**	6.3753	5.2435	6.7147
6	12.2050	12.592	12.5140	11.459	10.6930	**12.1930**	10.6930	14.707	12.1470	11.099	11.4850	11.099
7	3.6719	3.3600	2.9176	3.1722	2.6631	**3.4101**	2.6631	3.1319	2.5410	2.2701	2.9725	2.2701
8	5.6986	2.8924	2.6931	3.6128	2.4882	3.8374	2.4882	**4.9516**	3.9719	3.2995	3.7774	3.2995
9	5.7898	7.2621	7.1450	**6.3753**	6.3877	6.6298	6.3877	7.9160	7.2474	6.6838	6.8390	6.8162
10	2.4955	2.4124	2.3879	2.1055	2.0331	2.3010	2.3258	2.5876	2.2388	2.2131	2.2555	**2.4779**
11	4.4716	3.8649	3.5879	4.0971	3.3479	3.6025	3.3479	**4.6580**	3.8468	3.6865	3.6243	3.6865
12	2.8079	3.3724	3.4358	3.4979	3.1979	3.9771	3.1979	3.5198	3.3231	**3.0698**	4.0971	**3.0698**
13	9.4772	13.626	14.678	13.509	12.055	13.2870	12.3030	14.4750	12.7620	**10.8190**	13.5780	11.059
14	3.3076	4.8621	3.4546	3.8789	3.4671	3.6213	3.4671	4.3816	**3.2776**	3.0595	4.3289	3.0595
15	2.3455	3.3973	2.1561	3.5995	3.1743	3.4122	3.9037	2.6974	2.8637	**2.3485**	3.4774	**2.3485**
16	2.8276	3.8773	3.2571	3.7268	3.1174	4.0743	3.1174	3.7671	3.1452	**2.9476**	3.8695	**2.9476**
17	2.3125	3.3724	3.0004	3.0646	3.0368	3.3843	3.0368	3.9771	3.3376	**2.7325**	3.4516	**2.7325**
18	3.3552	3.8897	2.9476	**3.4195**	2.6528	2.3755	2.8576	3.2871	3.0604	2.9074	3.6522	2.9074
19	12.201	12.112	**12.286**	11.7010	11.407	12.8430	11.9910	13.2130	12.4790	9.8484	13.3960	10.3310
20	2.4149	2.9173	1.5985	2.0074	1.9431	2.1107	2.0558	**2.4158**	2.4115	1.8282	2.1179	2.4252
21	4.3619	5.8097	5.2859	4.8462	4.7759	4.9559	4.7759	5.2289	5.0695	**4.0743**	5.0026	**4.0743**
22	6.0435	9.7491	9.0787	8.3587	7.8362	9.1399	7.8362	8.8678	7.8590	**7.1184**	9.2102	**7.1184**
23	3.9574	4.3449	4.0876	4.0276	4.6216	4.9216	4.6216	4.9165	**3.9946**	3.5776	4.9383	3.5776
24	4.2213	5.8470	5.2280	4.6640	4.5462	5.9437	4.5462	4.6568	**4.0816**	3.8116	6.0483	3.8116
25	11.9109	13.5767	13.6197	12.8376	12.4848	13.8382	12.4848	14.0307	**12.1712**	10.4123	14.1112	10.4123
26	5.7165	7.7421	7.9490	6.5090	6.1498	7.0468	6.1498	7.6841	7.0880	**6.0226**	7.1162	6.3598
27	4.7604	5.3173	5.1037	**4.9537**	5.7080	5.2032	5.9253	6.2429	6.2437	5.1826	5.1607	5.7298
28	9.5984	9.1821	8.2717	8.0793	7.8598	8.9265	7.8598	10.9484	8.5884	8.0308	**9.3002**	8.0308
29	3.9316	4.3573	3.7671	3.7071	3.5922	4.0165	3.5922	4.9537	4.1746	3.7568	**3.9916**	3.7568
30	4.8607	5.7973	5.3232	**4.8762**	4.6713	4.9662	4.6713	5.0210	4.7352	4.0825	5.0210	4.0825
Average error		1.1223	0.9910	1.0981	1.1394	1.3259	1.1394	1.1766	0.6732	0.7354	1.4164	0.7218

Table 6-22 Comparison of compactness. Bold and underlined results indicate predictions closest to the ground data.

Lake	GD	Single image						Fused image				
		HC	PS (1)	PS (5)	HNN (E)	HNN (A)	HNN₂	PS (1)	PS (5)	HNN (E)	HNN (A)	HNN₂
1	0.3735	**0.3974**	0.41017	0.47874	0.59168	0.39914	0.59168	0.26502	0.43327	0.52545	0.34458	0.52545
2	0.5362	0.2919	0.3302	0.3551	0.3962	0.3248	0.3962	0.3039	0.3734	**0.4335**	0.3355	**0.4335**
3	0.7434	0.6320	0.7725	**0.7578**	0.8182	0.7202	0.8182	0.5410	0.6196	0.6976	0.7202	0.6976
4	0.7762	0.6414	0.74766	0.24998	0.27526	0.16792	0.27526	0.64421	**0.75851**	0.8852	0.1693	0.8852
5	0.3532	0.4866	0.51854	0.59651	0.63115	0.56231	0.63115	0.2895	**0.35588**	0.43833	0.52216	0.40037
6	0.4985	0.4795	**0.48569**	0.58106	0.66458	0.51487	0.66458	0.36611	0.54104	0.63869	0.57759	0.63869
7	0.4006	0.5132	0.62011	0.53779	0.74832	0.47863	0.74832	**0.4246**	0.66367	0.76128	0.6104	0.76128
8	0.2289	0.6058	0.64734	0.42718	0.75877	0.38604	0.75877	**0.29441**	0.4555	0.63098	0.39622	0.63098
9	0.7144	0.45308	0.47163	**0.58932**	0.58873	0.54661	0.58873	0.40357	0.49715	0.58038	0.51454	0.56054
10	0.6313	0.49798	0.5489	0.73537	0.7521	0.61869	**0.62906**	0.4932	0.70202	0.66187	0.63692	0.71213
11	0.6151	0.53323	0.58961	0.48486	0.68512	0.59586	0.68512	0.39192	0.58784	**0.60637**	0.58751	**0.60637**
12	0.7577	0.70019	0.70106	0.67996	**0.78836**	0.52949	**0.78836**	0.55071	0.62384	0.68604	0.50044	0.68604
13	0.5713	0.3159	0.27111	0.31936	0.39672	0.32653	0.38285	0.28357	0.36718	**0.49867**	0.31182	0.47975
14	0.6358	0.36772	0.57416	0.47704	0.57546	0.53858	0.57546	0.35346	**0.62889**	0.69973	0.39169	0.69973
15	0.7447	0.5021	0.6353	0.3652	0.4346	0.3825	0.3264	0.6204	0.5887	**0.8469**	0.3803	**0.8469**
16	2.8276	0.3856	0.5580	0.4389	0.5983	0.3761	0.5983	0.3816	0.5456	**0.6100**	0.4179	**0.6100**
17	0.8005	0.5730	0.6549	0.6319	0.6474	0.5332	0.6474	0.3336	0.5010	**0.6705**	0.5112	**0.6705**
18	0.4728	0.43094	0.5288	0.43683	0.66615	0.75207	0.59813	**0.47313**	0.56589	0.60444	0.38198	0.60444
19	0.3341	0.31592	0.30811	0.34198	0.36124	0.28345	**0.32924**	0.28796	0.32406	0.51326	0.26191	0.46933
20	0.5900	0.42575	0.76459	0.6238	0.67998	0.58295	**0.64224**	0.36941	0.41229	0.66109	0.5799	0.55667
21	0.62378	0.38626	0.43635	0.51973	**0.53725**	0.49697	**0.53725**	0.45015	0.49393	0.73257	0.48859	0.73257
22	0.55435	0.24388	0.2678	0.3162	0.35215	0.26571	0.35215	0.29298	0.38287	**0.46587**	0.26172	**0.46587**
23	0.6863	0.4604	0.5087	0.5263	0.4365	0.3913	0.4365	0.3979	0.6081	**0.7590**	0.3883	**0.7590**
24	0.5557	0.3602	0.4157	0.5288	**0.5587**	0.3246	**0.5587**	0.5189	0.6707	0.7481	0.3132	0.7481
25	0.3871	0.3339	0.3140	0.3533	**0.3763**	0.3050	**0.3763**	0.3077	0.4070	0.5570	0.2937	0.5570
26	0.5439	0.3021	0.2737	0.40026	0.45065	0.34533	0.45065	0.30043	0.36905	**0.4775**	0.33963	0.43704
27	0.5847	0.4354	0.4822	**0.5139**	0.4116	0.4720	0.3842	0.3487	0.3578	0.4915	0.4763	0.4143
28	0.3547	0.2920	**0.3734**	0.3942	0.4135	0.3242	0.4135	0.2377	0.3966	0.4468	0.3018	0.4468
29	0.6386	0.4959	0.6954	0.7230	0.7665	0.6271	0.7665	0.4477	0.6280	0.7620	**0.6286**	0.7620
30	0.4613	0.3448	0.3728	**0.4455**	0.4836	0.4338	0.4836	0.4239	0.4881	0.6396	0.4229	0.6396
Average error		0.2362	0.2023	0.2089	0.2289	0.2307	0.2257	0.2460	0.1858	0.1932	0.2397	0.1961

For the compactness measurement, the PS(5) applied on the fused image produce the lowest error with the average error was 0.1858, while the HNN(E) applied on the fused image produced 0.1932 error and the HNN_2 applied on the fused image produced 0.1961 error. The PS(1) applied on a fused image produced the highest error with the average error was 0.2460. This scenario suggested that in comparison with other techniques, the shape of the lakes represented by the PS(5) and HNN(E) produced the closest appearance to the corresponding lakes in the ground data.

For the small lakes (lakes 10, 15, 17, and 20), the HNN(E) applied on the fused image produced the lowest error on the compactness measurement with the average error was 0.0835. Other technique that produced the second lowest error was the HNN_2 technique that was applied on the fused image with the average error was 0.0866. The PS(1) technique that was applied on the fused image produced the highest error with the average error was 0.2375.

For the big lakes (lakes 6, 13, 19, 25, and 28), the PS(5) applied on the fused image produced the lowest error on the compactness measurement with the average error was 0.0637, while the HNN_2 applied on the fused image produced 0.1258 error. The PS(1) technique that was applied on the fused image produced the highest error with the average error was 0.1325.

Results from the characterization of the shape of the lakes demonstrated evaluations on the individual lakes represented by different techniques. Area, perimeter and compactness of lakes were measured. Overall, the proposed HNN_2 technique applied on the fused image was more accurate than the other techniques in predicting the

area of the lakes in particular small lakes with the area ~0.3 km^2. The HNN(E) was slightly more accurate than the HNN$_2$ in predicting the area of big lakes (> 2.6 km^2).

Overall, the PS(5) applied on the fused image was more accurate than the other techniques in predicting the perimeter of the lakes in particular big lakes. However, for small lakes, the prediction of the perimeter of the lake with the HNN$_2$ was more accurate than the other techniques.

The PS(5) applied on the fused image was also more accurate than the other techniques in predicting the compactness of the lakes in particular big lakes. For small lakes, the prediction of the compactness with the HNN(E) was more accurate than the other techniques. The HNN$_2$ was the second most accurate technique in predicting the compactness of the small lakes.

6.8.5. Positional accuracy

To evaluate the positional accuracy, the shoreline of the represented lakes produced from different land cover mapping techniques was compared with the boundary of the corresponding lakes in the ground data image. Several points along the shoreline of a represented lake were selected. These points were vectorised and compared with the closest points along the shoreline of the corresponding lake in the ground data. As an example, Figure 6.22 shows boundary fitting for different land cover mapping techniques on lake 25 from the image in Figure 6.21. The boundary of the represented

Ground data   Hard classifier   PS(1) on 1 image   PS(5) on 1 image

HNN(E) on 1 image   HNN(A) on 1 image   HNN$_2$ on 1 image   PS(1) on fused image

PS(1) on fused image   HNN(E) on fused image   HNN(A) on fused image   HNN$_2$ on fused image
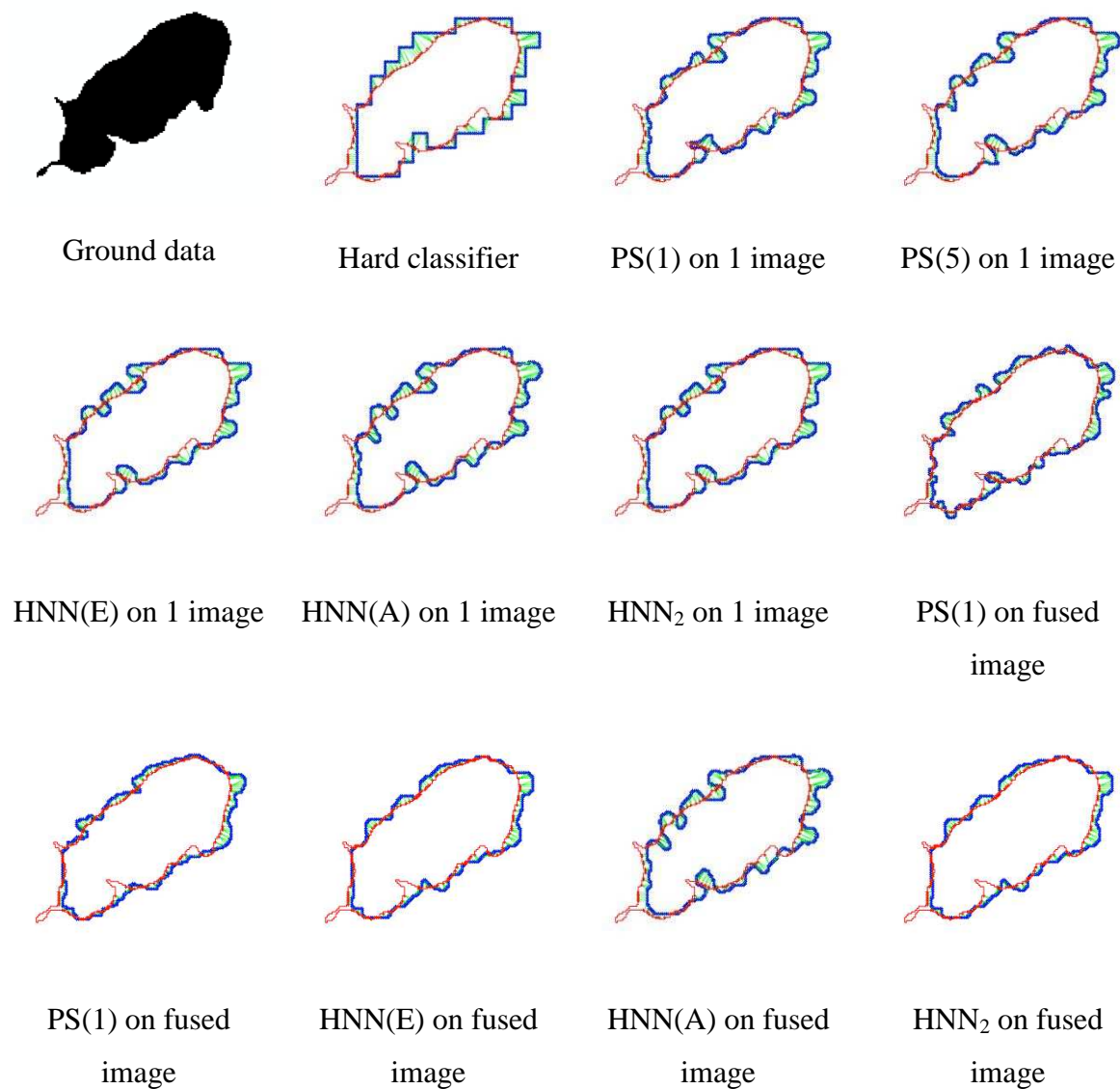
Figure 6-22 Boundary fitting for different techniques on lake 25. The red line indicates the boundary of the lake from the ground data image, and the blue line indicates the boundary of the represented lake.
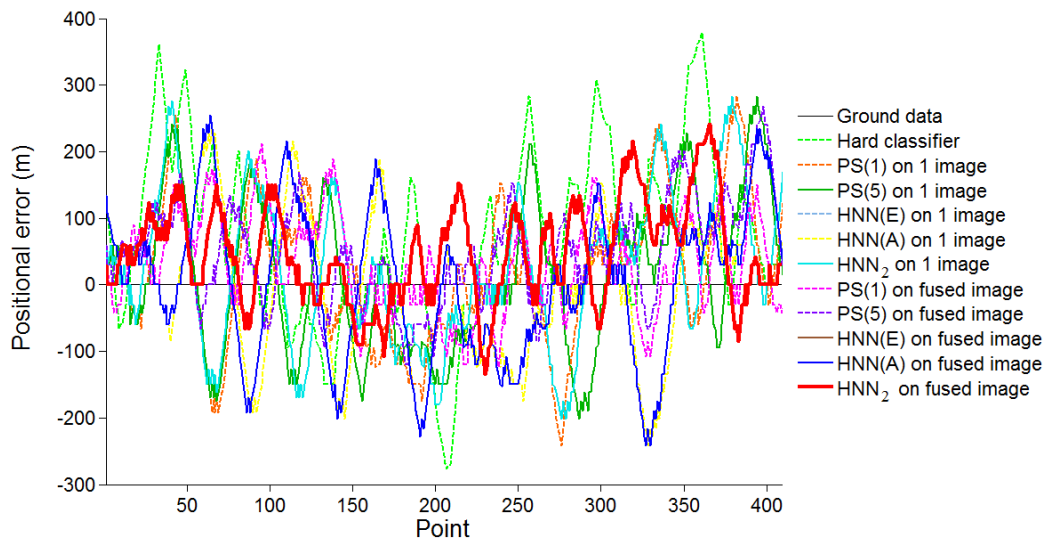
Figure 6-23 Positional error along the boundary of lake 25.

lakes was overlaid with the boundary of the corresponding lake in the ground data. The vector difference between the points along the boundary of the represented lakes and the points along the boundary of the corresponding lakes in the ground data was measured to produce positional accuracy information, as shown in an example in Figure 6.23.

The root mean squared error (RMSE) of the position error of the selected 30 lakes (Figure 6.21) was calculated and the result is presented in Table 6.23. Again, as the HNN_2 technique was a combination of the HNN(E) and HNN(A), several results of the HNN_2 technique in the Table 6.23 may identical or close to the results of the HNN(E) and HNN(A).

In general, the HNN(E) applied on the fused image produced the highest positional accuracy compared with other techniques with the average RMSE produced was 82.98 m. The proposed HNN_2 technique that was applied on the fused image

produced the second highest positional accuracy with the average RMSE was 85.00 m. The HNN(A) applied on a single image produced the lowest positional accuracy with the average of the RMSE was 145.93 m.

For the small lakes (lakes 10, 15, 17, and 20), the HNN(E) applied on the fused image produced the highest positional accuracy compared with other techniques when producing the average RMSE with 65.63 m, while the average RMSE of the HNN_2 applied on the fused image was 71.74 m. The hard classification technique produced the lowest positional accuracy as the average RMSE error was 111.23 m.

For the big lakes (6, 13, 19, 25, and 28), the HNN(E) applied on the fused image produced the highest positional accuracy compared with other techniques when producing the average RMSE with 77.97 m. Other technique that produced the second lowest RMSE was the HNN_2 technique that was applied on the fused image with the average RMSE was 77.95 m. The hard classification technique produced the lowest positional accuracy as the average RMSE error was 119.75 m.

A general trend was notable from the Table 6.23 that the PS(5), HNN(E), and the proposed HNN_2 techniques, all were applied on the fused image, tended to produce highly accurate positional prediction as the RMSE values from the three techniques were relatively low than that of the other techniques. This trend is highlighted in bold and underlined results of the Table 6.23. The boundary of the lakes represented by the PS(5), HNN(E) and the HNN_2 were generally smoother and less irregular than the boundary of the lakes represented by other techniques, notably the PS(1) and the HNN(A). The average RMSE of the boundary fitting of the hard classifier was also

high because the boundary of the lakes represented appeared to be blocky and jagged. The positional accuracy for the represented lakes in the fused image was higher than that in the single image. The boundary of the represented lakes in the fused image appears to be smoother and less irregular than the represented lakes in the single image. An example of this scenario is shown in Figure 6.22.

In addition, the error of the boundary fitting may also affected by the accuracy of image registration between the MODIS images and the Landsat image, which was used as a ground data. As the processing of the super-resolution mapping techniques only involved the MODIS images and not the ground data, which only used for comparison purposes, there were implications of the results that may affect the accuracy of the image registration. Notably for the techniques that used only single MODIS image, for example images shown in Figure 6.22. The boundary fitting of the results of the single MODIS images appear to be less accurate than that of the results of the fused MODIS images, suggesting that by fusing the MODIS images, the problem of the image registration between the MODIS images and the ground data could be minimized.

Results in this section demonstrated that the HNN(E) technique applied on the fused image was generally more accurate than the other techniques in predicting the positional accuracy of the lakes. The HNN_2 technique produced the second most accurate technique, followed by the PS(5) technique, although the difference of the positional accuracy between the two techniques was very small (RMSE 0.38 m). The positional accuracy of the lakes predicted with the PS(1), HNN(A) and hard classification techniques were generally low (RMSE > 109 m).

Table 6-23 Comparison of RMSE on boundary fitting (m). Bold and underlined results indicate predictions closest to the ground data.

Lake	Single image						Fused image				
	HC	PS (1)	PS (5)	HNN (E)	HNN (A)	HNN$_2$	PS (1)	PS (5)	HNN (E)	HNN (A)	HNN$_2$
1	104.57	91.40	88.68	86.57	88.09	86.57	90.88	92.62	**82.53**	92.41	**82.53**
2	130.17	114.23	116.03	123.56	129.09	123.56	81.36	**80.39**	86.57	127.98	86.57
3	112.02	102.72	101.55	102.48	105.87	102.48	87.79	94.04	**84.01**	105.87	**84.01**
4	131.71	141.26	1061.90	1065.50	1129.60	1065.50	74.10	72.58	**71.85**	1130.10	**71.85**
5	127.02	124.33	107.95	103.60	112.38	103.60	68.19	**57.31**	59.47	109.55	62.46
6	116.82	112.81	116.12	113.74	116.98	113.74	86.05	89.35	**76.69**	112.36	**76.69**
7	105.68	109.68	110.23	115.77	101.04	115.77	97.42	**91.68**	96.62	109.13	96.62
8	75.02	83.50	89.43	82.01	91.11	82.01	70.17	77.87	**67.61**	90.75	**67.61**
9	119.29	**90.38**	92.43	92.37	96.17	92.37	107.30	107.75	105.71	96.29	110.30
10	96.14	94.89	94.60	96.32	98.60	101.77	78.45	77.09	**76.08**	97.45	80.49
11	84.84	90.63	114.90	86.63	87.40	86.63	86.80	**76.57**	84.57	89.95	84.57
12	114.89	120.70	119.26	113.47	121.97	113.47	82.42	**79.61**	81.03	120.13	81.03
13	131.34	129.93	121.64	114.15	118.47	118.70	101.52	104.48	**86.86**	115.99	88.35
14	146.19	114.01	126.38	118.42	115.98	118.42	109.00	**98.96**	105.01	126.26	105.01
15	122.16	132.94	103.85	138.03	127.72	115.63	83.26	**71.97**	76.78	119.40	76.78
16	155.61	149.36	95.88	144.82	162.31	144.82	**65.54**	68.67	71.68	158.850	71.68
17	127.64	112.15	109.65	111.10	117.22	111.10	71.04	74.24	**55.95**	111.55	**55.95**
18	118.33	105.39	104.01	109.92	125.76	102.34	80.44	**62.94**	70.45	107.96	70.45
19	139.26	131.62	126.24	129.28	129.87	130.85	93.88	96.76	90.44	129.49	**88.85**
20	98.99	56.29	83.73	87.32	91.36	92.83	66.39	**47.22**	53.70	83.764	73.72
21	97.73	111.01	103.16	104.23	106.65	104.23	79.12	85.05	**77.55**	105.71	**77.55**
22	196.86	173.90	169.85	**168.53**	169.05	**168.53**	183.34	186.66	179.25	170.02	179.25
23	111.54	102.55	100.97	125.10	127.43	125.10	104.27	99.10	**93.95**	126.35	**93.95**
24	130.72	103.93	102.24	105.59	104.41	105.59	61.60	57.39	**51.09**	109.90	**51.09**
25	120.52	94.24	97.91	97.45	104.55	97.45	72.59	**67.42**	68.05	104.63	68.05
26	113.62	97.89	97.03	97.10	99.81	97.10	74.66	76.28	**68.86**	102.11	82.27
27	**119.14**	128.00	125.92	148.96	128.21	152.28	186.89	177.18	176.49	126.49	191.44
28	90.81	81.22	79.81	81.02	78.21	81.02	73.76	**63.83**	67.81	85.35	67.81
29	86.96	92.96	92.41	88.79	90.51	88.79	72.80	**67.78**	68.01	88.61	68.01
30	97.34	100.94	98.04	102.18	101.97	102.18	62.11	58.69	**54.73**	103.00	**54.73**
Average RMSE	117.44	109.83	138.39	141.80	145.93	141.48	88.44	85.38	82.98	145.25	85.00

6.9.   Conclusions

This chapter presents the application of different super-resolution mapping techniques on MODIS 250 m imagery. The improved HNN and pixel swapping techniques, which have been discussed in Chapter 4 and 5, were applied to the MODIS imagery. Particular attention was paid to a combination of two different configurations of the HNN techniques. The first HNN emphasis equal strength on effect the goal functions and the area proportion constraint (HNN(E)). The HNN(E) was suitable for the representation of large lakes. The second HNN weighted the area proportion constraint more than that of the goal functions (HNN(A)). The HNN(A) was suitable for the representation of small lakes. The best outcomes from the two HNN were combined. The combination of the two HNNs was known as a HNN_2 technique. For comparative purposes, pixel swapping techniques, PS(1) and PS(5) were used. All the techniques were used on a single MODIS 250 images and a fused image derived from a time series MODIS 250 m images.

A series of assessments was used to evaluate results of the different super-resolution mapping techniques, such as site specific thematic accuracy, texture variables, characterization of the shape of the lakes, and positional accuracy. In all of the assessments, generally, the use of the fused image in all the super-resolution mapping technique provided more accurate results than that of the single image. The HNN(E) and the HNN(A) were effective in predicting the site specific thematic assessment. Results of the PS(1) and PS(5) were tended to be dominated by speckled pattern, which may

wrongly classified as lakes. Therefore, the speckled pattern was removed by median filtering. However, the removal of the pattern may also eliminate the real lakes.

On the texture variables, four texture variables were measured: homogeneity, contrast, IDM, and entropy. The proposed HNN_2 was more accurate than the other techniques in predicting the homogeneity and entropy of the spatial distribution of the lakes, while the HNN(A) was more accurate than the other techniques in predicting the contrast and the IDM. Compared to the other techniques, the HNN(A) and HNN_2 techniques were more accurate for the representation of small lakes.

On the characterization of the shape of the lakes, standard measures such as area, perimeter and compactness were used. In general, the proposed HNN_2 technique was more accurate than the other techniques in predicting the area of the represented lakes, while the PS(5) was more accurate in predicting the perimeter and the compactness of the represented lakes.

On the positional accuracy, the HNN(E) was more accurate than the other techniques as the boundary of the lakes represented was smooth, which resemblance the boundary of the lakes in the ground data. The proposed HNN_2 technique was the second most accurate technique for the positional accuracy prediction.

Finally, results derived from the proposed HNN_2 technique demonstrated that the technique was more accurate than the other techniques in some aspects in representing lakes of different sizes, shapes and mosaic. Compared to the other techniques that may be suitable either for small or large lakes, the proposed HNN_2 was applicable for both cases.

7. Super-resolution mapping using the halftoning concept

This chapter proposes a new super-resolution mapping technique based on halftoning concept. The new technique provides an alternative to the existing super-resolution mapping techniques. The new technique is based on a combination of several techniques: temporal image fusion, halftoning, 2D multiple notch filter, and object based mapping using iterative morphological operation. Similar to the super-resolution mapping techniques discussed in the previous chapters, the proposed technique exploits the fine temporal resolution of coarse spatial resolution of remotely sensed imagery. Given that the proposed technique is new and not described elsewhere, some salient features will be given in this chapter.

7.1. Introduction

Many super-resolution mapping techniques that have been proposed (Tatem et al., 2001a; Verhoeye and Wulf , 2002; Atkinson, 2005; Mertens et al., 2006). In general, super-resolution mapping techniques represent land cover mapping derived from mixed pixels. Initially, the mixed pixel is decomposed into sub-pixels. Based on the proportion

of the land cover classes inside the mixed pixel, hard classification at sub-pixel scale is allocated randomly. Later, using a variety of super-resolution mapping techniques, sub-pixels of the same class are grouped together to form a land cover mapping class.

In this chapter the initial spatial arrangement of the hard classifier at the sub-pixel scale was arranged systematically in a periodic pattern using a halftoning technique (Ulichney, 1987). The systematic periodic pattern would enable non-iterative algorithm such as image filtering in order to represent land cover mapping, whereas for the random pattern that was commonly employed in the existing super-resolution mapping techniques, required iterative algorithms. Figure 7.1 illustrates the difference between initial random arrangement (Figure 7.1b) and arrangement derived from the halftoning technique (Figure 7.1c). Both of these spatial arrangements were derived from a synthetic image (Figure 7.1a) containing a transition from a pure black pixel into a pure white pixel. Between these two pixels, there are five mixed pixels with each one of them contains a proportion between black and white. The value of the proportion is given below every pixel. Every pixel was sub-divided into 50×50 sub-pixels.

The periodic pattern of the spatial arrangement of the hard class labels at the sub-pixel scale allows a frequency that caused the periodic pattern to be detected (Pei and Tseng, 1994; Tseng and Pei, 1996). The detection of this frequency inspired the development of inverse halftoning techniques (Venkata et al., 1998; Kite et al., 2000), which are able to transform the initial periodic pattern that appears to be dispersed into concentrated objects. This concept inspired a novel super-resolution mapping technique for the representation of land cover mapping. Further discussion of this concept will be provided in this chapter.
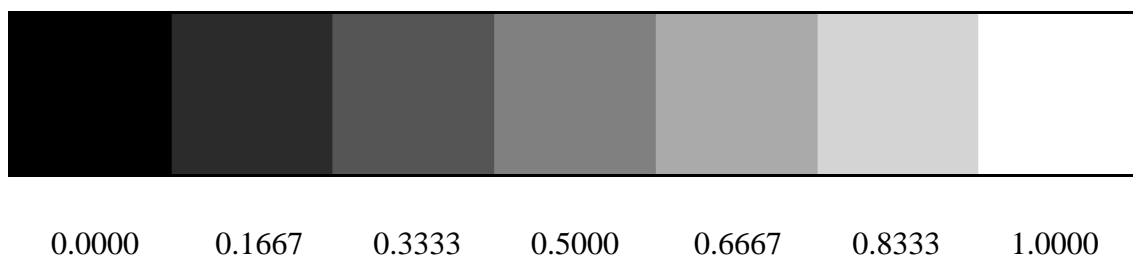
(a)

(b)
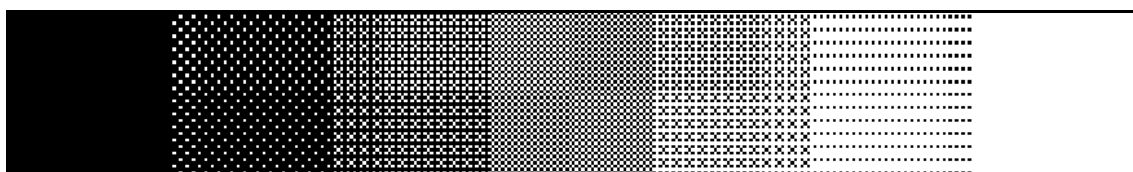
(c)

Figure 7-1 Illustration of the initial spatial arrangement of hard classifier at a sub-pixel scale. (a) Several mixed pixels with different proportion of black and white classes. Values at the bottom indicate the proportion of the white class. (b) Initial spatial arrangement using random technique. (c) Initial spatial arrangement using halftoning technique.

7.2. Test site and data

A ~25 km² area located in Quebec province, Canada, was selected for this study (Figure 7.2). It is situated between latitudes 55°08'35"N and 55°06'05"N and between longitudes 77°41 53"W and 77°36'27"W. This region contains a variety of lakes of differing size and shape that provide a challenge for mapping from remote sensing. Lakes are typically spectrally highly separable in the near-infrared wavelengths in which commonly used remote sensing systems operate in allowing the study to use data acquired in a single waveband to acquire information on important lakes. The approaches discussed should, however, be generalisable to other types of objects and data sets.

Two sets of image data were used. First, a Landsat ETM+ near infrared image (band 4) of the region acquired on 8 July 2002 was used to provide reference data on lakes. These data have a spatial resolution of 30 m and the mosaic of lakes is visually evident in the image (Figure 7.2a). As well as being used as reference data, the ETM+ data were spatially degraded by averaging pixel values in order to derive a coarse spatial resolution representation of the test site (Figure 7.3). Although this approach to the simulation of a coarse spatial resolution image is not ideal this approach has the advantage of ensuring that the simulated image and reference data sets are perfectly co-located, avoiding problems with spatial mis-registration that can greatly impact on studies by remote sensing (Roy, 2000). Here, coarse spatial resolution images from the original 30 m resolution ETM+ image were derived by down-sampling by a factor of 8

(a)   (b)

N

0   1   2   3   4   5
Kilometres
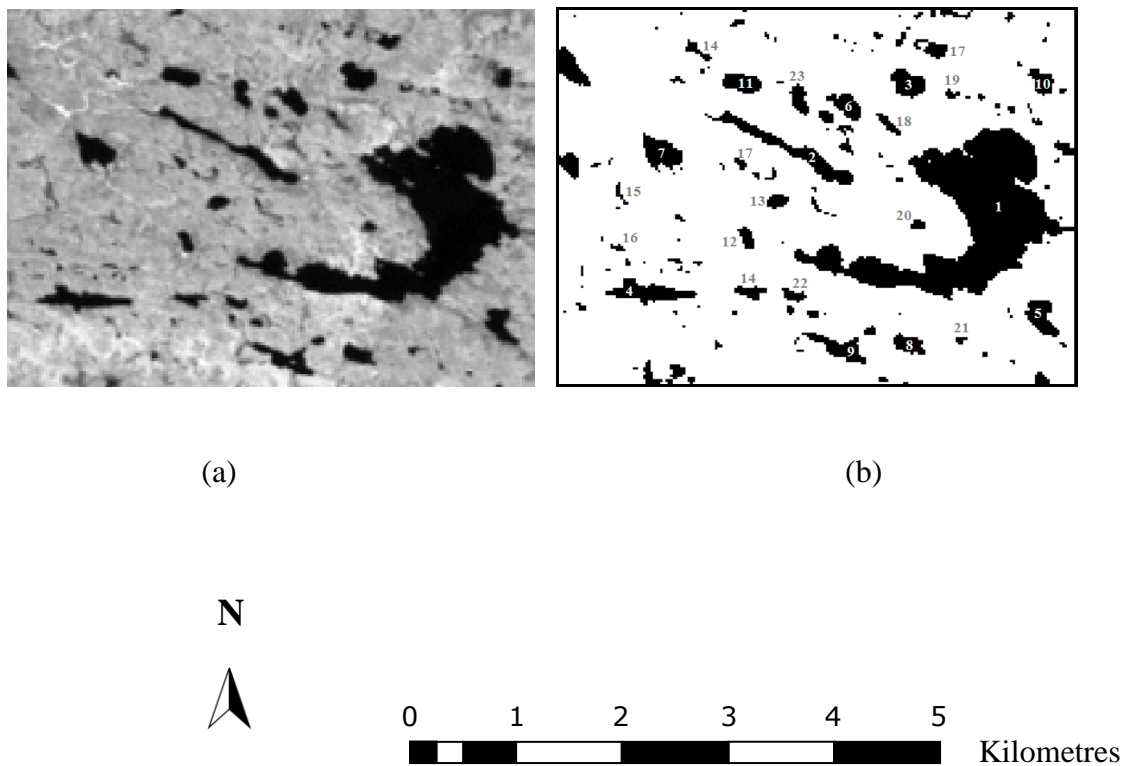
Figure 7-2 The Landsat ETM+ data of the test site. (a) near-infrared waveband image and (b) binary land cover map derived from hard classification.
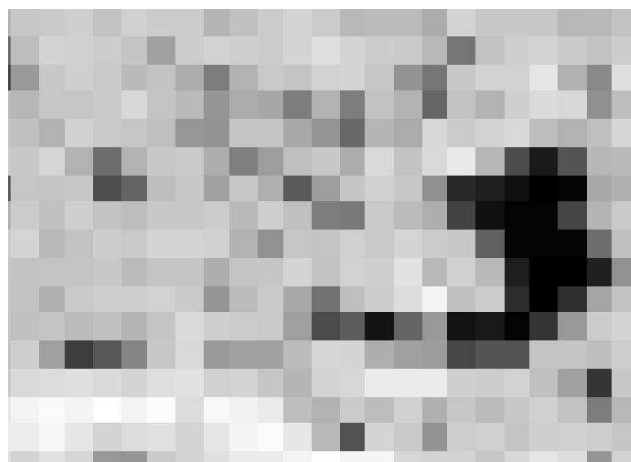
Figure 7-3 A simulated image with a spatial resolution of 240 m derived by spatial degradation of the Landsat ETM+ imagery.
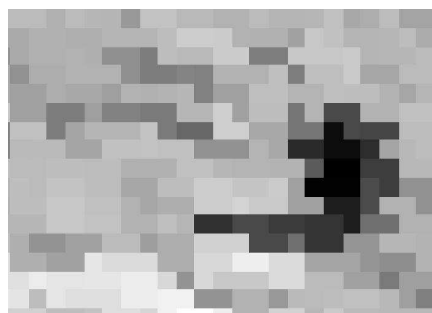
1 July 2002
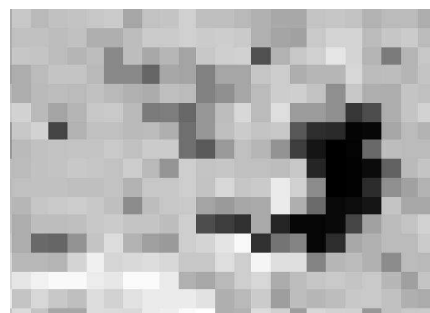
5 July 2002
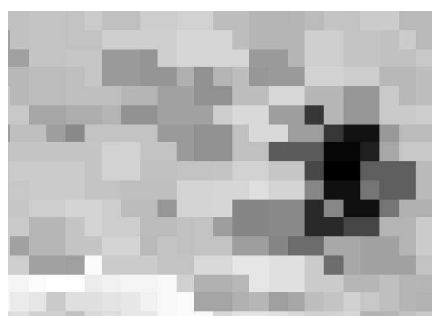
6 July 2002
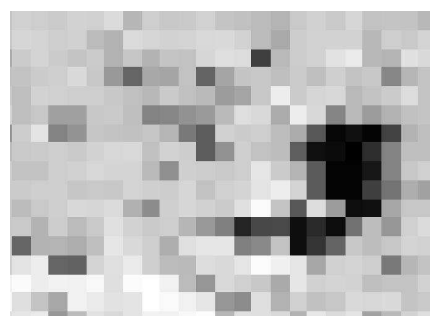
7 July 2002
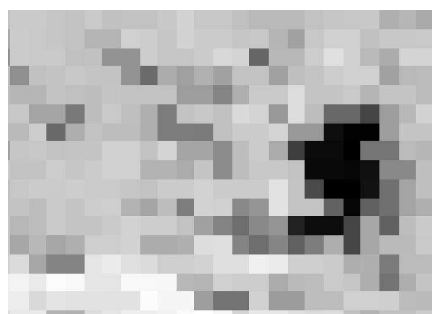
11 July 2002
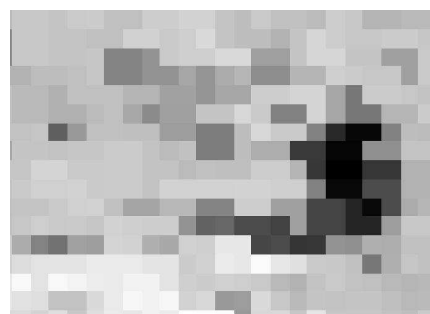
13 July 2002
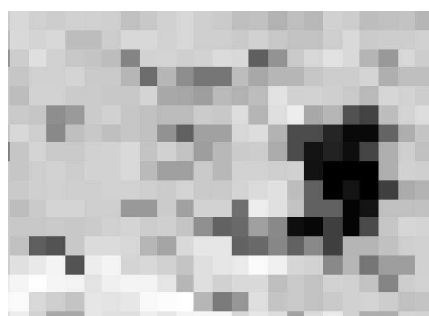
18 July 2002

Figure 7-4 The MODIS images

to a spatial resolution of 240 m pixel, broadly similar to the finest spatial resolution obtainable from MODIS (250 m).

Finally, a time series of coarse spatial resolution imagery acquired by the MODIS sensor around the date of the Landsat ETM+ data acquisition was acquired to illustrate the applicability of the method to a real data set (Figure 7.4). Seven cloud-free daily MODIS 250 m spatial resolution images of the test site acquired between 1 July 2002 and 18 July 2002 were obtained. Again, only the data acquired in the near infrared band were used because of the high separability of land and water in this part of the spectrum. Although similar and acquired over a short period of time there are clear inter-image differences (Figure 7.4).

7.3. Methods

The proposed new super-resolution mapping technique is based on a combination of several techniques as illustrated graphically in Figure 7.5. This technique exploits the fine temporal resolution that is typical of coarse spatial resolution images. The proportion of different classes within a mixed pixel in each image was derived using fuzzy c-means soft classification (Bezdek et al., 1984). Every image, then, was fused at a sub-pixel scale. A halftoning technique (Ulichney, 1987) was used to allocate hard classification at a sub-pixel scale in a halftoned image. This was later followed by 2D multiple notch filter (Pei and Tseng, 1994; Tseng and Pei, 1996) to suppress noisy frequencies of the halftoned image in a frequency domain using the Fourier spectrum.
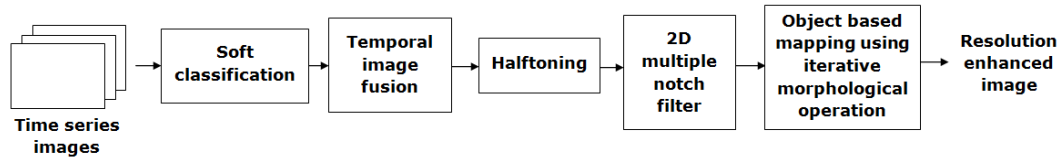
Figure 7-5 Diagram of the proposed new super-resolution mapping technique

The filtered image then was inversed into an image domain. Finally, the filtered image was segmented using object based mapping using adaptive morphological operation. Further details on the proposed method are given in this section

7.3.1. Time series image registration and data fusion

With the spatially degraded Landsat ETM+ data a time series of images was simulated. This was achieved by deriving multiple coarse spatial resolution images from the fine spatial resolution image in Figure 7.2a by down-sampling the ETM+ data by a factor of 8 to a spatial resolution of 240 m pixel. To model the slight orbital translations that might be expected to occur with real data, the initial position of an image for the down-sampling operation was sub-pixel shifted randomly in horizontal and vertical directions from one image to another (Lu and Inamura, 2003). Each image differs slightly from the others in the time series data and was assumed to be translated linearly (e.g. horizontal and vertical) in a sub-pixel scale.

In the time-series of MODIS data, all the images of the site were also highly similar but not completely identical. Due to factors such as slight orbital translations and

the Earth's rotation, the images may not represent the exact same area. In addition, atmospheric effects were likely to vary from image to image resulting in variable radiometric properties.

All the images were soft classified using fuzzy c-means clustering technique. The number of clusters was set to two (i.e. c = 2) to differentiate between land and water in the image. The algorithm's weighting parameter, m, which determines the degree of fuzziness was set, after a series of trial analyses, to m = 2.0.

With each coarse spatial resolution data set, the relative translation between images was determined based on phase correlation technique (Reddy and Chatterji, 1996) at a sub-pixel accuracy using Equation 5.11, which allowed linear transformation such as translation and rotation to be detected even under different radiometric conditions and corrected in a new registered image. The registered images then were combined into a fused image using Equation 5.14.

Figure 7.6a shows a proportion image derived from a soft classification of a single coarse spatial resolution image derived from the Landsat ETM+ data and the result derived from a fusion of multiple proportion images is shown in Figure 7.6b.

A MODIS image acquired on 7 July 2002 was used as a reference image for time series MODIS image registration because its date of acquisition is the closest temporally to that of the Landsat ETM+ image and lies in the middle of the set of dates over which the MODIS data set was acquired.

(a)   (b)
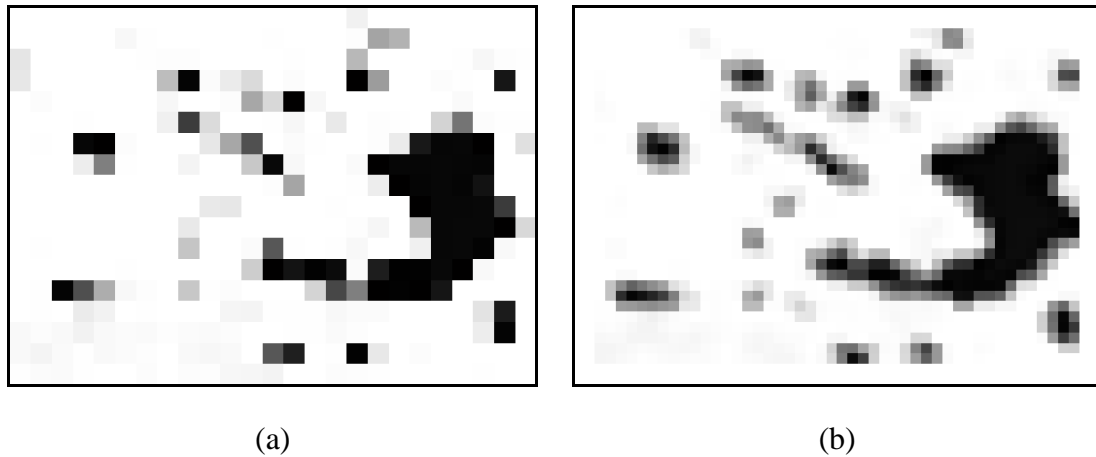
Figure 7-6 Soft classification on (a) a single coarse spatial resolution image, (b) a fusion of multiple coarse spatial resolution images.

7.3.2. Halftoning

A soft classification provides information about the proportion of different land cover classes within a pixel. Assuming that a mixed pixel only contains two classes, many super-resolution mapping techniques use the value of the soft classification in the mixed pixel to derive a binary class proportions at a sub-pixel level (Tatem et al., 2001a, Atkinson, 2005). The analysis typically begins with the location of these classes distributed randomly within a pixel before the super-resolution mapping techniques begin an iterative process to optimally locate them.

In this chapter, the initial distribution of binary class proportion at a sub-pixel level was distributed in a periodic pattern using a halftoning technique (Ulichney, 1987; Lau and Arce, 2001; Mese and Vaidyanathan, 2002). Halftoning is a process of converting a continuous tone image to black and white dots; it is widely used in printing

technology. The continuous tone image derived from a soft classification was quantized

into a dispersed dot pattern (Kite, 1998). This dot pattern was created by comparing a

continuous input image f_{In} with a threshold image t where the spatial resolution of

both images is equal.

$$f_{Halftone}(i, j) = \begin{cases} 1 & f_{In}(i, j) \geq t(i, j) \\ 0 & f_{In}(i, j) < t(i, j) \end{cases} \tag{7.1}$$

The threshold image was created by arranging a dither matrix (Bayer, 1973) over the

entire threshold image.

$$t(i, j) = D^n (i \bmod n, \ j \bmod n) \tag{7.2}$$

where D^n is a dither matrix with a size of $n \times n$. For $n = 4$, the dither matrix is given by

$$D^4 = \frac{1}{17} \begin{bmatrix} 6 & 11 & 7 & 10 \\ 14 & 1 & 15 & 4 \\ 8 & 9 & 5 & 12 \\ 16 & 3 & 13 & 2 \end{bmatrix} \tag{7.3}$$

The dither matrix was normalized with $n \times n + 1$ gray levels.

The pattern derived from the halftone can offer more usage flexibility than the

random pattern because through the implementation of inverse halftoning techniques

(Kite et al., 2000), the dot pattern can be transformed back into a continuous image and

several noises associated with the dot pattern can be suppressed. The application of

halftoning can be illustrated in Figure 7.7 that shows the initial class distributions

derived using random (Figure 7.7a) and halftoning (Figure 7.7b) allocation.

(a)　　　　　　　　　　　　　　　(b)

(c)　　　　　　　　　　　　　　　(d)
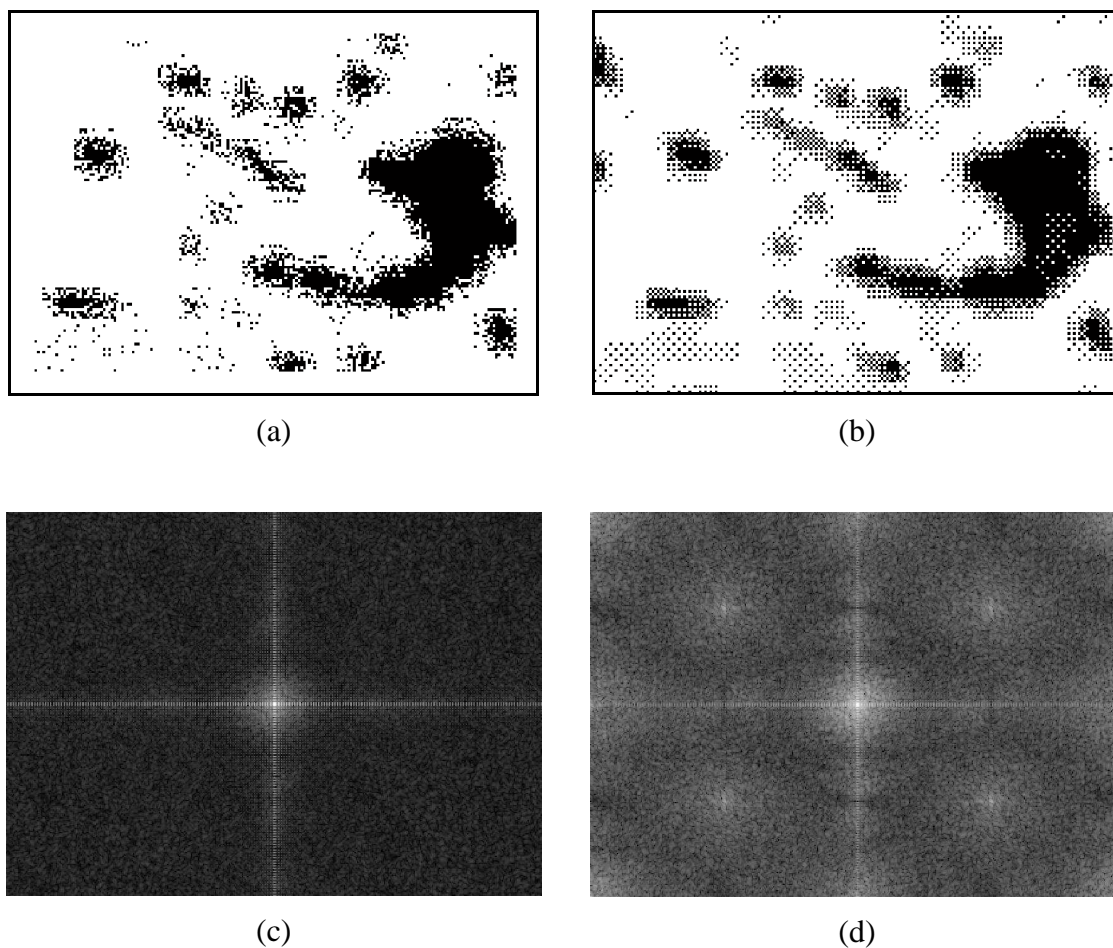
Figure 7-7 Initialization of binary class proportions on a sub-pixel scale using (a) random dot pattern, (b) dispersed halftoning dot pattern. Correspondence Fourier of (c) random dot pattern, (d) halftoning dot pattern.

The differences between both images can be analysed in Fourier spectrum. A Fourier spectrum of the image generated by random dot allocation is shown in Figure 7.7c. The spectrum displays apparent low frequency component in the middle of the spectrum that represents the gray scale image. Other than that, no other frequency component is apparent. On contrary, a Fourier spectrum (Figure 7.7d) of the image

generated by halftoning displays the low frequency component and several notch frequencies that are spread over the frequency plan in the spectrum. The reconstruction of continuous image can be performed by removing these notch frequencies and will be explained in the Section 7.3.3.

7.3.3. 2D multiple notch filter

A periodic pattern contained in an image can be treated in its Fourier spectrum to eliminate unwanted frequencies. A halftoned image may contain periodic or aperiodic dot pattern; and this can be observed in its Fourier spectrum (Ulichney, 1987). To suppress the periodic dotted pattern a 2D multiple notch filter was used (Pei and Tseng, 1994; Tseng and Pei, 1996). The Fourier spectrum of the image contains pairs of symmetric peak impulses due to the periodic pattern produced by the halftoning. These frequencies can be removed by setting a unit gain at all frequencies except at the notch frequencies at which their gain is zero. The frequency response for an ideal 2D multiple notch filter is given by

$$H_{Notch}(u,v) = \begin{cases} 0 & \text{if } (u,v) = \left(u_k^*, v_k^*\right) \text{ and } \left(-u_k^*, -v_k^*\right), \quad k = 1, \ldots, n \\ 1 & \text{if otherwise} \end{cases} \tag{7.3}$$

where $\left(u_k^*, v_k^*\right)$ are the notch frequencies and n is the number of notch frequency pair. For practical situations, other types of filter such as Gaussian could be used. Thus Equation 7.3 can be rewritten as

$$H_{Notch}(u,v) = \begin{cases} H_{High\ pass}(u,v) & \text{if } (u,v) = \left(u_k^*, v_k^*\right) \text{ and } \left(-u_k^*, -v_k^*\right), \quad k = 1, \ldots, n \\ 1 & \text{if otherwise} \end{cases}$$

$$(7.4)$$

where the notch filter is a product of multiple high pass filters at which their centre were translated to the centre of notch frequencies. For a Gaussian type of filter, $H_{Highpass}$ is given by

$$H_{High\ pass}\left(u_k^*, v_k^*\right) = 1 - e^{-D^2\left(u_k^*, v_k^*\right)/2\sigma^2}$$

$$(7.5)$$

where D is a distance from point $\left(u_k^*, v_k^*\right)$, $\sigma = D_0$, and D_0 is a cut-off frequency.

To remove the notch frequencies in the Fourier spectrum in Figure 7.7d, a 2D multiple notch filter was designed by setting the gain of these frequencies to 0 as shown in Figure 7.8a. In this spectrum, there are 12 notch frequency pairs that need to be suppressed. The location of each notch frequency was designed specifically according to this pattern

$$H_{Notch}\left(c\frac{M}{4}, c\frac{N}{4}\right), \quad \text{for} \quad c = -2, -1, 0, 1, 2$$

$$(7.6)$$

except at the middle of the spectrum , $H_{Notch}(0,0)$. The 2D multiple notch filter was multiplied with the Fourier spectrum given by

$$F_{Filtered}(u,v) = H_{Notch}(u,v) \cdot F(u,v)$$

$$(7.7)$$
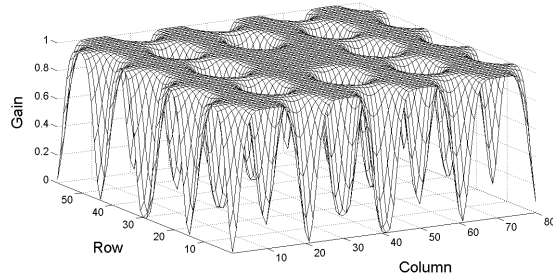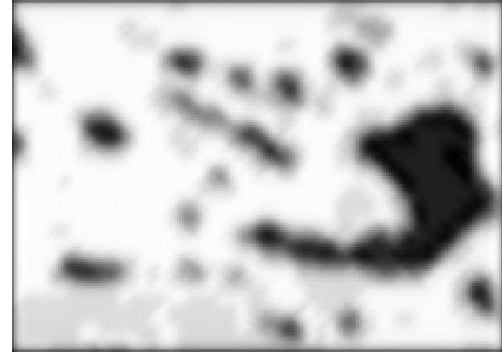
(a)   (b)

Figure 7-8 Image reconstruction using 2D multiple notch filter (a) a 2D multiple notch filter, (b) result of the filter derived from Figure 6b.

Then, the filtered image in the Fourier spectrum was inversely transformed into a spatial domain to produce a filtered image.

$$f_{\text{Filtered}}(i, j) = F_{\text{Filtered}}^{-1}(u, v)$$
(7.8)

To suppress the remaining high frequency components, a 3×3 Gaussian low pass filter was used in the spatial domain and the result is shown in Figure 7.8b. The size of the low pass filter was chosen as to minimize blurring effect that may degrade the information content of the image.

7.3.4. Iterative morphological filter

The result of the notch filter in Figure 7.8b was hardened using an adaptive thresholding technique based on moving average filter (Davies, 2005) to derive a binary land cover map. This thresholding technique was used to distinguish between lakes, which appear as dark maps in the image, and land (white). But most importantly, this technique was used to detect low contrast of small lakes (light grey) that are surrounded by land and to ignore artefact that may be caused by previous processing stages. The intensity of the grey level for the artefact is closely similar to the grey level intensity of the small lakes, but the size of the artefact is too large to be regarded as small lakes. The size of the small lakes to be detected can be limited by the size of the moving average kernel. The size of the kernel was set, after a series of trial analyses, to $\left(w/10\right)^{2}$, where w is the spatial resolution of a coarse spatial resolution image. If the size of the kernel is too large, artefact may be included, and if the size is too small, the small lakes may be ignored.

Further processing was performed using morphological filtering based on a thinning operation (Lam et al., 1992) to acquire accurate area estimation of the lakes. But there are two problems with the thinning operation. The first problem is that the thinning algorithm is a global operation that is applied to the entire image. This may cause all lakes to be eroded at an equal rate of shrinking. Although the treatment on all the lakes is equal, this may not be true as some lakes may have already been mapped at their actual size. Eroding the lakes further may cause the lakes to be smaller than their

actual size. The second problem of the thinning operation is that the rate of shrinkage to a desire size on each lake is unknown even if the lake is treated individually.

As one lake may need different rate of shrinkage than the others, iterative thinning operation was performed on each lake individually. Soft classification derived from mixed pixels of coarse spatial resolution image was incorporated as a constraint for the thinning operation. Initial result of lake mapping from the thresholding technique is shown in dashed line that represents the delineation of the lake's boundary in Figure 7.9. The line is overlaid on coarse spatial resolution pixel grids of a soft classification image showing a black object, which represents a lake, on a white background (land). The area of the lake derived from the thresholding was measured and denoted as A_{Map}. Coarse pixels that are enclosed within the boundary line of the lake were considered including the pixels that touches the line. The summation of soft classification values of these pixels represents the actual proportion of the area of the lake; therefore need to be maintained. The summation is denoted as A_{Soft}. A ratio of A_{Map}/A_{Soft} indicates the accuracy of the area estimation by the mapping, with perfect estimation when $A_{Map}/A_{Soft}=1$. The adaptive thresholding technique tends to map the lakes larger than their actual size making the ratio for a lake is > 1. To achieve the ratio 1, the thinning operation was applied to shrink the lake and a new delineation of the lake's boundary is represented by solid line in Figure 7.9. The thinning operation was applied iteratively until it immediately stopped when the ratio is equal or smaller than 1. The morphological filtering explained in this section only requires a small number of iteration for each lake, which is between 1 to 3 iterations.
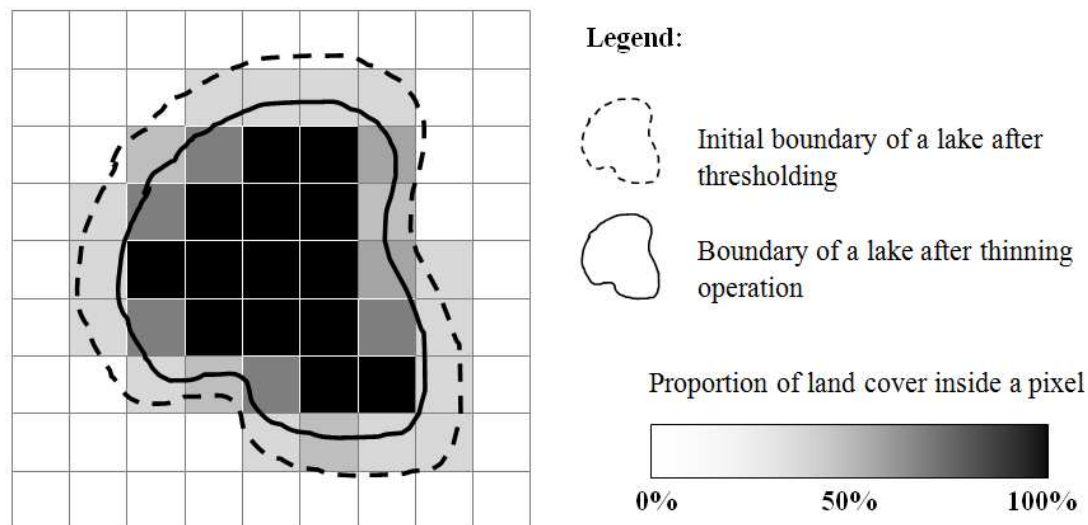
Figure 7-9 An illustration of an iterative morphological thinning filter considers area estimation from soft classification of pixels enclosed by the delineation of boundary lines to be used as a constraint while shrinking the lake.

7.4. Lake characterization

Attention focused on two main issues: the identification of lakes and the characterisation of their shape. Treating the lakes as objects, shape may be characterized in many ways (Nixon and Aguado, 2002) with a wide variety of indices used in landscape ecology (McGarigal et al, 2002). However, many of the popular landscape indices are correlated (Yang and Liu, 2005) and here focus on some standard measures: area, perimeter, length along main axis and compactness.

The simulated and real coarse spatial resolution data sets were used to derive binary land cover maps depicting the classes land and water within the test site from which the lakes could be characterised. From each data set, five maps were derived. First, a map was derived by a conventional hard image classification based on an unsupervised k-means clustering technique (Duda et al., 2001). Second and third, maps were derived by interpolation of soft classification from time series images using bilinear and bicubic interpolation techniques (Keys, 1981). Each set of the interpolation images were summed, normalized and their results were hardened. These two interpolation techniques were used as simplistic methods as a benchmark. Fourth, an established super-resolution mapping approach was used based on a standard HNN described by Tatem et al. (2001a) as formulated in Equation 3.19. The effect of the goal function and the constraint function was assumed to be equal, thus the value of the weighting coefficients k_1, k_2 and k_P were set to 1. The HNN was calculated numerically for 1000 iterations at which the HNN reach its optimum under the constraint of the parameter settings. Fifth, the proposed super-resolution mapping using the halftoning concept was used.

The accuracy with which lakes could be identified and characterised by each method applied to coarse spatial resolution imagery was evaluated relative to the depiction of the lakes in a standard hard classification of the 30 m Landsat ETM+ data (Figure 7.2b). For comparative purposes attention focused on the set of lakes in common to each derived map. To aid interpretation a set of specific lakes of interest were identified and each given a unique numerical identifier (Figure 7.2b and others). As the limitations of hard classification are well known most interest was on the relative

performance of the two super-resolution mapping techniques and two interpolation techniques. Particular concern is on the representation of the lakes, including small lakes and the value of using a time series rather than single coarse resolution image as input.

7.5. Results and discussion

A set of 5 binary land cover maps was derived from each coarse spatial resolution data set: from the hard classification, bilinear and bicubic interpolation of time series soft classification images, standard HNN, and the halftoning concept. Each map was evaluated against the ground reference data map derived from the 30 m Landsat ETM+ data (Figure 7.2b). The evaluation focused on the general representation derived in terms of the visual appearance of the lakes and the number of lakes represented as well as a more detailed assessment of the shape of the lakes that were common to all of the maps derived from the coarse spatial resolution data sets.

The limitation of the hard and soft classifications to represent land cover was evident in the outputs derived from the analyses of the simulated coarse spatial resolution data set. The hard classification provided a very blocky representation of the landscape and failed to represent many of the small lakes in the region (Figure 7.10a). The soft classification provided a richer representation but was also unable to provide a realistic representation of the actual distribution of land and water (Figure 7.10b).

Interpolation and super-resolution mapping techniques provided outputs that were much visually closer to the ground data (Figure 7.10c, 7.10d, 7.10e and 7.10f). It

was apparent, however, that more lakes, and typically small lakes, were represented in the output of the bilinear, bicubic and halftoning, than the HNN. Note, for example, that the smallest lake in the HNN output (lake 10) had an area of 0.035 km^2 (with -0.029 km^2 error). In the bilinear output, the smallest lake (20) had an area of 0.010 km^2 (-0.008 km^2), while in the bicubic output the smallest lake (19) had an area of 0.008 km^2 (-0.006 km^2) and with the PRSM output the smallest lake (19) had an area of 0.009 km^2 (-0.005 km^2). The parameter settings of the HNN used in this chapter were based on the standard practice, which place equal weights for the goal functions and the area proportion constraint of the HNN. Therefore, lakes that are smaller than a size of the spatial resolution of the MODIS 250 m could not be accurately represented using the HNN.

The characterization of the smallest lake in each of the output images was defined when the lake has the smallest area measurement compare to other lakes in the image. To eliminate artefact and not to regard them as lakes, area measurement error was calculated between lakes in the output image and their corresponding lakes in the ground data. Therefore, the characterization of the smallest lake must consider both the measurement of the area and the error. A measurement with the smallest error indicates that the map produced is highly accurate as it closely resembled the map in the ground data. The positive value of the error indicates over-estimation, which mean that the lake is mapped larger than it actual size. The negative error indicates that the lake is mapped smaller than its actual size. Based on the comparison on the smallest lakes detected in the output images, the halftoning produced more accurate representation of the smallest lake than the other outputs.

Other notable small lakes were lake 12 (HNN = not detected; bilinear = 0.080 km^2 error; bicubic = 0.078 km^2; halftoning = -0.006 km^2), lake 13 (HNN = not detected; bilinear = 0.060 km^2; bicubic = 0.069 km^2; halftoning = -0.008 km^2;), lake 15 (HNN = not detected; bilinear = -0.009 km^2; bicubic = 0.003 km^2; halftoning = -0.009 km^2), lake 16 (HNN = not detected; bilinear = not detected; bicubic = -0.009 km^2; halftoning = 0.006 km^2), and lake 21 (HNN = not detected; bilinear = 0.005 km^2; bicubic = 0.025 km^2; halftoning = 0.008 km^2). In the ground data, all these lakes were smaller than the size of a coarse spatial resolution image pixel (0.057 km^2). For these lakes, the super-resolution mapping using the halftoning concept was more consistent than other techniques in producing highly accurate area estimates when the errors were all < ±0.010 km^2.

The 5 land cover representations derived also varied in the accuracy with which they characterised shape of the individual lakes (Table 7.1 and 7.2). Only lakes that appear in all of the 5 land cover maps were selected in both tables. Although no one method was universally the most accurate some trends were apparent in the results. Critically, the super-resolution mapping using the halftoning concept tended to provide more accurate area estimates than the other outputs when the average of area estimates error was 0.023 km^2. Both interpolation techniques produced the most accurate perimeter estimates with the average error was < 0.600 km. Both interpolation techniques also produced the most accurate length estimates with the average error was < 0.130 km^2. Although hard classification produced the least average error in compactness estimates with 0.174 errors, the lakes appear to be blocky and were associated with some large over-estimates of lake area (e.g. lakes 1, 2, 3 and 6). Other

than the hard classification, the halftoning tended to produce lower average error for compactness estimates with the error was < 0.235.

Due to the influence of the spatial clustering goal function, the HNN tend to produce convex shape of land cover mapping. The limitation of this scenario is that linear features, such as lake 2, that lie diagonally in the image, tended to be split into several parts. Using the interpolation techniques, lake 2 can be represented by the width of the lake tended to be expanded. Using the halftoning technique and the iterative morphological filter, the width of the lake 2 can be retained as close as the width of the lake 2 in the ground data.

Similar general trends are apparent in the results derived from the MODIS imagery (Figure 7.11, Table 7.3 and 7.4). Critically, the halftoning included more small lakes in its output and appeared visually to provide the most accurate super-resolution map of the test site. Note for example, small lakes (e.g. lake 13 in Figure 11f, estimated area $= 0.011 \text{km}^2$, reference area $= 0.036 \text{ km}^2$) missed in the output of the HNN, bilinear and bicubic are represented in the halftoning output. In terms of the quantitative estimates of lake properties the halftoning was slightly less accurate the HNN in estimating the area of the lakes.

(a)

(b)

(c)

(d)

(e)

(f)
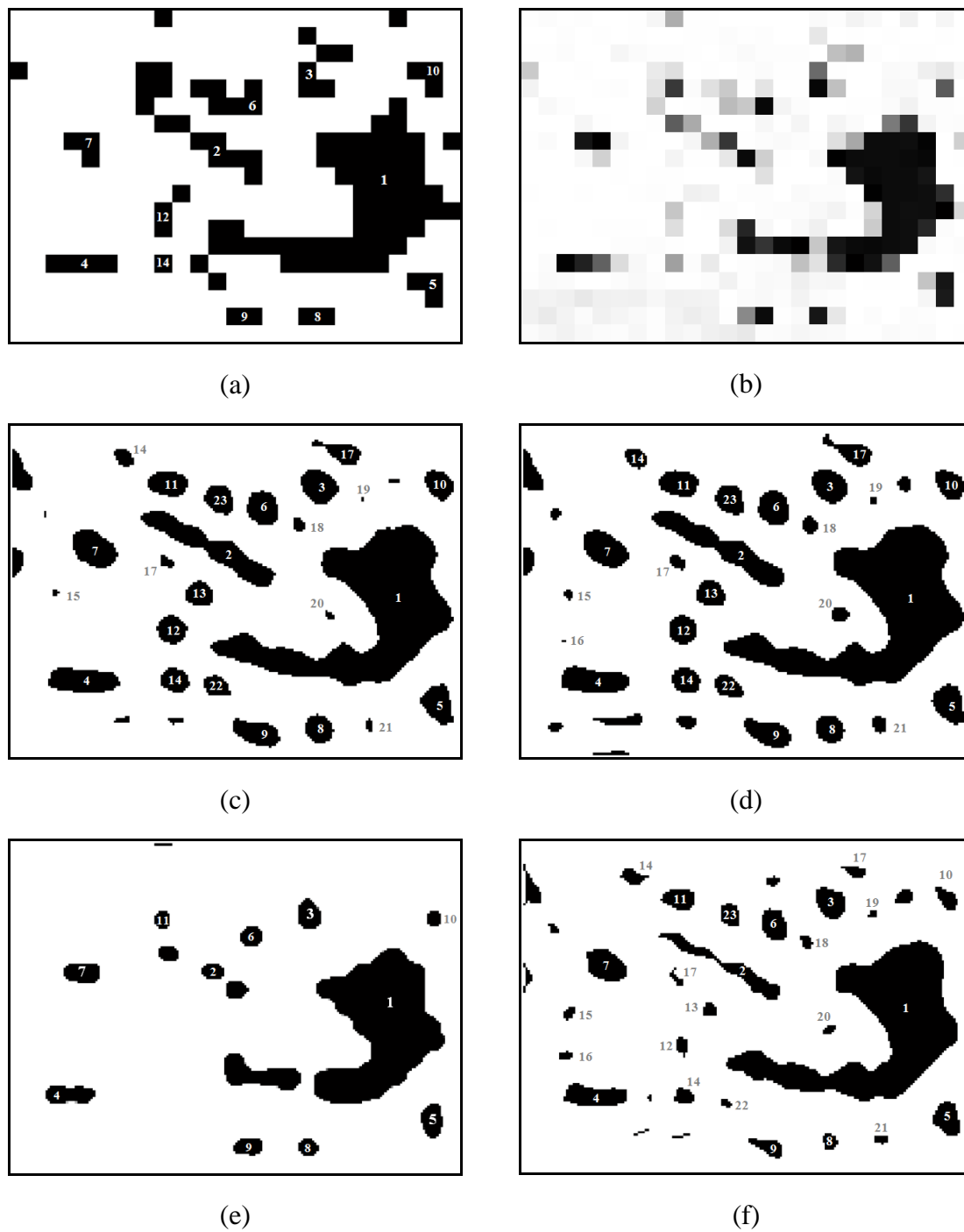
Figure 7-10 Results of the simulated coarse spatial resolution imagery. (a) the hard classification derived from a MODIS image acquired on 7 July 2002, (b) soft classification of the MODIS image, and (c) output from bilinear interpolation, (d) output from bicubic interpolation, (e) output from HNN, and (f) output from the super-resolution mapping using the halftoning concept.

234

(a)

(b)

(c)

(d)

(e)

(f)
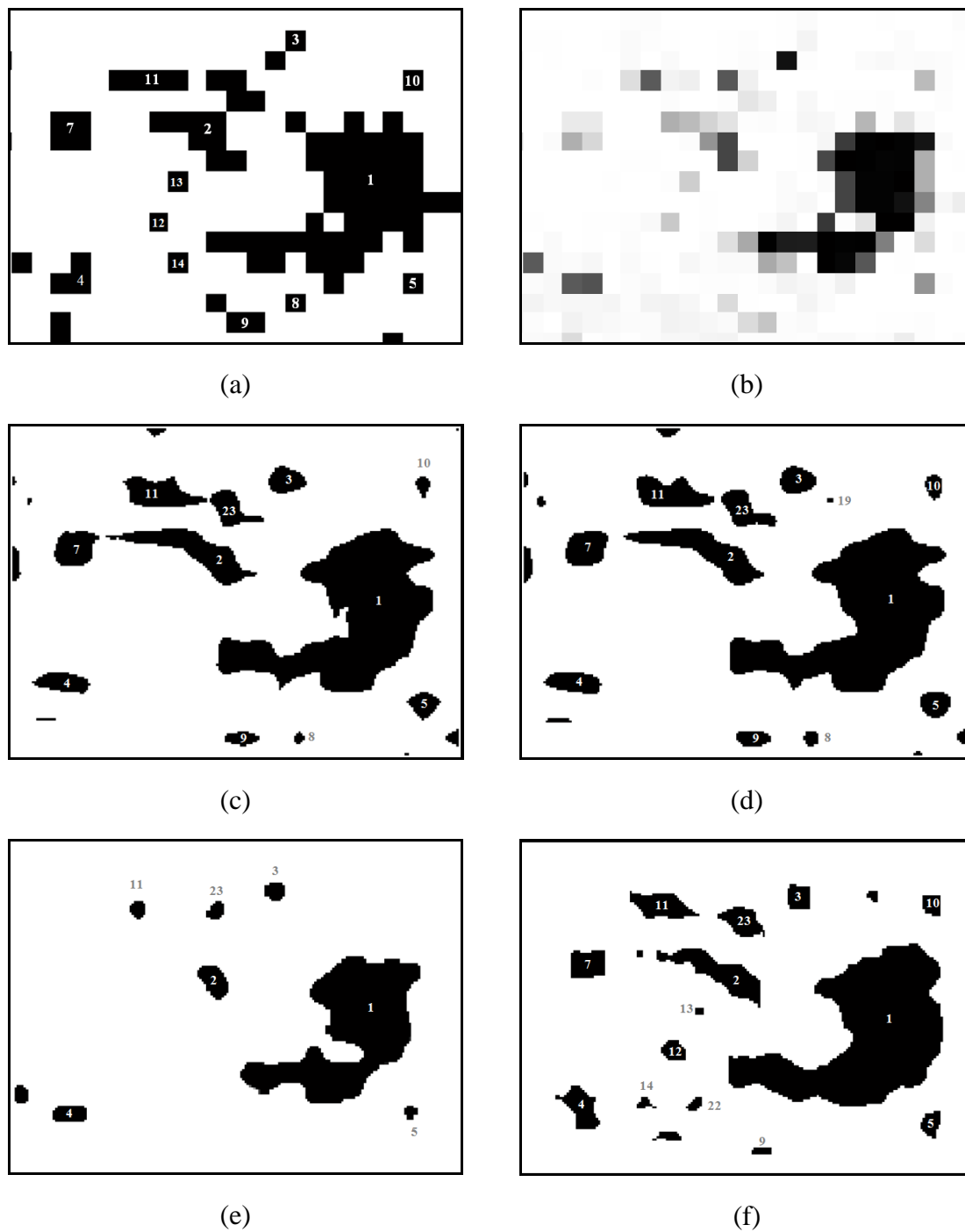
Figure 7-11 Results of the real MODIS data. (a) the hard classification derived from a MODIS image acquired on 7 July 2002, (b) soft classification of the MODIS image, and (c) output from bilinear interpolation, (d) output from bicubic interpolation, (e) output from HNN, and (f) output from the super-resolution mapping using the halftoning concept.

Table 7-1 Lake characterisations of area and perimeter from the simulated coarse spatial resolution imagery; the difference from the ground reference data is shown in brackets (positive values indicate over-estimation).

Lake	Area (km²)						Perimeter (km)					
	GD	HC	Bilinear	Bicubic	HNN	Halftoning	GD	HC	Bilinear	Bicubic	HNN	Halftoning
1	2.440	3.228	2.621	2.625	2.156	2.457	15.161	14.979	11.343	11.202	7.700	10.923
		(0.788)	(0.181)	(0.185)	(-0.284)	(0.017)		(-0.182)	(-3.818)	(-3.959)	(-7.461)	(-4.238)
2	0.255	0.750	0.486	0.484	0.052	0.248	4.591	7.237	4.630	4.503	0.809	4.105
		(0.495)	(0.231)	(0.229)	(-0.203)	(-0.007)		(2.646)	(0.039)	(-0.088)	(-3.782)	(-0.486)
3	0.102	0.346	0.170	0.162	0.102	0.127	1.340	4.320	1.473	1.546	1.159	1.386
		(0.244)	(0.068)	(0.060)	(0.000)	(0.025)		(2.980)	(0.133)	(0.206)	(-0.181)	(0.046)
4	0.169	0.230	0.251	0.244	0.139	0.183	2.924	2.400	2.269	2.202	1.609	2.087
		(0.061)	(0.082)	(0.075)	(-0.030)	(0.014)		(-0.524)	(-0.655)	(-0.722)	(-1.315)	(-0.837)
5	0.112	0.173	0.161	0.164	0.112	0.120	1.636	1.932	1.581	1.726	1.249	1.351
		(0.061)	(0.049)	(0.052)	(0.000)	(0.008)		(0.296)	(-0.055)	(0.090)	(-0.387)	(-0.285)
6	0.081	0.346	0.152	0.152	0.068	0.113	1.309	3.397	1.459	1.436	0.899	1.384
		(0.265)	(0.071)	(0.071)	(-0.013)	(0.032)		(2.088)	(0.150)	(0.127)	(-0.410)	(0.075)
7	0.136	0.173	0.220	0.212	0.116	0.174	1.752	1.932	1.803	1.738	1.289	1.554
		(0.037)	(0.084)	(0.076)	(-0.020)	(0.038)		(0.180)	(0.051)	(-0.014)	(-0.463)	(-0.198)
8	0.066	0.115	0.111	0.111	0.052	0.034	1.312	1.440	1.272	1.284	0.779	0.687
		(0.049)	(0.045)	(0.045)	(-0.014)	(-0.032)		(0.1280)	(-0.040)	(-0.028)	(-0.533)	(-0.753)
9	0.117	0.115	0.159	0.162	0.079	0.069	2.199	1.440	1.731	1.676	1.024	1.219
		(-0.002)	(0.042)	(0.045)	(-0.038)	(-0.048)		(-0.759)	(-0.468)	(-0.523)	(-1.175)	(-0.980)
10	0.064	0.173	0.113	0.116	0.035	0.057	1.264	1.932	1.306	1.302	0.639	0.964
		(0.109)	(0.049)	(0.052)	(-0.029)	(-0.007)		(0.668)	(0.042)	(0.038)	(-0.625)	(-0.300)
Average Error		0.211	0.090	0.089	0.063	0.023		1.045	0.545	0.578	1.633	0.820

GD = Ground data; HC = Hard classification; HNN = standard Hopfield neural network.

Table 7-2 Lake characterisations of length and compactness from the simulated coarse spatial resolution imagery; the difference from the ground reference data is shown in brackets (positive values indicate over-estimation).

Lake	Length (km)						Compactness					
	GD	HC	Bilinear	Bicubic	HNN	Halftoning	GD	HC	Bilinear	Bicubic	HNN	Halftoning
1	3.608	3.729	3.325	3.278	8.658	3.167	0.133	0.181	0.256	0.263	0.457	0.259
		(0.121)	(-0.283)	(-0.330)	(5.050)	(-0.441)		(0.048)	(0.123)	(0.130)	(0.324)	(0.078)
2	2.069	2.009	2.006	2.019	0.360	1.854	0.152	0.180	0.285	0.300	1.002	0.185
		(-0.060)	(-0.063)	(-0.050)	(-1.709)	(-0.215)		(0.028)	(0.133)	(0.148)	(0.850)	(0.033)
3	0.480	0.883	0.570	0.540	0.480	0.480	0.656	0.233	0.982	0.853	0.956	0.833
		(0.403)	(0.090)	(0.060)	(0.000)	(0.000)		(-0.423)	(0.326)	(0.197)	(0.300)	(0.177)
4	1.170	1.020	1.020	0.960	0.720	0.900	0.248	0.503	0.612	0.634	0.676	0.529
		(-0.150)	(-0.150)	(-0.210)	(-0.450)	(-0.270)		(0.255)	(0.364)	(0.386)	(0.428)	(0.281)
5	0.510	0.540	0.600	0.600	0.540	0.510	0.527	0.582	0.807	0.692	0.904	0.828
		(0.030)	(0.090)	(0.090)	(0.030)	(0.000)		(0.055)	(0.280)	(0.165)	(0.377)	(0.301)
6	0.480	1.108	0.510	0.510	0.360	0.480	0.593	0.377	0.896	0.925	1.065	0.739
		(0.628)	(0.030)	(0.030)	(-0.120)	(0.000)		(-0.216)	(0.303)	(0.332)	(0.472)	(0.146)
7	0.540	0.540	0.660	0.660	0.540	0.600	0.558	0.582	0.850	0.882	0.878	0.903
		(0.000)	(0.120)	(0.120)	(0.000)	(0.060)		(0.024)	(0.292)	(0.324)	(0.320)	(0.345)
8	0.497	0.540	0.450	0.450	0.330	0.270	0.484	0.698	0.867	0.847	1.083	0.905
		(0.043)	(-0.047)	(-0.047)	(-0.167)	(-0.227)		(0.214)	(0.383)	(0.363)	(0.599)	(0.421)
9	0.913	0.540	0.690	0.690	0.450	0.510	0.303	0.698	0.665	0.725	0.949	0.581
		(-0.373)	(-0.223)	(-0.223)	(-0.463)	(-0.403)		(0.395)	(0.362)	(0.422)	(0.646)	(0.278)
10	0.390	0.540	0.480	0.450	0.270	0.360	0.503	0.582	0.830	0.858	1.065	0.769
		(0.150)	(0.090)	(0.060)	(-0.120)	(-0.030)		(0.079)	(0.327)	(0.355)	(0.562)	(0.266)
Average Error		0.196	0.119	0.122	0.811	0.165		0.174	0.289	0.282	0.488	0.233

GD = Ground data; HC = Hard classification; HNN = standard Hopfield neural network.

Table 7-3 Lake characterisations of area and perimeter from the MODIS imagery; the difference from the ground reference data is shown in brackets (positive values indicate over-estimation).

Lake	Area (km^2)						Perimeter (km)					
	GD	HC	Bilinear	Bicubic	HNN	Halftoning	GD	HC	Bilinear	Bicubic	HNN	Halftoning
1	2.440	3.303	3.159	3.225	2.158	3.096	15.161	15.844	12.221	11.573	9.845	10.471
		(0.863)	(0.719)	(0.785)	(-0.282)	(0.656)		(0.683)	(-2.940)	(-3.588)	(-5.316)	(-4.690)
2	0.255	0.750	0.525	0.542	0.128	0.376	4.591	6.500	4.977	4.809	1.364	3.847
		(0.495)	(0.270)	(0.287)	(-0.127)	(0.121)		(1.909)	(0.386)	(0.218)	(-3.227)	(-0.744)
3	0.090	0.125	0.148	0.150	0.056	0.090	1.340	2.000	1.496	1.399	0.879	1.195
		(0.023)	(0.046)	(0.048)	(-0.046)	(0.000)		(0.660)	(0.156)	(0.059)	(-0.461)	(-0.145)
4	0.169	0.188	0.162	0.181	0.087	0.178	2.924	2.000	2.001	1.981	1.149	2.043
		(0.019)	(-0.007)	(0.012)	(-0.082)	(0.009)		(-0.924)	(-0.923)	(-0.943)	(-1.775)	(-0.881)
5	0.112	0.063	0.110	0.124	0.025	0.069	1.636	1.000	1.426	1.329	0.637	1.109
		(-0.049)	(-0.002)	(0.012)	(-0.087)	(-0.043)		(-0.636)	(-0.210)	(-0.307)	(-0.999)	(-0.527)
23	0.057	x	0.187	0.213	0.043	0.154	1.174	x	2.216	2.336	0.814	1.856
			(0.130)	(0.156)	(-0.014)	(0.097)			(1.042)	(1.162)	(-0.360)	(0.682)
11	0.088	0.250	0.317	0.326	0.037	0.209	1.242	2.500	3.058	2.799	0.689	2.209
		(0.162)	(0.229)	(0.238)	(-0.051)	(0.121)		(1.258)	(1.816)	(1.557)	(-0.553)	(0.967)
Average Error		0.269	0.200	0.220	0.098	0.150		1.012	1.068	1.119	1.813	1.234

GD = Ground data; HC = Hard classification; HNN = standard Hopfield neural network.

Table 7-4 Lake characterisations of length and compactness from the MODIS imagery; the difference from the ground reference data is shown in brackets (positive values indicate over-estimation).

Lake	Length (km)						Compactness					
	GD	HC	Bilinear	Bicubic	HNN	Halftoning	GD	HC	Bilinear	Bicubic	HNN	Halftoning
1	3.608	3.515	3.215	3.120	3.165	2.955	0.133	0.165	0.266	0.303	0.280	0.355
		(-0.093)	(-0.393)	(-0.488)	(-0.443)	(-0.653)		(0.032)	(0.133)	(0.170)	(0.147)	(0.222)
2	2.069	1.500	2.172	2.126	0.510	1.491	0.152	0.223	0.267	0.295	0.864	0.319
		(-0.569)	(0.103)	(0.057)	(-1.559)	(-0.578)		(0.071)	(0.115)	(0.143)	(0.712)	(0.167)
3	0.480	0.500	0.600	0.570	0.330	0.390	0.656	0.393	0.829	0.965	0.903	0.795
		(0.020)	(0.120)	(0.090)	(-0.150)	(-0.150)		(-0.263)	(0.173)	(0.309)	(0.247)	(0.139)
4	1.170	0.500	0.870	0.870	0.510	0.660	0.248	0.591	0.509	0.579	0.853	0.536
		(-0.670)	(-0.300)	(-0.300)	(-0.660)	(-0.090)		(0.343)	(0.261)	(0.331)	(0.605)	(0.288)
5	0.510	0.250	0.540	0.480	0.240	0.420	0.527	0.792	0.683	0.881	0.766	0.670
		(-0.260)	(0.030)	(-0.030)	(-0.270)	(-0.090)		(0.265)	(0.156)	(0.354)	(0.239)	(0.143)
23	0.450	x	0.868	0.927	0.300	0.690	0.522	x	0.480	0.490	0.816	0.563
			(0.418)	(0.477)	(-0.150)	(0.240)			(-0.042)	(-0.032)	(0.522)	(0.041)
11	0.540	1.000	1.258	1.140	0.300	0.990	0.720	0.503	0.425	0.522	1.048	0.539
		(0.460)	(0.718)	(0.600)	(-0.240)	(0.450)		(-0.217)	(-0.295)	(-0.198)	(0.328)	(-0.181)
Average Error		0.345	0.297	0.292	0.496	0.322		0.199	0.168	0.220	0.400	0.169

GD = Ground data; HC = Hard classification; HNN = standard Hopfield neural network

7.6.   Conclusions

The potential of a novel super-resolution mapping based on the haltoning concept for the representation of lakes has been evaluated. Both super-resolution mapping approaches, the proposed technique and the standard HNN, were able to provide land cover representations that were typically more accurate and realistic than the standard hard classification. The new super-resolution mapping method proposed in this chapter also maintained information on small lakes and so was able to identify and characterise more lakes than the established method. It was also shown that the use of a series of images rather than a single image can increase the accuracy of super-resolution mapping. This allows researchers to exploit the typically fine temporal resolution of coarse spatial resolution sensors for land cover mapping applications.

8. Conclusions

This thesis has been concerned with increasing the accuracy of super-resolution mapping of land cover from remotely sensed imagery. Two standard super-resolution mapping techniques were used: HNN and pixel swapping. Both techniques, especially the HNN, have been widely used in representing land cover patches from coarse spatial resolution imagery. In addition, a novel super-resolution mapping technique based on a halftoning concept is also proposed, developed and compared with the standard techniques.

Representation of land cover patches smaller than an image pixel is a very challenging task and poses some crucial problem even for existing standard super-resolution mapping techniques. There are not many published works about the representation of land cover patches smaller than an image pixel. Most of the attention of the previous works focuses on land cover patches larger than an image pixel. Not only do the existing techniques have difficulty in representing small land cover patches, they also have high difficulty in locating the patches

This chapter presents the main innovations of this thesis by summarizing several important findings presented in Chapter 4, 5, 6, and 7.

8.1. Summary

The overall aim of this thesis was to represent land cover patches of different sizes, shapes and spatial configuration of landscape mosaic, although the attention is focused especially on the small land cover patches. Most previous works assumed that the land cover patches are large. For instance, the parameter settings of the HNN only suitable for the representation of the large land cover patches. The effects of the parameter settings have not been fully investigated. Experiments in Chapter 4 demonstrated that the HNN was good for the representation of large land cover patches but poor for the small patches. However, the parameter settings for the HNN can be adjusted for the small patches. By placing more emphasis on the area proportion constraints than the goal functions of the HNN, and setting high iteration number, land cover patches smaller than a pixel can be represented.

Even when the small land cover patches can be represented, inaccurate spatial location prediction may increase the spatial variability of the patches. Consequently, the accuracy of the site specific assessment may be decreased, although the non-site specific assessment may be increased. This scenario could lead to the misinterpretation in the decision making when only one type of assessment is employed. Chapter 5 demonstrated that by using a fusion of multiple sub-pixel shifted coarse spatial resolution images with the HNN and pixel swapping techniques, the representation of small land cover patches can be predicted at accurate locations, increasing both the site and non-site specific accuracy assessments.

The HNN and pixel swapping algorithms were applied to MODIS 250 m imagery in Chapter 6. Here, the best outcomes derived from two different HNN configurations were combined. The first HNN placed equal emphasis on the goal functions and the area proportion constraint, HNN(E). The HNN(E) was suitable for large land cover patches representation. The second HNN placed more emphasis on the area proportion constraint than that of the goal functions, HNN(A). The HNN(A) was suitable for small land cover patches representation. The combination of the two HNNs was called HNN_2. This chapter also demonstrated that applications that used a fusion of time series MODIS 250 m images tended to produce better results in a series of assessments than by using only a single MODIS image.

A novel super-resolution mapping technique based on halftoning concept presented in Chapter 7 offers a different paradigm than many of the current techniques. In this chapter, an orderly initial allocation of the hard classifier at a sub-pixel scale inside a mixed pixel leads to the determination of apparent spatial frequency components, which could be exploited using frequency domain based techniques such as a 2D multiple notch filter. The number of iteration of this technique was lower than that in the HNN and pixel swapping techniques. This chapter also demonstrated the applications of the novel technique using MODIS 250 m imagery for lake characterization.

In addition, all the results obtained suggest considerable potential to enhance the value of coarse spatial resolution imagery such as MODIS 250 m for land cover mapping and patches representation. The focus of this thesis is on the application of representing lakes. Across the Arctic, there are abundance of lakes, but many of them

are shrinking and even vanished and turned into vegetation. The extent of the area across the Arctic region is wide; therefore observations on this region required remote sensing systems with wide coverage, such as MODIS, MERIS, and AVHRR (Weiss and Crabtree, 2011). Images of these systems are typically of coarse spatial resolution. Using super-resolution mapping on these images may increase the accuracy of earth observations.

Several parameters estimated from the lakes, such as area, perimeter, and spatial configuration of the landscape mosaic can be linked to the evaluation of environmental and ecological systems on that region. As water is essential for living creature, such as human and animals, the estimation of the area and the length of the shoreline of the lakes may provide linkage to the estimation of population of animals and their ecological systems in that region. The estimation accuracy of the ecological systems can be increased when the characteristics of the lakes is highly accurate.

Estimation of the area, perimeter and spatial configuration of landscape mosaic of lakes can also be useful to study the disappearing pattern of the Arctic lakes, which can be assessed by comparing images of different years or even decades. Based on the lakes characterization, the rate of the lake shrinkage can be estimated. This phenomenon may have several impacts on the wildlife, the environment, the weather and the ocean circulation pattern. The earlier indicator resulted from the shrinking and the vanishing phenomenon will be on the migratory of birds, fish and other wildlife. Therefore, the advantages of the super-resolution mapping can also be expanded to ecological and environmental studies (Cott et al., 2008).

8.2. Contributions

The main achievements of this thesis can be outlined as follows:

- Highlighting a limitation of the HNN for the representation of small land cover patches.

- Improvement on the standard HNN for the representation of small land cover patches.

- Identifying the best parameters of the HNN for the representation of land cover patches of different sizes, shapes and mosaic.

- Highlighting limitations of the HNN and pixel swapping for predicting the spatial location of land cover patches.

- A novel algorithm based on a derivation of quadrants in a mixed pixel that helps to predict the spatial location of the land cover patches.

- An approach that uses a fusion of time series coarse spatial resolution images as input data for super-resolution mapping techniques.

- A novel technique based on the Halftoning concept that provides low iterative solution for the land cover mapping at a sub-pixel scale.

8.3.   Future works

Results obtained from this study suggest a considerable potential for extending the investigation of the HNN_2 and the new super-resolution mapping technique based on the halftoning concept. Although the experiments conducted are limited to binary classification, the improved HNN and the new super-resolution mapping technique based on halftoning concept can be used for multiclass applications provided that multiple spectrum bands of remotely sensed imagery are available. The binary class representation demonstrated in this chapter also is not limited to the lakes representation, but can be extended to binary related situations, such as deforestation, flooding, diseases and many more. However, multiclass super-resolution mapping solution will provide more widely applications than the binary super-resolution mapping solution. In relating to the representation of small land cover patches, representing several land cover of different classes inside a mixed pixel will ultimately solve one of the mixed pixel problem, which is the existence of multiclass sub-pixel sized land cover. Therefore, allowing different small land covers, such as small lakes, small area of vegetation, and small area of urbanization to be represented using an integrated solution, and not representing them separately using the binary super-resolution mapping solutions.

Several parameters of the HNN_2 and the halftoning based super-resolution mapping techniques need further refinements. For the HNN_2, the refinements should minimize the number of iteration. Low number of iteration would be beneficial especially for applications that use large datasets. For the halftoning based super-resolution mapping technique, the refinements could possibly be on the improvement of

the dither matrix, used to create a dot pattern, and the 2D multiple notch filter in order to minimize artefacts.

The algorithm for the image fusion also needs to cater for images of different spatial resolution. Here, the quadrant algorithm in Chapter 5 needs to be improved in order to derive quadrants of different sizes and shapes.

In this thesis, two types of remotely sensed imagery from two different sensors were used. The first was the near infrared band of the Terra MODIS 250 m images with the wavelength is 0.841-0.876 µm. Second, the near infrared band of the Landsat ETM+ 30 m image with the wavelength is 0.750-0.900 µm. The Landsat image was used as a ground data. The relative spectral response (RSR) of the MODIS and Landsat ETM+ sensors may be different and need to be investigated. To ensure that the results of super-resolution mapping that uses the input MODIS imagery closely resemble the mapping of land covers in the Landsat image (ground data), the spectral band of the MODIS imagery need to be adjusted with regard to the spectral band of the Landsat image in order to provide more accurate cross-calibration between the sensors (Chander et al., 2010). This pre-processing stage may increase the accuracy of super-resolution mapping. This approach may also be applied to different remote sensing images.

In wider scale, the HNN_2 and the halftoning based super-resolution mapping techniques can potentially be applied to the low cost coarse spatial resolution image systems to provide information to support global monitoring systems, such as in relation to issues such as land cover change and global warming. Typically, the coarse spatial resolution image has fine temporal resolution allowing the monitoring of the dynamic of

the land cover such as lakes over a period of time. Historical archived satellite images can be compared with contemporary satellite data to monitor ongoing changes of the Arctic lakes (Riordan et al., 2006). The changes of the landscape in that region or even in other regions may be explored in the future as new directions for the super-resolution mapping techniques.

Bibliography

Addink, E.A., De Jong, S.M., Davis, S.A., Dubyanskiy, V., Burdelov, L.A. and Leirs, H. (2010), The use of high-resolution remote sensing for plague surveillance in Kazakhstan, Remote Sensing of Environment. **114**, 674-681.

Akgun, T., Altunbasak, Y. and Mersereau, R.M. (2005), Super-resolution reconstruction of hyperspectral images, IEEE Transactions on Image Processing. **14**(11), 1860-1875.

Atkinson, P.M. (1997), Mapping sub-pixel boundaries from remotely sensed images, In Kemp, Z. (Ed.), Innovations in GIS IV. Taylor and Francis, London, 166-180.

Atkinson, P.M. (2004), Resolution manipulation and sup-pixel mapping, In de Jong, S.M., van der Meer, F.K. (Eds.), Remote Sensing Image Analysis: Including the Spatial Domain. Kluwer Academic, New York, 51-70.

Atkinson, P.M. (2005), Sub-pixel target mapping from soft-classified, remotely sensed imagery, Photogrammetric Engineering and Remote Sensing. **71**(7), 839-846.

Atkinson, P.M. (2008), Super-resolution mapping using the two-point histogram and multi-source imagery, In Soares, A., Pereira, M.J., Dimitrakopoulos, R. (Eds) geoENV VI - Geostatistics for Environmental Applications. Springer Netherlands, **15**, 307-321.

Atkinson, P.M., Cutler, M.E.J. and Lewis, H. (1997), Mapping sub-pixel proportional land cover with AVHRR imagery, International Journal of Remote Sensing. **18**(4), 917-935.

Atkinson, P.M., Pardo-Iguzquiza, E. and Chica-Olmo, M. (2008), Downscaling cokriging for super-resolution mapping of continua in remotely sensed images, IEEE Transactions on Geoscience and Remote Sensing. **46**(2), 573-589.

Baker, S. and Kanade, T. (2002), Limits on super-resolution and how to break them, IEEE Transactions on Pattern Analysis and Machine Intelligence. **24**(9), 1167-1183.

Barrett, H.H. and Myers, K.J. (2004), Foundations of Image Science, John Wiley & Sons, New Jersey.

Bastin, L. (1997), Comparison of fuzzy c-means classification, linear mixture modelling and MLC probabilities as tools for unmixing coarse pixel, International Journal of Remote Sensing. **18**(17), 3629-3648.

Bayer, B.E. (1973). An optimum method for two level rendition of continuous-tone pictures. IEEE International Conference on Communications, Seattle, Washington, USA., June 11-13.

Benson, B.J. and MacKenzie, M.D. (1995), Effects of sensor spatial resolution on landscape structure parameters, Landscape Ecology. **10**(2), 113-120.

Bezdek, J.C. (1981), Pattern recognition with fuzzy objective function algorithm, Plenum Press, New York.

Bezdek, J.C., Ehrlich, R. and Full, W. (1984), FCM: The fuzzy c-means clustering algorithm, Computer and Geosciences. **10**, 191-203.

Blaschke, T. (2010), Object based image analysis for remote sensing, ISPRS Journal of Photogrammetry Remote Sensing. **65**, 2-16.

Borel, C.C. and Gerstl, S.A.W. (1994), Nonlinear spectral mixing models for vegetative and soil surfaces, Remote Sensing of Environment. **47**, 403-416.

Boucher, A. (2009), Sub-pixel mapping of coarse satellite remote sensing images with stochastic simulations from training images, Mathematical Geosciences. **41**, 265-290.

Boucher, A. and Kyriakidis, P.C. (2006), Super-resolution land cover mapping with indicator geostatistics, Remote Sensing of Environment. **104**, 264-282.

Boyd, D.S. and Foody, G.M. (2011), An overview of recent remote sensing and GIS based research in ecological informatics, Ecological Informatics. **6**, 25-36.

Brink, A.B. and Eva, H.D. (2009), Monitoring 25 years of land cover change dynamics in Africa: A sample based remote sensing approach, Applied Geography. **29**, 501-512.

Brown, M., Lewis, H.G. and Gunn, S.R. (2000), Linear spectral mixture models and support vector machines for remote sensing, IEEE Transactions on Geoscience and Remote Sensing. **38**(5), 2346-2360.

Buermann, W., Saatchi, S., Smith, T.B., Zutta, B.R., Chaves, J.A., Mila, B. and Graham, C.H. (2008), Predicting species distributions accross the Amazonian and Andean regions using remote sensing data, Journal of Biogeography. **35**, 1160-1176.

Carpenter, G.A., Gopal, S., Macomber, S., Martens, S. and Woodcock, C.E. (1999), A neural network method for mixture estimation for vegetation mapping, Remote Sensing of Environment. **70**(2), 138152.

Chander, G., Mishra, N., Helder, D.L., Aaron, D., Choi, T., Angal, A. and Xiong, X. (2010). Use of EO-1 Hyperion data to calculate spectral band adjustment factos (SBAF) between

the L7 ETM+ and Terra Modis Sensors. IEEE International Geoscience and Remote Sensing Symposium (IGARSS), Honolulu, Hawaii, USA, 25-30 July 2010.

Congalton, R.G. and Green, K. (2009), Assessing the Accuracy of Remotely Sensed Data: Principles and Practices, CRC Press, Boca Raton, FL.

Cote, S. and Tatnall, A.R.L. (1997), The Hopfield neural network as a tool for feature tracking and recognition from satellite sensor images, International Journal of Remote Sensing. **18**(4), 871-885.

Cott, P.A., Sibley, P.K., Somers, W.M., Lilly, M.R. and Gordon, A.M. (2008), A review of water level fluctuations on aquatic biota with an emphasis of fishes in ice-covered lakes, Journal of the American Water Resources Association. **44**(2), 343-359.

Cracknell, A.P. (1998), Synergy in remote sensing - what's in a pixel? International Journal of Remote Sensing. **19**(11), 2025-2047.

Daubechies, I. (1992), Ten lectures on wavelet, SIAM, Philadelphia, PA.

Davies, E.R. (2005), Machine Vision: Theory, Algorithms, Practicalities (Signal Processing and Its Applications), Morgan Kaufmann, San Francisco, CA.

Duda, R.O. and Hart, P.E. (1972), Use of the Hough transformation to detect lines and curves in pictures, Communicaton of the ACM. **15**(1), 11-15.

Duda, R.O., Hart, P.E. and Stork, D.G. (2001), Pattern Classification and Scene Analysis, 2nd ed. John Wiley & Sons, New York.

Dunn, J.C. (1973), A fuzzy relative of the ISODATA process and its use in detecting compact well-separated clusters, Journal of Cybernetics. **3**, 32-57.

Elad, M. and Feuer, A. (1997), Restoration of a Single Superresolution Image from Several Blurred, Noisy, and Undersampled Measured Images, IEEE Transactions on Image Processing. **6**(12), 1646-1658.

Falcucci, A., Maiorano, L. and Boitani, L. (2007), Changes in land-use/land-cover patterns in Italy and their implications for biodiversity conservation, Landscape Ecology. **22**, 617-631.

Fisher, P. (1997), The pixel: a snare or a delusion, International Journal of Remote Sensing. **18**(3), 679-685.

Fisher, P.F. and Pathirana, S. (1990), The evalution of fuzzy membership of land cover classes in the suburban zone, Remote Sensing of Environment. **34**, 121-132.

Fonseca, L.M.G. and Manjunath, B.S. (1996), Registration techniques for multisensor remotely sensed imagery, Photogrammetric Engineering and Remote Sensing. **62**, 1049-1056.

Foody, G.M. (1996), Approaches for the production and evaluation of fuzzy land cover classifications from remotely-sensed data, International Journal of Remote Sensing. **17**(7), 1317-1340.

Foody, G.M. (1999), The significance of border training patterns in classification by a feedforward neural network using back propagation learning, International Journal of Remote Sensing. **20**(18), 3549-3562.

Foody, G.M. (2000), Estimation of sub-pixel land cover composition in the presence of untrained classes, Computers and Geosciences. **26**, 469-478.

Foody, G.M. (2001), Thematic mapping from remotely sensed data with neural networks: MLP, RBF and PNN based approaches, Journal of Geographical Systems. **3**, 217-232.

Foody, G.M. (2002), Status of land cover classification accuracy assessment, Remote Sensing of Environment. **80**, 185-201.

Foody, G.M. (2005), Sub-pixel methods in remote sensing, In de Jong, S.M. and van der Meer, F.K. (Eds) Remote Sensing Image Analysis: Including the Spatial Domain, Springer, New York, 36-49.

Foody, G.M. and Arora, M.K. (1997), An evaluation of some factors affecting the accuracy of classification by an artificial neural network, International Journal of Remote Sensing. **18**(4), 799-810.

Foody, G.M., Campbell, N.A., Trodd, N.M. and Wood, T.F. (1992), Derivation and applications of probabilistic measures of class membership from the maximum likelihood classification, Photogrammetric Engineering and Remote Sensing, **58**, 1335-1341.

Friedl, M.A., McIver, D.K., Hodges, J.C.F., Zhang, X.Y., Muchoney, D., Strahler, A.H., Woodcock, C.E., Gopal, S., Schneider, A., Cooper, A., Baccini, A., Gao, F. and Schaaf, C. (2002), Global land cover mapping from MODIS: algorithms and early results, Remote Sensing of Environment. **83**, 287-302.

Geman, S. and Geman, D. (1984), Stochastic relaxation, Gibbs distributions, and the Bayesian restoration of images, IEEE Transactions on Pattern Analysis and Machine Intelligence. **6**, 721-741.

Goward, S. N., Arvidson, T., Williams, D. L., Irish, R., Irons, J. R. (2009), Moderate spatial resolution optical sensors, In Warner, T. A., Nellis, M. D., Foody, G. M. (Eds) The SAGE Handbook of Remote Sensing, Sage, London, 123-138.

Gu, Y., Zhang, Y. and Zhang, J. (2008), Integration of spatial-spectral information for resolution enhancement in hyperspectral images, IEEE Transactions on Geoscience and Remote Sensing. **46**(5), 1347-1358.

Haralick, R.M., Shanmugam, K. and Dinstein, I. (1973), Textural features for image classification, IEEE Transactions on Systems, Man and Cybernetics. **SMC-3**(6), 610-621.

Haykin, S. (1999), Neural Network: A Comprehensive Foundation, Prentice-Hall, New Jersey.

Hopfield, J.J. (1982), Neural networks and physical systems with emergent collective computational abilities, Proceedings of the National Academy of Sciences, USA. (79), 2554-2558.

Hopfield, J.J. (1984). Neurons with graded response have collective computational properties like those of two-state neurons. Proceedings of the National Academy of Sciences, USA.

Hough, P.V.C. (1962), Method and means for recognizing complex patterns. U.S. Patent 3069654, December 18, 1962,

http://glovis.usgs.gov/

https://lpdaac.usgs.gov/

Hu, M.G., Wang, J.F. and Ge, Y. (2009), Super-resolution reconstruction of remote sensing images using multifractal analysis, Sensors. **9**(11), 8669-8683.

Irani, M. and Peleg, S. (1991), Improving resolution by image registration, Computer Vision, Graphics and Image Processing: Graphical Models and Image Processing. **53**(3), 231-239.

Justice, C.O. and Tucker, C.J. (2009), Coarse spatial resolution optical sensors, In Warner, T. A., Nellis, M. D., Foody, G. M. (Eds) The SAGE Handbook of Remote Sensing, Sage, London, 139-150.

Kasetkasem, T., Arora, M.K. and Varshney, P.K. (2005), Super-resolution land cover mapping using a Markov random field based approach, Remote Sensing of Environment. **96**, 302-314.

Keys, R. (1981), Cubic convolution interpolation for digital image processing, IEEE Transactions on Acoustics, Speech, and Signal Processing. **29**(6), 1153-1160.

Kim, S.P. and Su, W.-Y. (1993), Recursive high-resolution reconstruction of blurred multiframe images, IEEE Transactions on Image Processing. **2**(4), 534-539.

Kim, S.P., Bose, N.K. and Valenzuela, H.M. (1990), Recursive reconstruction of high resolution image from noisy undersampled multiframes, IEEE Transactions on Acoustics, Speech, and Signal Processing. **38**(6), 1013-1027.

Kite, T.D. (1998), PhD Thesis: Design and quality assessment of forward and inverse error diffusion haltoning algorithms, The University of Texas at Austin.

Kite, T.D., -Venkata, N.D., Evans, B.L. and Bovic, A.C. (2000), A fast, high-quality inverse halftoning algorithm for error diffused halftones, IEEE Transactions on Image Processing. **9**(9), 1583-1592.

Krishnapuram, R. and Keller, J.M. (1993), A possibilistic approach to clustering, IEEE Transactions on Fuzzy Systems. **1**(2), 98-110.

Krishnapuram, R. and Keller, J.M. (1996), The possibilistic c-means algorithm: insights and recommendations, IEEE Transactions on Fuzzy Systems. **4**(3), 385-393.

Lam, L., Lee, S.W. and Suen, C.Y. (1992), Thinning methodologies - A comprehensive survey, IEEE Transactions on Pattern Analysis and Machine Intelligence. **14**(9), 869-885.

Lau, D.L. and Arce, G.R. (2001), Modern Digital Halftoning, Marcel Dekker, Inc., New York.

Li, F., X.P., J., Frazer, D. and Lambert, A. (2010), Super resolution for remote sensing images based on a universal hidden Markov tree model, IEEE Transactions on Geoscience and Remote Sensing. **48**(3), 1270-1278.

Liang, S., Schaepman, M., Jackson, T., Jupp, D., Li, X., Liu, J., Liu, R., Strahler, A., Townshend, J. and Wickland, D. (2008), Emerging issues in land remote sensing, In Liang, S. (Ed.) Advances in Land Remote Sensing: Systems, Modelling, Inversion and Application, Springer, 485-494.

Ling, F., Du, Y., Xiao, F., Xue, H. and Wu, S. (2010), Super-resolution land-cover mapping using multiple sub-pixel shifted remotely sensed images, International Journal of Remote Sensing. **31**(19), 5023-5040.

Liu, W., Seto, K.C., Wu, E.Y., Gopal, S. and Woodcock, C.E. (2004), ART-MMAP: A neural network approach to subpixel classification, IEEE Transactions on Geoscience and Remote Sensing. **42**(9), 1976-1983.

Lu, Y. and Inamura, M. (2003), Spatial resolution improvement of remote sensing images by fusion of subpixel-shifted multi-observation images, International Journal of Remote Sensing. **24**(23), 4647-4660.

Lucas, N.S., Shanmugam, S. and Barnsley, M. (2002), Sub-pixel habitat mapping of a coastal dune ecosystem, Applied Geography. **22**, 253-270.

Lucas, R., Rowlands, A., Brown, A., Keyworth, S. and Bunting, P. (2007), Rule-based classification of multi-temporal satellite imagery for habitat and agricultural land cover mapping, ISPRS Journal of Photogrammetry and Remote Sensing. **62**, 165-185.

Mallat, S.G. (1989), A theory for multiresolution signal decomposition: the wavelet representation, IEEE Transactions on Pattern Analysis and Machine Intelligence. **11**(7), 674-693.

Matheron, G. (1965), Les variables régionalisées et leur estimation. Paris, Masson et Cie.

Mathur, A. and Foody, G.M. (2008), Crop classification by support vector machine with intelligently selected training data for an operational application, International Journal of Remote Sensing. **29**(8), 2227-2240.

McDonald, R. (1995), CORONA: success for space reconnaissance, a look into the Cold War, and a revolution for intelligence, Photogrammetric Engineering and Remote Sensing, **61**, 689-720.

McGarigal, K, Cushman, S. A., Neel, M. C., Ene, E. (2002), FRAGSTATS: Spatial Pattern Analysis Program for Categorical Maps (Available from http:/www.umass.edu/landeco/research/fragstats/fragstats.html).

Merino, M.T. and Nunez, J. (2007), Super-resolution of remotely sensed images with variable-pixel linear reconstruction, IEEE Transactions on Geoscience and Remote Sensing. **45**(5), 1446-1457.

Mertens, K.C., De Baets, B., Verbeke, L.P.C. and De Wulf, R.R. (2006), A sub-pixel mapping algorithm based on sub-pixel/pixel spatial attraction models, International Journal of Remote Sensing. **27**(15), 3239-3310.

Mertens, K.C., Verbeke, L.P.C., Westra, T. and Wulf, R.R.D. (2004), Sub-pixel mapping and sub-pixel sharpening using neural network predicted wavelet coefficients, Remote Sensing of Environment. **91**, 225-236.

Mese, M. and Vaidyanathan, P.P. (2002), Recent advances in digital halftoning and inverse halftoning methods, IEEE Transactions on Circuits and Systems - 1: Fundamental Theory and Applications. **49**(6), 790-805.

Mianji, F.A., Gu, Y., Zhang, Y. and Zhang, J. (2011), Enhanced self-training superresolution mapping technique for hyperspectral imagery, IEEE Geoscience and Remote Sensing Letters. **8**(4), 671-675.

Muad, A.M. and Foody, G.M. (2010). Super-resolution analysis for accurate mapping of land cover and land cover pattern. In Proceeding of the IEEE International Geoscience and Remote Sensing Symposium (IGARSS), Honolulu, Hawaii, USA, 25-30 July 2010.

Muad, A.M. and Foody, G.M. (2011), Super-resolution mapping of lakes from imagery with a coarse spatial and fine temporal resolution, International Journal of Applied Earth Observation and Geoinformation. In press.

Nellis, M.D. and Briggs, J.M. (1989), The effect of spatial scale on Konza landscape classification using textural analysis, Landscape Ecology. **2**(2), 93-100.

Newton, A.C., Hill, R.A., Echeverria, C., Golicher, D., Benayas, J.M.R., Cayuela, L. and Hinsley, S.A. (2009), Remote sensing and the future of landscape ecology, Progress in Physical Geography. **33**(4), 528-546.

Nguyen, M.G., Atkinson, P.M. and Lewis, H.G. (2011), Super-resolution mapping using Hopfield neural network with panchromatic imagery, International Journal of Remote Sensing. In press.

Nguyen, M.Q., Atkinson, P.M. and Lewis, H.G. (2005), Superresolution mapping using a Hopfield neural network with LIDAR data, IEEE Geoscience and Remote Sensing Letters. **2**(3), 366-307.

Nguyen, M.Q., Atkinson, P.M. and Lewis, H.G. (2006), Superresolution mapping using a Hopfield neural network with fused images, IEEE Transactions on Geoscience and Remote Sensing. **44**(3), 736-749.

Nigussie, D., Milla, R.Z.-. and Clevers, J.G.P.W. (2011), Possibilities and limitations of artificial neural networks for subpixel mapping of land cover, International Journal of Remote Sensing.In press.

Nikhil, R.P., and J. C. Bezdek. (1995). On cluster validity for the fuzzy c-means model, IEEE Transactions on Fuzzy Systems. **3**(3), 370-379.

Nixon, M.S. and Aguado, A.S. (2002), Feature Extraction and Image Processing, Newnes, Oxford.

Oskui, P. and Stark, H. (1988), Tomographic image reconstruction using the theory of convex projections, IEEE Transactions on Medical Imaging. **MI-3**, 45-58.

Packalen, P., Tokola, T., Saastamoinen, J. and Maltamo, M. (2006), Use of a super-resolution method in interpretation of forests from multiple NOAA/AVHRR images, International Journal of Remote Sensing. **27**(24), 5341-5357.

Paik, J.K. and Katsaggelos, A.K. (1992), Image restoration using a modified Hopfield network, IEEE Transactions on Image Processing. **1**(1), 49-63.

Park, S.C., Park, M.K. and Kang, M.G. (2003), Super-resolution image reconstruction: a technical overview, IEEE Signal Processing Magazine. **20**(3), 21-36.

Park, S.K. and Schowengerdt, R.A. (1982), Image sampling, reconstruction, and the effect of sample scene phasing, Applied Optics. **21**(17), 3142-3151.

Pei, S.C. and Tseng, C.C. (1994), Two dimensional IIR digital notch filter design, IEEE Transactions on Circuits and Systems - II: Analog and Digital Signal Processing. **41**(3), 227-231.

Pitas, I. (2000), Digital Image Processing Algorithms and Applications, John-Wiley & Sons, Inc., New York.

Press, W.H., Teukolsky, S.A., Vetterling, W.T. and Flannery, B.P. (2007), Numerical Recipes: The Art of Scientific Computing, 3rd ed. Cambridge University Press, Cambridge.

Riordan, B., Verbyla, D. and McGuire, D. (2006), Shrinking ponds in subarctic Alaska based on 1950-2002 remotely sensed images, Journal of Geophysical Research **111**(G04002), 1-11.

Rosin, P.L. (2001), Robust pixel unmixing, IEEE Transactions on Geoscience and Remote Sensing. **39**(9), 1978-1983.

Roy, D. P. (2000), The impact of misregistration upon composited wide field of view satellite data and implications for change detection, IEEE Transactions on Geoscience and Remote Sensing, **38**(4), 2017-2032.

Ruelland, D., Levavasseur, F. and Tribotte, A. (2010), Patterns and dynamics of land-cover changes since the 1960s over three experimental areas in Mali, International Journal of Applied Earth Observation and Geoinformation. **125**, S11-S17.

Saura, S. (2002), Effects of minimum mapping unit on land cover data spatial configuration and composition, International Journal of Remote Sensing. **23**(22), 4853-4880.

Schneider, W. (1993), Land use mapping with subpixel accuracy from landsat TM image data, Final Proceedings of the 25th International Symposium on Remote Sensing and Global Environment Change. 155-161.

Schowengerdt, R.A. (1995), On the estimation of spatial-spectral mixing with classifier likelihood functions, Pattern Recognition Letters. **17**(13), 1379-1387.

Schowengerdt, R.A. (2007), Remote Sensing: Models and Methods for Image Processing, Academic Press, Burlington MA.

Serra, J. (1984), Image analysis and mathematical morphology, Academic Press, Orlando, FL.

Serra, P., Pons, X. and Sauri, D. (2008), Land-cover and land-use change in a Mediterranean landscape: A spatial analysis of driving forces integrating biophysical and human factors, Applied Geography. **28**, 189-209.

Settle, J.J. and Drake, N.A. (1993), Linear mixing and the estimation of ground cover proportions, International Journal of Remote Sensing. **14**(6), 1159-1177.

Shao, G. and Wu, J. (2008), On the accuracy of landscape pattern analysis using remote sensing data, Landscape Ecology. **23**, 505-511.

Shen, D. and Ip, H.H.S. (1997), A Hopfield neural network for adaptive image segmentation: An active surface paradigm, Pattern Recognition Letters. **18**, 37-48.

Shen, H.-F., Ng, M.K., Li, P.-X. and Zhang, L.-P. (2009), Super-resolution reconstruction algorithm to MODIS remote sensing images, The Computer Journal. **52**(1), 90-100.

Sicairos, M.G.-., Thurman, S.T. and Fienup, J., R. (2008), Efficient subpixel image registration algorithms, Optics Letters. **33**(2), 156-158.

Smith, L.C., Sheng, Y. and Macdonald, G.M. (2005), Disappearing Arctic Lakes, Science. **308**(5727), 1429.

Soummer, R., Pueyo, L., Sivaramakrishnan, A. and Vanderbei, R.J. (2007), Fast computation of Lyot-style coronagraph propagation, Optics Express. **15**(24), 15935-15951.

Stark, H. and Oskui, P. (1989), High-resolution image recovery from image-plane arrays, using convex projections, Journal of the Optical Society of America. **6**(11), 1715-1726.

Tatem, A.J., Lewis, H.G., Atkinson, P.M. and Nixon, M.S. (2001a), Super-resolution target identification from remotely sensed image using a Hopfield neural network, IEEE Transactions on Geoscience and Remote Sensing. **39**(4), 781-796.

Tatem, A.J., Lewis, H.G., Atkinson, P.M. and Nixon, M.S. (2001b), Multiple-class land-cover mapping at the sub-pixel scale using a Hopfield neural network, International Journal of Applied Earth Observation and Geoinformation. **3**(2), 184-190.

Tatem, A.J., Lewis, H.G., Atkinson, P.M. and Nixon, M.S. (2002), Super-resolution land cover pattern prediction using a Hopfield neural network, Remote Sensing of Environment. **79**, 1-14.

Thornton, M.W., Atkinson, P.M. and Holland, D.A. (2006), Sub-pixel mapping of rural land cover objects from fine spatial resolution satellite sensor imagery using super-resolution pixel-swapping, International Journal of Remote Sensing. **27**(3), 473-491.

Thornton, M.W., Atkinson, P.M. and Holland, D.A. (2007), A linearised pixel-swapping method for mapping rural linear land cover features from fine spatial resolution remotely sensed imagery, Computers and Geosciences. **33**, 1261-1272.

Tikhonov, A. and Arsenin, V. (1977), Solution of Ill-Posed Problems, John Wiley and Sons.

Tipping, M.E. (2001), Sparse Bayesian learning and the relevance vector machine, Journal of Machine Learning Research. **1**, 211-244.

Topan, M., Maktav, D., Jacobsen, K. and Buyuksalih, G. (2009), Information content of optical satellite images for topographic mapping, International Journal of Remote Sensing. **30**(7), 1819-1827.

Toutin, T. (2009), Fine spatial resolution optical sensors, In Warner, T. A., Nellis, M. D., Foody, G. M. (Eds) The SAGE Handbook of Remote Sensing, Sage, London, 108-122.

Tsai, R.Y. and Huang, T.S. (1984), Multiframe image restoration and registration, Advances in Computer Vision and Image Processing. **1**, 317-319.

Tseng, C.C. and Pei, S.C. (1996), 2D multiple notch filter design, Electronics Letters. **32**(22), 2065-2066.

Tso, B. and Mather, P.M. (2009), Classification Methods for Remotely Sensed Data, 2nd ed., Taylor and Francis, London.

Ulichney, R.A. (1987), Digital Halftoning, MIT Press, Cambridge, MA.

Vapnik, V. (1995), The Nature of Statistical Learning Theory, Springer-Verlag, New York.

Venkata, N.D., Kite, T.D., Venkataraman, M. and Evans, B.L. (1998), Fast Blind Inverse Halftoning, In Proceedings of the IEEE International Conference on Image Processing, Chicago, IL, USA, **2**, 64-68.

Verhoeye, J. and De Wulf, R. (2002), Land cover mapping at sub-pixel scales using linear optimization techniques, Remote Sensing of Environment. **79**(1), 96-104.

Vermote, E.F., El Saleous, N.Z. and Justice, C.O. (2002), Atmospheric correction of MODIS data in the visible to middle-infrared: first results, Remote Sensing of Environment. **83**, 97-111.

Warner, T. A, Nellis, M. D., Foody, G. M. (2009), Remote sensing scale and data selection issues, In Warner, T. A., Nellis, M. D., Foody, G. M. (Eds) The SAGE Handbook of Remote Sensing, Sage, London, 3-17.

Weiss, D.J. and Crabtree, R.L. (2011), Percent surface water estimation from MODIS BRDF 16-day image composites, Remote Sensing of Environment. **115**, 2035-2046.

Woodcock, C. and Strahler, A. (1987), The factor of scale in remote sensing, Remote Sensing of Environment. **21**, 311-332.

Yang, J. and Huang, T. (2011), Image super-resolution: Historical overview and future challenges, In Milanfar, P. (Ed.), Super-resolution Imaging, CRC Press, Boca Raton, FL, 1-33.

Yang, X. J., Liu, Z. (2005), Quantifying landscape pattern and its change in an estuarine watershed using satellite imagery and landscape metrics, International Journal of Remote Sensing, **26**(23), 5297-5323.

Zhan, Q., Molenaar, M. and Lucieer, A. (2002), Pixel unmixing at the sub-pixel scale based on land cover class probabilities: application to urban areas, In Foody. G.M. and Atkinson,

P.M. (Eds) Uncertainty in Remote Sensing and GIS, John Wiley & Sons, West Sussex, 59-76.

Zitova, B. and Flusser, J. (2003), Image registration methods: a survey, Image and Vision Computing. **21**, 977-1000.